Understanding the Crystalline Landscape of Metal Chalcogenide Materials

By

Jeremy Randy Bairan Espano

Dissertation

Submitted to the Faculty of the

Graduate School of Vanderbilt University

in partial fulfillment of the requirements

for the degree of

DOCTOR IN PHILOSOPHY

in

Interdisciplinary Materials Science

May 10, 2024

Nashville Tennessee

Approved:

Janet Macdonald, Ph.D.

Josh Caldwell, Ph.D.

Timothy Hanusa, Ph.D.

Sandra Rosenthal, Ph.D.

De-en Jiang, Ph.D.

This work is dedicated to Neon Newton Espano: dog, best friend, and the light of my life.
With love and happiness.

If the sky that we look upon
Should tumble and fall
Or the mountains should crumble to the sea
I won't cry, I won't cry
No, I won't shed a tear
Just as long as you stand
Stand by me
-Ben E. King

Acknowledgements

Contrary to my scientific endeavors, I strongly believe that I have been very superstitiously lucky throughout this process of growing as a scientist. It is almost as if I had won some supernatural lottery that enabled me to have one of the most enjoyable Ph.D. journeys ever. My journey thus far has been exhilarating—full of love, full of discovery, and full of laughter. It is a chapter in my life that I'll look at with extreme nostalgia. So, as a scientist, this is the part where I show proof of how lucky I truly have been.

My mother and my brother come first, as all these things would not have been possible without them. Thank you, mom, for your hard work, intelligence, humor, and resilience. I could not have asked for a better role model. I am truly lucky to have been born your son and filled with your love. You've given me an example to follow as someone who perseveres and laughs and smiles while doing so. Robby, you are literally one of the smartest, hardworking, people I know. I am never truly worried about where you'll end up because I know that success will follow wherever you go. Thank you for being such an inspiring younger brother, and I am truly fortunate to be able to share the same campus as you.

I am lucky for my big, caring, supportive, and loving Asian family, most specifically Geoff, Kim, Grandma Rosa, Auntie Lourdes, Uncle Kevin, Nelson, Eunsoo, Ronald, Roland, Grizeline, Rhaeylne, Reianne, Tabitha, Kai, and Renzo. To the family that comes before me, I am lucky to have been instilled with your hardworking traits, to aspire and dream of successful careers and lifestyles like yours, and for your traditions to be transformed into some of mine. To the family that has traversed with me, I am lucky for your wisdom, for your guidance that helped me translate these old values into the new world, and for helping me establish my identity as an Asian-born American. To the family that comes after me, I'm lucky to have the loving, supportive next generation that pushes me to be the most authentic and compassionate version of myself.

I think that my luck really started to expand at Boston College: the nucleation of who I am as a person—not necessarily Boston College *the place*, but Boston College *the people*. The people here truly made me who I am; they made me feel competent, powerful, and deserving. To Alex, compassion has saved my life and changed it for the better. I'm glad that you have been able to help me grow into the scientist and the person I am today. Matt, your smarts, talents, and strengths inspire me to also be my smartest and strongest self. Lauren, your happiness turned what could be a bleak and depressing 5 years into 5 years of light. Liv, thank you for your constant support. Pablo,

you always know how to make me laugh and have really transformed my life into a make-shift comedy. I have two mentors from Boston College who were integral for me becoming the scientist I am today. To Dr. David Healey and the Boston College Marching Band, thank you for helping me grow my confidence. To the late Dr. Neil Wolfman, who knew what kind of scientist I could become and pushed for that best version of myself, I will be forever grateful.

My fortune did not halt at college or after my childhood; in fact, it flourished during my time at Vanderbilt University. It was almost like cosmic intervention that I joined the Interdisciplinary Materials Science (IMS) Program. I was sitting down in Professor Neil Wolfman's office, talking about my time at Boston College, when I received a call from Dr. Janet Macdonald telling me that she thinks I should apply to the IMS program. I find it almost too perfect, like a torch of mentorship being passed from my old undergraduate chemistry mentor to who I would ironically find to be my new Ph.D. advisor, Dr. Janet Macdonald. Janet, thank you for being such an invaluable member of my Ph.D. experience. Your guidance helped me find my own success and allowed me to thrive in ways I could have never imagined. Your excitement and enthusiasm about science were as contagious as COVID-19 and allowed me to find a deep, profound admiration of science. I am extremely fortunate to have picked up your phone call. To Dr. McCabe, Dr. Jiang, Dr. Rosenthal, Dr. Hanusa, and Dr. Caldwell for your guidance as well. To the Macdonald Lab members, your community gave me a home, and your excitement for science pushed me to be the best scientist I could be. To Chris, thank you for your mentorship and great food. To Peter, thank you for being the best student a mentor could ask for.

My luck is vast, and my home here at Vanderbilt is just as vast. I have been truly lucky to have the support and care of the IMS program. First off, thank you, Sarah, for being one of my biggest supporters, points of guidance, and voices of reason. You have pushed me to develop skills that have made me successful in graduate school, and I am confident that they will keep pushing me forward. You are the anchor of the IMS program, and I couldn't have asked for a better place to complete my Ph.D. To the IMS program, thank you for being such a great family. I truly don't think there is a more special Ph.D. program in the world that quite emulates what I have experienced with you all. Cal, Ryan, and Brayden, thank you for making the IMS program more of a family than a group of colleagues. You all helped me feel like I truly found my people and helped me own my place. I will truly miss all our game nights and fun times that we have had with each other. To Lexi, you've truly been a voice of kindness and care during this time.

But this village extends past the IMS program, as I have been very lucky to grow with other smart, kind graduate students here at Vanderbilt University. To Xavier, thank you for allowing me to be my most authentic self. To Alyssa, thank you for sharing your wise words of wisdom, balancing my chaotic nature, and showing me kindness and love throughout these four years. Lauren**,** you have really helped me grow these past couple of years. You have challenged me, made me grow, calmed me, pushed me to be the best scientist I could be, assured me that I was the best scientist I could be, and made me laugh with tears in my eyes more times than I could count. I am very grateful that I could share this Ph.D. journey with you, and even in the rough times of this journey—I still look back at it with laughter and smiles, and you are a big reason for that.

In this time of fortune, there are four people I need to thank particularly. These people make me feel like I am the smartest person in the room and the luckiest person in the world. I am lucky to have gotten to know them and to love them. To Austin, I am lucky for your loyalty and love. You have truly been by my side through the good and the bad. You've seen the times when I've been smart, brave, and compassionate, as well as the times when I've been dumb, scared, and angry. Yet throughout all of this, you have continued to be one of my strongest supporters, as well as one of my wisest consultants. I'm excited when we get to rule the world together. To Matthew, the way that you light up the world with your selflessness, kindness, and hope has made me a better person. You've truly helped me make this place a home. You've helped me laugh, lifted me up when I was down, and made me one of the happiest and proudest graduate students in the world. I'm excited to become lifelong friends with you. To Andres, Neon and I have truly been lucky to have become close with you and Panda. I consider you like a brother; sometimes you drive me insane, but at the end of the day, I still love you. You've made this journey exciting, funny, and something that I could smile about. To Lexie, thank you for being the calm to my chaos, and one of the best labmates a scientist could ever ask for. You made science fun and exhilarating while also keeping me grounded. Working next to you helped me push myself to the next level because I don't think I've ever met such a meticulous, precise, and hardworking person as you. I am truly lucky that I got to experience the Macdonald Lab with you as my desk and COVID buddy.

This could not have been possible without Vanderbilt University, the Vanderbilt Institute of Nanoscale Science and Engineering, the Russel G. Hamilton Dissertation Enhancement Grant, the Chemistry Department, and the National Science Foundation (CHE1905265 and CHE2305161). With much love, luck, and thanks.

TABLE OF CONTENTS

Page

LIST OF TABLES..... ix

LIST OF FIGURES. x

Chapter 1: Introduction 1

1.1 The Atomic Arrangements of Binary Crystals.....1
1.2 Synthesis of Metal Chalcogenide Nanocrystals.....3
1.3 The Kinetic and Thermodynamic Arguments of Polymorphic Control.....5
1.4 Precursor Decomposition: Mechanics *vs.* Kinetics.....7
1.5 The Scope of this Dissertation 11

Chapter 2: Phase Control in the Synthesis of Iron Sulfides 19

2.1. The Phase Space of Iron Sulfide Nanocrystals 19
2.2. Synthesis of Iron Sulfide Nanocrystals.....21
2.3. Using a Library of Thioureas to Control Iron Sulfide Phase 27
2.4. Understanding the Phase Landscape of the Iron Sulfides.....31
2.5. Targeting the Iron Sulfides Using a Rationale 36
2.6. Conclusion 38

Chapter 3: Phase Control in the Synthesis of Cobalt Sulfides.....43

3.1. The Cobalt Sulfides.....43
3.2. Synthesizing Cobalt Sulfides Using Tunable Thioureas.....44
3.3. Phase Control of the Cobalt Sulfides 48
3.4. Rational Synthesis of the Cobalt Sulfides.....51
3.5. Conclusion 53

Chapter 4: Phase Control in the Synthesis of Nickel Sulfides 55

4.1. The Nickel Sulfides.....55
4.2. Synthesizing Nickel Sulfides 57
4.3. Phase Control in the Nickel Sulfides 63
4.4. Targeting the Nickel Sulfide Phases 66
4.5. Conclusion 69

Chapter 5: Conclusion and Future Outlook.....73

5.1. Summary.....73
5.2. Field Outlook 76

Chapter 6 Appendix.....79

6.1. Appendix A 79
6.2. Appendix B 106
6.3. Appendix C 114

List of Tables

Table		Page
2.1.	The Iron Sulfides	20
3.1.	The Cobalt Sulfides	43
4.1.	The Nickel Sulfides	56
A.1.	Quantification of the iron sulfides	88
B.1.	Quantification of the nickel sulfides	106
C.1.	Quantification of the cobalt sulfides	114

List of Figures

Figure		Page
1.1.	Two types of anion stackings and cation complexes	2
1.2.	Kinetic and thermodynamic approaches to controlling phase	6
1.3.	Phase control correlated to C-S bond strength	9
2.1.	Chemical scheme and XRD of synthesized iron sulfides	30
2.2.	A bottom-up, synthetic phase diagram of the iron sulfides	31
2.3.	A map describing the transformations in the iron sulfides	32
2.4.	Timed studies of the iron sulfides	35
2.5.	The rational synthesis of the iron sulfides	38
3.1.	The synthesis of the cobalt sulfides	49
3.2.	A bottom-up synthetic phase diagram of the cobalt sulfides	50
3.3.	The rational synthesis of all the cobalt sulfides	52
4.1.	Synthesis and corresponding XRD of the nickel sulfides	62
4.2.	Time and temperature studies of nickel sulfides	63
4.3.	Nickel sulfide transformation pathways	65
4.4.	The rational synthesis of the nickel sulfides	67
A.1.	^{13}C NMR of the C=S peak in substituted thioureas	79
A.2.	Ratio studies of the iron sulfides	81
A.3.	Thiourea and oleylamine NMR reactivity and iron sulfide synthesis	82
A.4.	Octadecene NMR reactivity studies	84
A.5.	Tetraglyme and thiourea reactivity studies	85
A.6.	XRD of iron sulfide synthesis in tetraglyme	86

A.7. Phase pure synthesis of the iron sulfides 87

A.8. XRD of the marcasite one-pot synthesis.....87

A.9. Rietveld refinements of the iron sulfides 105

B.1. Rietveld refinements of the cobalt sulfides.....113

C.1. Rietveld refinements of the nickel sulfides.....125

List of Abbreviations

ccp	Cubic closed packed
hcp	Hexagonal closed packed
O_h	Octahedral
T_h	Tetrahedral
S_{py}	Square pyramidal
XRD	X-ray diffraction
TEM	Transmission electron microscopy
NMR	Nuclear magnetic resonance
SAED	Selected area electron diffraction
WAXS	Wide angle X-ray scattering
SAXS	Small angle X-ray scattering
UV-VIS	Ultraviolet-visible spectroscopy
mmol	millimole
ODE	Octadecene
OLAM	Oleylamine

List of Publications

Parts of the dissertation have been adapted with permission from the following publications

In Preparation

(1) Phase Control in the Synthesis of Cobalt Sulfides. Edwards, P.; **Bairan Espano, J.R**.; Macdonald, J. E. in prep (2024)

(2) Using a Library of Thioureas and Thiophenols for Nickel Sulfide Phase Control. **Bairan Espano, J.R.;** Hinojosa, R.; Veglak, J.; Macdonald, J. E. in prep (2024).

Published (*denotes equal contributions)

(1) Controlling Phase in Colloidal Synthesis. Endres, E.*; **Bairan Espano, J. R.***; Koziel , A.*; Peng, A.*; Shults, A.*; Macdonald, J. E.* *ACS Nanoscience AU*. Accepted (2024).

(2) Phase Control in the Synthesis of Iron Sulfides. **Bairan Espano, J. R**.; Macdonald, J. E. *J Am Chem Soc (* 2023), *145* , 18948-18955. DOI: 10.1021/jacs.3c05653

Chapter 1: Introduction

1.1 The Atomic Arrangements of Binary Crystals

The arrangement and identity of atoms determines the properties of all solids. Our ability to implement crystalline materials in a wide array of applications is heavily determined by our ability to controllably synthesize them. However, controlling the atomic arrangement of atoms in solids proves to be complex, even as combinations of two atoms can exist as multiple crystal structures by varying stoichiometries and symmetries.

The iron sulfides are a great example of this complexity. The iron sulfides consist of eight different polymorphs, each with different stoichiometries and crystal packing. Pyrite, cubic FeS_2, is most suitable in solar cell applications due to its electronic structure and large band gap.[1-3] Mackinawite, cubic Fe_3S_4, is a great candidate for environmental remediation applications due to its highly reactive surfaces, high solubility, and reducing abilities.[4-6] The applications that are shown in these metal chalcogenides cannot be truly realized unless synthetic routes and methods are established. This is most evident with the synthetic gaps with marcasite, hexagonal FeS_2.[9, 10] Our ability to use this great battery anode material[11] is primarily due to our inability to target and synthesize the marcasite iron sulfide.

Understanding how these crystals repeat and are structured is an important aspect in nanocrystalline synthesis and correlates to the electronic and chemical behaviors of these materials. In a crystal containing two different elements the identity of each element is the first underlying aspect of the crystal structure. The atomic identity is then followed by the stoichiometry. Finally, we can organize the crystal based on its crystal structure. In regards to this dissertation, the crystal structure will be divided into two main aspects: how the anion stacks and how the chalcogenide, in this case the sulfur, surrounded the cation.

Most of the metal chalcogenides discussed in this dissertation can be organized in either a cubic arrangement, a hexagonal arrangement, or a body centered cubic arrangement. In crystals where the atoms exhibit a cubic structure, the anions are arranged in an ABC closed pack layer structure, where the A layer and the C layer are offset. In contrast, the hexagonal symmetry has a repeating AB anion stacking pattern, where the A and B layers alternate and every other layer lies

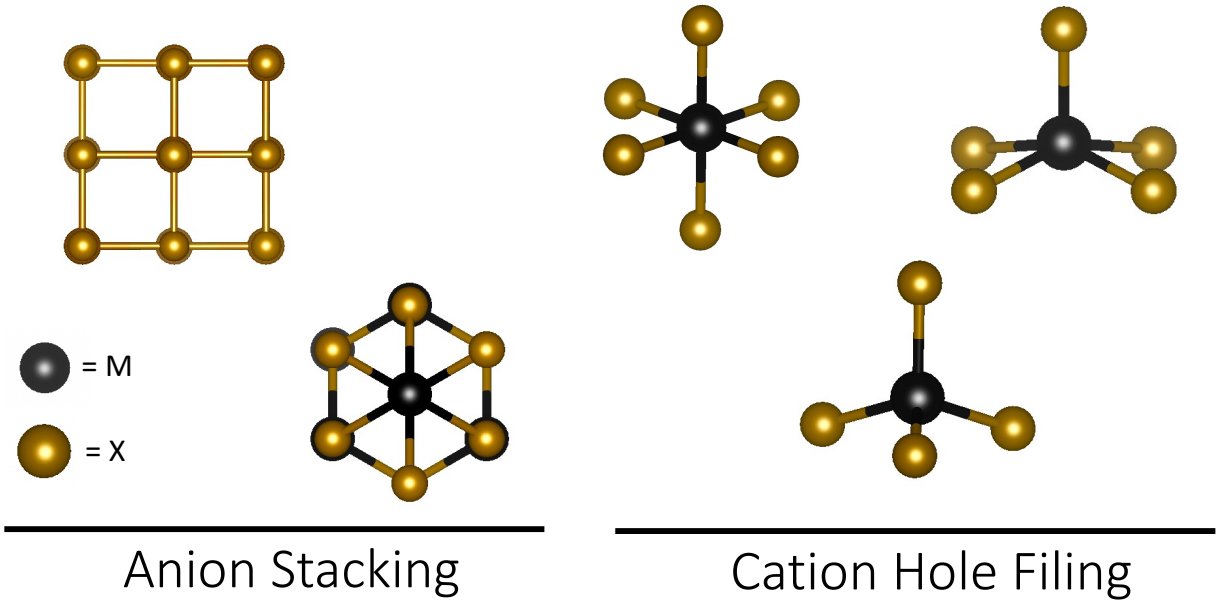

Figure 1.1. Crystal structures showing the two different type of anion stackings and cation hole filing that are discussed in this dissertation. Crystal structures were made using VESTA.[8]

directly above one another. In a body centered cubic crystal structure, one atom is surrounded by 8 neighboring atoms in a cubelike structure.

When studying the cation holes of these crystal structures and examining how the metal sits within the chalcogenide atoms, they most often exhibit a tetrahedral cation hole or an octahedral cation hole. The tetrahedral holes have a coordination number of four, and a bond angle of 109.5° (this angle can be distorted depending on the crystal structure) , whereas the octahedral holes have a coordination number of six and a bond angle of 90°. While most of the crystals discussed in this dissertation exhibit an anion stacking in either hexagonal or cubic fashion, crystals can adopt a wide variety of different cation hole configurations. Crystals such as millerite (NiS) can adopt a square pyramidal cation hole with a coordination of five, and some of the metal sulfide allotropes contain combinations of tetrahedral and octahedral holes such as greigite (Fe_3S_4) and polydymite (Ni_3S_4). Additionally, in the copper sulfides, some of the cations will adopt a trigonal hole filing complex, where the metal anion is bonded to 3 surrounding atoms.

The combination of these anion and cations will make what we call ionic structures. Ionic structures are crystals that contain a combination of a metal (in this case iron, cobalt, or nickel) and a nonmetal (in this case sulfur) and held by the attraction of the negative and positive forces

from the anion and cation. The cations and anions both adopt individual repeating crystal structures, while being simultaneously bonded to their counterpart. The identity of the ionic crystal can be determined by a few factors such as the overall stoichiometry of the elements, the charges on each ion, coordination of the anions, and sizes of the atoms.

While most of this introduction discusses thermodynamics and organochalcogenide chemistry, it is important to take into account the crystal structure of these materials in order to more confidently traverse the landscape.

1.2 Synthesis of Metal Chalcogenide Nanocrystals

In discussing about the synthesis of metal sulfide phases, many variables can affect the resulting crystal. The first and most apparent is the synthetic technique. Each synthetic technique comprises different components such as solvent, temperature, time of reaction, pressure, metal precursor source, sulfur precursor source, and coordinating ligand. Each component plays an important role in phase selection, and as noted later, changing individual components can lead to massive shifts in the resulting phase.

There are many reports of the synthesis of various metal chalcogenides, and each method allows for varying control over morphology, size, and most importantly atomic arrangements, as well as offers some range of ability to understand what happens *in situ*. The four main synthetic techniques most widely used for the synthesis of metal chalcogenides are (1) hydrothermal, (2) solvothermal (3) gas/annealing reactions, and (4) colloidal synthesis.

Hydrothermal synthesis constitutes one of the more common techniques to prepare metal sulfide nanocrystals and has been reported to show controllable phase control on rhodium sulfide, manganese sulfide, nickel sulfide, copper sulfide, and cadmium sulfide.[12-21] As suggested by its name, the crystal nucleation and growth occurs in a sealed autoclave in water at high temperatures (greater than 100ºC which allows for the water to boil and in turn create a high pressure) and pressures (20-100 MPA).[12, 13] While much work has been done on synthesizing these materials using hydrothermal methods, it is much harder to understand the chemical mechanisms happening within the synthesis when compared to colloidal synthesis because of the inability to monitor the reaction *in situ*.

There are only a few studies that show the control of metal sulfide phases using hydrothermal methods, and most only control the phase of these binary metal sulfides by simply varying the amount of available sulfur precursors in the reaction in both rhodium sulfide, copper

sulfide, and manganese sulfide nanocrystals.[18-20] Additionally, the temperature at which these hydrothermal reactions take place has a huge effect on the resulting phase as seen in synthesis and transformation of manganese sulfide, copper sulfide, and nickel sulfide phases.[15, 20, 22] Most notably, *Hu et al.* show that by changing the coordination agents post hydrothermal synthesis, they were able to induce nickel sulfide phase control. This denoted one of the only studies in this genre to attempt to understand how one synthetic aspect of hydrothermal synthesis can affect the overall reaction.[17]

Solvothermal is a synthetic technique very similar to hydrothermal synthesis. This technique involves synthetic reactions in which sealed containers and solvents other than water can be brought up to temperatures higher than their boiling points in an autoclave. At these high temperatures (100º-1000ºC) and pressures (1-1000 atm) the solubility and the reactivity of reactants can greatly increase.[23, 24] As of date, there are some reports of controllable phase control using this synthetic technique including nickel sulfide, cobalt sulfide, copper sulfide, and cadmium sulfide.[25-29]

Similarly, to hydrothermal methods, most studies show that by simply changing the sulfur containing precursor, the sulfur content, the reaction times, and the solvent can also have a large effect on the overall synthesized phase.[25-27, 29] A few studies take a more in-depth study of nickel sulfide nanocrystals. The phases of these crystals were controlled by changing sulfur content and reaction times.[26] Most notably, the influence of a surfactant has also been shown as a phase control agent as it was hypothesized to affect the anion diffusion and ultimately the overall growth mechanisms of nickel sulfides.[25]

There are very few solid-state synthetic techniques that can boast metal chalcogenide nanocrystalline growth. Currently, gas/annealing solid-state reactions can boast in its abilities to make thin film metal chalcogenide materials. This technique has a lot of nuances behind its mechanism due to the integration of both crystal chemistry and chemical engineering. For example, the phases and crystals generated in this process are dictated by substrate, annealing process, gas flow, heating temperature, heating process, and even precursor transport processes. A lot of this work focuses on epitaxial growth to try to ensure that these films grow in a uniform and controlled fashion.[30]

Similarly to solvothermal and hydrothermal methods, changing the amount of sulfur precursor also seems to have large effect on the resulting phase.[31] Recently, the phase engineering

of iron sulfides, selenides, and tellurides was investigated using chemical vapor deposition, and it was found that by changing both the temperatures of the iron source as well as the chalcogenide source, the phase and composition of the synthesized 2D material could be controlled. Notably, the preparation of the precursor powder in this method can lead to different exposed surface area amounts which also has a large effect on phase.[32]

The work discussed in this dissertation revolves around colloidal synthesis. Colloidal synthesis overall permits a closer, more careful look into the reaction vessel. Unlike solvothermal, hydrothermal, and gas phase reactions, where reaction conditions such as pressure, pH, and solvent volume are hard to measure, colloidal synthesis allows for a more controlled reaction, with the ability to take a more in-depth analysis of the reaction conditions and mechanisms.

Colloidal synthesis a standard practice used to make inorganic nanocrystals, and the ability to measure reaction conditions during synthesis allows for better reproducibility. During colloidal synthesis of metal chalcogenides, the metal atoms and chalcogenide atoms are produced *via* a chemical reduction, decomposition of a precursor from high temperatures, or even reducing agents.[33] The ways that reaction conditions can be manipulated and changed in this experimental set-up are manyfold. Solvent, temperature, time, metal precursors, sulfur precursor choice, precursor concentration, ligands, reducing agents, and injection methods can all be changed and have been shown to have drastic effects on overall resulting phase. Taking a systematic approach to understanding the role of each reaction condition's effect on phase will be imperative in moving towards a more rational synthesis. The bulk of this thesis uses colloidal synthetic methods to attempt the control the phase of metal chalcogenide nanocrystals.

1.3 The Kinetic and Thermodynamic Arguments of Polymorphic Control

These synthetic techniques (hydrothermal, solvothermal, gas/annealing, and colloidal) control the resulting phase by changing a wide number of reaction conditions. There are two main schools of thought that explain the growth and formation of phases: the kinetic argument and the thermodynamic argument. Understanding these arguments can help synthetic material scientists deconvolute *why* certain phases form at certain conditions.

In the kinetic argument, Ostwald's rule of stages states that metastable phases form first in nucleation, and transform into their most thermodynamically stable phase.[34] When thinking about different phases, each crystalline structure has different thermodynamic enthalpies and entropies of formations. From this, we can distinguish between the metastable phases (phases with lower

enthalpies of formation -ΔH_f) from the thermodynamically stable phases (phases with higher enthalpies of formation -ΔH_f). A great example of this was presented by Chung *et al.* who shows the nucleation and crystallization of $LiFePO_4$ as it transforms from a metastable transient state to its final cubic crystalline form.[35] Others have attributed the formation of metastable phases at these short times due to the surface energy. The large surface chemistry may in fact make these metastable phases the thermodynamically stable phases at these small sizes, also known as remnant metastability.[36] Statistical mechanics states that the energy of the surface is opposing the energy of the bulk, and at small sizes (**Eq. 1**), we enter the regime where surface area energy dominates overall energy. When these particles grow larger, the surface energy become less dominant, and the crystal will rearrange to the bulk thermodynamic structure.[37]

Equation 1: $\Delta G = \Delta G_S + \Delta G_V$

The thermodynamic argument suggests that at small sizes, when the surface area is high, the appropriate ligand, and the number of ligands during the reaction can force "metastable phases" to be the thermodynamic products at small sizes. When considering **equation 1,** where ΔG is the Gibbs free energy of the entire particle,ΔG_S is the Gibbs free energy of the surface, and ΔG_V is the

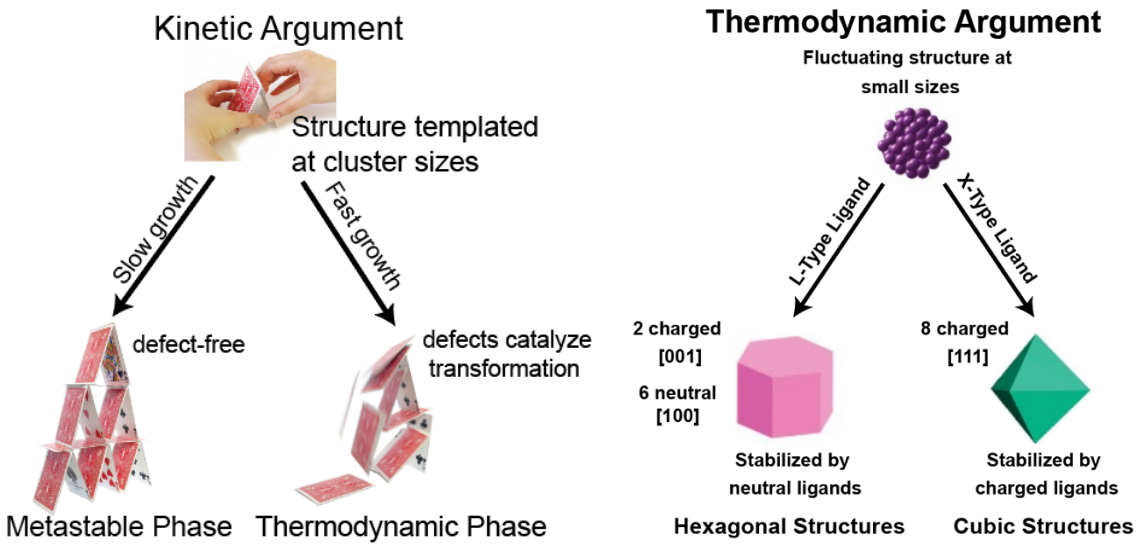

Figure 1.2. The kinetic and thermodynamic approaches to controlling phase in crystal growth. The kinetic argument suggests that metastable phases form first but slowly transform into their more thermodynamically stable version. The thermodynamic argument suggests that high surface: volume ratios and the ligand choice can form metastable phases perfer thermodynamic phases at small sizes.

energy of the bulk. At these small sizes we enter a regime where surface energy dominates. There is much more surface and much less bulk at these small sizes. Thus ligands, tools that highly mitigate this energy, become overwhelmingly dominating. Gao and Peng later made the argument that for 2 nm CdSe particles, the difference in enthalpy between the zinc blende and wurtzite structures (~0.11 eV) is negligible compared to the surface interactions. A single hydrogen bond, for comparison, is 0.21 eV, so surface ligand binding effects dominate.[38]

The bulk of this dissertation focuses on the kinetic argument, i.e., How molecules decompose, and how the speed, or the mechanism affects the growth and nucleation of nanocrystals. Most importantly, this dissertation takes a crystallographic look at the ways in which a metastable phase transforms into its more thermodynamically stable phase. Including this dialogue into the conversation of organochalcogenide decomposition allows us to understand crystalline growth more fully.

1.4 Precursor Decomposition: Mechanism *vs.* Kinetics

The thermodynamic and crystalline properties of crystals help illuminates the overall landscape of these metal chalcogenide allotropes, but it is our knowledge of inorganic and organic chemistry that enables us to traverse this landscape. For the metal sulfides, a wide range of sulfur containing materials have been used in the synthesis, such as thioureas,[39] dialkyl disulfides,[7] thiols,[7] elemental sulfur,[3] sodium sulfide[40] and many more sulfur-containing precursors. Although a wide variety of metal chalcogenide phases have been synthesized, rational phase control in bottom-up synthesis has not been completely understood - partly because the molecular transformations that preclude crystal formation in solution have been mostly overlooked.[7, 41, 42] In order to study systematic phase control, the speed at which organic molecules decompose in nanocrystalline synthesis needs to be studied separately from the mechanism by which organic molecules decompose.[7] Rhode*s et al.* showed that there is a correlation between the C-S bond strength of the organosulfide reagent and the sulfur content of the resulting phase in iron sulfide phases. Organosulfide bonds that had smaller bond dissociation energies led to more sulfur rich iron phases such as pyrite (FeS_2), whereas organosulfide bonds that had larger bond dissociation energies led to sulfur deficient phases such as pyrrhotite ($Fe_{1-x}S$). A closer look at the decomposition pathways of these materials shows that the diallyl disulfide molecule undergoes a direct formation of pyrite, indicating that the ways these molecules break down has a large influence on the resulting phase.[7] Similarly, Tappan *et al.* worked with ternary copper indium

selenide nanocrystals. Their work shows a similar trend where diselenide precursors with different bond dissociations lead to completely different products, a stronger C-Se bond caused a more metastable Cu_3Se_2 which will in turn transform into a wurtzite-like $CuInSe_2$, while weaker C-Se bonds will lead to the intermediate formation of $Cu_{2-x}Se$ and ultimately chalcopyrite, $CuInSe_2$.[43]

The Rhodes *et al.* study emphasized that the ways in which molecules decompose dictates crystal formation in iron sulfides. This work was built upon by Koziel *et al.*, who more closely studied the ways that diaryl diselenides decomposed and correlated these decomposition mechanisms to the formation of different copper selenide nanocrystals. Their work shows the importance of nuclear magnetic resonance (NMR) as a powerful tool to comprehensively understand the role of organochalcogeonide mechanism in phase control. Their work is an excellent example of how the use of NMR instrumentation can be used to observe and support precursor pathways that play a role in nanocrystal synthesis.[41] There is a large range of studies to this note that also support the idea that the mechanisms of precursor decomposition prelude and determine phase formation.[41, 44-46]

But the ways that precursors decompose and react with not only the metal but also the solvent and other chemical species will drastically affect the overall resulting phase. The Ozin group's use of ^{1}H and ^{13}C NMR showed that polysulfides react with excess oleylamine - the solvent- to generate H_2S, an intermediate that led to the production and formation of metal sulfide nanocrystals.[44] In our own group, Shults *et al.* showed that the oleate ligand influences the crystalline phase of colloidal metal sulfides through molecular side reactions with the precursor. Not only is it imperative to understand how these molecules will decompose, but it is equally important to understand how these molecules, or their decomposition products, could ultimately affect the overall synthetic reaction.

Decomposition pathways are not the only factor at play — the speeds at which these precursors decompose also plays a huge role in phase control. Jonathan Owen and his group at Columbia University have shown that by using a library of tunable thioureas and selenoureas, the rate at which sulfur and selenium is released into the system can be controlled.[39, 47, 48] In the study of the thioureas, by tuning the substituents of disubstituted thioureas, the rate of sulfur release into the system can be distinguished between four orders of magnitudes. The selenoureas, due to the larger selenium atom, are more reactive, and by changing the substituents on tri-substituted selenoureas, they tune the release of selenium into the system by four orders of magnitude.

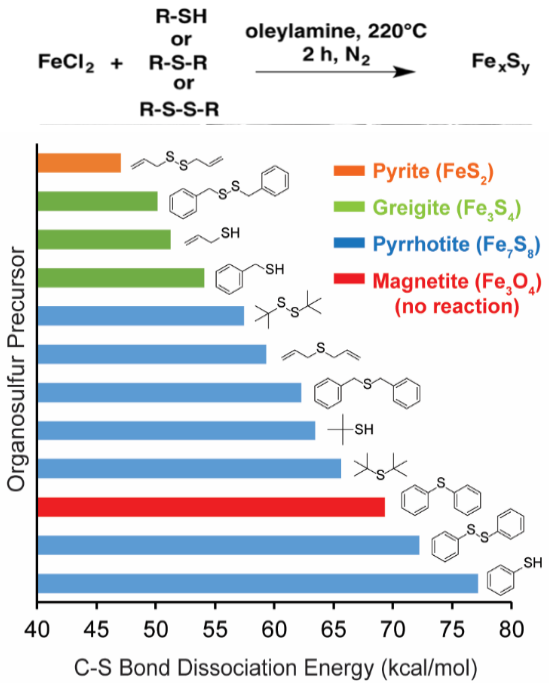

Figure 1.3. Sulfur content of the phase of Fe_xS_y correlated with C-S bond strength. Adapted from *Rhodes et al.*[7]

The pursuit of rational and comprehensive phase control has been challenging due to the complexity of the synthetic system, as even small changes in conditions can have a drastic effect on the resulting phase. Taking a systematic approach to understanding *all* the ways we can control phases will allow us to more easily, more reproducibly, and more rationally target each material with a level of synthetic control that has not previously been possible.

1.5 Characterization Techniques that aid in Phase Control

The most prominent and influential characterization technique used for identifying and quantifying crystalline materials is powder X-ray diffraction (pXRD). With it we are able characterize multiple crystalline phases with a low limit of detection, measure especially small nano-sized crystals, and measure the phase of the material in *ex-situ* and *in-situ* environments. While pXRD is a powerful technique that is accessible and versatile, the limits of current diffraction techniques make it challenging to identify and solve novel crystalline structures. As the field of phase control and phase targeting expands, the need to comprehensively characterize these novel phases will increase. pXRD is not the sole characterization technique used to characterize crystalline structures. Selected area electron diffraction (SAED) in the transmission electron microscope (TEM) can be used on individual nano-sized crystals, allowing for the identification of crystals even in mixtures.[49]

Overall, both TEM and pXRD are imperative workhorses of the phase control field and help characterize crystalline structures and document changes in these structures as synthetic conditions are changed. These two characterization techniques can be upgraded to follow and observe diffraction phenomena during colloidal growth. For example, heated chambers are very common in pXRD[50] but are limited due to the *in situ* particle concentration. *In situ* TEM can be used, and has been very successful at observing nucleation and growth events,[51] but the high electron dose can not only force phase transformations[52] but can also force unique chemistry reactions that likely do not reflect in-flask phenomena. Even heated *in situ* scanning TEM has been used to show the phase evolution of Nd-Ce-Fe-B nanocrystals.[53]

There are two powerful x-ray scattering techniques that overcome current barriers to *in situ* measurements: small angle X-ray scattering and wide-angle X-ray scattering. Synchrotron light sources provide a strong enough signal to allow for *in situ* measurements of crystalline phase in colloidal synthesis, typically using small angle and wide-angle X-ray scattering (SAX and WAX). There have been some studies using SAXS to observe *in situ* phase formations or structural changes in metal chalcogenide nanocrystals as a reaction progresses.[54-56] The use of these techniques can help clarify the roles of certain precursor roles in crystalline formation and/or transformation.[57] Others have used synchrotron techniques to study nucleation behaviors of nanocrystals.[58] While these two synchrotron experiments offer great resolution and can monitor phase transformation *in situ*, they remain mostly inaccessible to many nanocrystal chemists.

While XRD, TEM, SAXS, and WAXS are the four most used characterization techniques employed in phase control studies, often forgotten are techniques used by our colleagues in other fields of chemistry for *in situ* measurements from which phase or mechanism can be indirectly inferred. Techniques like ultra violet-visible spectroscopy (UV-Vis), steady state absorption spectroscopy, and even RAMAN spectroscopy are all great tools that enable close measuring of particles in solution; of these techniques some even distinguish phase transformations in nanocrystal nucleation[59] or help identify multiphase crystal structures.[60] Finally, NMR can be used in tandem with pXRD analysis to determine the organic mechanisms that preclude phase formation as previously shown by Koziel *et al*.[41] This wide range of analytical techniques can be used in interesting ways to determine how these crystal phases are transforming and help paint a more picture of bottom-up synthesis that can help illuminate the overall phase control story.

1.6 The Scope of this Dissertation

This dissertation willemploy the overarching themes in metal chalcogenide nanocrystalline synthesis. The bulk of this dissertation will be concerned with understanding how to rationally target iron sulfides, nickel sulfides, and cobalt sulfides comprehensively.

In the second chapter, the bottom-up synthesis of iron sulfide nanocrystals, the use of a tunable library of thioureas to control the kinetic decomposition speeds of sulfur precursors, solvent precursor effects in nanocrystalline synthesis, and the rational targeting of phases based on their anion crystal stacking will be described. The effect of temperature and thiourea decomposition speed will be analyzed and the landscape of iron sulfide nanocrystals will be established - mapping thermodynamics with crystal structures. The analysis and crystalline pathways generated by these studies will enable the rational targeting of six out of the eight iron sulfide phases.

The third chapter will use the knowledge discussed in chapter two to control the synthesis of cobalt sulfide nanocrystals. The kinetic decomposition effects of a wide variety of different thioureas on cobalt and the effect of phase templating will be observed. Using the knowledge gained in chapter two, the phase pure synthesis of all four cobalt sulfides can be achieved.

The fourth chapter will examine how phase control operates as we move down the periodic table to the nickel sulfides. The decomposition speeds of thioureas, concentration of thioureas, and the combination of both concentration and kinetic effects will be measured in nickel sulfide nanocrystalline synthesis. The effect of coordination and cation hole filing on nickel sulfide nanocrystals will be examined, and pathways that distinguish thermodynamics and crystal structure packing will be defined. In doing so, these studies will enable the phase pure synthesis of six out of seven nickel sulfide phases, as well as an additional study showing the effect of coordinated precursors on the resulting nickel sulfide phase.

The fifth chapter will conclude the dissertation with an overall summary of the work contained and an outlook of future research prospects for phase control of binary metal chalcogenide nanocrystals in a bottom-up synthesis.

References

(1) Kaur, G.; Kaur, M.; Thakur, A.; Kumar, A. *Recent Progress on Pyrite FeS_2 Nanomaterials for Energy and Environment Applications: Synthesis, Properties and Future Prospects*; Springer US, 2020. DOI: 10.1007/s10876-019-01708-3.

(2) Bi, Y.; Yuan, Y.; Exstrom, C. L.; Darveau, S. A.; Huang, J. Air stable, photosensitive, phase pure iron pyrite nanocrystal thin films for photovoltaic application. *Nano Letters* **2011**, *11* (11), 4953-4957. DOI: 10.1021/nl202902z.

(3) Li, W.; Döblinger, M.; Vaneski, A.; Rogach, A. L.; Jäckel, F.; Feldmann, J. Pyrite nanocrystals: Shape-controlled synthesis and tunable optical properties via reversible self-assembly. *Journal of Materials Chemistry* **2011**, *21* (44), 17946-17952. DOI: 10.1039/c1jm13336e.

(4) Luther, G. W.; Rickard, D. T. Metal sulfide cluster complexes and their biogeochemical importance in the environment. *Journal of Nanoparticle Research* **2005**, *7* (4-5), 389-407. DOI: 10.1007/s11051-005-4272-4.

(5) Bone, S. E.; Bargar, J. R.; Sposito, G. Mackinawite (FeS) reduces mercury(II) under sulfidic conditions. *Environ Sci Technol* **2014**, *48* (18), 10681-10689. DOI: 10.1021/es501514r .

(6) Zhang, Y.; Zhu, Z.; Liao, Y.; Dang, Z.; Guo, C. Effects of Fe(II) source on the formation and reduction rate of biosynthetic mackinawite: Biosynthesis process and removal of Cr(VI). *Chemical Engineering Journal* **2021**, *421*. DOI: 10.1016/j.cej.2021.129723.

(7) Rhodes, J. M.; Jones, C. A.; Thal, L. B.; MacDonald, J. E. Phase-controlled colloidal syntheses of iron sulfide nanocrystals via sulfur precursor reactivity and direct pyrite precipitation. *Chemistry of Materials* **2017**, *29* (19), 8521-8530. DOI: 10.1021/acs.chemmater.7b03550.

(8) Momma, K.; Izumi, F. VESTA 3 for three-dimensional visualization of crystal, volumetric and morphology data. *Journal of Applied Crystallography* **2011**, *44* (6), 1272-1276. DOI: 10.1107/S0021889811038970.

(9) Buerger, M. J. The Crystal Structure of Marcasite. *American Mineralogist* **1931**, *16* (9), 361-395.

(10) Kitchaev, D. A.; Ceder, G. Evaluating structure selection in the hydrothermal growth of FeS 2 pyrite and marcasite. *Nature Communications* **2016**, *7*, 1-7. DOI: 10.1038/ncomms13799.

(11) Li, T.; Guo, Z.; Li, X.; Wu, Z.; Zhang, K.; Liu, H.; Sun, H.; Liu, Y.; Zhang, H. Colloidal synthesis of marcasite FeS2 nanoparticles with improved electrochemical performance. *RSC Advances* **2015**, *5* (120), 98967-98970. DOI: 10.1039/c5ra22610d.

(12) Gan, Y. X.; Jayatissa, A. H.; Yu, Z.; Chen, X.; Li, M. Hydrothermal Synthesis of Nanomaterials. In *Journal of Nanomaterials*, Hindawi Limited: 2020; Vol. 2020.

(13) Meng, L. Y.; Wang, B.; Ma, M. G.; Lin, K. L. The progress of microwave-assisted hydrothermal method in the synthesis of functional nanomaterials. In *Materials Today Chemistry*, Elsevier Ltd: 2016; Vol. 1-2, pp 63-83.

(14) Cao, Y.; Hu, P.; Jia, D. Phase- and shape-controlled hydrothermal synthesis of CdS nanoparticles, and oriented attachment growth of its hierarchical architectures. *Applied Surface Science* **2013**, *265*, 771-777. DOI: 10.1016/j.apsusc.2012.11.107.

(15) Zarah, P.; Logam, S.; Bersaiz, P.; Melalui, N.; Hidroterma, K. *Preparation of Transition Metal Sulfide Nanoparticles via Hydrothermal Route FEI-LING PUA, CHIN-HUA CHIA, SARANI ZAKARIA*, TZE-KHONG LIEW, MOHD AMBAR YARMO & NAY-MING HUANG*; 2010.

(16) Xu, C. *CONTINUOUS AND BATCH HYDROTHERMAL SYNTHESIS OF METAL OXIDE NANOPARTICLES AND METAL OXIDE-ACTIVATED CARBON NANOCOMPOSITES A Dissertation Presented to The Academic Faculty*; 2006.

(17) Hu, Q.; Zhang, S.; Zou, X.; Hao, J.; Bai, Y.; Yan, L.; Li, W. Coordination agent-dominated phase control of nickel sulfide for high-performance hybrid supercapacitor. *Journal of Colloid and Interface Science* **2022**, *607*, 45-52. DOI: 10.1016/j.jcis.2021.08.185.

(18) Zhang, W.; Yanagisawa, K.; Kamiya, S.; Shou, T. Phase controllable synthesis of well-crystallized rhodium sulfides by the hydrothermal method. *Crystal Growth and Design* **2009**, *9* (8), 3765-3770. DOI: 10.1021/cg900454g.

(19) Khan, S.; Lei, W.; Takagi, K.; Uchida, A.; Suzuki, N.; Terashima, C.; Rodríguez-González, V.; Fujishima, A.; Katsumata, K. i. Phase control of manganese sulfides during hydrothermal synthesis and their photocatalytic activity for H2 generation. *Materials Letters* **2021**, *300*. DOI: 10.1016/j.matlet.2021.130174.

(20) Kundu, J.; Pradhan, D. Influence of precursor concentration, surfactant and temperature on the hydrothermal synthesis of CuS: Structural, thermal and optical properties. *New Journal of Chemistry* **2013**, *37* (5), 1470-1478. DOI: 10.1039/c3nj41142g.

(21) Hayashi, H.; Hakuta, Y. Hydrothermal Synthesis of metal oxide nanoparticles in supercritical water. In *Materials*, 2010; Vol. 3, pp 3794-3817.

(22) Zang, X.; Dai, Z.; Yang, J.; Zhang, Y.; Huang, W.; Dong, X. Template-Assisted Synthesis of Nickel Sulfide Nanowires: Tuning the Compositions for Supercapacitors with Improved Electrochemical

Stability. *ACS Applied Materials and Interfaces* **2016**, *8* (37), 24645-24651. DOI: 10.1021/acsami.6b08409.

(23) Das Talukdar, A.; Sarker, S. D.; Patra, J. K.; Das Talukdar, A.; Sarker, S. D.; Kumar Patra, J. K. *Advances in Nanotechnology-Based Drug Delivery Systems*; Elsevier, 2022.

(24) Lai, J.; Niu, W.; Luque, R.; Xu, G. Solvothermal synthesis of metal nanocrystals and their applications. In *Nano Today*, Elsevier B.V.: 2015; Vol. 10, pp 240-267.

(25) Huang, L.; Hou, H.; Liu, B.; Zeinu, K.; Yuan, X.; Zhu, X.; He, X.; Wu, L.; Hu, J.; Yang, J. Phase-controlled solvothermal synthesis and morphology evolution of nickel sulfide and its pseudocapacitance performance. *Ceramics International* **2017**, *43* (3), 3080-3088. DOI: 10.1016/j.ceramint.2016.11.118.

(26) Meng, Z.; Peng, Y.; Yu, W.; Qian, Y. *Solvothermal synthesis and phase control of nickel sulfides with different morphologies*; 2002.

(27) Hu, Q. R.; Wang, S. L.; Zhang, Y.; Tang, W. H. Synthesis of cobalt sulfide nanostructures by a facile solvothermal growth process. *Journal of Alloys and Compounds* **2010**, *491* (1-2), 707-711. DOI: 10.1016/j.jallcom.2009.11.050.

(28) Olatunde, O. C.; Onwudiwe, D. C. Temperature Controlled Evolution of Pure Phase Cu9S5 Nanoparticles by Solvothermal Process. *Frontiers in Materials* **2021**, *8*. DOI: 10.3389/fmats.2021.687562.

(29) Murugan, A. V.; Sonawane, R. S.; Kale, B. B.; Apte, S. K.; Kulkarni, A. V. *Microwave-solvothermal synthesis of nanocrystalline cadmium sulfide*; 2001.

(30) You, J.; Hossain, M. D.; Luo, Z. Synthesis of 2D transition metal dichalcogenides by chemical vapor deposition with controlled layer number and morphology. *Nano Converg* **2018**, *5* (1), 26. DOI: 10.1186/s40580-018-0158-x.

(31) Chen, P.; Zhang, N.; Wang, S.; Zhou, T.; Tong, Y.; Ao, C.; Yan, W.; Zhang, L.; Chu, W.; Wu, C.; et al. Interfacial engineering of cobalt sulfide/graphene hybrids for highly efficient ammonia electrosynthesis. *Proceedings of the National Academy of Sciences of the United States of America* **2019**, *116* (14), 6635-6640. DOI: 10.1073/pnas.1817881116.

(32) Zhou, J.; Zhu, C.; Zhou, Y.; Dong, J.; Li, P.; Zhang, Z.; Wang, Z.; Lin, Y. C.; Shi, J.; Zhang, R.; et al. Composition and phase engineering of metal chalcogenides and phosphorous chalcogenides. *Nature Materials* **2022**. DOI: 10.1038/s41563-022-01291-5.

(33) Nguyen, Q. N.; Wang, C.; Shang, Y.; Janssen, A.; Xia, Y. Colloidal Synthesis of Metal Nanocrystals: From Asymmetrical Growth to Symmetry Breaking. *Chem Rev* **2023**, *123* (7), 3693-3760. DOI: 10.1021/acs.chemrev.2c00468.

(34) Ostwald, W. Studien über die Bildung und Umwandlung fester Körper 1. Abhandlung: Übersättigung und Überkaltung. *Zeitschrift für Physikalische Chemie* **1897**, *22*, 289-330.

(35) Chung, S. Y.; Kim, Y. M.; Kim, J. G.; Kim, Y. J. Multiphase transformation and Ostwalds rule of stages during crystallization ofametal phosphate. *Nature Physics* **2009**, *5* (1), 68-73. DOI: 10.1038/nphys1148.

(36) Sun, W.; Dacek, S. T.; Ong, S. P.; Hautier, G.; Jain, A.; Richards, W. D.; Gamst, A. C.; Persson, K. A.; Ceder, G. The thermodynamic scale of inorganic crystalline metastability. *Science Advances* **2016**, *2* (11). DOI: 10.1126/sciadv.1600225.

(37) Whitehead, C. B.; Özkar, S.; Finke, R. G. LaMer's 1950 model of particle formation: a review and critical analysis of its classical nucleation and fluctuation theory basis, of competing models and mechanisms for phase-changes and particle formation, and then of its application to silver halide, semiconductor, metal, and metal-oxide nanoparticles. *Materials Advances* **2021**, *2* (1), 186-235. DOI: 10.1039/d0ma00439a.

(38) Gao, Y.; Peng, X. Crystal structure control of CdSe nanocrystals in growth and nucleation: dominating effects of surface versus interior structure. *J Am Chem Soc* **2014**, *136* (18), 6724-6732. DOI: 10.1021/ja5020025 From NLM PubMed-not-MEDLINE.

(39) Hendricks, M. P.; Campos, M. P.; Cleveland, G. T.; Plante, I. J.-L.; Owen, J. S. A Tunable library of substituted thiourea precursors to metal sulfide nanocrystals. *Science* **2015**, *348* (6240), 1226-1230. DOI: 10.1126/science.aaa2951.

(40) Wang, M.; Xie, F.; Li, W.; Chen, M.; Zhao, Y. Preparation of various kinds of copper sulfides in a facile way and the enhanced catalytic activity by visible light. *Journal of Materials Chemistry A* **2013**, *1* (30), 8616-8621. DOI: 10.1039/c3ta11739a.

(41) Koziel, A. C.; Goldfarb, R. B.; Endres, E. J.; Macdonald, J. E. Molecular Decomposition Routes of Diaryl Diselenide Precursors in Relation to the Phase Determination of Copper Selenides. *Inorg Chem* **2022**, *61* (37), 14673-14683. DOI: 10.1021/acs.inorgchem.2c02042.

(42) Williamson, E. M.; Sun, Z.; Tappan, B. A.; Brutchey, R. L. Predictive Synthesis of Copper Selenides Using a Multidimensional Phase Map Constructed with a Data-Driven Classifier. *J Am Chem Soc* **2023**, *145* (32), 17954-17964. DOI: 10.1021/jacs.3c05490.

(43) Tappan, B. A.; Barim, G.; Kwok, J. C.; Brutchey, R. L. Utilizing Diselenide Precursors toward Rationally Controlled Synthesis of Metastable CuInSe2 Nanocrystals. *Chemistry of Materials* **2018**, *30* (16), 5704-5713. DOI: 10.1021/acs.chemmater.8b02205.

(44) Thomson, J. W.; Nagashima, K.; MacDonald, P. M.; Ozin, G. A. From sulfur-amine solutions to metal sulfide nanocrystals: Peering into the oleylamine-sulfur black box. *Journal of the American Chemical Society* **2011**, *133* (13), 5036-5041. DOI: 10.1021/ja1109997.

(45) Roffey, A.; Hollingsworth, N.; Islam, H. U.; Mercy, M.; Sankar, G.; Catlow, C. R. A.; Hogarth, G.; De Leeuw, N. H. Phase control during the synthesis of nickel sulfide nanoparticles from dithiocarbamate precursors. *Nanoscale* **2016**, *8* (21), 11067-11075. DOI: 10.1039/c6nr00053c.

(46) Hollingsworth, N.; Roffey, A.; Islam, H. U.; Mercy, M.; Roldan, A.; Bras, W.; Wolthers, M.; Catlow, C. R. A.; Sankar, G.; Hogarth, G.; et al. Active nature of primary amines during thermal decomposition of nickel dithiocarbamates to nickel sulfide nanoparticles. *Chemistry of Materials* **2014**, *26* (21), 6281-6292. DOI: 10.1021/cm503174z.

(47) Campos, M. P.; Hendricks, M. P.; Beecher, A. N.; Walravens, W.; Swain, R. A.; Cleveland, G. T.; Hens, Z.; Sfeir, M. Y.; Owen, J. S. A Library of Selenourea Precursors to PbSe Nanocrystals with Size Distributions near the Homogeneous Limit. *Journal of the American Chemical Society* **2017**, *139* (6), 2296-2305. DOI: 10.1021/jacs.6b11021.

(48) Hamachi, L. S.; Jen-La Plante, I.; Coryell, A. C.; De Roo, J.; Owen, J. S. Kinetic Control over CdS Nanocrystal Nucleation Using a Library of Thiocarbonates, Thiocarbamates, and Thioureas. *Chemistry of Materials* **2017**, *29* (20), 8711-8719. DOI: 10.1021/acs.chemmater.7b02861.

(49) Park, J. Y.; Kim, S. J.; Chang, J. H.; Seo, H. K.; Lee, J. Y.; Yuk, J. M. Atomic visualization of a non-equilibrium sodiation pathway in copper sulfide. *Nat Commun* **2018**, *9* (1), 922. DOI: 10.1038/s41467-018-03322-9 .

(50) Bhargava, S. K.; Garg, A.; Subasinghe, N. D. In situ high-temperature phase transformation studies on pyrite. *Fuel* **2009**, *88* (6), 988-993. DOI: 10.1016/j.fuel.2008.12.005.

(51) Jin, B.; Wang, Y.; Liu, Z.; France-Lanord, A.; Grossman, J. C.; Jin, C.; Tang, R. Revealing the Cluster-Cloud and Its Role in Nanocrystallization. *Advanced Materials* **2019**, *31* (16), 1-6. DOI: 10.1002/adma.201808225.

(52) Moehring, N. K.; Fort, M. J.; McBride, J. R.; Kato, M.; Macdonald, J. E.; Kidambi, P. R. In situ observations of thermally induced phase transformations in iron sulfide nanoparticles. *Materials Today Advances* **2020**, *6*, 100057-100057. DOI: 10.1016/j.mtadv.2020.100057.

(53) Zhu, X.; Oh Jung, B.; Wang, Q.; Hu, Y.; Choi, M.; Song, S.; Namkung, S.; Kang, N.; Shin, H.-Y.; Joo, M.; et al. In-situ STEM study on thermally induced phase transformation of magnetic (Nd0.75Ce0.25)2Fe14B ribbons. *Materials & Design* **2022**, *216*. DOI: 10.1016/j.matdes.2022.110525.

(54) van der Stam, W.; Rabouw, F. T.; Geuchies, J. J.; Berends, A. C.; Hinterding, S. O. M.; Geitenbeek, R. G.; van der Lit, J.; Prévost, S.; Petukhov, A. V.; de Mello Donega, C. In Situ Probing of Stack-Templated Growth of Ultrathin Cu2–xS Nanosheets. *Chemistry of Materials* **2016**, *28* (17), 6381-6389. DOI: 10.1021/acs.chemmater.6b02787.

(55) Loughney, P. A.; Martin, K. L.; Cuillier, P.; Trigg, E. B.; Posey, N. D.; Dickerson, M. B.; Pruyn, T. L.; Doan-Nguyen, V. Pre-ceramic polymer-assisted nucleation and growth of copper sulfide nanoplates. *Communications Materials* **2023**, *4* (1). DOI: 10.1038/s43246-023-00380-5.

(56) Peter Nørby; Simon Johnsen; Iversen, B. B. In-Situ X-ray Diffraction Study of Fthe Formation, Growth, and Phase Transition of Clloidal $Cu_{2-X\ Nanocrystals}$. *ACS Nano* **2014**, *8* (5), 4295-4303.

(57) Carmen M. Goodell; Benjamin Gilbert; Steven J. Weigand; Bainfield, J. F. Kinetics of Water Adsorption-Driven Structural Transformation of ZnS Nanoparticles. *The Journal of Physical Chemistry C* **2008**, *112* (13), 4791–4796.

(58) Campos, M. P.; De Roo, J.; Greenberg, M. W.; McMurtry, B. M.; Hendricks, M. P.; Bennett, E.; Saenz, N.; Sfeir, M. Y.; Abecassis, B.; Ghose, S. K.; et al. Growth kinetics determine the polydispersity and size of PbS and PbSe nanocrystals. *Chem Sci* **2022**, *13* (16), 4555-4565. DOI: 10.1039/d1sc06098h.

(59) Friedfeld, M. R.; Stein, J. L.; Cossairt, B. M. Main-Group-Semiconductor Cluster Molecules as Synthetic Intermediates to Nanostructures. *Inorg Chem* **2017**, *56* (15), 8689-8697. DOI: 10.1021/acs.inorgchem.7b00291.

(60) Wu, L.; Dzade, N. Y.; Gao, L.; Scanlon, D. O.; Ozturk, Z.; Hollingsworth, N.; Weckhuysen, B. M.; Hensen, E. J.; de Leeuw, N. H.; Hofmann, J. P. Enhanced Photoresponse of FeS(2) Films: The Role of Marcasite-Pyrite Phase Junctions. *Adv Mater* **2016**, *28* (43), 9602-9607. DOI: 10.1002/adma.201602222.

Chapter 2: Phase Control in the Synthesis of Iron Sulfides

2.1 The Phase Space of Iron Sulfide Nanocrystals

The geological record demonstrates a diverse array of metal chalcogenides with varying composition and crystal structures. For example, there are eight known geological iron sulfides (Table 1), four cobalt sulfides, seven nickel sulfides and ten copper sulfides. These compounds have myriad possibilities in technological applications because of their diverse electronic, optical, magnetic, chemical and catalytic properties. However, these applications cannot be realized without reliable synthetic routes that can target each desired crystalline phase.

So far there seems to be little progress on understanding how phase can be controlled in colloidal synthesis. While there are many one-off syntheses in the literature to individual metal sulfide phases, most are serendipitous without logical links between syntheses to other phases. When discussing synthetic routes, it is important to understand the intermediate phase "destinations" one can run into. There has been some progress; for example, Lennie et al.[2] mapped some of the pathways between iron sulfide phases in aqueous media but the understanding is incomplete. In organic colloidal synthesis, even rudimentary synthetic maps of the phase space do not exist.

Rational phase control in bottom-up syntheses is not completely understood, in part because the mechanisms of the molecular transformations that preclude crystal formation in solution have been mostly overlooked.[3-6] As well, systematic phase control studies that separated *how fast* from *how* a reaction occurs have not been performed. As an example, we studied the effect of organo-sulfur precursors on the phase of iron sulfide produced. Weaker S-C bond strength in the organo-sulfur reagents correlated with producing a phase with higher sulfur content. However, closer study of the reagent diallyldisulfide revealed that there was a decomposition mechanism separate from that of the other reagents that uniquely facilitated pyrite formation.[7] Therefore, while there was a correlation between the availability of the S (through C-S bond strength) and the phase, the results were convoluted with *how* the particular reagents decomposed. What is needed is a series of reagents that decompose at varying rates, without changing the decomposition mechanism.

Substituted thioureas are highly tunable in the rate in which they release sulfur. The number and identity of the substituents vary the rates of reaction in nanocrystal syntheses by several orders of magnitude.[3] Here, the use of substituted thioureas in bottom-up syntheses are used as tunable sulfur

reagents to study and isolate how reaction kinetics influence the phase of the resulting metal sulfides in bottom-up synthesis.

Table 2.1 The Iron Sulfides

Phase	Chemical Formula	Space Group	Approximate Sulfur packing	Cation Hole Filling	DS_f (J/mol K)	DH_f (kJ/mol)	Reference Author
Vaesite	NiS_2	Pa3	S_2^{2-} in ccp	All Oh	80	-124.9, -128, -133.9	Cemič[12], Gamsjäger[13]
Millerite	NiS	R3m	S^{2-} in hcp	All Ph	53.0	-91.0, -94.0	Cemič[12], Gamsjäger[13]
NiS	NiS	P 6_3/mmc	S^{2-} in hcp	All Oh	60.9	-88.1, -88.1	Cemič[12], Gamsjäger[13]
Godlevskite	Ni_9S_8	I42d	S^{2-} in ccp	Td, Square Pyramidal	481	-760	Gamsjäger[13]
	Ni_7S_6	Bmmb	S^{2-} in ccp	Td, Square Pyramidal	390.2		Cemič[12],Waldner
Polydymite	Ni_3S_4	$Fd\bar{3}m$	S^{2-} in ccp	All Oh, ½ Td (spinel)	191.9	-309.1	Waldner
Heazlewoodite	Ni_3S_2	R32	S^{2-} in bcc	Distorted Td	133.5	-217.24, -215.9	Gamsjager[13], Waldner

based on the observation that cubic iron sulfide decomposes to mackinawite. Materials project database has calculated that the enthalpy of formation for smythite is slightly more negative than that of greigite.[1]

The iron sulfides are excellent target materials for systematic study of phase control because the phase space is complex; there are known phases of several Fe:S stoichiometries of approximately 1:1, 3:4 and 1:2 with hexagonal and cubic polymorphs (Table 1). Many of the iron sulfides are of technological relevance in solar energy capture, magnetic storage, and biomedical applications.[8-10] While the iron sulfides have well-studied aqueous and geochemistry relevant to minerology and the study of the origins of life, the overarching themes to phase trends are elusive.[11]

Here we employ the use of tunable thioureas in a bottom-up synthesis. By doing so, we identified all eight of the known geological iron sulfides [pyrite (FeS_2), marcasite (orthorhombic, *o*-FeS_2), greigite (Fe_3S_4), smythite ($Fe_{3+x}S_4$), mackinawite ($Fe_{1+x}S$), pyrrhotite ($Fe_{1-x}S$), troilite (FeS), and cubic iron sulfide (FeS)]. These experiments allowed for the mapping of the kinetic, thermodynamic, and crystalline relationships between the phases adding a layer of understanding to the existing literature preparations of these phases. Analyzing these results show that anion stacking structure plays a determining role in nanocrystalline growth and phase transformations.

Here we show that the identified relationships can be used to make hypothesis driven changes to the synthetic conditions to target specific phases. The way we rationalize and strategize synthetic pathways in bottom-up synthesis is a new approach and way of thinking about nanocrystalline synthesis.

2.2: Synthesis of Iron Sulfide Nanocrystals

Materials

Chemicals. 1-Octadecene ($C_{18}H_{36,}$ 90%,), oleylamine ($C_{18}H_{35}NH_{2,}$ 70%,), thiourea (99%), acetylthiourea (99.5%), methylthiourea (97%), phenylthiourea (98%), diphenylthiourea (98%), 3,5-bis(trifluoromethyl)phenyl isothiocyanate (98%), phenyl thiocyanate (99%), hexylamine (98%), aniline(99.5), toluene (HPLC grade), and iron (II) chloride ($FeCl_2$, 99.8%) was purchased from Sigma Aldrich. Iron Stearate (99.8%) was purchased {from STREM Chemicals. Tetraethylene glycol dimethyl ether (98%) was purchased from Alfa Aesar.

Methods

Synthesis of 1-3,5-bis(trifluoromethyl)phenyl-3-phenyl-2-thiourea

Synthesis modified from *Hendricks et al*.[3] (3) A solution of aniline (6 mmol) in toluene (5 mL) was added to a solution of 3,5-bis(trifluoromethyl) (6 mmol) in toluene (5 mL). The solution was allowed to stir for 5 min. The clear liquid turned white and the volatiles removed under vacuum. Characterization: ^{1}H NMR ($CDCl_3$, 400 MHz) : 7.34 (d, 2H, *o*-CH (unsub.), 7.41 (t, 1H, *p*-CH (unsub.)), 7.52 (t, 2H, *m*-CH (unsub.)), 7.69 (s, 1H, p-CH (sub.)), 7.70 (br, 1H, NH (unsub.)), 8.00 (s, 1H, *p*-CH (sub.)), 8.29 (br, 1H, NH (sub.))

Synthesis of 1-hexyl-3-phenyl-2-thiourea thiourea

Synthesis modified from *Hendricks et al*.[3] (3) A solution of hexylamine (6 mmol) in toluene (5 mL) was added to a solution of phenyl thiocyanate (6 mmol) in toluene (5 mL). The solution was allowed to stir for 5 min. The clear liquid turned white liquid and the volatiles were removed under vacuum. Characterization: ^{1}H NMR ($CDCl_3$, 400 MHz): 0.87 (t, 3H, -CH_3), 1.28 (m, 6H, $(CH_2)_3$), 1.56 (p, 2H, CH_2), 3.62 (q, 2H, CH_2), 5.98 (br, 1H, NH), 7.16 (d, 2H, *o*-CH), 7.25 (t, 1H, *p*-CH), 7.43 (t, 2H, *m*-CH), 7.73 (br, 1H, NH)

Iron Sulfide Nanoparticle Synthesis in Octadecene using an Addition Funnel

Iron(III) stearate (450 mg, 0.5 mmol) was dissolved in 10 mL of ODE in a 25 mL 3-neck round-bottom flask with a connected addition funnel with a pressure equalizing arm. The 3-neck round-bottom flask was attached to the Schlenk line via condenser and gas adapter. Thiourea (3 mmol or

1.5 mmol) was combined with octadecene (5 mL) in the addition funnel. The addition funnel was sealed with a septa and pierced with a thermocouple down to the solution level. A second thermocouple was placed in the solution of the 3 -neck flask. The apparatus was degassed under vacuum and the round-bottom flask stirred for 30 min at 60°C using a heating mantle. The vacuum was replaced with argon and the temperature in the round-bottom flask was raised to 170°C for 1h, then raised to the desired reaction temperature (170°C, 195°C, 220°C, or 245°C). The contents of the addition funnel were heated to the same desired temperature using a heat gun (MHT Products Inc.), allowing the thiourea to dissolve, which was then added swiftly to the contents of the round-bottom flask. The solution was left at the desired temperature of 1 min, 10 min, 1 h or 4 h. To isolate the product iron sulfides, after cooling, chloroform (5 mL) was added to suspend the particles. Ethanol (5 mL) was then added as an antisolvent. The mixture was centrifuged at 4500 rpm for 5 min. The liquid component was decanted, and the nanoparticles were resuspended in chloroform. This process was repeated 4 times.

Two Step Iron Sulfide Nanoparticle Synthesis in Octadecene using 4-neck flasks and two Addition Funnels

Iron (III) stearate (450mg, 0.5 mmol) was dissolved in ODE (10 mL) in a 50 mL 4-neck round-bottom flask with an attached condenser. Two addition funnels with pressure equalizing arms were attached and loaded with 5 ml of ODE each and diphenylthiourea (3 mmol) or thiourea (1.5 mmol). The addition funnels were sealed with septum and pieced with thermocouples to below the liquid line. The apparatus was degassed under vacuum and the round bottom flask was placed under vigorous stirring at 60°C for 30 min using a heating mantle. The vacuum was replaced with Argon and contents of the round-bottom flask raised to 170°C for 1h, then further raised to 245°C. At this time, the addition funnel with diphenylthiourea and ODE was heated to 245°C using a heat gun, at which time it was added swiftly to the contents of the round bottom flask. The contents were heated and stirred for 1h. The second addition funnel with thiourea and ODE was heated to 245°C using the heat gun and the contents was added swiftly. The reaction was allowed to continue for 1h at 245°C. To isolate the product iron sulfides, after cooling, chloroform (5 mL) was added to suspend the particles. Ethanol (5 mL) was then added as an antisolvent. The mixture was centrifuged at 4500 rpm for 5 min. The liquid component was decanted, and the nanoparticles were resuspended in chloroform. This process was repeated 4 times.

Proton Nuclear Magnetic Resonance Studies

In a N_2 filled glove box, thiourea (0.262 mmol) was loaded into a standard NMR tube with approximately 0.131 mmol of distilled oleylamine or a 2:1 ration of ODE: tetraglyme. The tube was capped with a septum and brought out of the glove box. An 18-gauge needle with a nitrogen balloon was injected into the septa on top of the NMR tube. The NMR tube was placed in a silicon oil bath at the desired temperature for 30 min. After cooling, 600 μL of $CDCl_3$ was added. The resulting product was then analyzed by 400 MHz NMR.

Iron Sulfide synthesis in Oleylamine

Anhydrous iron (II) chloride (63.4 mg, 0.5 mmol) was dissolved in 10 mL of oleylamine (OLAM) in a 25 mL 3-neck round-bottom flask and degassed under vacuum and vigorous stirring at 60°C for 30 min. The vacuum was replaced with an inert gas (N_2 or Ar) and the solution was raised to 170°C for 1h. Simultaneously, in a 6-dram vial, 3 mmol of desired thiourea was dissolved in OLAM and placed under vacuum for 30 min, then placed under inert gas. The solution from the 6-dram vial was collected in a syringe and injected into the round bottom flask and the solution turned black. The temperature drop was measured, and the flask was raised to 220°C for 2 h. The iron sulfide product was isolated by the addition of 5mL ethanol followed by centrifugation at 4500 rpm for 5 min. The liquid was decanted and the product resuspended in 5 mL chloroform. The cleaning step was repeated 4 times.

Iron Sulfide synthesis in Octadecene and Tetraglyme

Iron (III) stearate (450 mg, 0.5 mmol) of was dissolved in 10 mL of octadecene (ODA) in a 25 mL 3-neck round-bottom flask. The reaction mixture was heated to 60°C under vacuum and vigorously stirred for 30 min. The vacuum was then replaced by inert gas (N_2 or Ar) and heated to 170°C for 1 h. Simultaneously in a 6-dram vial, 3 mmol of the desired thiourea was dissolved in 5 mL of tetraglyme. The tetraglyme solution was placed under vacuum for 30 min, then under inert gas. The 6-dram vial solution was then injected with a syringe into the round-bottom flask. The temperature drop was recorded and the flask was allowed to return to 170°C where it remained for 1 h. The iron sulfide product was isolated by the addition of 5 mL ethanol followed by centrifugation at 4500 rpm for 5 min. The liquid was decanted and the product resuspended in 5 mL chloroform. The cleaning step was repeated 4 times.

Mackinawite Synthesis

Iron(III) stearate (450 mg, 0.5 mmol) was dissolved in 10 mL of ODE in a 25 mL 3-neck round-bottom flask with a connected addition funnel with a pressure equalizing arm. The 3-neck round-

bottom flask was attached to the Schlenk line via condenser and gas adapter. 3 mmols of 1-hexyl-3-phenyl-2-thiourea was combined with octadecene (5 mL) in the addition funnel. The addition funnel was sealed with a septum and pierced with a thermocouple down to the solution level. A second thermocouple was placed in the solution of the 3 -neck flask. The apparatus was degassed under vacuum and the round-bottom flask stirred for 30 min at 60°C using a heating mantle. The vacuum was replaced with argon and the temperature in the round-bottom flask was raised to 170°C for 1 h, then the contents of the addition funnel were heated to the same desired temperature using a heat gun (MHT Products Inc.), allowing the thiourea to dissolve, which was then added swiftly to the contents of the round-bottom flask. The solution was left at the desired temperature 1 h. To isolate the product iron sulfides, after cooling, chloroform (5 mL) was added to suspend the particles. Ethanol (5 mL) was then added as an antisolvent. The mixture was centrifuged at 4500 rpm for 5 min. The liquid component was decanted, and the nanoparticles were resuspended in chloroform. This process was repeated 4 times.

Greigite Synthesis

Iron(III) stearate (450 mg, 0.5 mmol) was dissolved in 10 mL of ODE in a 25 mL 3-neck round-bottom flask with a connected addition funnel with a pressure equalizing arm. The 3-neck round-bottom flask was attached to the Schlenk line via condenser and gas adapter. 3 mmol of phenylthiourea was combined with octadecene (5 mL) in the addition funnel. The addition funnel was sealed with a septum and pierced with a thermocouple down to the solution level. A second thermocouple was placed in the solution of the 3 -neck flask. The apparatus was degassed under vacuum and the round-bottom flask stirred for 30 min at 60°C using a heating mantle. The vacuum was replaced with argon and the temperature in the round-bottom flask was raised to 170°C for 1h, then raised to the desired reaction temperature 195°C. The contents of the addition funnel were heated to the same desired temperature using a heat gun (MHT Products Inc.), allowing the thiourea to dissolve, which was then added swiftly to the contents of the round-bottom flask. The solution was left at the desired temperature of 1 h. To isolate the product iron sulfides, after cooling, chloroform (5 mL) was added to suspend the particles. Ethanol (5 mL) was then added as an antisolvent. The mixture was centrifuged at 4500 rpm for 5 min. The liquid component was decanted, and the nanoparticles were resuspended in chloroform. This process was repeated 4 times.

Pyrite Synthesis

Iron(III) stearate (450 mg, 0.5 mmol) was dissolved in 10 mL of ODE in a 25 mL 3-neck round-bottom flask with a connected addition funnel with a pressure equalizing arm. The 3-neck round-bottom flask was attached to the Schlenk line via condenser and gas adapter. 6 mmol of acetylthiourea was combined with octadecene (5 mL) in the addition funnel. The addition funnel was sealed with a septum and pierced with a thermocouple down to the solution level. A second thermocouple was placed in the solution of the 3 -neck flask. The apparatus was degassed under vacuum and the round-bottom flask stirred for 30 min at 60°C using a heating mantle. The vacuum was replaced with argon and the temperature in the round-bottom flask was raised to 170°C for 1h, then raised to the desired reaction temperature 245°C. The contents of the addition funnel were heated to the same desired temperature using a heat gun (MHT Products Inc.), allowing the thiourea to dissolve, which was then added swiftly to the contents of the round-bottom flask. The solution was left at the desired temperature of 2 h. To isolate the product iron sulfides, after cooling, chloroform (5 mL) was added to suspend the particles. Ethanol (5 mL) was then added as an antisolvent. The mixture was centrifuged at 4500 rpm for 5 min. The liquid component was decanted, and the nanoparticles were resuspended in chloroform. This process was repeated 4 times.

Pyrrhotite Synthesis

Iron(III) stearate (450 mg, 0.5 mmol) was dissolved in 10 mL of ODE in a 25 mL 3-neck round-bottom flask with a connected addition funnel with a pressure equalizing arm. The 3-neck round-bottom flask was attached to the Schlenk line via condenser and gas adapter. 3 mmol of diphenylthiourea was combined with octadecene (5 mL) in the addition funnel. The addition funnel was sealed with a septum and pierced with a thermocouple down to the solution level. A second thermocouple was placed in the solution of the 3 -neck flask. The apparatus was degassed under vacuum and the round-bottom flask stirred for 30 min at 60°C using a heating mantle. The vacuum was replaced with argon and the temperature in the round-bottom flask was raised to 170°C for 1h, then raised to the desired reaction temperature 245°C. The contents of the addition funnel were heated to the same desired temperature using a heat gun (MHT Products Inc.), allowing the thiourea to dissolve, which was then added swiftly to the contents of the round-bottom flask. The solution was left at the desired temperature of 1 h. To isolate the product iron sulfides, after cooling, chloroform (5 mL) was added to suspend the particles. Ethanol (5 mL) was then added as an antisolvent. The mixture was centrifuged at 4500 rpm for 5 min. The liquid component was

decanted, and the nanoparticles were resuspended in chloroform. This process was repeated 4 times.

Smythite Synthesis

Iron (III) stearate (450mg, 0.5 mmol) was dissolved in ODE (10 mL) in a 50 mL 4-neck round-bottom flask with an attached condenser. Two addition funnels with pressure equalizing arms were attached and loaded with 5 ml of ODE each and diphenylthiourea (3 mmol) in the first addition funnel and acetylthiourea (1.5 mmol) in the second. The addition funnels were sealed with septum and pieced with thermocouples to below the liquid line. The apparatus was degassed under vacuum and the round bottom flask was placed under vigorous stirring at 60°C for 30 min using a heating mantle. The vacuum was replaced with Argon and contents of the round-bottom flask raised to 170°C for 1h, then further raised to 245°C. At this time, the addition funnel with diphenyl thiourea and ODE was heated to 245°C temperature using a heat gun, upon which time it was added swiftly to the contents of the round bottom flask. The contents were heated and stirred for 1h. The reaction vessel was cooled to 160°C and the second addition funnel with thiourea and ODE was heated 160°C using the heat gun and the contents was added swiftly. The reaction was allowed to continue for 4h at 160°C. To isolate the product iron sulfides, after cooling chloroform (5 mL) was added to suspend the particles. Ethanol (5 mL) was then added as an antisolvent. The mixture was centrifuged at 4500 rpm for 5 min. The liquid component was decanted, and the nanoparticles were resuspended in chloroform. This process was repeated 4 times.

Marcasite Synthesis

Iron (III) stearate (450 mg, 0.5 mmol) of was dissolved in 10 mL of oleylamine (OLAM) in a 25 mL 3- neck round bottom flask and degassed under vacuum and vigorous stirring at 100°C for 30 min. The vacuum was replaced with an inert gas (N_2 or Ar) and the solution was raised to 245°C for 1h. Simultaneously, in a 5 mL one neck flask vial, 1 mmol of diphenyl thiourea was dissolved in OLAM and placed under vacuum for 30 min, then placed under inert gas. The solution from the 6-dram vial was collected in a syringe and injected into the round bottom flask and the solution turned black. The temperature drop was measured, and the flask was raised to 245°C for 2 h. The pyrrhotite product was isolated by the addition of 5mL ethanol followed by centrifugation at 4500 rpm for 5 min. The liquid was decanted and the product resuspended in 5 mL chloroform. The cleaning step was repeated 4 times. The cleaned pyrrhotite and 1.5 mmol of acetyl thiourea was then dissolved in 15 mL of octadecene (ODE) in a 25 mL 3- neck round bottom flask and degassed

under vacuum and vigorous stirring at 100°C for 1 hour. The vacuum was replaced with an inert gas (N_2 or Ar) and the reaction was heated to 245 °C for 1 hour. To isolate the product iron sulfides, after cooling, chloroform (5 mL) was added to suspend the particles. Ethanol (5 mL) was then added as an antisolvent. The mixture was centrifuged at 4500 rpm for 5 min. The liquid component was decanted, and the nanoparticles were resuspended in chloroform. This process was repeated 4 times.

Material Characterization

Powder X-ray Diffraction (XRD) spectra were obtained using a Rigaku SmartLab® X-ray Diffractometer with a CuK□ source and a D/TeX Ultra 250 detector. The operating voltage and current were 40 kV and 44 mA respectively. Samples were prepared by drop casting particle suspensions onto low-background silicon XRD wafers. The step size was 0.1 degree at a rate of 10 degrees per minute.

Samples were typically characterized with 1h of dropcasting. Unless otherwise noted in Table S1, no evidence of oxides was observed in the XRD or by color changes.

Rietveld Refinement Method and quantification

Refinements were performed using Rigaku PDXL. The .cif files employed were the JCPDS cards noted on the figure 2.1. Each pattern was allowed to be fit freely with the cards noted in Table S1 with percentages. Blank squares indicate a phase was not included in the fit.

The quantification of semi-crystalline FeS needed to be approximated since the structure has not been identified beyond recognizing its layered structure. A .cif file has yet to be prepared. However, as identified by Posfai et al.(REF), a peak at 16.65° 2Q is indicative of semi-crystalline FeS. To approximate its concentration in mixtures, the assumption was made that the structure factor for this peak was the same as the nearby (001) peak of mackinawite (also layered) at 17.58° 2Q. After refinement excluding the peak at 16.65° 2Q, the ratios of the peaks at 16.65° and 17.85° were taken to approximate the ratio of the amount of semi-crystalline FeS to that of mackinawite. The percentages provided by the refinement were adjusted to account for the new component.

2.3 Using a Library of Tunable Thioureas to Control Iron Sulfide Phases

Iron sulfides were synthesized by heating a solution of iron(III) stearate ($Fe(C_{18}H_{37}CO_2)_3$, 0.5 mmol) in octadecene (ODE) to the desired reaction temperature (170°C-245°C). A solution of a substituted thiourea (3 mmol) in ODE (either at a Fe:S molar ratio of 1:3 or 1:6) was heated to a matching temperature before being added swiftly to the reaction flask (**Figure 2.1**). Throughout

the different iron sulfide synthesis, a stoichiometric excess of thiourea is employed. This allows the thiourea to release sulfur as a monomer for nanocrystal formation and also as a redox flexible species, as both the iron ($Fe^{3+/2+}$) and sulfur (S_2^{2-}/ S^{2-}) oxidation states vary in the known iron sulfides.

To determine the extent to which kinetics plays a role in phase control phenomenon, a library of thioureas was employed with differing conversion rates. The Owen group used slow reaction kinetics (over minutes) and *in situ* UV-vis to follow the synthesis of PbS nanocrystals.[3] We use two of the same thioureas as the Owen group, but add to some more reactive species as well. A direct application of their approach to follow the reactions is not possible for the iron sulfides since there are multiple possible nucleating phases, each with their own absorption profiles. Instead, we use the ^{13}C NMR chemical shift of the C=S as a measure of the electron density on the carbon and adjoining sulfur. From the ^{13}C NMR we infer the reactivity order to follow : thiourea (**1**) > methylthiourea (**2**) > acetylthiourea (**3**) > phenylthiourea (**4**) > 1-3,5-bis(trifluoromethyl)phenyl-3-phenyl-2-thiourea (**5**) > diphenylthiourea (**6**) (Figure 2.1). Extrapolating from the Owen work, we approximate this library covering several orders of magnitude of conversion rate.

After isolation through successive precipitation and dispersion with ethanol and chloroform, all solid products were analyzed by powder X-ray diffraction with Rietveld refinements of the pattern (supporting information table S1). Powder XRD has a limit of detection of about 1-2% composition by volume. Many of the products in these experiments were nanocrystalline with broad peaks, further increasing the limit. In some reactions, the products were phase pure within the limits of powder XRD experiments, while in others a complex mixture of phases resulted. Marcasite (*o*-FeS_2), pyrite (FeS_2), mackinawite ($Fe_{1+x}S$), smythite ($Fe_{3+x}S_4$), cubic iron sulfide, greigite (Fe_3S_4), pyrrhotite ($Fe_{1-x}S$), and semicrystalline FeS were all identified as products (Figure 2.1 c: 170°C, d: 195°C, e: 220°C, f: 245°C, the explicit percentages are included in the SI). Refinements were performed using Rigaku PDXL2 software and the PDF files noted in Figure 2.1. Quantification of semi-crystalline FeS was obtained by assuming that the (001) of macknawite (17.61°) has a similar reflection of semicrystalline FeS (16.68°).

To the best of our knowledge, this is the first time all the known geological iron sulfides have been synthesized in a single set of systematically varied set of experimental conditions. A synthetic phase diagram was created to illuminate the intersectionality of reaction conditions and phase (Figure 2.1f). At the lower synthetic temperatures < 200ºC, mixtures of smythite ($Fe_{3+x}S_4$), cubic

iron sulfide (FeS), troilite (FeS), mackinawite ($Fe_{1+x}S$) and greigite (Fe_3S_4) were synthesized with the fastest reacting thioureas. The low temperatures and fast reacting thioureas work in concert to kinetically trap these phases with small $\Delta H°_f$ (Table 1) (We ignore the influence of ΔS_f since the standard enthalpies of formation ΔS_f are similar throughout the family of iron sulfides (50-64 J/mol K). The difference in value of the ΔS contribution to ΔG is at most 7 kJ/mol (between mackinawite and troilite) at the highest synthetic temperature of 245°C which is smaller than the ΔH contribution.) When using slower reacting thioureas at the low temperatures, greigite (Fe_3S_4) was the dominant product, which has the next largest negative $\Delta H°_f$ —with some remaining mackinawite ($Fe_{1+x}S$) for the very slowest reacting thioureas.

Increasing the reaction temperatures to >200ºC afforded different phase mixtures, but with generally more negative $\Delta H°_f$ and higher sulfur content than at the lower temperatures. Fast reacting thioureas (thiourea and methylthiourea) yielded a mixture of smythite ($Fe_{3+x}S_4$), pyrite (FeS_2), marcasite (*o*-FeS_2) and greigite (Fe_3S_4). Medium reacting thioureas (acetylthiourea and phenylthiourea) yielded a mixture of pyrite (FeS_2) and greigite (Fe_3S_4). Slow reacting thioureas (1-3,5-bis(trifluoromethyl)phenyl-3-phenyl-2-thioure and diphenyl thiourea) yielded a mixture of greigite (Fe_3S_4) and pyrrhotite ($Fe_{1-x}S$). As the reaction temperature was further increased to 245°C, pyrite (FeS_2), marcasite (*o*-FeS_2) and pyrrhotite ($Fe_{1-x}S$) became more dominant.

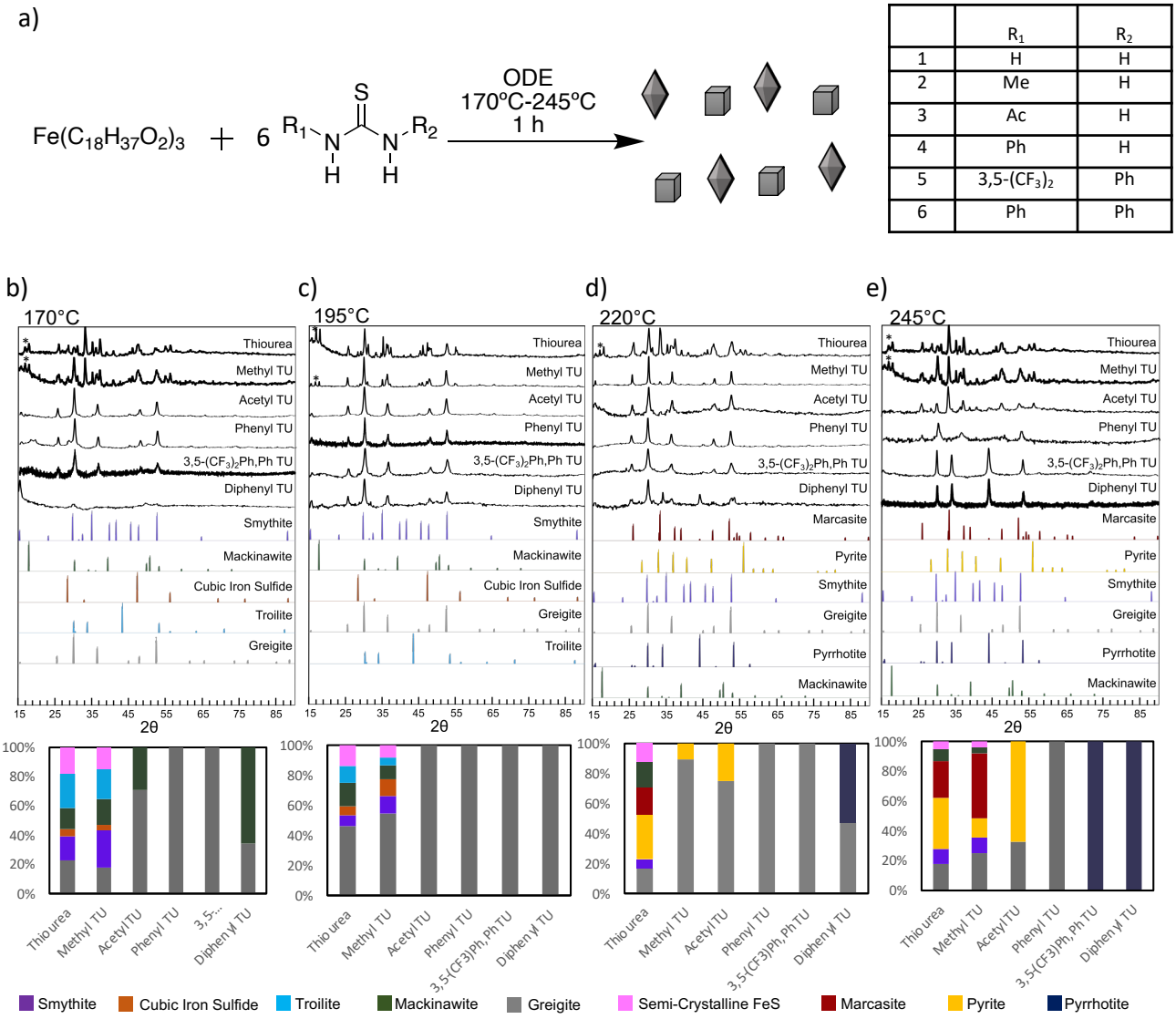

	R_1	R_2
1	H	H
2	Me	H
3	Ac	H
4	Ph	H
5	3,5-$(CF_3)_2$	Ph
6	Ph	Ph

Figure 2.1 a) Schematic of the solution phase synthesis of various crystalline phases of iron sulfides using substituted thioureas (TU) as sulfur reagents. Powder XRD of the products and percent compositions at synthetic temperatures of b) 170ºC c) 195ºC d) 220ºC and e) 245ºC. (ICSD smythite: 900077, troilite: 68852, mackinawite: 182250, greigite: 160713, marcasite: 9013067, pyrite: 10422, pyrrhotite: 240220, cubic iron sulfide reference powder obtained from Médicis et al., semi-crystalline FeS reference powder obtained from Pósfai et al. and Benning et al. denoted * (Supporting information table S1).

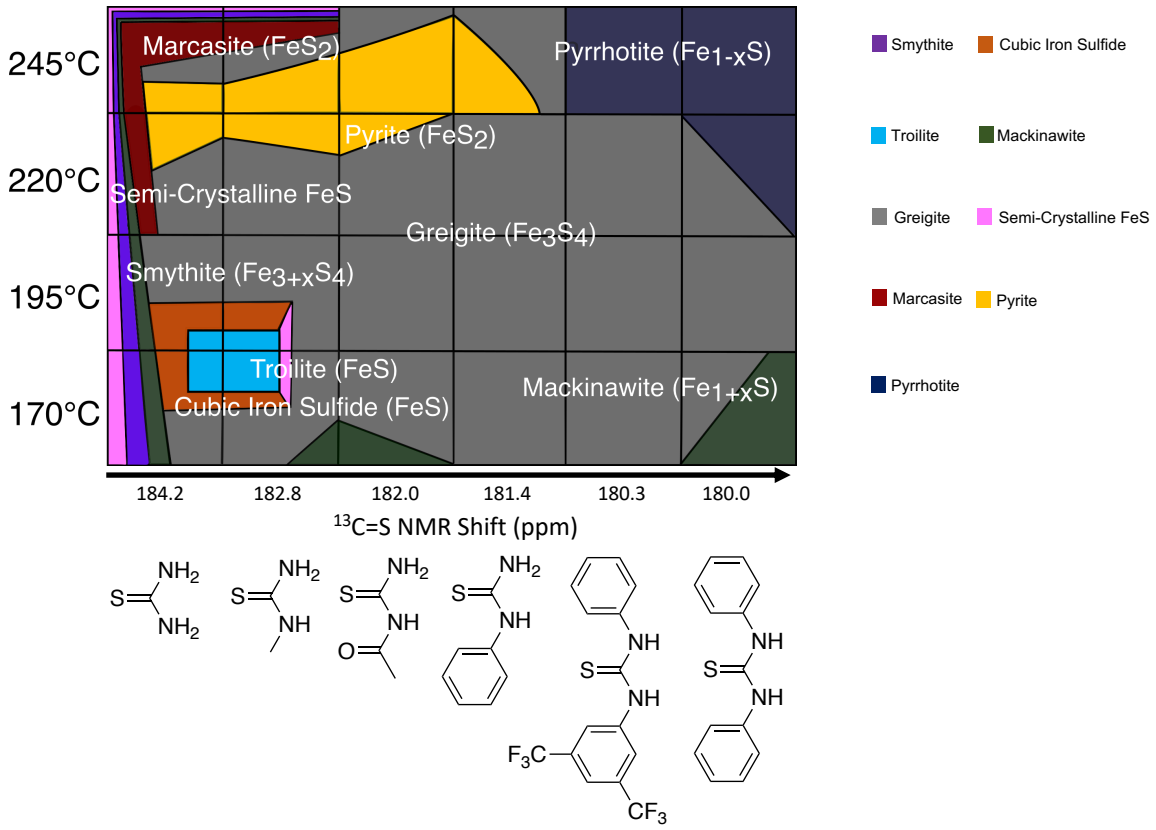

Figure 2.2) A bottom-up, synthetic phase diagram representing the approximate compositions of the generated phases gathered from the XRD patterns above. The X-axis represents the substituted thioureas used in the iron sulfide synthesis, ranging from most reactive thiourea on the left to least reactive thiourea on the right as judge by the $^{13}C{=}S$ chemical shift.

2.4 Understanding the Landscape of the Iron Sulfides

The synthetic phase diagram was prepared to aid in visualization of results (Figure 2.2) where each box is colored to represent the approximate ratios of phases observed. The diagram highlights both intuitive and unexpected relationships. It is not surprising that to achieve the most sulfur rich phases, pyrite (FeS_2) and marcasite (o-FeS_2), a temperature greater than 200°C and fast reacting thioureas are needed.[14] But curious anomalies also become apparent. For example, with slow reacting thioureas, low temperatures give greigite (Fe_3S_4), but increasing the temperature causes the exclusive formation of a more sulfur poor phase, pyrrhotite ($Fe_{1-x}S$).

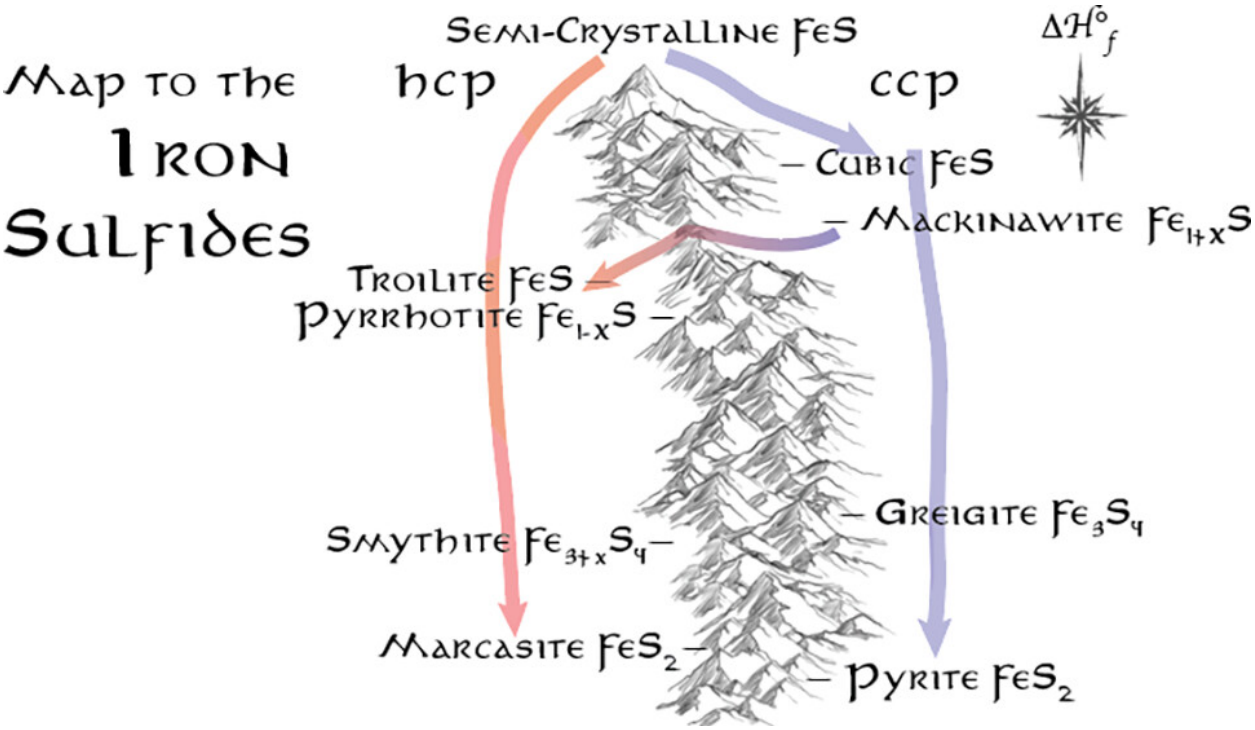

Figure 2.3 A map that describes the synthetic transformations in colloidal synthesis

The results are highly complex at first glance. Upon considering the thermodynamic stability of the phases, and splitting them into two categories—those based on approximate ccp and hcp stacking of the anions—explanations for the results clarify and are consistent with many of the observations of phase transformations made by the mineralogical and solid-state communities.[2, 15-20]

We build from Ostwald's 1897 "Rule of Stages" observation that when multiple polytypes are possible (phases of the same stoichiometry, but different arrangements of atoms), metastable phases form first, then transform into more thermodynamically stable phases.[21] More recently, it has been postulated that the metastable phases are actually the thermodynamically more stable phase at small nuclei sizes where surface energy dominates the thermodynamics.[21, 22] In the iron sulfur family, there are several hexagonal/cubic polymorphic pairs of similar composition [troilite (FeS)/mackinawite ($Fe_{1+x}S$); smythite ($Fe_{3+x}S4$)/greigite (Fe_3S_4); FeS_2 marcasite (o-FeS_2)/pyrite (FeS_2)] but transformation between polytypes is usually not observed. Instead, under forcing conditions such as elevated temperatures and additional sulfur content, phases are transformed to one of a differing stoichiometry rather than one with a different polytype.[2, 15-20]

Here, we build from Ostwald's postulate, and add that the ccp or hcp stacking of the anions in the nucleated phase is a key determinant in the subsequent phase transformations to phases of differing

stoichiometry. The iron sulfides can be imagined as two enthalpic "valley paths," dictated by their anion packing in the thermodynamic landscape separated by a high activation energy "mountain range." Troilite (FeS), pyrrhotite ($Fe_{1-x}S$), smythite ($Fe_{3+x}S_4$) and marcasite (*o*-FeS_2) all have approximate hcp stacking of the anions, either as S^{2-} or S_2^{2-} in the case of marcasite (*o*-FeS_2). In contrast, cubic iron sulfide (FeS), mackinawite ($Fe_{1-x}S$), greigite (Fe_3S_4) and pyrite (FeS_2) all have approximate ccp stacking (with pyrite having S_2^{-2} units) (Figure 2.3).

Of all the phases, cubic FeS is the highest energy, and Ostwald's rule of stages suggests that this local minimum will be found first.[21] Under conditions where excess sulfur can be incorporated, the nucleation of the ccp cubic FeS leads down the ccp path to mackinawite ($Fe_{1+x}S$), greigite (Fe_3S_4) and then pyrite (FeS_2). Transformation of the ccp lattice to hcp is kinetically hindered [23], even though there are hcp phases of intermediate enthalpy. The reactivity of the medium reacting thioureas (acetylthiourea and phenylthiourea) provide an example of how nucleation in the ccp stacking forces a specific path of phase transformations. At low temperatures, the metastable ccp structure mackinawite ($Fe_{1-x}S$) resulted. With elevated reaction temperature and excess thiourea reagents, only greigite (Fe_3S_4) resulted, suggesting that any nucleated ccp mackinawite ($Fe_{1+x}S$) was transformed to ccp greigite (Fe_3S_4), skipping hcp troilite (FeS) or pyrrhotite ($Fe_{1-x}S$), even though they are of intermediate thermodynamic stability. Only at the highest temperatures was additional sulfur incorporated to cause ccp pyrite (FeS_2) to form and, again, there was no evidence that the next thermodynamic steps of hcp smythite ($Fe_{3+x}S_4$) or hcp marcasite (*o*-FeS_2) formed as intermediates.

The concentrations of each of the thioureas were halved for a series of reactions at 220°C (Supporting information). In comparison to the full 6:1 ratio (Figure 2.1), unsurprisingly the sulfur rich phases of pyrite and marcasite (FeS_2) were absent from the products. However, like the reactions with high concentrations, at low concentrations the fastest thiourea still gave a mixture of hcp and ccp products (troilite FeS and greigite Fe_3S_4, respectively), and the intermediate reacting thioureas all gave only ccp products (greigite Fe_3S_4). With the slowest reacting thioureas, only pyrrhotite (hcp, $Fe_{1-x}S$) was obtained, instead of a mixture with greigite (Fe_3S_4), further indicating that sulfur incorporation to sulfur rich phases is hindered.

The paths of the ccp phases have been studied previously under aqueous conditions showing interconversion, avoiding the hcp phases. [2, 15-20] Hunger et al. reported that under sulfur-limited conditions, a mixture of mackinawite ($Fe_{1+x}S$), greigite (Fe_3S_4) and pyrite (FeS_2) can be observed

and not the hcp phases.[17] With sulfur as an oxidant, mackinawite ($Fe_{1+x}S$) can transform to pyrite (FeS_2), with greigite (Fe_3S_4) hypothesized as an intermediate.[17] Greigite ($Fe^{2+}Fe_2^{3+}S_4$) can transform to pyrite ($Fe^{2+}S_2^{2-}$), with the formation of persulfide resulting from a coupled reduction of ferric iron and the oxidation of sulfide ions.[24] In general, the ccp phases, pyrite (FeS_2) and greigite (Fe_3S_4), dominate the synthetic literature [with the exception of pyrrhotite ($Fe_{1-x}S$), *vide infra*] and are readily synthesized. It can be hypothesized then that the high-energy local minima of cubic FeS and mackinawite ($Fe_{1+x}S$) makes the ccp valley the "path most traveled."

In nature and in synthetic studies, the hcp family of iron sulfide phases are much more difficult to achieve. The exception is pyrrhotite ($Fe_{1-x}S$), which forms under conditions with high temperatures and low sulfur content.[23] The more sulfur rich hcp smythite ($Fe_{3+x}S_4$) and marcasite (*o*-FeS_2) are very rare in nature, forming most often when templated onto other hcp minerals such as siderite ($FeCO_3$) or nickel sulfide, which lowers their surface energy.[19] Some recent theoretical calculations have hinted that at low pH and small size, marcasite (*o*-FeS_2) is actually more stable than pyrite (FeS_2) because it has a lower surface energy.[25]

In this study, the hcp family of phases were co-nucleated with the ccp family of phases under highly reactive conditions with the fastest reacting thioureas (Figure 2.4). Even at 170°C, where conversion from mackinawite to pyrrhotite is kinetically hindered [23], hcp phases were observed. Several groups have recognized that fast aqueous precipitations to iron sulfides can lead to an intermediate semi-crystalline FeS phase [26-28] which can anneal into both ccp mackinawite or hcp pyrrhotite <150°C. This is similar to a semi-amorphous phase of Ni_2P which forms before crystallization of hexagonal Ni_2P in colloidal synthesis.[29] Here, the fast-reacting thioureas also caused the formation of the semicrystalline phase, which was identified by XRD (Figure 2.1*) but was not observed with the slower reacting thioureas.

In these experiments, the semi-crystalline FeS intermediate caused indiscriminate nucleation into both the ccp path [cubic FeS, to mackinawite ($Fe_{1+x}S$), to greigite (Fe_3S_4), to pyrite (FeS_2)] and the hcp path [troilite (FeS), to pyrrhotite ($Fe_{1-x}S$), to smythite ($Fe_{3+x}S_4$) , to marcasite (*o*-FeS_2)].

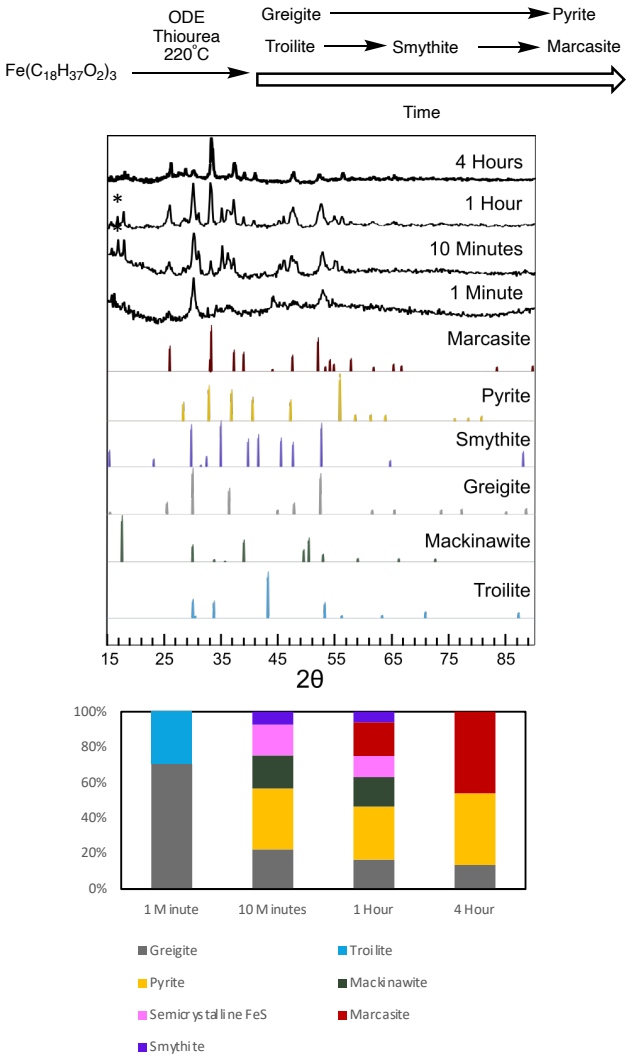

Figure 2.4 The progression of iron sulfide phase with time. XRD of the products and standard patterns (ICSD marcasite: 9013067, pyrite: 10422, smythite: 900077, greigite

Extending the reaction time fully transforms the mixture into marcasite (*o*-FeS_2) and pyrite (Figure 2.4). The indiscriminate nucleation into the amorphous intermediate with highly reactive sulfur precursors will therefore create a mixture of hcp and ccp phases.

The hcp family was also approached through a second route, which led to increased phase purity and revealed a high temperature route between the ccp and hcp paths. Reactions with slow reacting thioureas ensured the formation of ccp nuclei, initiating the cubic path through mackinawite ($Fe_{1-x}S$) to greigite (Fe_3S_4). Increasing the temperature should increase the reactivity of the thiourea to encourage pyrite (FeS_2) formation. However, at 245°C, pyrrhotite ($Fe_{1-x}S$) instead formed. An energetic barrier from ccp mackinawite ($Fe_{1+x}S$) to hcp pyrrhotite ($Fe_{1-x}S$) can be considered a

"low mountain pass" between the ccp and hcp valleys. 245°C provides enough thermal energy for ccp mackinawite ($Fe_{1+x}S$) nuclei to transform to the more thermodynamically stable polytype hcp pyrrhotite ($Fe_{1-x}S$) [23].

At 245°C, after crossing the mountain pass, the hcp pyrrhotite ($Fe_{1-x}S$) was kinetically trapped; hcp smythite ($Fe_{3+x}S_4$) did not form, even though its ccp cousin greigite (Fe_3S_4) can form under milder conditions on the ccp path. The lowered starting enthalpy of pyrrhotite ($Fe_{1-x}S$) compared with mackinawite ($Fe_{1+x}S$) creates a larger and hindering activation energy to continue adding sulfur on the hcp path to smythite ($Fe_{3+x}S_4$) and marcasite (*o*-FeS_2).

2.5 Targeting the Phases of Iron Sulfides Using a Rationale

With the developed phase map in hand, it is possible to target phases that are elusive either due to their metastability or because of their sulfur anion packing. By taking account both chemical toolkits as well as crystalline pathways, we can strategize how to navigate between the iron sulfide phases. Below are pioneering cases where instead of a serendipitous outcome, rational phase control can be achieved (Figure 2.5).

Conditions to Mackinawite

Mackinawite ($Fe_{1-x}S$) is a highly metastable phase that is typically is prepared from aqueous precipitations. At temperatures below 100°C, it can be sulfurized to give the ccp phases greigite (Fe_3S_4) or pyrite (FeS_2).[11] A preparation of pure mackinawite ($Fe_{1+x}S$) in organic media is not known, but now can be targeted using information from the developed phase diagram. The synthetic phase diagram indicates greigite (Fe_3S_4) is grown by using slow reacting thioureas at temperatures below 200°C and it can be hypothesized that that further slowing the reactivity of the thiourea will lead to isolation of mackinawite ($Fe_{1+x}S$). Therefore, very unreactive 1-hexyl-3-phenyl-2-thiourea was synthesized and used for nanocrystal synthesis at 170°C, which yielded pure mackinawite ($Fe_{1+x}S$) within the limitations of quantification by pXRD. Similarly, slow reactions and the trapping of mackinawite ($Fe_{1+x}S$) can be facilitated by employing a coordinating solvent to lower surface energy. Slower thioureas at 170°C predominately yielded a mixture of greigite (Fe_3S_4) and mackinawite ($Fe_{1+x}S$) in ODE). (Supporting Information).

Conditions to Synthesize Greigite and Pyrite

Pyrite (FeS_2) is the most thermodynamically stable phase in the iron sulfide library but is often synthesized with impurities of its hexagonal counterpart marcasite (*o*-FeS_2). We can hypothesize this can be prevented by keeping temperatures below the pass between ccp and hcp valleys and

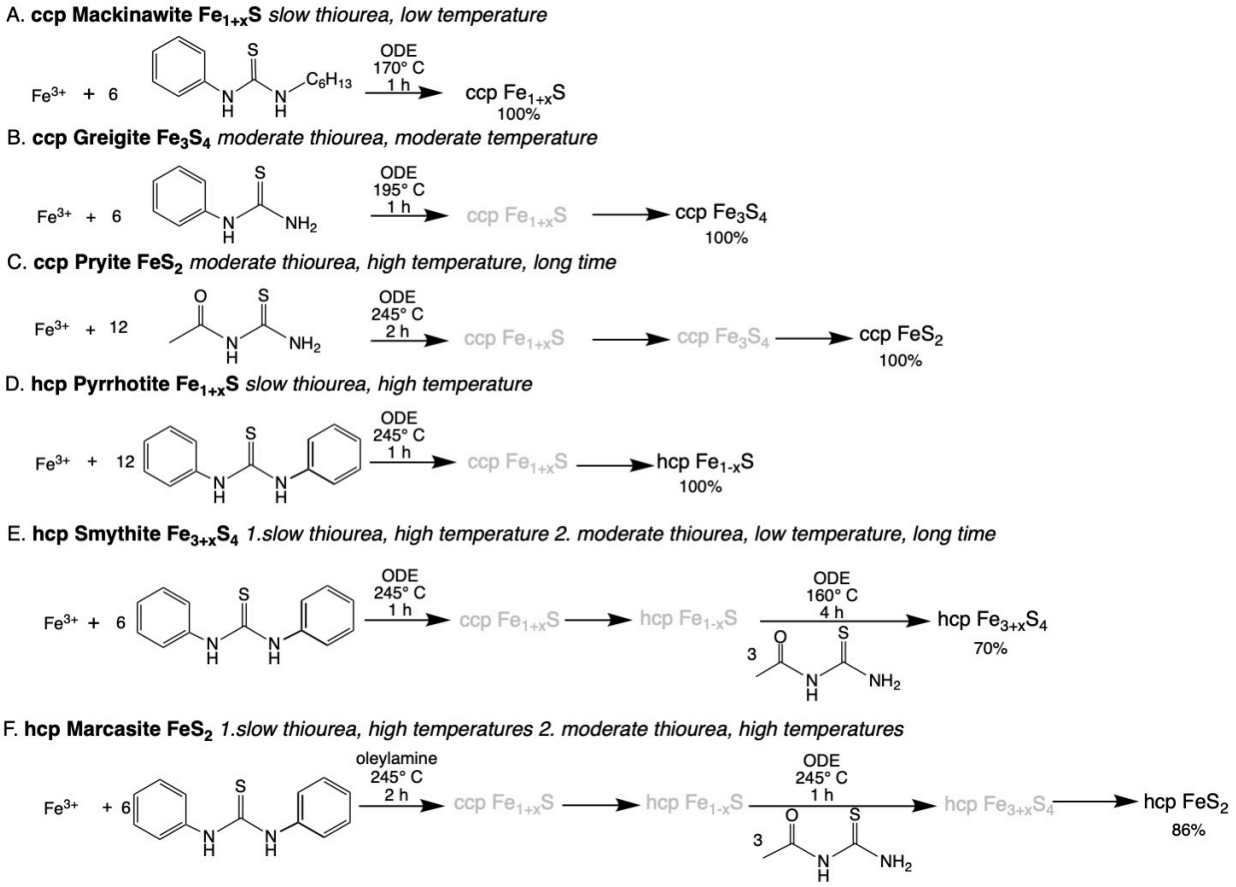

Figure 2.5 Rational syntheses to six iron sulfides. Grey compounds are presumed and non-isolated intermediates.

using slow thioureas to favor nucleation into only the ccp path. The initial study showed that ccp greigite (Fe_3S_4) can be achieved by using a medium reacting thiourea, such as acetyl thiourea or phenyl thiourea, at 195°C. From these conditions, more sulfur needs to be included to follow the ccp valley to pyrite. Raising the temperature to 245°C, doubling the molar ratio of acetylthiourea:Fe to 12:1, and doubling the reaction time to 2h, gave pyrite (FeS_2) as the only identified iron sulfide by XRD.

Accessing the HCP Valley of Pyrrhotite, Smythite and Marcasite

Smythite ($Fe_{3+x}S_4$) and marcasite (*o*-FeS_2) are challenging materials to synthesize. Fast reacting thioureas can nucleate into the hexagonal valley, but always with concomitant nucleation of ccp phases. Alternatively, the mountain pass is a second route to access the hcp valley. Using the landscape described, it appears that two different sets of reaction conditions are needed in succession: first one with low sulfur reactivity and high temperature, followed by one with high

sulfur reactivity. There is only one other reported colloidal synthesis of marcasite (*o*-FeS_2), which coincidentally also had two sulfur sources of differing reactivity.[30]

First, to achieve pyrrhotite ($Fe_{1-x}S$), a low reactivity sulfur reagent, such as diphenyl thiourea, is needed to avoid the mackinawite ($Fe_{1+x}S$) to greigite (Fe_3S_4) and pyrite (FeS_2) transformation path. High temperatures (245°C) are needed to convert ccp mackinawite ($Fe_{1+x}S$) nuclei over the mountain pass to the slightly more stable hcp pyrrhotite ($Fe_{1-x}S$). These conditions gave pyrrhotite in pure form within the limitations of powder diffraction. We did not observe the stoichiometric endmember of the pyrrhotite family, troilite (FeS), under these conditions likely due to the excess of sulfur reagent employed.

In a second step, and in parallel approach to achieving pyrite, more reactive sulfur is needed to convert the pyrrhotite ($Fe_{1-x}S$) exclusively to smythite ($Fe_{3+x}S_4$) and marcasite (*o*-FeS_2). Using a second addition of 3:1 acetyl thiourea:Fe at 160°C, gave 30% pyrrhotite and 70% smythite ($Fe_{3+x}S_4$). Increasing the reaction temperature of this second step to 245°C gave predominantly marcasite (*o*-FeS_2).

It was found the proportion of marcasite could be increased by substituting the ODE solvent with oleylamine in the first step. Oleylamine substitutes the thiourea *in situ* (supporting information), to give a very slow reacting thiourea. These conditions seemed to give a highly crystalline pyrrhotite intermediate which in turn, yielded 82% marcasite with only 18% pyrite impurity.

2.6 Conclusion

By using a library of thioureas with tunable reactivity, we were able to observe all eight of the known iron sulfides as products and a semi-crystalline phase. Fast reacting thioureas, such as unsubstituted thiourea, gave a complex mixture of iron sulfides. At low temperatures of 170°C, sulfur poor phases dominate, especially ~FeS phases. At high temperatures of 245°C sulfur rich phases dominate including pyrite and marcasite (FeS_2). With medium reacting thioureas, such as acetylthiourea, at low temperature greigite (Fe_3S_4) dominates and is replaced by pyrite (FeS_2) at high temperatures. With slow reacting thioureas, such as diphenylthiourea, at low temperatures, mackinawite ($Fe_{1+x}S$) and greigite (Fe_3S_4) form, yet at high temperatures, pyrrhotite ($Fe_{1-x}S$) dominates.

Using these experiments, we developed the first ever synthetic phase diagram to visualize the trends between thiourea reactivity, reaction temperature, and the sulfur content in the product phases observed. We hypothesize that the anion stacking of the nucleated sulfur-poor phase is a

large determinant in the paths subsequently taken to the other phases of differing stoichiometry. Most notably, this study is the first of its kind to strategically and rationally target specific phases in the iron sulfides. Here we show that it is imperative to consider both synthetic mechanisms, decomposition pathways, crystal structures and phase transformation pathways when targeting the desired structure. This understanding of phase control can be applied to other compound materials enabling their targeted synthesis and will ultimately contribute to further development of a wide range of technologies requiring crystalline materials.

References

(1) Jain, A.; Ong, S. P.; Hautier, G.; Chen, W.; Richards, W. D.; Dacek, S.; Cholia, S.; Gunter, D.; Skinner, D.; Ceder, G.; et al. Commentary: The materials project: A materials genome approach to accelerating materials innovation. *APL Materials* **2013**, *1* (1). DOI: 10.1063/1.4812323.

(2) Lennie, A. R.; Vaughan, D. J. Spectroscopic studies of iron sulfide formation and phase relations at low temperatures. *Mineral Spectroscopy: a Tribute to Roger G. Burns* **1996**, (5), 117-131.

(3) Hendricks, M. P.; Campos, M. P.; Cleveland, G. T.; Plante, I. J.-L.; Owen, J. S. A Tunable library of substituted thiourea precursors to metal sulfide nanocrystals. *Science* **2015**, *348* (6240), 1226-1230. DOI: 10.1126/science.aaa2951.

(4) Hollingsworth, N.; Roffey, A.; Islam, H. U.; Mercy, M.; Roldan, A.; Bras, W.; Wolthers, M.; Catlow, C. R. A.; Sankar, G.; Hogarth, G.; et al. Active nature of primary amines during thermal decomposition of nickel dithiocarbamates to nickel sulfide nanoparticles. *Chemistry of Materials* **2014**, *26* (21), 6281-6292. DOI: 10.1021/cm503174z.

(5) Thomson, J. W.; Nagashima, K.; MacDonald, P. M.; Ozin, G. A. From sulfur-amine solutions to metal sulfide nanocrystals: Peering into the oleylamine-sulfur black box. *Journal of the American Chemical Society* **2011**, *133* (13), 5036-5041. DOI: 10.1021/ja1109997.

(6) Frenette, L. C.; Krauss, T. D. Uncovering active precursors in colloidal quantum dot synthesis. *Nature Communications* **2017**, *8* (1), 1-8. DOI: 10.1038/s41467-017-01936-z.

(7) Rhodes, J. M.; Jones, C. A.; Thal, L. B.; MacDonald, J. E. Phase-controlled colloidal syntheses of iron sulfide nanocrystals via sulfur precursor reactivity and direct pyrite precipitation. *Chemistry of Materials* **2017**, *29* (19), 8521-8530. DOI: 10.1021/acs.chemmater.7b03550.

(8) Bi, Y.; Yuan, Y.; Exstrom, C. L.; Darveau, S. A.; Huang, J. Air stable, photosensitive, phase pure iron pyrite nanocrystal thin films for photovoltaic application. *Nano Letters* **2011**, *11* (11), 4953-4957. DOI: 10.1021/nl202902z.
(9) Fan, H. H.; Li, H. H.; Huang, K. C.; Fan, C. Y.; Zhang, X. Y.; Wu, X. L.; Zhang, J. P. Metastable Marcasite-FeS2 as a New Anode Material for Lithium Ion Batteries: CNFs-Improved Lithiation/Delithiation Reversibility and Li-Storage Properties. *ACS Applied Materials and Interfaces* **2017**, *9* (12), 10708-10716. DOI: 10.1021/acsami.7b00578.
(10) Chang, Y. S.; Savitha, S.; Sadhasivam, S.; Hsu, C. K.; Lin, F. H. Fabrication, characterization, and application of greigite nanoparticles for cancer hyperthermia. *Journal of Colloid and Interface Science* **2011**, *363* (1), 314-319. DOI: 10.1016/j.jcis.2010.06.069.
(11) Rickard, D.; Luther, G. W. *Chemistry of iron sulfides*; 2007. DOI: 10.1021/cr0503658.
(12) Cemic, L.; Kleppa, O. J. High temperature calorimetry of sulfide systems. I. Thermochemistry of liquid and solid phases of Ni + S. *Geochimica et Cosmochimica Acta* **1986**, *50* (8), 1633-1641. DOI: 10.1016/0016-7037(86)90126-2.
(13) Gamsjäger, H.; Mompean, F. J.; Issy les, M.; Bank, N. E. A. D.; Agency, O. N. E. Chemical thermodynamics of nickel. *Chemical thermodynamics* **2005**, (6), xxx, 617 p.-xxx, 617 p.
(14) Kaur, G.; Kaur, M.; Thakur, A.; Kumar, A. *Recent Progress on Pyrite FeS2 Nanomaterials for Energy and Environment Applications: Synthesis, Properties and Future Prospects*; Springer US, 2020. DOI: 10.1007/s10876-019-01708-3.
(15) Murowchick, J. B.; Barnes, H. L. Formation of cubic FeS. *American Mineralogist* **1986**, *71* (9-10), 1243-1246.
(16) Bourdoiseau, J. A.; Jeannin, M.; Rémazeilles, C.; Sabot, R.; Refait, P. The transformation of mackinawite into greigite studied by Raman spectroscopy. *Journal of Raman Spectroscopy* **2011**, *42* (3), 496-504. DOI: 10.1002/jrs.2729.
(17) Hunger, S.; Benning, L. G. Greigite: A true intermediate on the polysulfide pathway to pyrite. *Geochemical Transactions* **2007**, *8*, 1-20. DOI: 10.1186/1467-4866-8-1.
(18) Novikov, G. V.; Egorov, V. K.; Popov, V. I.; Sipavina, L. V. Kinetics and mechanism of transformations in iron-rich pyrrhotites and in troilite-pyrrhotite metastable assemblages. *Physics and Chemistry of Minerals* **1977**, *1* (1), 1-14. DOI: 10.1007/BF00307975.

(19) Furukawa, Y.; Barnes, H. L. Reactions forming smythite, Fe9S11. *Geochimica et Cosmochimica Acta* **1996**, *60* (19), 3581-3591. DOI: 10.1016/0016-7037(96)00187-1.
(20) Bai, P.; Zheng, S.; Chen, C.; Zhao, H. Investigation of the iron-sulfide phase transformation in nanoscale. *Crystal Growth and Design* **2014**, *14* (9), 4295-4302. DOI: 10.1021/cg500333p.
(21) Ostwald, W. Studien über die Bildung und Umwandlung fester Körper 1. Abhandlung: Übersättigung und Überkaltung. *Zeitschrift für Physikalische Chemie* **1897**, *22*, 289-330.
(22) Sun, W.; Dacek, S. T.; Ong, S. P.; Hautier, G.; Jain, A.; Richards, W. D.; Gamst, A. C.; Persson, K. A.; Ceder, G. The thermodynamic scale of inorganic crystalline metastability. *Science Advances* **2016**, *2* (11). DOI: 10.1126/sciadv.1600225.
(23) Lennie, A. R.; England, K. E. R.; Vaughan, D. J. Transformation of synthetic mackinawite to hexagonal pyrrhotite: a kinetic study. *American Mineralogist* **1995**, *80* (9-10), 960-967. DOI: 10.2138/am-1995-9-1012.
(24) Wilkin, R. T.; Barnes, H. L. Pyrite formation by reactions of iron monosulfides with dissolved inorganic and organic sulfur species. *Geochimica et Cosmochimica Acta* **1996**, *60* (21), 4167-4179. DOI: 10.1016/S0016-7037(97)81466-4.
(25) Kitchaev, D. A.; Ceder, G. Evaluating structure selection in the hydrothermal growth of FeS 2 pyrite and marcasite. *Nature Communications* **2016**, *7*, 1-7. DOI: 10.1038/ncomms13799.
(26) Csákberényi-Malasics, D.; Rodriguez-Blanco, J. D.; Kis, V. K.; Rečnik, A.; Benning, L. G.; Pósfai, M. Structural properties and transformations of precipitated FeS. *Chemical Geology* **2012**, *294-295*, 249-258. DOI: 10.1016/j.chemgeo.2011.12.009.
(27) Matamoros-Veloza, A.; Cespedes, O.; Johnson, B. R. G.; Stawski, T. M.; Terranova, U.; de Leeuw, N. H.; Benning, L. G. A highly reactive precursor in the iron sulfide system. *Nature Communications* **2018**, *9* (1). DOI: 10.1038/s41467-018-05493-x.
(28) Beauvais, M. L.; Chupas, P. J.; O'Nolan, D.; Parise, J. B.; Chapman, K. W. Resolving Single-layer Nanosheets as Short-lived Intermediates in the Solution Synthesis of FeS. *ACS Materials Letters* **2021**, *3* (6), 698-703. DOI: 10.1021/acsmaterialslett.1c00193.
(29) Moreau, L. M.; Ha, D.-H.; Zhang, H.; Hovden, R.; Muller, D. A.; Robinson, R. D. Defining Crystalline/Amorphous Phases of Nanoparticles through X-ray Absorption Spectroscopy and X-

ray Diffraction: The Case of Nickel Phosphide. *Chemistry of Materials* **2013**, *25* (12), 2394-2403. DOI: 10.1021/cm303490y.

(30) Li, T.; Guo, Z.; Li, X.; Wu, Z.; Zhang, K.; Liu, H.; Sun, H.; Liu, Y.; Zhang, H. Colloidal synthesis of marcasite FeS2 nanoparticles with improved electrochemical performance. *RSC Advances* **2015**, *5* (120), 98967-98970. DOI: 10.1039/c5ra22610d.

Chapter 3: Phase Control in the Synthesis of Cobalt Sulfides

3.1 The Cobalt Sulfides

There are four known cobalt sulfides **Table 3.1**, catterite (CoS_2) linneaite (Co_3S_4) jaipurite (CoS) and cobaltpentlandite (Co_9S_8). Each have differing electronic, optical, electrochemical, and chemical properties and some are are exceptional candidates for battery applications[1-3] and electrocatalysis.[4, 5] Even small changes in crystalline structure can lead to drastic differences in their overall behavior. Understanding how to synthesize one cobalt sulfide over the other will not only help us understand overarching trends in bottom-synthesis and phase control, but it will also allow us to develop reliable synthetic routes that can target each desired crystalline phase and thus achieve specific material properties.

Table 3.1

Phase	**Formula**	**Space Group**	**Approximate Sulfur Closed Packing**	**Cation Hole Filling**	**ΔH_f° (kJ/mol)[8]**
Cattierite	CoS_2	Pa3	Cubic	O_h	-287 kJ/mol
Jaipurite	CoS	$P6_3/mmc$	Hexagonal	O_h	-150 kJ/mol
Linnaeite	Co_3S_4	Fd3m	Cubic	T_d, O_h	-585 kJ/mol
Cobalt Pentlandite	Co_9S_8	Fm3m	Cubic	T_d, O_h	-1326 kJ/mol

In our previous work with the iron sulfides, it was observed that the anion stacking of the nucleated phase dictated the path of to other phase transformations. For example, metastable phase with cubic closed packed anion stackings would transform into more thermodynamically stable cubic closed pack phases. Mackinawite (cubic FeS, ΔH_f -91.6 kJ/mol) would transform into greigite (cubic Fe_3S_4, ΔH_f -144.1 kJ/mol) which would then transform to the more thermodynamically stable pyrite (cubic FeS_2, ΔH_f -171.1 kJ/mol). When looking at hexagonal closed packed phases, a similar phenomenon could be observed: metastable hexagonal phases would transform into more thermodynamically stable hexagonal phases. Understanding this, we

were able to synthesize pyrrhotite seeds (Hexagonal Fe_9S_8, ΔH_f -106.2kJ/mol) then react it with a more reactive thiourea, to obtain a large amount of marcasite (Hexagonal FeS_2, ΔH_f -169.5 kJ/mol).[7]

To obtain a comprehensive understanding of phase control, we can expand these strategies to more transition metal sulfide systems like the cobalt sulfides. We want to know if the trends we observe in the iron sulfides can be extended more generally across the periodic table.

The iron sulfide system is filled with many polymorphic pairs- pairs of crystal structures that have matching stoichiometries, but varying anion stackings. For example, pyrite (FeS_2) has a polymorphic pair with marcasite (FeS_2), with similar thermodynamic enthalpies of formation, but have ccp and hcp anion stacking, respectively This made phase targeting very difficult, as most cubic phase in the iron sulfide library almost seemed to have a counterpart hexagonal phase- and targeting one over the other required a high level of precision and control. The cobalt sulfides lack polymorphic pairs, and are lower in number. There are three cubic cobalt sulfides: catterite (CoS_2), linnaeite (Co_3S_4), and cobaltpentlandite (Co_9S_8), and there is one hexagonal cobalt sulfide: jaipurite (CoS). Without the presence of these polymorphic pairs, it could prove easier to target each cobalt sulfide phase.

Here, a library of thioureas is employed to map the nucleation and phase transformations of cobalt sulfides during bottom-up colloidal synthesis. As seen in Jonathan Owen's work, thiourea can be used to change the rates in which it releases sulfur. Both the number and identity of the thiourea substituents will vary the rates of reaction in nanocrystalline synthesis.[8] Here we use the substituted thioureas in the synthesis of cobalt sulfides to study how reaction kinetics influences the phase of the resulting cobalt sulfides in bottom-up synthesis, and use the cobalt sulfides as a material system of comparison to the iron sulfides. In doing so, we are able to synthesize all four natural cobalt sulfides- cattierite (CoS_2), jaipurite (CoS), linnaeite (Co_3S_4), and cobaltpentlandite (Co_9S_8)- phase pure. Here we confirm that the trends seen for the iron sulfides extend to the cobalt sulfides that anion hole stacking in the nucleated phase dictates the resulting nanoparticle phase. In doing so, we are able to gain a more comprehensive understanding on how we can control and target phases in bottom-up synthesis of metal chalcogenides.

3.2 Synthesizing Cobalt Sulfides Using Tunable Thioureas

General Cobalt Sulfide Nanoparticles Synthesis in 1-Octadecene using Addition Funnel Hot Addition Method

Cobalt (II) stearate (1 mmol, 626 mg), 10 mL of 1-octadecene (ODE), and a magnetic stir bar were added to a 25mL, 3-neck round bottom flask. In a 10mL glass addition funnel, 6 mmol of thiourea was added to 5 mL of ODE, and the funnel was fixed to the round bottom flask using grease and keck clips. A condenser is connected to the three-neck flask to account for possible reflux, and the system was attached to a Schlenk line via gas adapter atop the condenser. All openings in the system were capped with rubber septa, and thermocouples were placed through the septa into ODE in both the round bottom flask and the addition funnel. The system was wrapped in glass wool and heated to 60˚C using a heating mantle and degassed for 30 minutes under vacuum. The vacuum was then switched to Argon gas, and the system was heated to the desired temperature (170˚C, 220˚C, and 270˚C). The contents of the addition funnel were then injected into the round bottom flask, yielding a near immediate color change from blue to black. The solution was left to react for the desired length of time (1 min – 2 hours). The heating mantle was removed from the system and left to cool to 100˚C, at which point the reaction was quenched with ethanol then chloroform. These served as the antisolvent and solvent, respectively, used to clean the particles. The nanoparticles were centrifuged at 8700 rpm for 5 minutes and the solvents decanted. This process was repeated twice more before dispersing the nanoparticles in minimal amounts of chloroform.

Cattierite Synthesis

1 mmol (626 mg) of cobalt (II) stearate, 10 mL of 1-octadecene (ODE), and a magnetic stir bar were added to a 25mL, 3-neck round bottom flask. In a 10mL glass addition funnel, 12 mmol of thiourea (0.913 g) was added to 5 mL of ODE. A condenser is connected to the three-neck flask to account for possible reflux, and the system was attached to a Schlenk line via gas adapter atop the condenser. All openings in the system were capped with rubber septa, and thermocouples were placed through the septa into ODE in both the round bottom flask and the addition funnel. The system was wrapped in glass wool and heated to 60˚C using a heating mantle and degassed for 30 minutes under vacuum. The vacuum was then switched to Argon gas, and the system was heated to 220˚C. The contents of the addition funnel were then quickly added into the round bottom flask, yielding a near-immediate color change from blue to black. The solution was left to react for one hour. Once complete, the heating mantle was removed from the system and left to

cool to 100˚C, at which point the reaction was quenched with ethanol then chloroform. These served as the antisolvent and solvent, respectively, used to clean the particles. The nanoparticles were centrifuged at 8700 rpm for 5 minutes and the solvents decanted. This process was repeated twice more before dispersing the nanoparticles in minimal amounts of chloroform.

Cobaltpentlandite Synthesis

1 mmol (626 mg) of cobalt (II) stearate, 10 mL of 1-octadecene (ODE), and a magnetic stir bar were added to a 25mL, 3-neck round bottom flask. In a 10mL glass addition funnel, 0.5 mmol of 1-hexyl-3-phenyl thiourea (0.119 g) was added to 5 mL of ODE. A condenser is connected to the three-neck flask to account for possible reflux, and the system was attached to a Schlenk line via gas adapter atop the condenser. All openings in the system were capped with rubber septa, and thermocouples were placed through the septa into ODE in both the round bottom flask and the addition funnel. The system was wrapped in glass wool and heated to 60˚C using a heating mantle and degassed for 30 minutes under vacuum. The vacuum was then switched to Argon gas, and the system was heated to 220˚C. The contents of the addition funnel were then quickly added into the round bottom flask, yielding a color change from blue to black over the span of several seconds. The solution was left to react for one hour. Once complete, the heating mantle was removed from the system and left to cool to 100˚C, at which point the reaction was quenched with ethanol then chloroform. These served as the antisolvent and solvent, respectively, used to clean the particles. The nanoparticles were centrifuged at 8700 rpm for 5 minutes and the solvents decanted. This process was repeated twice more before dispersing the nanoparticles in minimal amounts of chloroform.

Jaipurite Synthesis

1 mmol (626 mg) of cobalt (II) stearate, 15 mL of 1-octadecene (ODE), 18 mmol of diethylthiourea (2.38 g), and a magnetic stir bar were added to a 25mL, 3-neck round bottom flask. A condenser is connected to the three-neck flask to account for possible reflux, and the system was attached to a Schlenk line via gas adapter atop the condenser. The two side necks were in the system were capped with rubber septa, and a thermocouple was placed through one of the septa and submerged into the ODE. The system was wrapped in glass wool and heated to 60˚C using a heating mantle and degassed for 30 minutes under vacuum. The vacuum was then switched to Argon gas, and the system was heated to 155˚C. The gradual heating yielded a color change from blue to black which took place over most of the heating. The solution was left to

react for one hour once the round-bottom reached 155˚C. After reacting, the heating mantle was removed from the system and left to cool to 100˚C, at which point the reaction was quenched with ethanol then chloroform. These served as the antisolvent and solvent, respectively, used to clean the particles. The nanoparticles were centrifuged at 8700 rpm for 5 minutes and the solvents decanted. This process was repeated twice more before dispersing the nanoparticles in minimal amounts of chloroform.

Linnaeite Synthesis

Phase-pure cobaltpentlandite nanoparticles were made in accordance with the previously described synthesis. Once these nanoparticles were made, and their purity was confirmed via XRD, they were resuspended in a minimal amount of chloroform.

The suspended cobaltpentlandite nanoparticles were transferred in a 10 mL ODE in 25mL, 3-neck round bottom flask. In a 10mL glass addition funnel, 6 mmol of diphenylthiourea (1.37 g) was added to 5 mL of ODE. A condenser is connected to the three-neck flask to account for possible reflux, and the system was attached to a Schlenk line via gas adapter atop the condenser. All openings in the system were capped with rubber septa, and thermocouples were placed through the septa into ODE in both the round bottom flask and the addition funnel. The system was wrapped in glass wool, heated to 100˚C using a heating mantle, and degassed for 60 minutes under vacuum. The vacuum was then switched to Argon gas, and the system was heated to 220˚C. The contents of the addition funnel were then injected into the round bottom flask. No color change was observed since the original cobaltpentlandite nanoparticle solution was initially black. The solution was left to react for one hour, after which the heating mantle was removed from the system, and it was left to cool to 100˚C. At this point, the reaction was quenched with ethanol then chloroform. These served as the antisolvent and solvent, respectively, used to clean the particles. The nanoparticles were centrifuged at 8700 rpm for 5 minutes and the solvents decanted. This process was repeated twice more before dispersing the nanoparticles in minimal amounts of chloroform.

Material Characterization

Powder X-ray Diffraction (XRD) spectra were obtained using a Rigaku SmartLab® X-ray Diffractometer. This diffractometer had a CuK□ source and a D/TeX Ultra 250 detector. The operating voltage was 40 kV and the operating current was 44 mA. Samples were drop casted particle suspensions onto low-background silicon XRD wafers. The step size was 0.1 degree at a

rate of 10 degrees per minute. There was no evidence oxidation occurring during XRD characterization

Rietveld Refinement Method and quantification

Rietveld refinements were performed by Rigaku PDXL. The .cif files employed are noted as table 1 as the Powder diffraction file cards. The patterns was allowed to be fit freely with the cards noted in Table S1 with percentages.

3.3 Phase Control the Cobalt Sulfides

A general synthesis method similar to *Espano et al*.[7] was used to yield cobalt sulfide nanocrystals and was mostly carried out byhonors undergraduate student Peter Edwards under the supervision of Jeremy Espano. Cobalt (II) stearate (1 mmol) in 1-octadecne (ODE) in a 25 mL 3-neck round-bottom flask with an connected addition funnel with a pressure equalizing arm. The 3-neck round bottom flask was attached to the Schlenk line via condenser and gas adapter. 6 mmol of the chosen substituted thiourea [thiourea, methylthiourea, phenylthiourea, 1-3,5-bis(trifluoromethyl)phenyl-3-phenyl-2-thiourea, diphenylthiourea] was dissolved in ODE in the separate addition funnel and sealed with a septum and pierced with a thermocouple down to the solution level. The apparatus was degassed under vacuum and the round-bottom flask stirred for 30 min at 60°C using a heating mantle. The vacuum was replaced with argon and the temperature in the round-bottom flask was raised to to the desired temperature (170°C -270°C). the contents of the addition funnel were heated to the same desired temperature using a heat gun (MHT Products Inc.), allowing the thiourea to dissolve. After dissolution, the contents of the addition funnel were added swiftly to the round bottom flask and the solution was left at the desired temperature of 1 min, 10 min, 1 h or 4 h. to isolate the product cobalt sulfides, after cooling, chloroform (5 mL was added to suspend the particles. The mixture was centrifuged at 4500 rpm for 5 min. The liquid component was decanted, and the nanoparticles were resuspended in chloroform and ethanol was added as an antisolvent. This process was repeated 4 times.

The $^{13}C{=}S$ NMR chemical shift of the thioureas can be used as an indicator of the electron density on the neighboring sulfur as shown by *Espano et al.* The substituted thioureas employed in decreasing electron density and reactivity from thiourea > methylthiourea > phenylthiourea > -3,5-bis(trifluoromethyl)phenyl-3-phenyl-2-thiourea > diphenylthiourea.

The products were analyzed using powder X-ray diffraction (XRD) using a Rigaku Smart® X-ray Diffractometer with a CuKα source and a D/TeX Ultra 250 detector with an operating

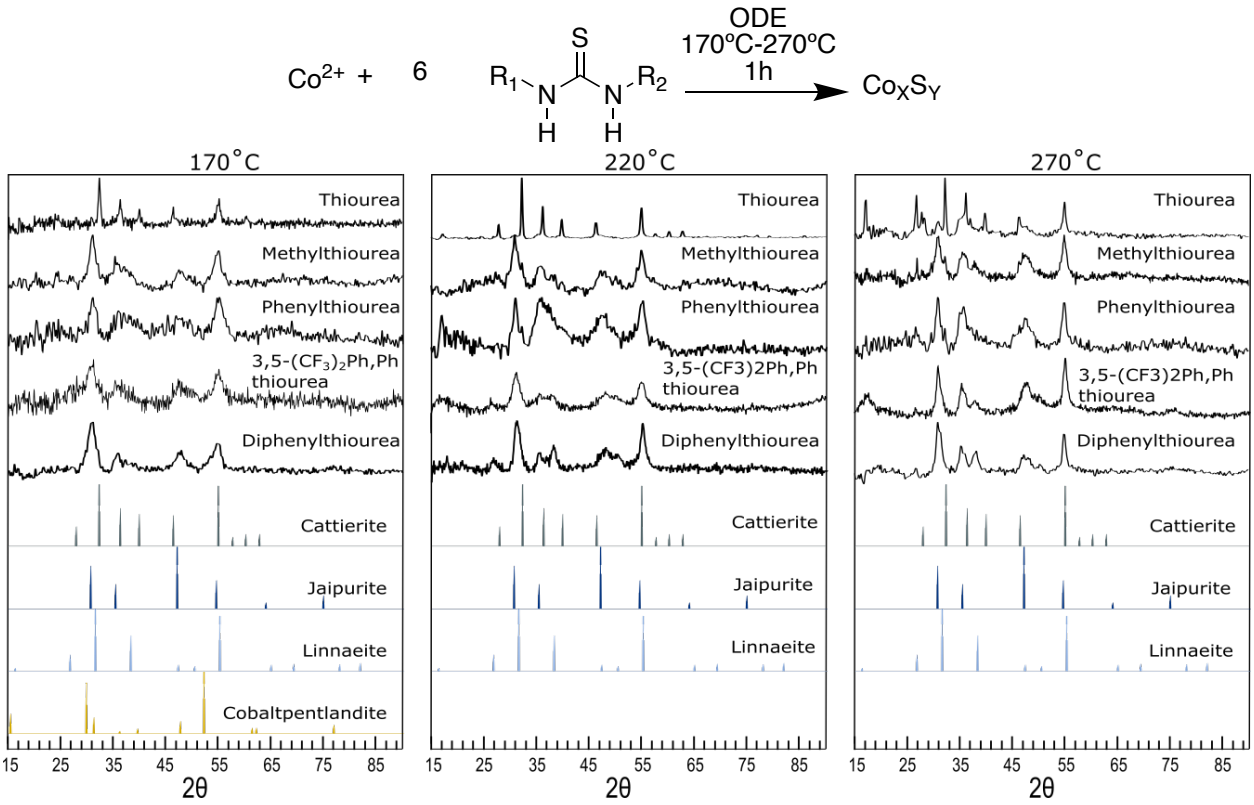

Figure 3.1: A reaction scheme to synthesize cobalt sulfide nanocrystals. Powder X-ray diffraction (XRD) of the products of different substited thioureas reacting with cobalt (II) stearate at 170, 220, and 270. (ICSD Catterite: 624838, Jaipurite: 9008884, Linnaeite: 1011056, Cobaltpentlandite: 31753.)

voltage and current of 40 kV and 44 mA respectively. Samples were prepared by the drop casting particle suspensions onto low-background silicon XRD wafers in ambient conditions and allowing the solvent to evaporate. No evidence of oxides were observed in the XRD or by color changes. After the XRD patterns were obtained, refinements were performed using Rigaku PDXL and the.cif files employed were the PDF cards Each pattern was allowed to be fit freely with the cards noted.

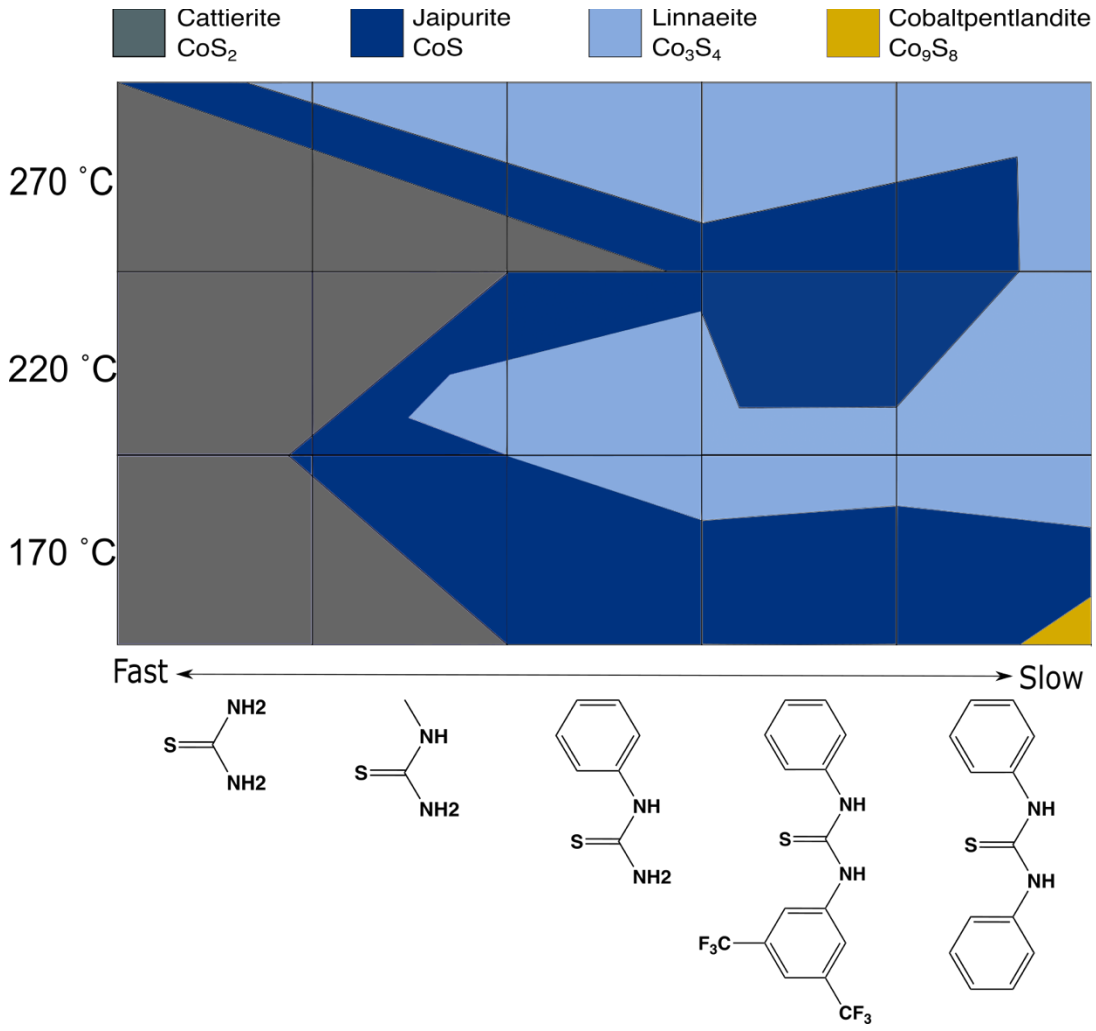

Figure 3.2: Bottom-up, synthetic phase diagram representing the approximate compositions of the generated phases gathered from the XRD patterns in figure 3.1. The X-axis represents the substituted thioureas used in the cobalt sulfide synthesis ranging from fastest thiourea on the left to slowest thiourea on the right.

Initial syntheses were performed using reactions temperatures of 170˚C, 220˚C, and 270˚C with the substituted thiourea library and initially each of the four phases of cobalt sulfides were synthesized in varying quantities (Figure 3.1). A synthetic phase map to show the relative proportions of each phase was also made (Figure 3.2). Overall, the initial data strongly correlates to our previous work with the iron sulfides[7] where the decomposition of the sulfur precursor has a large effect on the resulting phase. When using fast reactive thiourea, catterite (CoS_2) was observed to be the main product. Slowing down the reactivity to methylthiourea and phenylthiourea leads

to the inclusion of both jaipurite (CoS) and linnaeite (Co_3S_4). When using the slowest reactive thiourea (diphenylthiourea), we see the disappearance of catterite (CoS_2), a larger formation of jaipurite (CoS) and linnaeite (Co_3S_4), and at low temperatures (170˚C) the formation of a minority component of cobaltpentlandite (Co_9S_8).

Generally, there seems to be an inverse relationship among the cobalt sulfides between their sulfur content and thermodynamic stability. The most thermodynamically stable cobalt sulfide is cobaltpentlandite (Co_9S_8), while the most metastable cobalat sulfide is catterite (CoS_2).[9] With the fastest thiourea, we see that an increase in temperature seems to lead to the formation of the more thermodynamically stable phases such as jaipurite (CoS) and linnaeite (Co_3S_4), but the case does not necessarily follow as we decrease in reactivity with diphenylthiourea. In fact, at the lower temperatures we obtain the highly stable cobaltpentlandite (Co_9S_8) with diphenylthiourea, which disappears as we increase the temperature.

Understanding some of the overall key trends and using our hypothesis from *Espano et al.* that states that phase transformations of a nanocrystal is dictated by the underlying anion hole stacking of the nucleated phase,[7] we can try to rationalize the syntheses of the cobalt sulfides are target the each specific phase. With the developed synthetic phase diagram in hand, we can take into account the stoichiometry and sulfur anion packing to rationalize how to force transformations between each cobalt sulfide phases. Below are the cases where rational phase control cobalt sulfides can be achieved.

3.4 Rational Synthesis of the Cobalt Sulfides

Synthesizing Cattierite

When using 6 mmol of unsubstituted thiourea, the fastest sulfur reacting thiourea, we obtained the most cattierite (CoS_2) in our bottom-up synthetic phase map. For most of the previous reactions, there was co-nucleation between the hexagonal and cubic phases of cobalt sulfide, but by taking advantage of the high sulfur content in cattierite (CoS_2), we can favor this phase by increasing the concentration in solution. Thus, we can target phase pure cattierite (CoS_2) by increasing the amount of thiourea used from 6 mmol to 12 mmol at low temperatures to nucleate the most sulfur- rich cobalt phase.

Synthesizing Cobaltpentlandite

In the initial set of experiments, we observed the formation of cobaltpentlandite (Co_9S_8) when using both low temperatures and slow reacting diphenyl thiourea. A more slowly

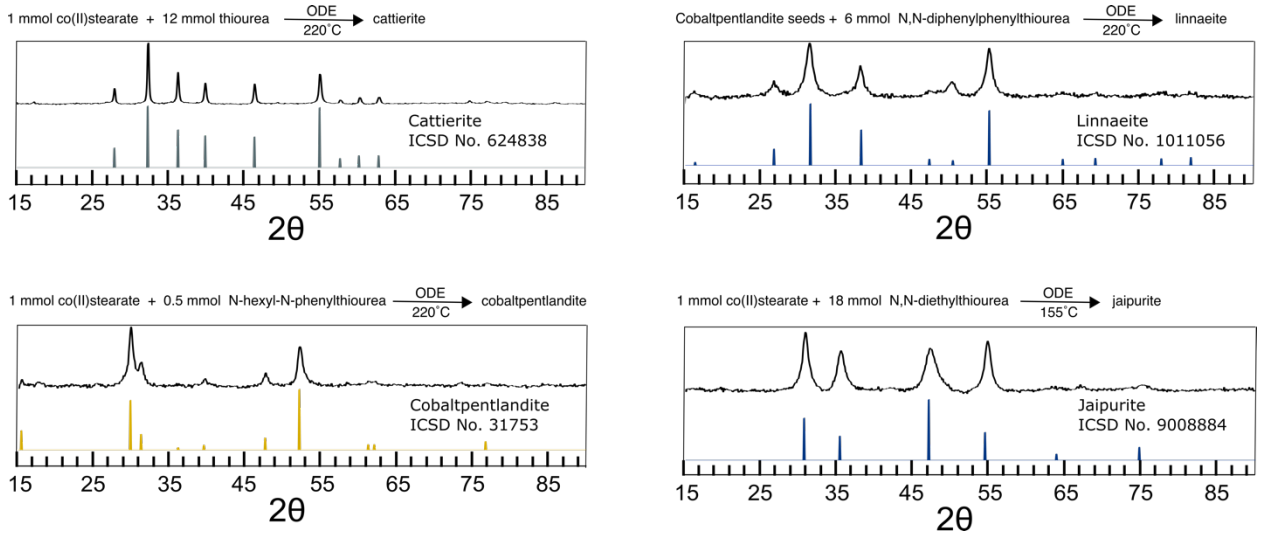

Figure 3.3. The rational phase control the cobalt sulfides followed by their perspective powder XRD patterns.

decomposing thiourea, 1-hexyl-3-phenyl-2-thiourea was synthesized to slow down reactivity even more.[8] When using 6 mmol of 1-hexyl-3-phenyl-2-thiourea at 170ºC, we observed a linnaeite (Co_3S_4), jaipurite (CoS), and cobaltpentlandite (Co_9S_8). Thus, we decided to decrease the amount of sulfur monomer to control the formation of these phases and hopefully decrease the overall number of phases in this mixture. When we decrease the amount of 1-hexyl-3-phenyl-2-thiourea we find that cobaltpentlandite (Co_9S_8) becomes the increasingly dominant product in the powder mixture until use 0.5 mmol of 1-hexyl-3-phenyl-2-thiourea, which yields pure cobaltpentlandite (Co_9S_8). This seems to suggest that the sulfur availability during these colloidal syntheses are the main driving force behind phase determination in cobalt sulfide nanocrystals.

Synthesizing Linneaite

In the previous work of chapter 2, it was shown that phases can act as seeds when reacted with a highly reactive thiourea to yield more sulfur rich phases. This was shown through the synthesis of marcasite (hcp-FeS_2) through pyrrhotite (hcp-$Fe_{1-x}S$). We can use the anion stacking of cobatlpentlandite (Co_9S_8) to our advantage and try to target the other cubic phases. Because cobaltpentlandite is a cubic closed pack phase, similar to linneate (Co_3S_4) and cattierite (CoS_2), it could be a phase intermediate that allows to target one of these other cubic phases.

To target cubic linnaeite (Co_3S_4), cobaltpentlandite (Co_9S_8) seeds were purified. then dispersed in 10 mL of ODE and heated up to 220ºC. Then a slowly reactive diphenylthioruea was used to force excess sulfur into the cobaltpentlandite (Co_9S_8) crystal to yield linnaete (Co_3S_4). By

using slow reactive thioureas, we were able to prevent any nucleation of the hexagonal jaipurite (CoS). This experiment is very integral to this dissertation as it proves that phase templating and a seeded growth method, as shown in *Espano et al.*[7] is a reproducible and repeatable way to rationally target phases. Here we adapt this method and show that this synthetic strategy can be used with other crystal systems.

Synthesizing Jaipurite

Jaipurite (CoS), is the lone hexagonal phase of the cobalt sulfides. It is relatively metastable when compared to the other cobalt sulfides, and has a intermediate sulfur content when compared to the other cobalt sulfides. When looking at the phase map, it seemed that slowly reacting disubstituted thioureas led to the formation of mainly jaipurite (CoS) and linnaeite (Co_3S_4), but too slow would allow for the formation of cobaltpentlandite. Thus, we decided to use diethylthiourea, a precursor that would have in-between reactivity between the slow reactive diphenylthioruea and the fast reactive mono-substituted thioureas. Optimizing this synthesis by using a one-pot method instead of a hot addition method, lowering the temperature, and high amount of sulfur precursor enabled us to incorporate the sulfur into the cobalt sulfide in a more controlled way and prevent the nucleation of the cubic cobaltpentlandite (Co_9S_8).\

3.5 Conclusion

By using a library of thioureas with different organic substitutions, the kinetic decomposition speed, and its effect on cobalt sulfide nanocrystalline synthesis was able to be studied. Using this system, we can make really important comparisons with the iron sulfide library and thus gain a more comprehensive understanding of transition metal chalcogenide phase control. Like the iron sulfide system, the cobalt sulfide system seems to be dictated and dominated by both kinetics and anion sublattice stacking. Cubic closed packed phases will transform into more thermodynamically stable cubic closed pack phases, and the hexagonal closed packed phase jaipurite (CoS) was able to be synthesized phase pure by inhibiting cubic nucleation. The vacancies of polymorphic pairs in the cobalt sulfide system could be one of the reasons why we can force either hexagonal or cubic nucleation whereas in the iron sulfide system, we could not do so with such high precision.

By understanding the trends within the cobalt sulfides, the effects of temperature, suflur monomer content, and thiourea reactivity was able to be controlled to create rational synthetic routes to target all four phases of the cobalt sulfides- a feat that has yet to be accomplished and

comprehensively understood until now. Not only does this show overarching themes in phase control phenomenon, but it allows us to synthetically access these phases easily and reproducibly.

References

(1) Jin, R.; Zhou, J.; Guan, Y.; Liu, H.; Chen, G. Mesocrystal Co9S8 hollow sphere anodes for high performance lithium ion batteries. *J. Mater. Chem. A* **2014**, *2* (33), 13241-13244. DOI: 10.1039/c4ta02551b.

(2) Payne, J. L.; Percival, J. D.; Giagloglou, K.; Crouch, C. J.; Carins, G. M.; Smith, R. I.; Gover, R. K. B.; Irvine, J. T. S. In Situ Thermal Battery Discharge Using CoS2 as a Cathode Material. *Journal of The Electrochemical Society* **2019**, *166* (12), A2660-A2664. DOI: 10.1149/2.1431912jes.

(3) Shi, W.; Zhu, J.; Rui, X.; Cao, X.; Chen, C.; Zhang, H.; Hng, H. H.; Yan, Q. Controlled synthesis of carbon-coated cobalt sulfide nanostructures in oil phase with enhanced li storage performances. *ACS Appl Mater Interfaces* **2012**, *4* (6), 2999-3006. DOI: 10.1021/am3003654.

(4) Chen, P.; Zhang, N.; Wang, S.; Zhou, T.; Tong, Y.; Ao, C.; Yan, W.; Zhang, L.; Chu, W.; Wu, C.; et al. Interfacial engineering of cobalt sulfide/graphene hybrids for highly efficient ammonia electrosynthesis. *Proceedings of the National Academy of Sciences of the United States of America* **2019**, *116* (14), 6635-6640. DOI: 10.1073/pnas.1817881116.

(5) Song, Y.; Sha, W.; Jiao, T.; Wang, C.; Tian, J.; Liu, P.; Xu, B.; Guo, J.; Liang, J. Interface-engineered Co(3)S(4)/CoMo(2)S(4)nanosheets as efficient bifunctional electrocatalysts for alkaline overall water splitting. *Nanotechnology* **2021**, *32* (45). DOI: 10.1088/1361-6528/ac1a41

(6) Kumar, N.; Raman, N.; Sundaresan, A. Synthesis and properties of cobalt sulfide phases: CoS2 and Co9S8. *Zeitschrift fur Anorganische und Allgemeine Chemie* **2014**, *640* (6), 1069-1074. DOI: 10.1002/zaac.201300649.

(7) Bairan Espano, J. R.; Macdonald, J. E. Phase Control in the Synthesis of Iron Sulfides. *J Am Chem Soc* **2023**, *145* (34), 18948-18955. DOI: 10.1021/jacs.3c05653 .

(8) Hendricks, M. P.; Campos, M. P.; Cleveland, G. T.; Plante, I. J.-L.; Owen, J. S. A Tunable library of substituted thiourea precursors to metal sulfide nanocrystals. *Science* **2015**, *348* (6240), 1226-1230. DOI: 10.1126/science.aaa2951.

(9) Rosenquist, T. A Thermodynamic Study of Iron, Cobalt, and Nickel Sulfides. *Journal of the Iron and Steel Institute* **1954**, *176*, 37-57.

Chapter 4: Phase Control in the Synthesis of Nickel Sulfides

4.1: The Nickel Sulfides

The nickel sulfides are great example of the complexity seen in transition metal chalcogenides,[1] as seven unique crystal structures are known of varying stoichiometries and polymorphs. The structures have a large range of enthalpies of formations (– 88 kJ/mol to -760 kJ/mol) and can contain Ni-S bonds, S-S bonds and —somewhat uniquely for transition metal chalcogenides— metal-metal bonds. One example is millerite (NiS), which has a nickel coordination number of 5 with repeating square pyramidal units that are thought to have characteristics of Ni-Ni bonding.[2]

The seven known nickel sulfides have chemical and electronic properties that makes them great candidates for a variety of applications.[3-7] Heazlewoodite (Ni_3S_2) was reported to be a strong hydrogen evolution reaction electrocatalyst, and is a better electrocatalyst when compared to Vaesite (NiS_2) and α-NiS.[3] Millerite (NiS) and α-NiS have shown to have good performance as supercapacitors.[8, 9] Understanding how we can target crystalline phases and thus their electronic properties is important for next generation technologies and applications.

The ability to selectively synthesize one nickel sulfide phase over another is still challenging. In fact, while some geological chemists have identified relationships between the iron sulfides,[10, 11] the lines and relationships between the nickel sulfides are obscured. Nickel sulfide phase control has been achieved by changing the amount of nickel to sulfur precursor ratios, using unique nickel precursors, and using coordinating agents but there is little understanding as to why these changes work.[4, 12-14] Hu et al. hinted that the ligand coordination can change the resulting phase of nickel sulfide nucleation and growth, and attributes coordination agents to the slow release of Ni^{2+} ions.[15] But an overall understanding on how we can truly target these materials is still missing. To move forward with phase control and selection, the pathways between the nickel sulfides need to be clarified.

The nucleation and transformation of these crystalline phases are dictated by molecular pathways from precursor to monomer. Mechanistically, there is little understanding of *why* one phase prefers to transform into another, or how to force these transformations using chemical toolkits. When trying to form a nanocrystalline synthetic rationale, it is important to make a distinction between phase control as a result of different molecular mechanisms and phase control as a result of differing kinetic speeds.[16-20] In order better understand phase formation and selection,

kinetic studies focusing on phase determination must be performed. Other studies have hinted that nickel in general is very sensitive in changes in coordination chemistry, and that these changes have a drastic

effect on the resulting phase.[21-23] These studies control the availability of nickel in solution and only synthesize a limited number of phases, here we will change sulfur availability and observe its effects on nickel sulfide phase determination.

In chapter 2, we studied the effects that kinetics has on phase formation on iron sulfide nanocrystals. By using a library of thioureas, the rate at which sulfur precursors release sulfur into the reaction conditions is tuned. It was shown that the rate of thiourea decomposition speed has a huge influence on phase selection and formation in iron sulfide nanocrystals. Our findings showed that the thermodynamics and the anion stacking of the iron sulfides can map out the ways in which these nanocrystals transform, enabling us to rationally target specific phases. In chapter 3 we extended that to the cobalt sulfides and found similar trends.

While the iron sulfides proved to be an excellent target material to systematically study phase control, it is only one of many metal sulfide phases. The iron and cobalt sulfides can all be described as by approximate hcp or ccp anion stacking with various filling of Td and Oh holes. The nickel sulfides **Table 4.1** are not so easily reduced to such simple terms especially because of the presence of square pyramidal coordination in millerite (NiS) godlevskite (Ni_9S_8) and Ni_7S_6.

Table 4.1 The Nickel Sulfides

Phase	Chemical Formula	Space Group	Approximate Sulfur packing	Cation Hole Filling	DS_f (J/mol K)	DH_f (kJ/mol)	Reference Author
Vaesite	NiS_2	Pa3	S_2^{2-} in ccp	All Oh	80	-124.9, -128, -133.9	Cemič[24], Gamsjäger[25]
Millerite	NiS	R3m	S^{2-} in hcp	All Sqr. Pyr.	53.0	-91.0, -94.0	Cemič[24], Gamsjäger[25]
α-NiS	NiS	P 6_3/mmc	S^{2-} in hcp	All Oh	60.9	-88.1, -88.1	Cemič[24], Gamsjäger[25]
Godlevskite	Ni_9S_8	I42d	S^{2-} in ccp	Td, Sqr. Pyr.	481	-760	Gamsjäger[25]
	Ni_7S_6	Bmmb	S^{2-} in ccp	Td, Sqr. Pyr	390.2		Cemič[24],Waldner[26]
Polydymite	Ni_3S_4	$Fd\bar{3}m$	S^{2-} in ccp	All Oh, ½ Td (spinel)	191.9	-309.1	Waldner[26]
Heazlewoodite	Ni_3S_2	R32	S^{2-} in bcc	Distorted Td	133.5	-217.24, -215.9	Gamsjager[25], Waldner[26]

The nickel sulfides can be organized by their coordination numbers and cation hole filings. Vaesite (NiS_2) and α-NiS are the two phases with octahedral hole filing, with α-NiS having a hexagonal sulfur packing structure, whereas Vaesite (NiS_2) contains double sulfur units in a cubic closed packed structure. Millerite (NiS), the polymorphic pair of α-NiS, also exists in a hexagonal closed packed arrangement, but has a square pyramidal cation hole filing. Reducing the coordination numbers of the cation gives way to godlevskite (Ni_9S_8), which is a cubic closed packed crystal with both tetrahedral and square pyramidal cation hole filings. With the cation lowest coordination number is heazlewoodite (Ni_3S_2) which is a body center cubic cell with cation holes in a tetrahedral formation. Finally, polydymite (Ni_3S_4) has a combination of both octahedral and tetrahedral holes in a cubic closed pack cell.

Understanding the kinetic induced phase control behavior in the nickel sulfides, and comparison to the existing studies on the iron sulfides and the cobalt sulfides, will test what may be universal behaviors across the periodic table and highlight potential pitfalls of generalization in phase control.

Here, we employ tunable thioureas to understand the nucleation and formation of nickel sulfides. Not only do we see widely varying behaviors of nucleation and transformations, but we are able to use our knowledge base to sequentially target metal sulfides in a phase pure synthesis. Unlike our previous metal sulfides, which follow a path templated by anion stacking, the cation hole filling and coordination number of the nickel sulfides is the driving template in its phase transformation behavior. By understanding the thermodynamics and crystal packing of the nickel sulfides, we can selectively synthesize six out of the seven of the naturally occurring nickel sulfides phases: vaesite (NiS_2), α-NiS, millerite (NiS), heazlewoodite (Ni_3S_2), polydymite (Ni_3S_4), and godlevskite (Ni_9S_8). Here we show and confirm that the identified relationships between crystal structure and thermodynamics can be used to make hypothesis driven changes to the synthetic conditions to target specific phases.

4.2 Synthesizing Nickel Sulfides

Synthesis of 1-hexyl-3-phenyl-2-thiourea thiourea

Synthesis modified from reference 1.(3) A solution of hexylamine (6 mmol) in toluene (5 mL) was added to a solution of phenyl thiocyanate (6 mmol) in toluene (5 mL). The solution was allowed to stir for 5 min. The clear liquid turned white liquid and the volatiles were removed under vacuum. Characterization: ^{1}H NMR ($CdCl_3$, 400 MHz): 0.87 (t, 3H, -CH_3), 1.28 (m, 6H, (CH_2)$_3$),

1.56 (p, 2H, CH_2), 3.62 (q, 2H, CH_2), 5.98 (br, 1H, NH), 7.16 (d, 2H, *o*-CH), 7.25 (t, 1H, *p*-CH), 7.43 (t, 2H, *m*-CH), 7.73 (br, 1H, NH)

Nickel Sulfide Nanoparticle Synthesis in Octadecene using an Addition Funnel

In a 25 mL 3-neck round-bottom flask, nickel (II) stearate (313 mg, 0.5 mmol) was dissolved in 10 mL of ODE and connected to an addition funnel with a pressure equalizing arm. A septum was placed on one of the necks to seal the round-bottom flask. It was then connected to a schlenk line using a condenser and a gas adapter. A substituted thiourea (0.5 mmol – 12 mmol) was placed in the addition funnel along with 5 mL of ODE. The addition funnel was sealed with a septum and both septa were pierced with thermocouples down to the level of the solution. The vacuum from the Schlenk was then turned on and the 3-neck round-bottom flask was stirred for 30 min and heated to 60°C using a heating mantel. After degassing, the Schlenk line was switched to Argon and the temperature was raised to the desired temperature (170°C – 270°C). The addition funnel was heated to 170°C using a heat gun (MHT Products Inc.), allowing the thiourea to be fully dissolved in the ODE. The solution was then dispensed into the 3-neck round-bottom flask and stirred for the desired time (1 min – 4 hrs). The flask was then taken off the heating mantel and allowed to cool down to room temperature. To isolate the products, the solution was placed in a centrifuge tube along with chloroform to suspend the particles and ethanol as an antisolvent. The mixture was centrifuged at 4500 rpm for 5 mins. The liquid component was decanted, and the nanoparticles were resuspended in chloroform. This process was repeated 2 more times.

α-NiS Synthesis

Anhydrous nickel stearate (313 mg, 0.5 mmol) was dissolved in 10 mL of oleylamine in a 25 mL 3-neck round bottom flask with a connected addition funnel with a pressure equalizing arm. The 3- neck round-bottom flask was attached to the Shlenk line via line condenser and gas adaptor. Thiourea (228 mg, 3 mmol) was combined with octadecene (5 mL) in the addition funnel the addition funnel as sealed with a septum and pierced with a thermocouple down to the solution level. A second thermocouple was placed in the solution of the 3-neck flask. The apparatus was degassed under vacuum and the round-bottom flask stirred for 30 min at 60°C using a heating mantle. The vacuum was replaced with argon and the temperature in the round-bottom flask was raised to 170°C, then the contents of the addition funnel were heated to the same desired temperature using a heat gun (MHT Products Inc.), allowing the thiourea to dissolve, which was then added swiftly to the contents of the round-bottom flask. The solution was left at the desired

temperature 1 h. To isolate the product, after cooling, chloroform (5 mL) was added to suspend the particles. Ethanol (5 mL) was then added as an antisolvent. The mixture was centrifuged at 4500 rpm for 5 min. The liquid component was decanted, and the nanoparticles were resuspended in chloroform. This process was repeated 4 times.

Vaesite (NiS_2) Synthesis

Anhydrous nickel stearate (313 mg, 0.5 mmol) was dissolved in 10 mL of oleylamine in a 25 mL 3-neck round bottom flask with a connected addition funnel with a pressure equalizing arm. The 3- neck round-bottom flask was attached to the Shlenk line via line condenser and gas adaptor. Phenylthiourea (2.739g, 18 mmol) was combined with octadecene (5 mL) in the addition funnel the addition funnel as sealed with a septum and pierced with a thermocouple down to the solution level. A second thermocouple was placed in the solution of the 3-neck flask. The apparatus was degassed under vacuum and the round-bottom flask stirred for 30 min at 60°C using a heating mantle. The vacuum was replaced with argon and the temperature in the round-bottom flask was raised to 220°C, then the contents of the addition funnel were heated to the same desired temperature using a heat gun (MHT Products Inc.), allowing the thiourea to dissolve, which was then added swiftly to the contents of the round-bottom flask. The solution was left at the desired temperature 1 h. To isolate the product, after cooling, chloroform (5 mL) was added to suspend the particles. Ethanol (5 mL) was then added as an antisolvent. The mixture was centrifuged at 4500 rpm for 5 min. The liquid component was decanted, and the nanoparticles were resuspended in chloroform. This process was repeated 4 times.

Millerite (β-NiS) Synthesis

Anhydrous nickel stearate (313 mg, 0.5 mmol) was dissolved in 10 mL of oleylamine in a 25 mL 3-neck round bottom flask with a connected addition funnel with a pressure equalizing arm. In a separate 5 ml pear flask 1,3-Diphenylthiourea (388 g, 1.7 mmol) was dissolved with oleylamine (5 mL). The 5 mL flask was degassed under vacuum for 30 minutes and then filled with argon. The 25 mL 3 neck round bottom flask was degassed under vacuum and stirred for 30 min at 60°C using a heating mantle. The vacuum was replaced with argon and the temperature in the round-bottom flask was raised to 220°C, then the contents of the 5 mL flask collected in a syringe and injected into the 25 mL round-bottom flask. The solution was left at the desired temperature 1 h. To isolate the product, after cooling, chloroform (5 mL) was added to suspend the particles. Ethanol (5 mL) was then added as an antisolvent. The mixture was centrifuged at 4500 rpm for 5

min. The liquid component was decanted, and the nanoparticles were resuspended in chloroform. This process was repeated 4 times.

Heazlewoodite (Ni_3S_2) Synthesis

Anhydrous nickel stearate (313 mg, 0.5 mmol) was dissolved in 10 mL of oleylamine in a 25 mL 3-neck round bottom flask with a connected addition funnel with a pressure equalizing arm. In a separate 5 ml pear flask 1,3-Diphenylthiourea (228 mg, 1 mmol) was dissolved with oleylamine (5 mL). The 5 mL flask was degassed under vacuum for 30 minutes and then filled with argon. The 25 mL 3 neck round bottom flask was degassed under vacuum and stirred for 30 min at 60°C using a heating mantle. The vacuum was replaced with argon and the temperature in the round-bottom flask was raised to 310°C, then the contents of the 5 mL flask collected in a syringe and injected into the 25 mL round-bottom flask. The solution was left at the desired temperature 2 h. To isolate the product, after cooling, chloroform (5 mL) was added to suspend the particles. Ethanol (5 mL) was then added as an antisolvent. The mixture was centrifuged at 4500 rpm for 5 min. The liquid component was decanted, and the nanoparticles were resuspended in chloroform. This process was repeated 4 times.

Godlevskite (Ni_9S_8) Synthesis

Anhydrous nickel stearate (313 mg, 0.5 mmol) was dissolved in 10 mL of octadecene in a 25 mL 3-neck round bottom flask with a connected addition funnel with a pressure equalizing arm. The 3- neck round-bottom flask was attached to the Shlenk line via line condenser and gas adaptor. 1,3-diphenyl-2-thiourea (114 mg ,0.5 mmol) was combined with octadecene (5 mL) in the addition funnel the addition funnel as sealed with a septum and pierced with a thermocouple down to the solution level. A second thermocouple was placed in the solution of the 3-neck flask. The apparatus was degassed under vacuum and the round-bottom flask stirred for 30 min at 60°C using a heating mantle. The vacuum was replaced with argon and the temperature in the round-bottom flask was raised to 250°C, then the contents of the addition funnel were heated to the same desired temperature using a heat gun (MHT Products Inc.), allowing the thiourea to dissolve, which was then added swiftly to the contents of the round-bottom flask. The solution was left at the desired temperature 4 h. To isolate the product, after cooling, chloroform (5 mL) was added to suspend the particles. Ethanol (5 mL) was then added as an antisolvent. The mixture was centrifuged at 4500 rpm for 5 min. The liquid component was decanted, and the nanoparticles were resuspended in chloroform. This process was repeated 4 times.

Polydymite (Ni_3S_4) Synthesis

Anhydrous nickel stearate (313 mg, 0.5 mmol) was dissolved in 10 mL of octadecene in a 25 mL 3-neck round bottom flask with a connected addition funnel with a pressure equalizing arm. The 3- neck round-bottom flask was attached to the Shlenk line via line condenser and gas adaptor. 1-hexyl-3-phenyl-2-thiourea (100 mg, 0.425 mmol) was combined with octadecene (5 mL) in the addition funnel the addition funnel as sealed with a septum and pierced with a thermocouple down to the solution level. A second thermocouple was placed in the solution of the 3-neck flask. The apparatus was degassed under vacuum and the round-bottom flask stirred for 30 min at 60°C using a heating mantle. The vacuum was replaced with argon and the temperature in the round-bottom flask was raised to 290°C, then the contents of the addition funnel were heated to the same desired temperature using a heat gun (MHT Products Inc.), allowing the thiourea to dissolve, which was then added swiftly to the contents of the round-bottom flask. The solution was left at the desired temperature 2 h. To isolate the product, after cooling, chloroform (5 mL) was added to suspend the particles. Ethanol (5 mL) was then added as an antisolvent. The mixture was centrifuged at 4500 rpm for 5 min. The final product dispersed in ODE and placed in a 3-neck flack with phenylthiourea (288 mg, 1.9 mmol). The reaction was degassed at 100ºC for 1 hour. The vacuum was replaced with argon, and the temperature in the round bottom was raised to 200ºC for 10 minutes before it was swiftly cooled using an ice bath. To isolate the product, after cooling, chloroform (5 mL) was added to suspend the particles. Ethanol (5 mL) was then added as an antisolvent. The mixture was centrifuged at 4500 rpm for 5 min.

Material Characterization

Powder X-ray Diffraction (XRD) spectra were obtained using a Rigaku SmartLab® X-ray Diffractometer. This diffractometer had a CuK source and a D/TeX Ultra 250 detector. The operating voltage was 40 kV and the operating current was 44 mA. Samples were drop casted as particle suspensions onto low-background silicon XRD wafers and the solvent was allowed to evaporate. The step size was 0.1 degree at a rate of 10 degrees per minute. There was no evidence oxidation occurring during XRD characterization

Rietveld Refinement Method and quantification

Rietveld refinements were performed by Rigaku PDXL. The .cif files employed are noted as table 1 as the Powder diffraction file cards. The patterns was allowed to be fit freely with the cards noted in Table C.1 with percentages.

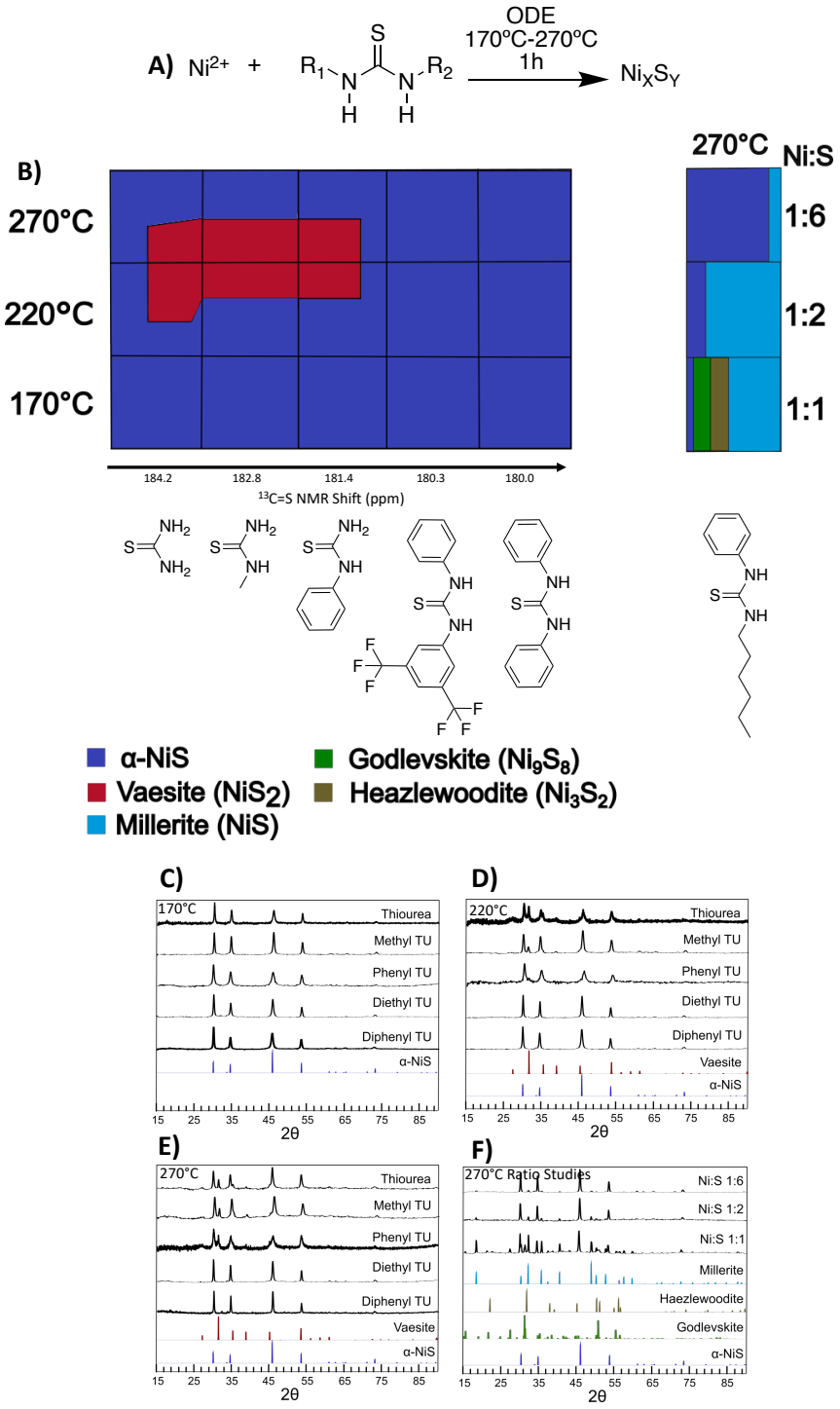

Figure 4.1 A) A chemical scheme depicting the synthesis of nicle sulfides **B) a** bottom-up synthetic diagram of the nickel sulfides showing the approximate compositions of the general phases with their corresponding X-ray diffraction patterns below at **C)** 170°C, **D)** 220°C, **E)** 270°C, and **F)** ratio studies with 1-hexyl-2-phenyl-3-thiourea at 270°C.

4.3 Phase Control in the Nickel Sulfides

A library of thioureas was employed as sulfur sources in the synthesis of nickel sulfides. The thioureas chosen cover at least four orders of magnitude of conversion rates in the synthesis of PbS.[16] In these experiments nickel sulfides were synthesized by heating a solution of nickel (II) stearate in a three-neck round-bottom flask to the desired reaction temperature (170°C-270°C). The substituted thiourea in octadecene (ODE, where the Ni:S was 1:6) was heated in an addition funnel and added swiftly to the reaction flask. Using their ^{13}C NMR shifts as an indicator of electron density on the adjacent S, the sulfur electron density and presumed relativity follows thiourea > methylthiourea > phenylthiourea > diethylthiourea > diphenylthiourea. The nanocrystals were isolated through successive precipitation and dispersion with ethanol and chloroform, all solid products were analyzed by powder x-ray diffraction. Rietveld refinements of the patterns were taken to determine the phase composition when multiple phases were present (**Figure 4.1**).

At low temperatures (170°C), α-NiS was the only observed product. As well, this was the only phase even at higher temperatures (220°C and 270°C) when the least reactive thioureas of our library were employed (phenyl, diethyl, and diphenyl) thiourea were employed. We attribute

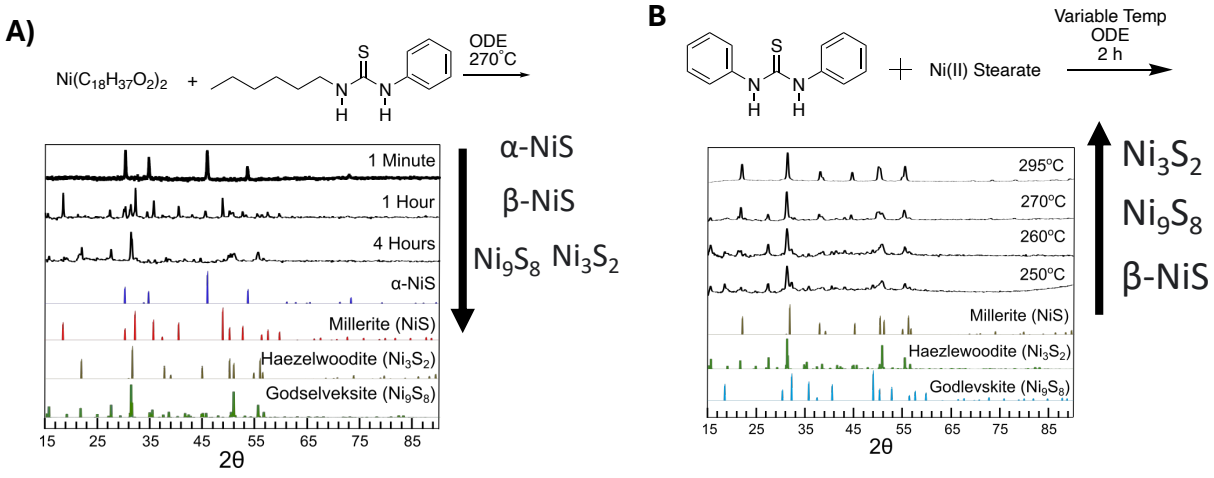

Figure 4.2) XRD followed by the reaction scheme of timed studies of nickel (II) stearate and 1-hexyl-3-phenyl-2-thiourea in octadecene at 270°C **B)** Temperature studies of nickel (II) stearate and 1-hexyl-3-phenyl-2-thiourea in octadecene. Arrows depict phase transformations of the nickel sulfides

this phase domination due to the low temperatures and high sulfur content working in concert to produce the highly metastable α-NiS ($\Delta H°_f$ = -88.1 kJ/mol).

When using the most reactive thioureas of the library (thiourea, methyl thiourea), elevated temperatures of 220°C and 270°C gave a mixture of the α-NiS along with sulfur rich vaesite NiS_2, which is more thermodynamically stable ($\Delta H°_f$ = -128 kJ/mol).

Only two phases of NiS_x were seen in the limited reaction space of temperature and thiourea reactivity (**Figure 4.1**). Mysteries remain as to why the the other nickel sulfides were seen, especially since godlevskite (Ni_9S_8) and heazlewoodite (Ni_3S_2) were seen as products from thiophenol reagents but not the thioureas. It is possible that the thiourea and thiophenol reagents cover a very different kinetic space, or a specific molecular decomposition mechanism may play an important role in phase selection.

To help answer these mysteries, a third reaction parameter was varied, the Ni:S ratio, while using extremely unreactive 1-hexyl-3-phenylthiourea as the sulfur source at 270°C (**Figure 4.1**). When using an excess (6:1 S:Ni) of slow reacting 1-hexyl-3-phenylthiourea, α-NiS is formed with some impurities of its polymorph millerite β-NiS. When the sulfur amount was dropped to nickel to sulfur ratio of 1:2, millerite dominated the mixture with a minority portion of metastable α-NiS. When the nickel to sulfur ratio was decreased further to 1:1, then millerite (β-NiS), heazlewoodite (Ni_2S_3), and godlevskite (Ni_9S_8), were added to the mixture with α-NiS. With exception polydymite (*vida infra*), we can conclude that all of the nickel sulfides can be achieved by varying the chemical potential of the sulfur reagents and does not require a specific molecular decomposition mechanism.

To understand if some of the nickel sulfides were intermediates to others, reactions with 1-hexyl-3-phenyl-2-thiourea precursor, at a 1:1 Ni:S ratio 270°C in octadecene were arrested at different time points. (**Figure 4.2**). At 1 minute metastable α-NiS was the only product. At 1 hour α-NiS was in a mixture with millerite (b-NiS), godlevskite (Ni_9S_8), and heazlewoodite (Ni_3S_2). At 4 hours, the only product was godlevskite (Ni_9S_8). The timed studies suggest that α-NiS is an intermediate to millerite (b-NiS), which in turn is an intermediate to both godlevskite (Ni_9S_8) and heazlewoodite (Ni_3S_2) decreasing the sulfur content with time.

Temperature also influences phase in an unexpected trend where increased temperature decreases the sulfur content of the products when slow reacting thioureas are employed (**Figure 4.2)**. When diphenyl thiourea was reacted with nickel (II) stearate at 250°C for 2h, a mixture of

millerite (β-NiS) and godlevskite (Ni_9S_8) was produced. Increasing the temperature ensured that the millerite (β-NiS) disappeared and was replaced by both godlevskite (Ni_9S_8) and heazlewoodite (Ni_3S_2). Increasing the temperature to 295°C yielded pure heazlewoodite (Ni_3S_2). This again suggests that millerite (β-NiS) transforms first into godlevskite (Ni_9S_8) as an intermediate, and then transforms into the most sulfur deficient nickel sulfide phase heazlewoodite (Ni_3S_2).

4.4 Understanding the Transformation Pathways of the Nickel Sulfides

In our previous work with iron, the rate at which substituted thioureas decomposed into sulfur monomers played an important role in phase selection. It was concluded that the decomposition rate influenced the anion stacking (ccp or hcp) of the nucleated phase, and secondarily controlled how much sulfur was incorporated within the time and temperatures chosen.[27] Once nucleation occurred in a ccp or hcp stacking, interconversion of the stacking was very difficult. For example, hcp pyrrhotite $Fe_{1-x}S$ was a necessary intermediate to hcp marcasite (FeS_2), whereas ccp mackinawite $Fe_{1+x}S$ lead to ccp pyrite (FeS_2).

Here with the nickel sulfides the anion stacking trend doesn't work, and we observe a significantly different behaviors compared to the iron sulfides. First of all hcp α-NiS appears to be a possible intermediate to ccp vaesite (NiS_2) or vaesite nucleates directly from solution without sulfur poor intermediates (**Figure 4.1**). In another deviation, extended times cause the formation of sulfur rich phases for the iron sulfides, whereas in the nickel sulfides the opposite was observed

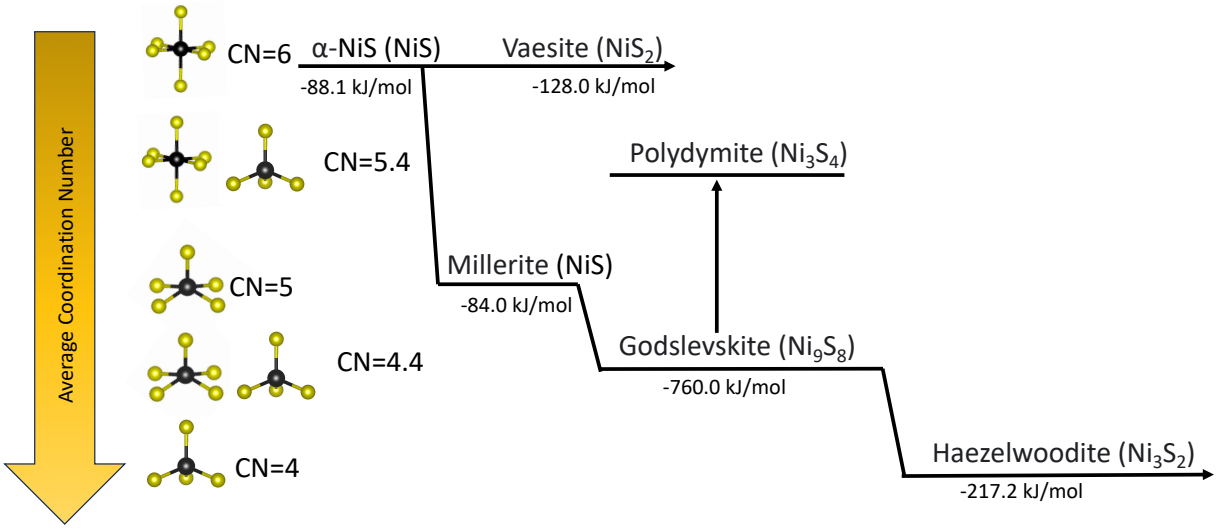

Figure 4.3 The nickel sulfide transformation pathways showing how they can be organized by coordination number..

where α-NiS and millerite (b-NiS) give way to sulfur poor heazlewoodite (Ni_3S_2) and godlevskite (Ni_9S_8) (**Figure 4.2**).

Instead of anion stacking like the iron sulfides, the observations here can be explained through examining the trends in the coordination number (CN) of the Ni in the nickel sulfide phases. Both α-NiS and vaesite (NiS_2) have the nickel entirely in octahedral (O_h, CN=6) holes. Polydymite (Ni_3S_4) is a spinel with both O_h and tetrahedral (T_d, CN=4) coordination with and average CN=5.3. Millerite (b-NiS) has the nickel in distorted square pyramidal ($S_{py,}$ CN=5) coordination. Godlevskite (Ni_9S_8) has both S_{py} and tetrahedral (T_d, CN=4) hole filling. Heazlewoodite (Ni_3S_2) has the lowest coordination number for the nickel with only T_d hole filling. We propose that the conditions of fast reacting thioureas and high sulfur reagent ratios lend themselves to high coordination number of nickel, and for this reason favor α-NiS and vaesite (NiS_2) over the other phases as products. Only very slowly reacting thioureas and low sulfur ratios allow for the formation of phases with lower coordination numbers around nickel, successively millerite (β-NiS), godlevskite (Ni_9S_8) and heazlewoodite (Ni_3S_2). Polydymite, with its T_d and O_h hole filling provides a synthetic challenge and was not seen under the one-step conditions studied (*vide infra*).

These hypotheses can now be used to rationally find conditions that favor one phase of each of the nickel sulfides.

4.4 Targeting the Nickel Sulfide Phases

Path to O_h coordinated Ni in α-NiS and Vaesite (NiS_2)

The preliminary studies (**Figure 4.1**) indicate that α-NiS can easily transform into O_h vaesite (NiS_2) under highly reactive conditions. Being the most metastable nickel sulfide, we can target α-NiS using a high ratio of sulfur to nickel (6:1) to promote the O_h coordination, but also use a medium speed thiourea (phenyl thiourea), to prevent the formation vaesite (NiS_2). This successfully yields phase pure α-NiS. Using a fast thiourea such as thiourea caused impurities of elemental sulfur.

Alternatively, vaesite (NiS_2) can be achieved by changing the conditions for the formation of α-NiS to promote more sulfur including in the product. Phase pure vaesite (NiS_2) was achieved by increasing the Ni to phenylthiourea ratio from 1:6 to 1:18 and increasing the temperature to 270°C.

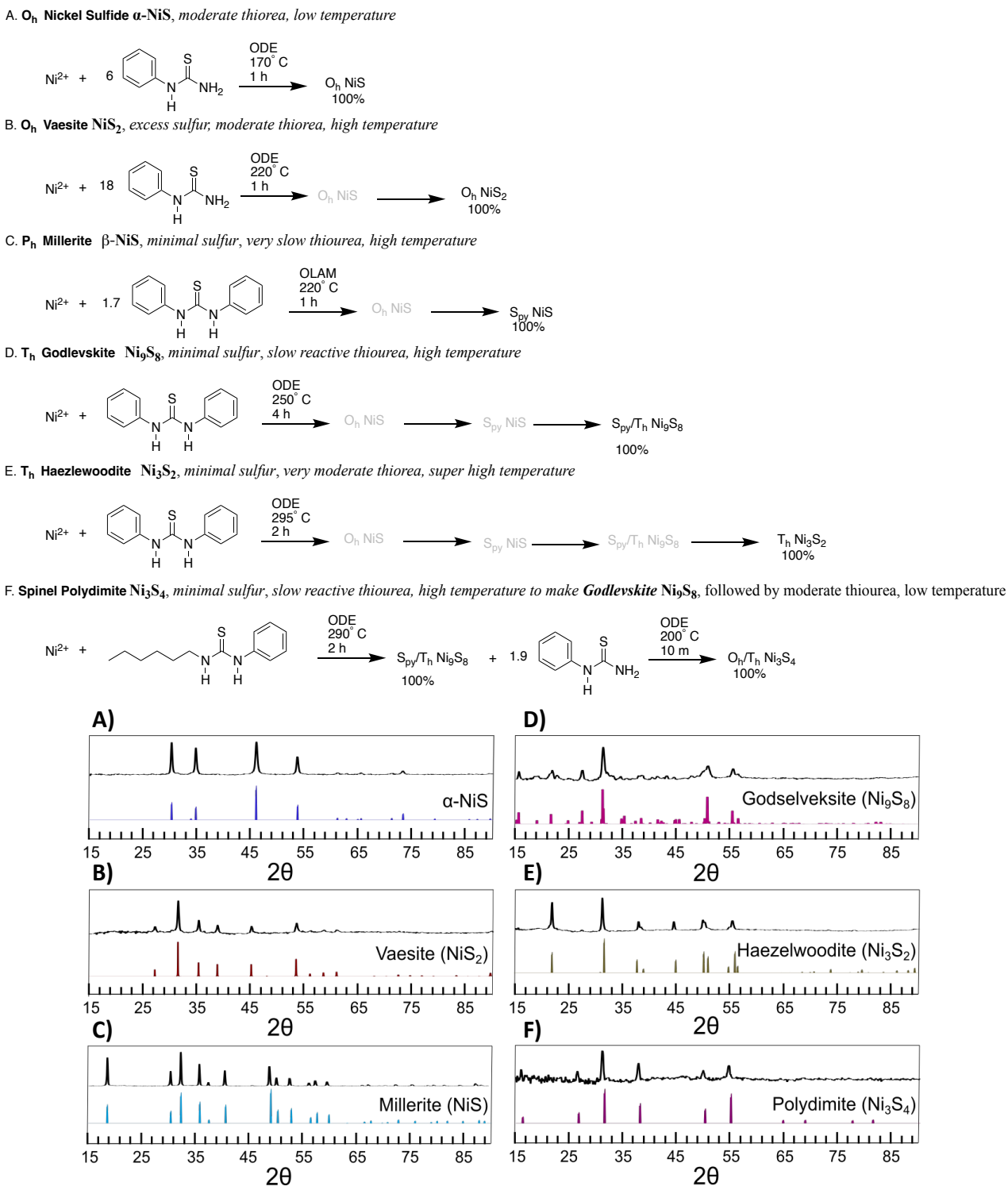

Figure 4.4 Scheme depicting conditions to target specific nickel sulfide phases followed by the resulting XRD pattern. (ICSD α-NiS: 29313, Millerite: 40053, Vaesite: 40328, Heazlewoodite:10424, Godlevskite:9013880, Polydimite: 5910137

Path to S_{py} coordinated Ni in Millerite (b-NiS)

The initial studies identified Millerite (b-NiS) as an important intermediate that readily transforms to heazlewoodite (Ni_3S_2) and godlevskite (Ni_9S_8) and is a polymorph of α -NiS. Millerite (β-NiS) has a lower coordination number around nickel (CN=5) than in α-NiS (CN=6). Therefore, millerite b-NiS can be favored over α-NiS by decreasing the sulfur content of the reaction. However, too low of sulfur content would favor the transformation to sulfur poor godlevskite (Ni_9S_8). We found trapping phase pure millerite to be challenging, because it often was accompanied by α -NiS or godlevskite (Ni_9S_8) from having too much or too little thiourea. The "Goldilocks" conditions to phase pure millerite used diphenyl thiourea in combination with oleylamine solvent, which is known to substitute thiourea *in situ*, to produce a very slow reacting oleylamine substituted thiourea.[27] 1.7 mol ratio of diphenyl thiourea to nickel(II) stearate in oleylamine at 220°C yielded phase pure millerite (b-NiS).

Path to S_{py} and T_d coordinated Ni in Godlevskite (Ni_9S_8)

Like millerite, the synthesis of phase pure godlevskite (Ni_9S_8) required balanced conditions because it is an intermediate between millerite (b-NiS) and heazlewoodite (Ni_2S_3). Godlevskite (Ni_9S_8) can be selectively synthesided by reacting nickel (II) stearate with diphenyl thiourea in a 1:1 ratio at 250°C or 270°C for 4 hours. The long time allows the millerite to transform completely into godlevskite (Ni_9S_8). These temperatures were chosen since earlier experiments showed that increasing the temperature to 295°C would cause heazlewoodite (Ni_3S_2) to form. Alternatively, godlevskite (Ni_9S_8) (average CN=4.5) can be synthesized at 295°C (2h), but more sulfur (0.75:1, S:Ni) is needed to keep the average coordination number high and prevent the formation of heazlewoodite (Ni_3S_2) which has a CN=4.

Path to T_d coordinated Ni in Heazlewoodite (Ni_3S_2)

As shown by previous reactions, millerite (NiS) and godlevskite (Ni_9S_8) are intermediates before completely transforming into the most sulfur deficient phase, with the lowest coordiatnion number heazlewoodite (Ni_3S_2, CN=4). Therefore, haezlewoodite is favored when under highly sulfur deficient conditons at temperatures high enough to allow transformation through the intermediates. Heazlewoodite (Ni_3S_2) can be synthesized with a 1:1 ratio of diphenyl thiourea, at high temperatures of 295 °C for 2 h.

Path to T_d and O_h coordinated Ni in Polydymite (Ni_3S_4)

There are very few reported syntheses to polydymite (Ni_3S_4) and now we can hypothesize why. As a spinel with both T_d and O_h coordination of nickel, it is not in a linear path between O_h, S_{py}, and T_d coordination seen in the other phases. Since phase control of the nickel sulfides is dictated by trends in the coordination of the nickel, polydymite is an outlier that provides a unique synthetic challenge.

To achieve phase pure polydymite, we take a two-step approach. We first will use conditions to yield godlevskite (Ni_9S_8) with its mixture of T_d and $S_{py.}$ Ni coordination. We then will use a more reactive thiourea to push more sulfur into the crystal presumably push the S_{py} coordination sites to O_h. Godlevskite (Ni_9S_8) was synthesized using the conditions denoted above and purified from the reaction mixture using successive precipitations in ethanol and resuspension in chloroform. The final resuspension was in 10 mL of octadecene, to which phenylthiourea as added and the temperature raised to 200°C for 10 min. The product was phase pure polydymite (Ni_3S_4)

This approach is reminiscent of the previous phase targeting used to achieve smythite ($Fe_{3-x}S_4$) and marcasite (FeS_2). One set of sulfur-poor conditions was needed to synthesized pyrrhotite (Fe_1-xS) followed by a more sulfur rich set of conditions to achieve the other phases.

4.5 Conclusion

By using a library of thioureas and thiophenols with tunable reactivity we were able to obtain an almost comprehensive control over nickel sulfide nanocrystals and report the synthesis of 6 out of 7 of the known nickel sulfides phase pure. Our library of thiophenols only gave sulfur poor phases such as heazlewoodite (Ni_3S_2) and godlevskite (Ni_9S_8). To obtain a larger kinetic library, the thioureas were used. Fast reactive thioureas gave a mixture of only α-NiS and Vaesite (NiS_2). It is only when slow reactive thioureas, high temperatures, and low sulfur contents are employed that the other phases of the nickel sulfides were observed such as millerite (NiS), heazlewoodite (Ni_3S_2) and godlevskite (Ni_9S_8).

Using these experiments, we developed a synthetic phase diagram visualizing the trends among thiourea reactivity, reaction temperature, and sulfur content. Here we show cation hole filling and nickel coordination dictates the subsequent transformations of the nickel sulfides. Using this knowledge, we can rationally target 6 of the nickel sulfides in a phase pure synthesis. Here, we show that while crystal structure is an imperative consideration to understanding phase transformations, the cation hole filing and coordination numbers of these structures are equally as

important as the anion and cation sublattice stacking. The understanding of phase control will allow us to synthesis more crystalline materials and will help develop a wide range of technologies requiring such materials.

References

(1) Rao, C. N. R.; Pisharody, K. P. R. Transition metal sulfides. *Progress in Solid State Chemistry* **1976**, *10* (PART 4), 207-270. DOI: 10.1016/0079-6786(76)90009-1.

(2) Krishnakumar, S. R.; Shanthi, N.; Sarma, D. D. Electronic structure of millerite NiS. *Physical Review B* **2002**, *66* (11). DOI: 10.1103/PhysRevB.66.115105.

(3) Jiang, N.; Tang, Q.; Sheng, M.; You, B.; Jiang, D. E.; Sun, Y. Nickel sulfides for electrocatalytic hydrogen evolution under alkaline conditions: A case study of crystalline NiS, NiS2, and Ni3S2 nanoparticles. *Catalysis Science and Technology* **2016**, *6* (4), 1077-1084. DOI: 10.1039/c5cy01111f.

(4) Karthikeyan, R.; Thangaraju, D.; Prakash, N.; Hayakawa, Y. Single-step synthesis and catalytic activity of structure-controlled nickel sulfide nanoparticles. *CrystEngComm* **2015**, *17* (29), 5431-5439. DOI: 10.1039/c5ce00742a.

(5) Wang, P.; Zhang, X.; Zhang, J.; Wan, S.; Guo, S.; Lu, G.; Yao, J.; Huang, X. Precise tuning in platinum-nickel/nickel sulfide interface nanowires for synergistic hydrogen evolution catalysis. *Nature Communications* **2017**, *8*, 1-9. DOI: 10.1038/ncomms14580.

(6) Zang, X.; Dai, Z.; Yang, J.; Zhang, Y.; Huang, W.; Dong, X. Template-Assisted Synthesis of Nickel Sulfide Nanowires: Tuning the Compositions for Supercapacitors with Improved Electrochemical Stability. *ACS Applied Materials and Interfaces* **2016**, *8* (37), 24645-24651. DOI: 10.1021/acsami.6b08409.

(7) Wei, W.; Mi, L.; Gao, Y.; Zheng, Z.; Chen, W.; Guan, X. Partial Ion-Exchange of Nickel-Sulfide-Derived Electrodes for High Performance Supercapacitors. *Chemistry of Materials* **2014**, *26* (11), 3418-3426. DOI: 10.1021/cm5006482.

(8) Ouyang, Y.; Chen, Y.; Peng, J.; Yang, J.; Wu, C.; Chang, B.; Guo, X.; Chen, G.; Luo, Z.; Wang, X. Nickel sulfide/activated carbon nanotubes nanocomposites as advanced electrode of high-performance aqueous asymmetric supercapacitors. *Journal of Alloys and Compounds* **2021**, *885*. DOI: 10.1016/j.jallcom.2021.160979.

(9) Hu, Q.; Zhang, S.; Zou, X.; Hao, J.; Bai, Y.; Yan, L.; Li, W. Coordination agent-dominated phase control of nickel sulfide for high-performance hybrid supercapacitor. *Journal of Colloid and Interface Science* **2022**, *607*, 45-52. DOI: 10.1016/j.jcis.2021.08.185.

(10) Lennie, A. R.; Vaughan, D. J. Spectroscopic studies of iron sulfide formation and phase relations at low temperatures. *Mineral Spectroscopy: a Tribute to Roger G. Burns* **1996**, (5), 117-131.

(11) Balayeva, O. O.; Azizov, A. A.; Muradov, M. B.; Maharramov, A. M.; Eyvazova, G. M.; Gasimov, R. J.; Dadashov, Z. X. Effect of thermal annealing on the properties of nickel sulfide nanostructures: Structural phase transition. *Materials Science in Semiconductor Processing* **2017**, *64*, 130-136. DOI: 10.1016/j.mssp.2017.03.021.

(12) Shombe, G. B.; Khan, M. D.; Zequine, C.; Zhao, C.; Gupta, R. K.; Revaprasadu, N. Direct solvent free synthesis of bare alpha-NiS, beta-NiS and alpha-beta-NiS composite as excellent electrocatalysts: Effect of self-capping on supercapacitance and overall water splitting activity. *Sci Rep* **2020**, *10* (1), 3260. DOI: 10.1038/s41598-020-59714-9.

(13) Karthikeyan, R.; Navaneethan, M.; Archana, J.; Thangaraju, D.; Arivanandhan, M.; Hayakawa, Y. Shape controlled synthesis of hierarchical nickel sulfide by the hydrothermal method. *Dalton Trans* **2014**, *43* (46), 17445-17452. DOI: 10.1039/c4dt02059f.

(14) Manjunatha, C.; Srinivasa, N.; Chaitra, S. K.; Sudeep, M.; Chandra Kumar, R.; Ashoka, S. Controlled synthesis of nickel sulfide polymorphs: studies on the effect of morphology and crystal structure on OER performancec. *Materials Today Energy* **2020**, *16*. DOI: 10.1016/j.mtener.2020.100414.

(15) Hu, Q.; Zhang, S.; Zou, X.; Hao, J.; Bai, Y.; Yan, L.; Li, W. Coordination agent-dominated phase control of nickel sulfide for high-performance hybrid supercapacitor. *J Colloid Interface Sci* **2022**, *607* (Pt 1), 45-52. DOI: 10.1016/j.jcis.2021.08.185.

(16) Hendricks, M. P.; Campos, M. P.; Cleveland, G. T.; Plante, I. J.-L.; Owen, J. S. A Tunable library of substituted thiourea precursors to metal sulfide nanocrystals. *Science* **2015**, *348* (6240), 1226-1230. DOI: 10.1126/science.aaa2951.

(17) Hollingsworth, N.; Roffey, A.; Islam, H. U.; Mercy, M.; Roldan, A.; Bras, W.; Wolthers, M.; Catlow, C. R. A.; Sankar, G.; Hogarth, G.; et al. Active nature of primary amines during thermal decomposition of nickel dithiocarbamates to nickel sulfide nanoparticles. *Chemistry of Materials* **2014**, *26* (21), 6281-6292. DOI: 10.1021/cm503174z.

(18) Thomson, J. W.; Nagashima, K.; MacDonald, P. M.; Ozin, G. A. From sulfur-amine solutions to metal sulfide nanocrystals: Peering into the oleylamine-sulfur black box. *Journal of the American Chemical Society* **2011**, *133* (13), 5036-5041. DOI: 10.1021/ja1109997.

(19) Frenette, L. C.; Krauss, T. D. Uncovering active precursors in colloidal quantum dot synthesis. *Nature Communications* **2017**, *8* (1), 1-8. DOI: 10.1038/s41467-017-01936-z.

(20) Rhodes, J. M.; Jones, C. A.; Thal, L. B.; MacDonald, J. E. Phase-controlled colloidal syntheses of iron sulfide nanocrystals via sulfur precursor reactivity and direct pyrite precipitation. *Chemistry of Materials* **2017**, *29* (19), 8521-8530. DOI: 10.1021/acs.chemmater.7b03550.

(21) Qin, F.; Ma, Y.; Miao, L.; Wang, Z.; Gan, L. Influence of Metal-Ligand Coordination on the Elemental Growth and Alloying Composition of Pt-Ni Octahedral Nanoparticles for Oxygen Reduction Electrocatalysis. *ACS Omega* **2019**, *4* (5), 8305-8311. DOI: 10.1021/acsomega.8b03366.

(22) Babashkina, M. G.; Safin, D. A.; Garcia, Y. Influence of the coordination mode in [NiRC(S)NP(S)(OiPr)22] for the formation of nickel-containing nanoparticles. *Dalton Trans* **2012**, *41* (8), 2234-2236. DOI: 10.1039/c1dt11755f.

(23) Sun, Y.; Wu, J.; Zhang, Z.; Liao, Q.; Zhang, S.; Wang, X.; Xie, Y.; Ma, K.; Kang, Z.; Zhang, Y. Phase reconfiguration of multivalent nickel sulfides in hydrogen evolution. *Energy & Environmental Science* **2022**, *15* (2), 633-644. DOI: 10.1039/d1ee02985a.

(24) Cemic, L.; Kleppa, O. J. High temperature calorimetry of sulfide systems. I. Thermochemistry of liquid and solid phases of Ni + S. *Geochimica et Cosmochimica Acta* **1986**, *50* (8), 1633-1641. DOI: 10.1016/0016-7037(86)90126-2.

(25) Gamsjäger, H.; Mompean, F. J.; Issy les, M.; Bank, N. E. A. D.; Agency, O. N. E. Chemical thermodynamics of nickel. *Chemical thermodynamics* **2005**, (6), xxx, 617 p.-xxx, 617 p.

(26) Waldner, P.; Pelton, A. D. Thermodynamic modeling of the Ni – S system. **2022**.

(27) Bairan Espano, J. R.; Macdonald, J. E. Phase Control in the Synthesis of Iron Sulfides. *J Am Chem Soc* **2023**, *145* (34), 18948-18955. DOI: 10.1021/jacs.3c05653.

Chapter 5: Future Looks and Outlook

5.1 Summary

The goal of this dissertation was started with trying to understand how precursor kinetics affects bottom-up synthetic phase control in colloidal syntheses. As the projects transformed, so did the goal, and the goal of this dissertation grew to also include understanding how crystalline structure dictates and determines phase. There has been much work trying to undercover the mechanisms that preclude nanocrystalline formation[1-5] and transformations in situ of colloidal reactions,[6, 7] but there are limited studies that consider the crystalline structure of synthesized materials or the target materials. Adding this component will allow the pursuit of phase control to be more holistic, and hopefully successful. It is my hope that my dissertation offers a unique perspective on how to control crystalline structures of materials by taking a more unique approach to crystal engineering: not only is mechanism important, but also the crystal structures themselves.

This dissertation studied the effects of precursor kinetics on phase formation. Each chapter used a library of substituted thioureas as the sulfur containing precursor in the metal sulfide synthesis. In chapter 2, the iron sulfides were used as the first target system due to the existent polymorphic pairs, and the heavy study of geological records. Through this study, it was determined thiourea and solvent interactions can heavily dictate phase formation. Additionally, this chapter showed that precursor kinetics played strong role in phase determination, and that phase determinations of binary solids can be logically predicted by the anion stacking and thermodynamic relationships of the iron sulfide phases. Chapter 3 compared the results of the iron sulfide phase control the cobalt sulfides. The cobalt sulfides have no existing polymorphic pairs and are fewer in number than the iron sulfides, so obtaining a more comprehensive phase control rationale is within reach. The studies with cobalt sulfides indicated that phase determination may be driven by more stoichiometric reasonings, rather than by thermodynamics, but overall confirms our hypothesis that crystalline structure dictates phase. It is interesting when the considering metastability of the cobalt sulfides, we didn't see metastable phases at low temperatures, or these metastable phases transform into more thermodynamic ones at higher temperatures. In fact, the synthetic behavior of the cobalt sulfides transcended our own thermodynamic understandin. In chapter 4, the nickel sulfides were studied, in part because nickel can adopt square pyramidal

cation holing structures**,** and can exist as unique crystal structures such as millerite (NiS phase with a square pyramidal cation hole filing). In this study we discovered that while crystalline structures dictate phase transformation, it also depends on the how these materials transform is dependent on the metal chalcogenide system**.** Here, it was determined that the nickel sulfides are dictated by their cation hole filing and coordination numbers instead of anion stackings as seen with the cobalt and iron sulfides. Understanding all the trends in these metal sulfides systems, we can synthesize all 8 of the iron sulfides and rationally target 6 of them, all 4 of the cobalt sulfides phases pure, and 6 of the 7 nickels sulfides phase pure. In doing so, we boast a synthetic control over these materials that has not been seen before in bottom-up synthetic studies. Most notably, this dissertation achieves a rational control over metal chalcogenide materials that has not been reported before and proves that crystalline structures dictate phase transformation.

Future Direction

While this dissertation has attempted to more concretely understand how to control phase, there is still much work to be done to truly realize these materials for next generation applications. More comprehensive work on the transition metal sulfides needs to be gathered, and the overall landscape of these materials need to be studied closely. Some work with the copper sulfides, chromium sulfides, and manganese sulfides have been carried out to this extent and will be studied further.

While the extent that we have studied these metal sulfides is far-reaching, we have only scraped the surface of metal chalcogenides in general. The Owen group at Columbia did not only synthesize a library of tunable thioureas,[8] but was successful in also synthesizing a library of selenoureas that can control precursor decomposition kinetics of selenium containing compounds.[9] There has been some experiments carried out to try to understand the effects that selenourea decomposition kinetics have on phase determination on iron selenides, but Alexandra Koziel found that in the iron selenides are much more sensitive to solvent effects and recently observed how these solvents can potentially alter the way and speeds that he metal is released into solution. After gaining a good understanding on how to isolate the effects of kinetics on these iron selenides, experiments should be carried out to try to understand selenium phase control using a library of selenorueas.

The bulk of this dissertation tries to understand phase control in a bottom-up synthetic rationale, but bottom-up synthesis is only one small tool in a larger chemical toolkit. To truly

realize phase control, we must explore other toolkits such as anion and cation exchange. These skills enable us to create more pathways to both natural and unnatural phases and offer a unique opportunity to manipulate crystal structures in a way that bottom-up synthesis cannot. To this end there are a few metal chalcogenide projects that could be explored. In metal chalcogenide systems where polymorphic pairs do not exist (ie. Cubic and hexagonal phase pairs with identical stoichiometries), can we access the nonexistent "unnatural" polymorphic pair using cation exchange? To this end, I have synthesized $NiSe_2$ (cubic, Pa3) and $FeSe_2$ (hexagonal, pnnm) - phases that are missing polymorphic pairs - in hopes that someone will attempt a range of cation exchange syntheses on these materials. Is it possible for these materials to undergo cation exchange reactions while keeping the same crystal structure and in doing so creating phases that do not naturally exist?

A similar exchange strategy can also be used to synthesize phases that are uncommon or synthetically difficult. Can we use anion exchange to access these uncommon phases. Marcasite (FeS_2) proved especially hard to synthesize and even after many optimizations could only be synthesized 82% pure with a 18% pyrite impurity. Fortunately, due to hexagonal $FeSe_2$ and its lack of a polymorphic pair, it is much easier to synthesize phase pure. Exploring anion exchange reactions with this material to yield phase pure marcasite (FeS_2) could give the field new ideas to accessing previously thought unobtainable phases.

As discussed in this thesis, there is value in mapping out and understanding the pathways that dictate phase transformation and growth. Most of the discussed experimental results required a large amount of experimental data, time, and materials. Using computational methods to circumvent that would allow for a more rationale synthesis and potentially the ability to target yet to be discovered materials. So far, scientists have incorporated design of experiments and machine learning to optimize the synthesis of nanocrystals,[10] but this usually requires a large data set of previously completed experiments and does little to help us understand these systems at first glance. Moving forward machine learning approaches and design of experiment approaches should further account for the crystalline structures of the metastable materials to more accurately predict rational syntheses.

The Van der Ven group have shown tremendous efforts in understanding phase transitions and pathways using a wide variety of computational methods. Their work includes the unique use of crystal structures to understand phase transformations, and suggest that crystal structures with

similar geometries and symmetries are more likely to transform to one another.[11] They can use density functional theory to map out the thermodynamics of these existing phases, and even can suggest the existence of new, undiscovered phases. Most notably, their efforts suggest that these methods can predict the activation barriers needed to transform from one phase to another, an aspect of these phases that has been very illusive until now.[12]

More work should be done to see if these computational methods can be used to map out and predict the landscapes of transition metal chalcogenides. To this end, my collaborators Wook Shin and Jongha Choi have been working to develop a code based on a study from Zimmerman's *et al.*[13] that enables us to compare metal chalcogenide crystal structures and determine structures that are the most similar in hopes of finding hints of why these materials transform the way they do. In doing so, we might be able to achieve computational methods that allows us to predict phase transformations and even suggest synthetic parameters to find previously undiscoverable materials.

Field Outlook

To realize next generation technologies, we must first realize next generation materials. Understanding how we can control phase is an integral step in the material synthesis process. In tandem with phase control, efforts to control both size and shape of these materials are also important to obtain powerful and versatile materials for a wide range of applications. Overall, we need to increase our synthetic control and abilities to meet the technological standards of the next generation. Although this dissertation has established a more holistic approach into synthesizing metal sulfide crystalline materials, more work needs to be done to truly integrate them in next generation technologies. Ironically, the field of phase control still requires growth.

References

(1) Koziel, A. C.; Goldfarb, R. B.; Endres, E. J.; Macdonald, J. E. Molecular Decomposition Routes of Diaryl Diselenide Precursors in Relation to the Phase Determination of Copper Selenides. *Inorg Chem* **2022**, *61* (37), 14673-14683. DOI: 10.1021/acs.inorgchem.2c02042 From NLM PubMed-not-MEDLINE.

(2) Thomson, J. W.; Nagashima, K.; MacDonald, P. M.; Ozin, G. A. From sulfur-amine solutions to metal sulfide nanocrystals: Peering into the oleylamine-sulfur black box. *Journal of the American Chemical Society* **2011**, *133* (13), 5036-5041. DOI: 10.1021/ja1109997.

(3) Roffey, A.; Hollingsworth, N.; Islam, H. U.; Mercy, M.; Sankar, G.; Catlow, C. R. A.; Hogarth, G.; De Leeuw, N. H. Phase control during the synthesis of nickel sulfide nanoparticles from dithiocarbamate precursors. *Nanoscale* **2016**, *8* (21), 11067-11075. DOI: 10.1039/c6nr00053c.
(4) Rhodes, J. M.; Jones, C. A.; Thal, L. B.; MacDonald, J. E. Phase-controlled colloidal syntheses of iron sulfide nanocrystals via sulfur precursor reactivity and direct pyrite precipitation. *Chemistry of Materials* **2017**, *29* (19), 8521-8530. DOI: 10.1021/acs.chemmater.7b03550.
(5) Penk, D. N.; Endres, E. J.; Nuriye, A. Y.; Macdonald, J. E. Dependence of Transition-Metal Telluride Phases on Metal Precursor Reactivity and Mechanistic Implications. *Inorg Chem* **2023**, *62* (9), 3947-3956. DOI: 10.1021/acs.inorgchem.2c04342 From NLM PubMed-not-MEDLINE.
(6) Jin, B.; Wang, Y.; Liu, Z.; France-Lanord, A.; Grossman, J. C.; Jin, C.; Tang, R. Revealing the Cluster-Cloud and Its Role in Nanocrystallization. *Advanced Materials* **2019**, *31* (16), 1-6. DOI: 10.1002/adma.201808225.
(7) Moehring, N. K.; Fort, M. J.; McBride, J. R.; Kato, M.; Macdonald, J. E.; Kidambi, P. R. In situ observations of thermally induced phase transformations in iron sulfide nanoparticles. *Materials Today Advances* **2020**, *6*, 100057-100057. DOI: 10.1016/j.mtadv.2020.100057.
(8) Hendricks, M. P.; Campos, M. P.; Cleveland, G. T.; Plante, I. J.-L.; Owen, J. S. A Tunable library of substituted thiourea precursors to metal sulfide nanocrystals. *Science* **2015**, *348* (6240), 1226-1230. DOI: 10.1126/science.aaa2951.
(9) Campos, M. P.; Hendricks, M. P.; Beecher, A. N.; Walravens, W.; Swain, R. A.; Cleveland, G. T.; Hens, Z.; Sfeir, M. Y.; Owen, J. S. A Library of Selenourea Precursors to PbSe Nanocrystals with Size Distributions near the Homogeneous Limit. *Journal of the American Chemical Society* **2017**, *139* (6), 2296-2305. DOI: 10.1021/jacs.6b11021.
(10) Williamson, E. M.; Sun, Z.; Tappan, B. A.; Brutchey, R. L. Predictive Synthesis of Copper Selenides Using a Multidimensional Phase Map Constructed with a Data-Driven Classifier. *J Am Chem Soc* **2023**, *145* (32), 17954-17964. DOI: 10.1021/jacs.3c05490 From NLM PubMed-not-MEDLINE.
(11) Thomas, J. C.; Natarajan, A. R.; Van der Ven, A. Comparing crystal structures with symmetry and geometry. *npj Computational Materials* **2021**, *7* (1). DOI: 10.1038/s41524-021-00627-0.

(12) Kolli, S. K.; Natarajan, A. R.; Van der Ven, A. Six new transformation pathways connecting simple crystal structures and common intermetallic crystal structures. *Acta Materialia* **2021**, *221*. DOI: 10.1016/j.actamat.2021.117429.
(13) Zimmermann, N. E. R.; Jain, A. Local structure order parameters and site fingerprints for quantification of coordination environment and crystal structure similarity. *RSC Adv* **2020**, *10* (10), 6063-6081. DOI: 10.1039/c9ra07755c

Chapter 6: Appendix

Appendix A Supplemental Figures for Chapter 2

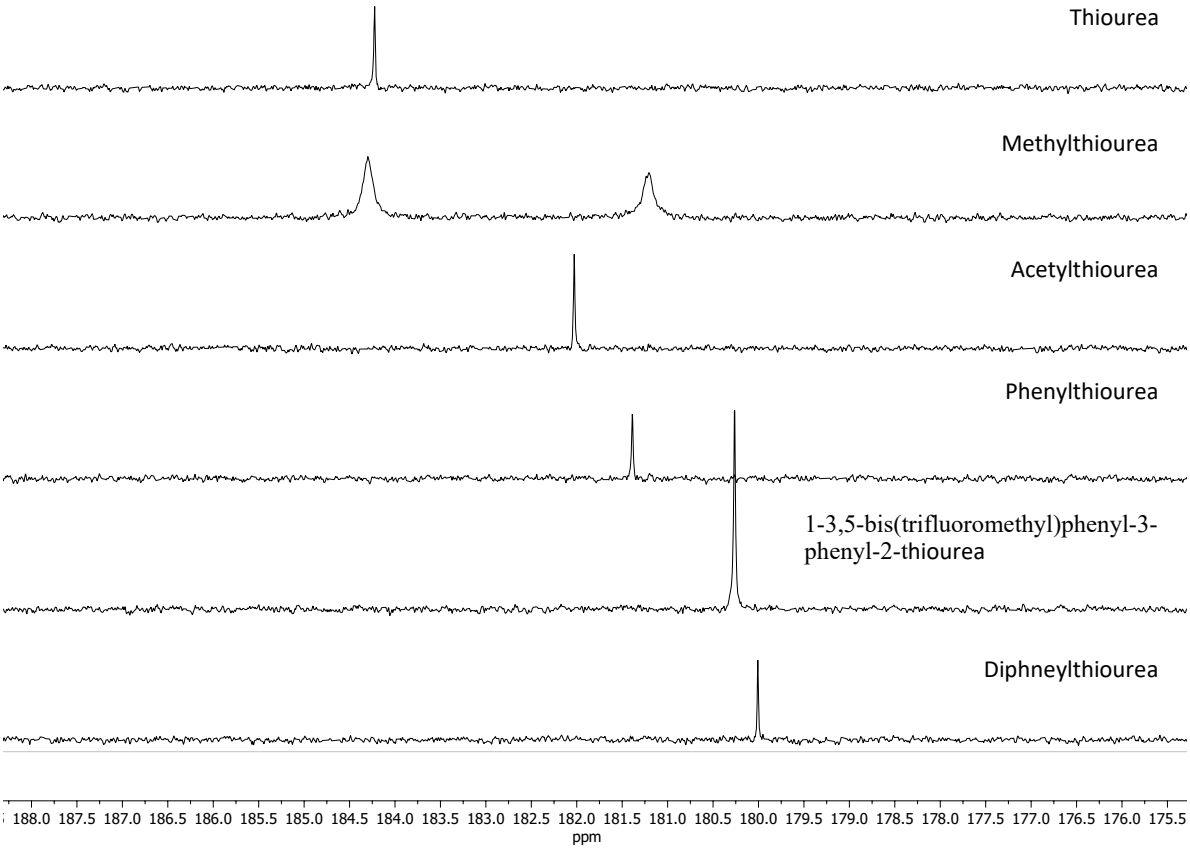

Figure A.1 ^{13}C NMR of the C=S peak in thiourea and several substituted thioureas. Methylthiourea shows 2 peaks due to cis trans rotation barrier height. In terms of relating this to chemical kinetic reactivity, we average the two peaks as both exist when attached in Pt complexes.[2] The results indicate as we attach different substituents to our thioureas, their thiourea carbon peak shifts downfield, which indicates the slowing down of the decomposition reaction speed.

Ratio Study

The sulfur to iron ratio was studied for its impact on crystal phase. The sulfur to iron ratio was decreased from 6:1 in the process of record to 3:1 for a series of reactions at 220ºC with each of the studied thioureas. The generated phases were similar to that of the 6:1data set (Figure 1 in the main text), except the most sulfur rich phases were excluded or decreased in concentration to the benefit of the sulfur poor phases were. For example, unlike the 6:1 experiments, no pyrite or marcasite (FeS_2) were isolated when thiourea was employed, and instead the products contained only the more sulfur poor phases greigite and mackinawite. In another example, the content of sulfur deficient pyrrhotite ($Fe_{1-x}S$) over greigite (Fe_3S_4) ratio was increased when less of the thiourea was employed. Similarly, only greigite (Fe_3S_4) was observed when 1-3,5-bis(trifluoromethyl)phenyl-3-phenyl-2-thiourea and diphenylthiourea were employed at a 6:1 ratio; at a 3:1 ratio, the sulfur deficient pyrrhotite ($Fe_{1-x}S$) was identified in addition to greigite (Fe_3S_4).

Even though excess of sulfur is still present in the reaction at a 3:1 S:Fe ratio, the low sulfur content of the solution when only 3 equivalents of thioureas is used provides a lower chemical potential for reduction, sulfur inclusion and eventual persulfide formation. Previous studies have also shown phase control phenomenon by changing the metal: sulfur ratio and both show some relationship between the sulfur content in the phase and initial sulfur content in the flask.(2)

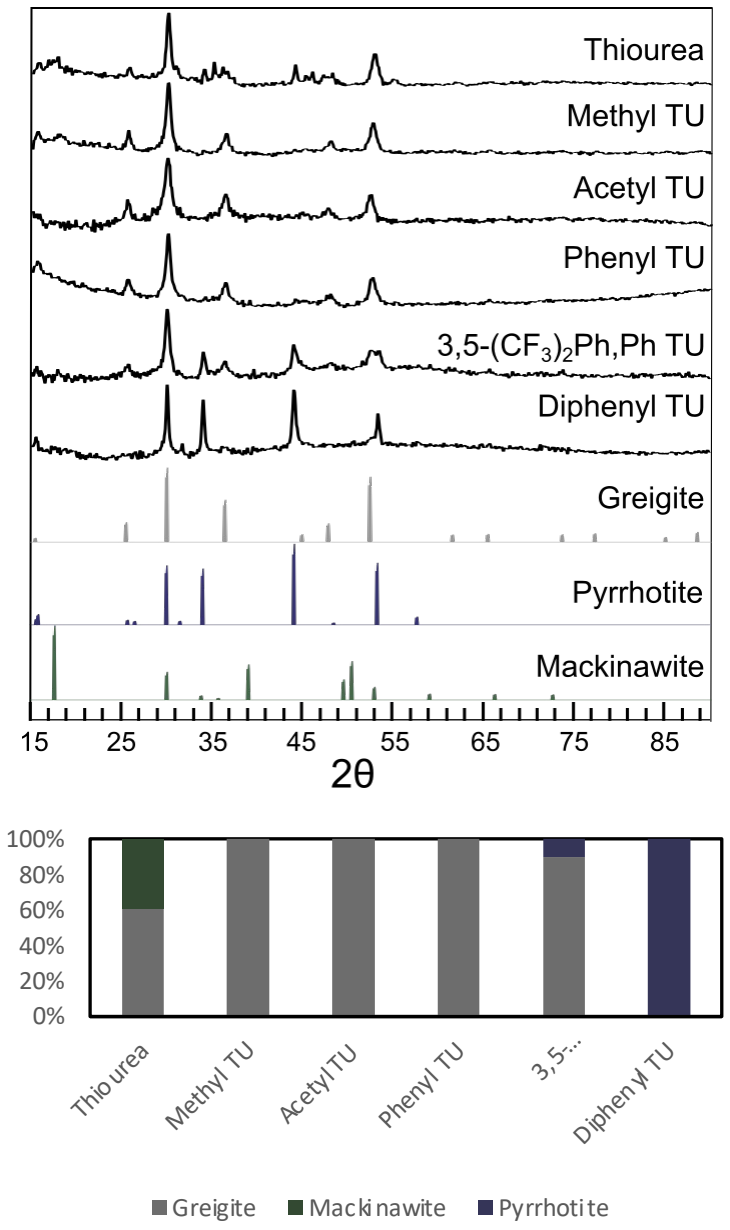

Figure A.2 XRD of the crystalline products of the reaction of iron(III) stearate with noted substituted thioureas at 220°C with a sulfur to iron ratio of 3:1. Corresponding precent compositions provided by Rietveld refinement of the data.

Solvent and Precursor Interactions

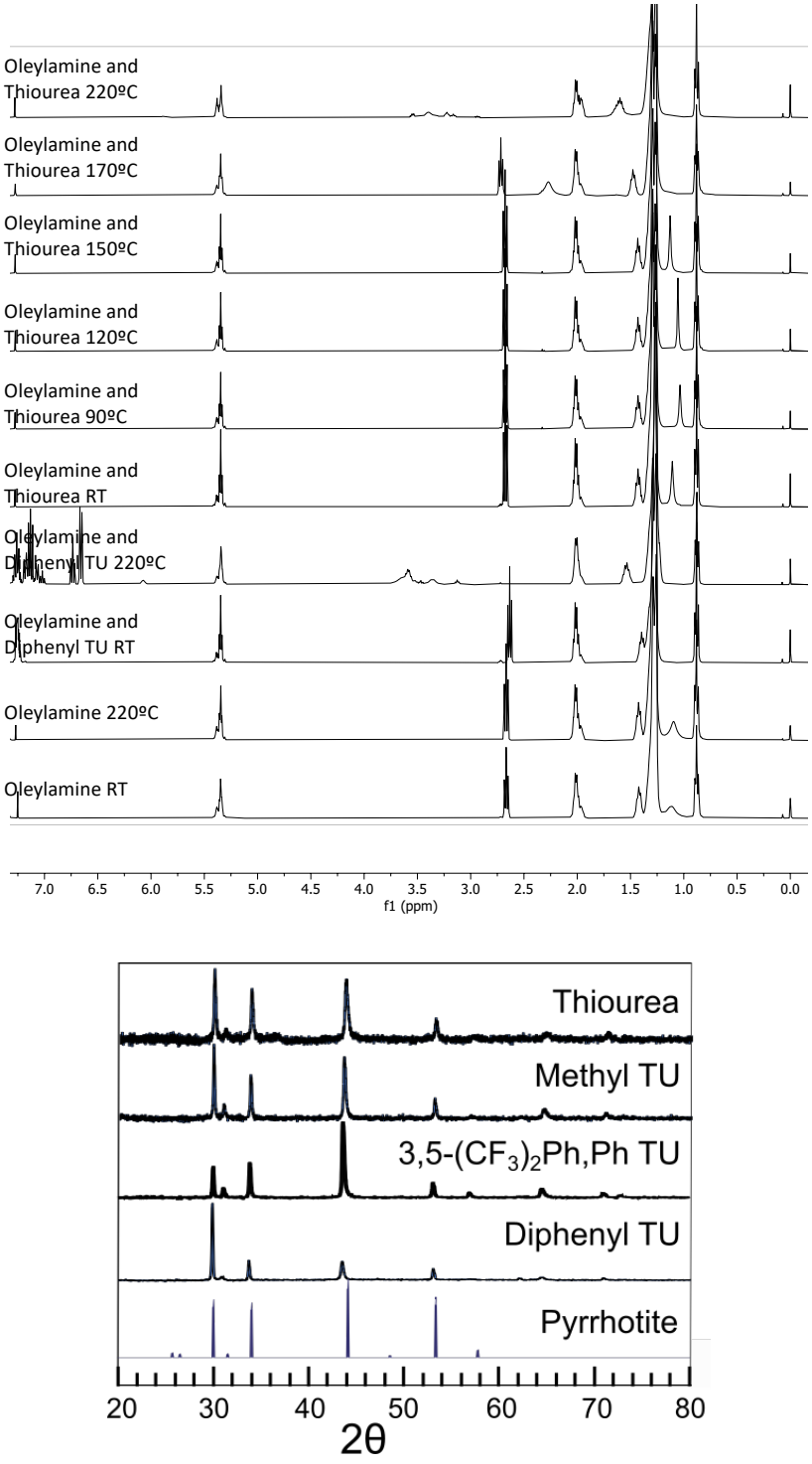

Figure A.3 Top: $FeCl_2$ ^1H NMR ($CDCl_3$) of a 1:2 molar ratio of thiourea and oleylamine after heating for 30 min at the noted temperature. The downfield shift of the oleylamine $NH_2CH_2C\mathbf{H}_2$

protons (triplet, 1.42 ppm) and the loss of oleylamine $NH_2C\mathbf{H}_2$ signal (triplet, 2.69 ppm) indicate reaction to oleylamine substituted thioureas. Bottom: XRD of the crystalline products of the reaction of $FeCl_2$ with the noted thiourea in oleylamine at 220°C for 1h. The products are all the same crystalline phase because the thioureas become substituted *in situ* with oleylamine.

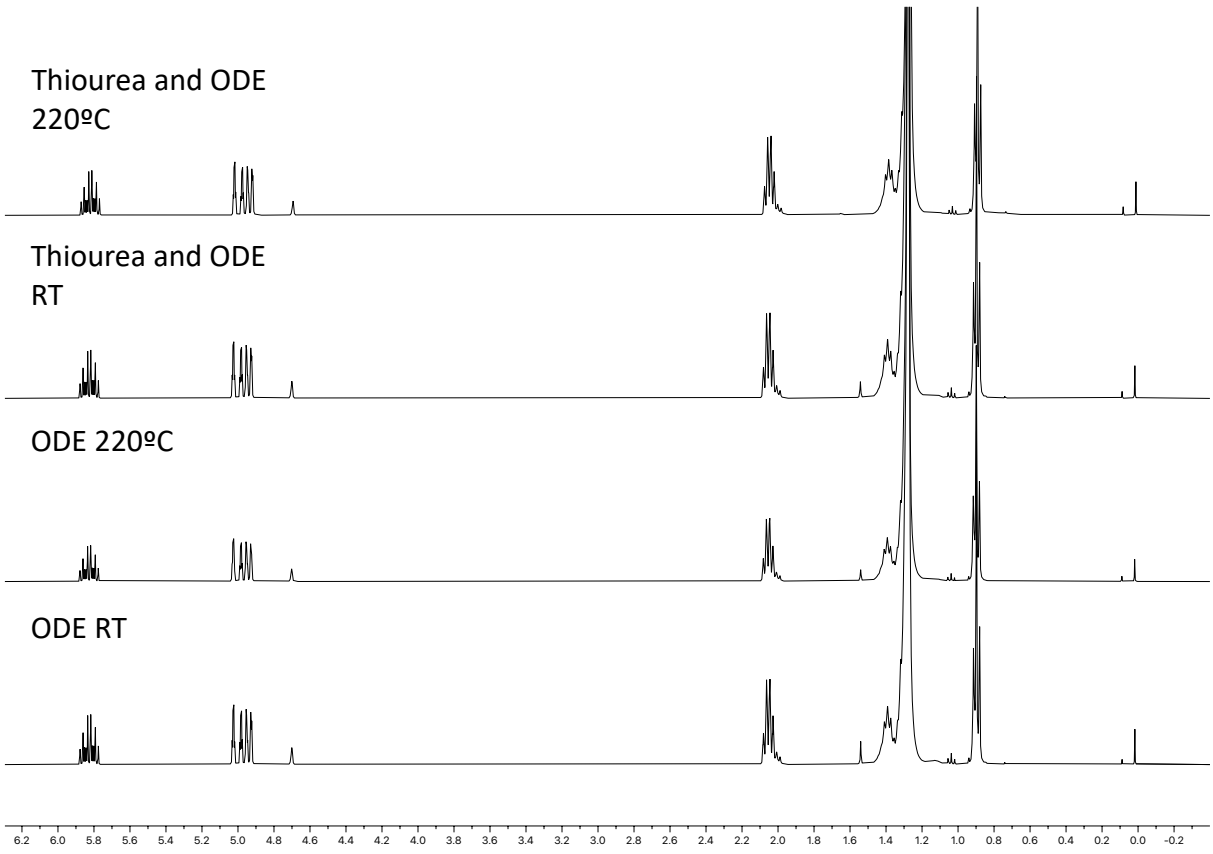

Figure A.4 ^{1}H NMR of the control of octadecene at room temperature and heated at 220°C for 30 min with and without the addition of thiourea (1:2 thiourea:octadecene). The results indicate stability and chemical inertness of ODE with thiourea at the reaction temperatures of the synthetic experiments.

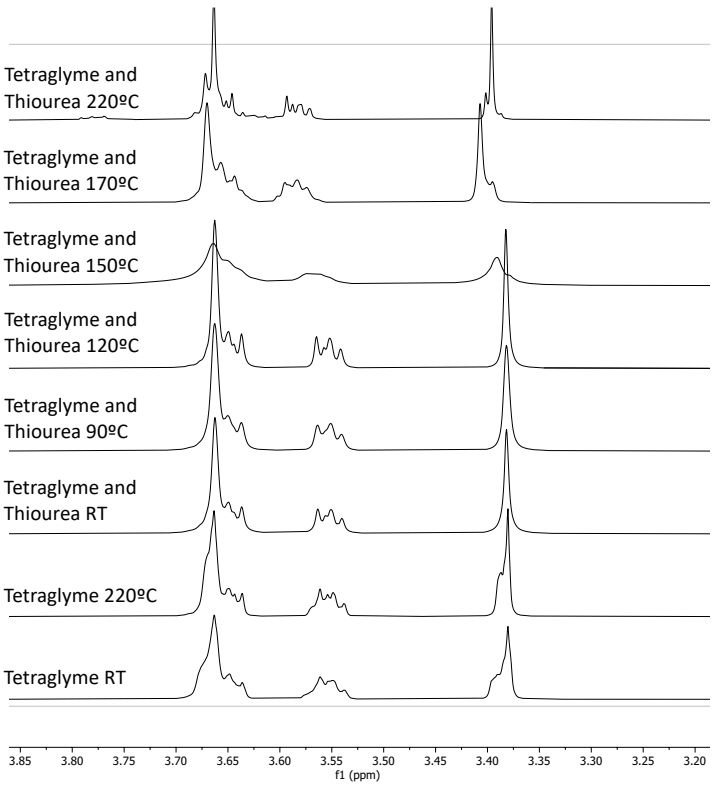
Tetraglyme and Thiourea 220ºC
Tetraglyme and Thiourea 170ºC
Tetraglyme and Thiourea 150ºC
Tetraglyme and Thiourea 120ºC
Tetraglyme and Thiourea 90ºC
Tetraglyme and Thiourea RT
Tetraglyme 220ºC
Tetraglyme RT
3.85 3.80 3.75 3.70 3.65 3.60 3.55 3.50 3.45 3.40 3.35 3.30 3.25 3.20
f1 (ppm)

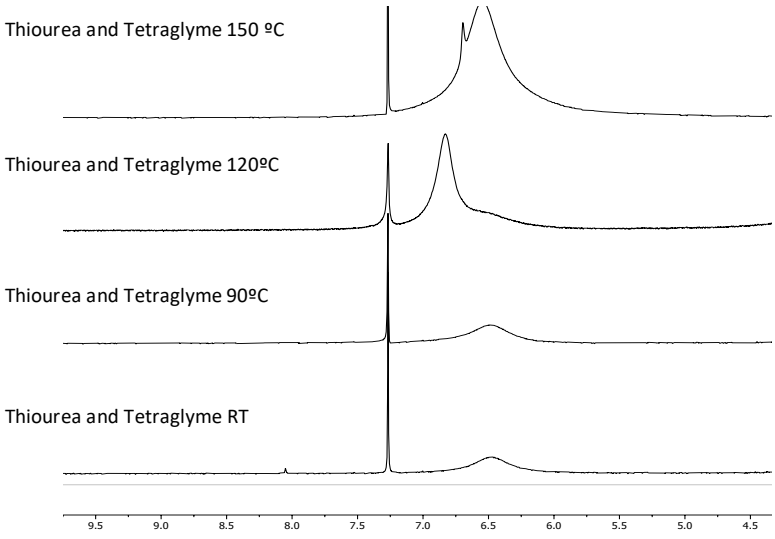
Thiourea and Tetraglyme 150 ºC
Thiourea and Tetraglyme 120ºC
Thiourea and Tetraglyme 90ºC
Thiourea and Tetraglyme RT
9.5 9.0 8.5 8.0 7.5 7.0 6.5 6.0 5.5 5.0 4.5

Figure A.5 ^{1}H NMR of the alkyl region (top) and thiourea region (bottom) of a 1:2 molar ratio of thiourea heated in tetraglyme at the indicated temperatures for 30 min. The shifting proton signals at temperatures above 150°C indicate reactivity between thiourea and tetraglyme at temperatures relevant to the synthetic FeS experiments.

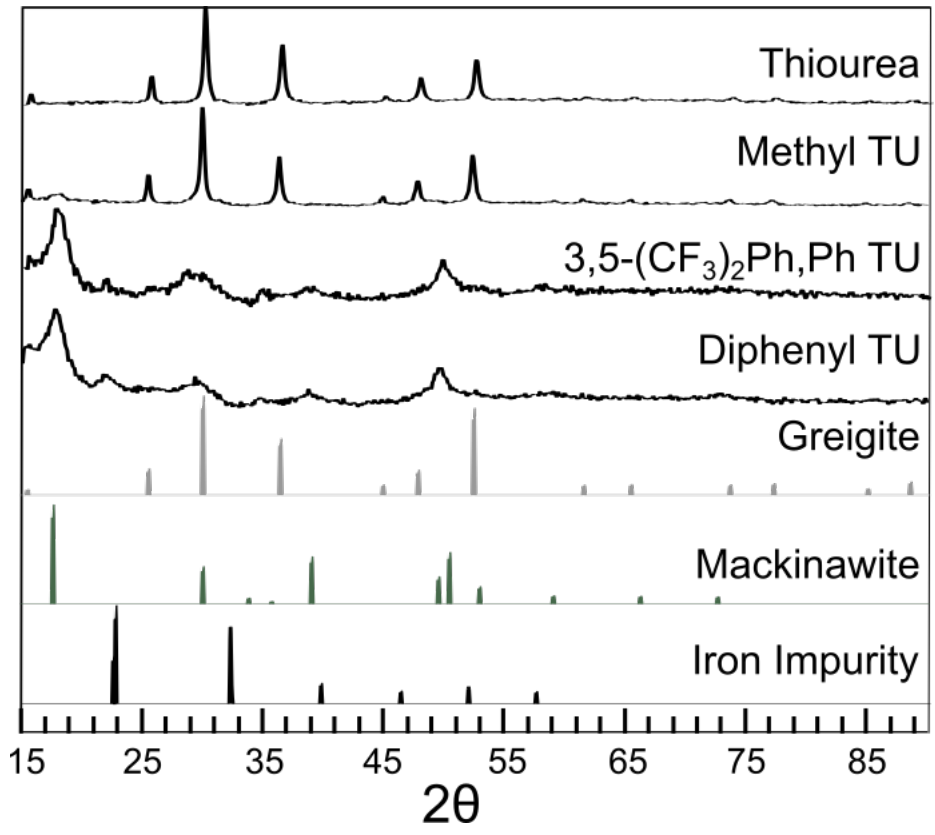

Figure A.6 XRD of the crystalline products of the reaction of Fe(III) stearate with the noted thiourea in octadecene and tetraglyme (2:1 by volume) at 220°C for 1h. Some unreacted iron was seen with the slower reactive thioureas (1-3,5-bis(trifluoromethyl)phenyl-3-phenyl-2-thiourea and diphenylthiourea).

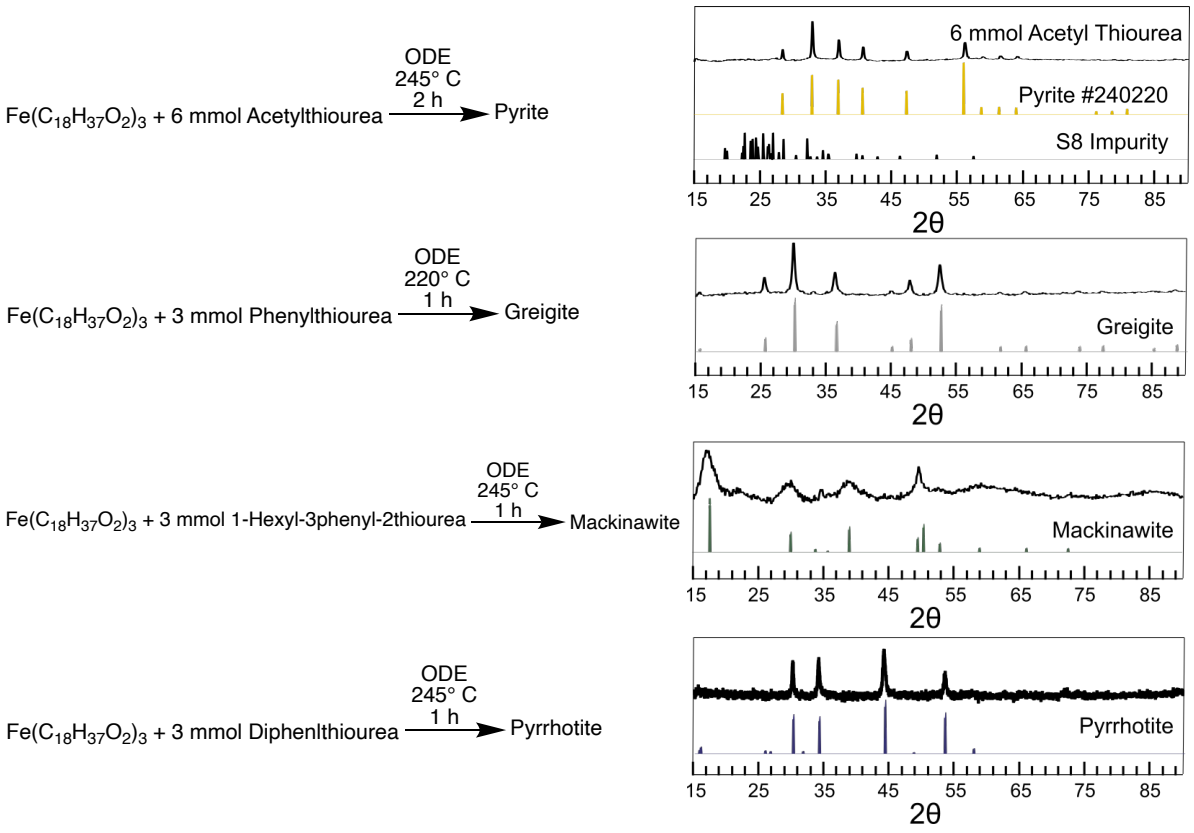

Figure A.7 Reaction conditions to form phase pure pyrite, greigite, mackinawite, and pyrrhotite, followed by the powder XRD.

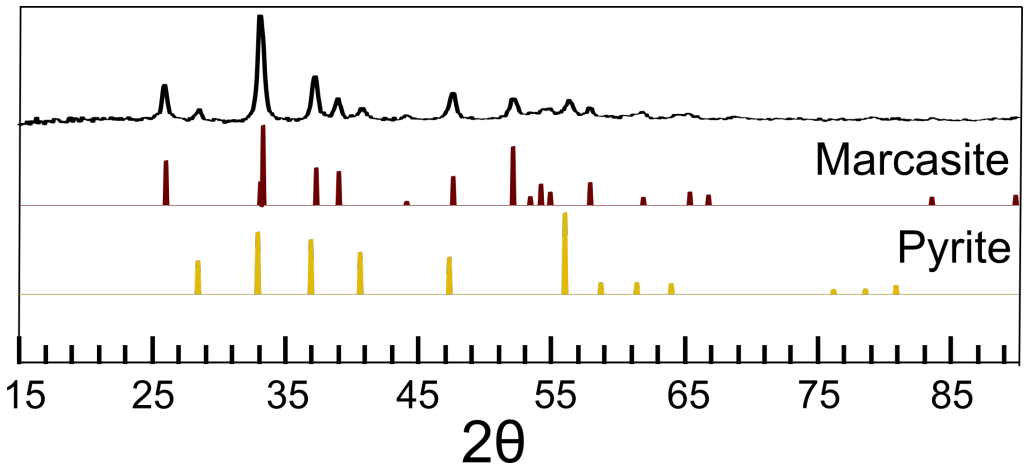

Figure A.8: Powder XRD from one pot marcasite synthesis. In brief, pure pyrrhotite was placed with acetyl thiourea in a 3-neck flask in ODE and raised to 245°C for 1 h.

Rietveld Refinements

Table S1: Summary of refinements

	Solvent	T(°C)	Thiourea	S:Fe	Time	Pyrite (10422)	Marcasite (9013067)	Smythite (900077)	Greigite (160713)	Pyrrhotite (240220)	Mackina-wite (182250)	Troilite (68852)	Cubic Iron Sulfide	Semi-Crysta l-line FeS	Other
1	OLAM	220	Thiourea	6 to 1	2 h					100%					
2	OLAM	220	Methyl Thiourea	6 to 1	2 h					100%					
3	OLAM	220	3,5-(CF_3)Ph,Ph Thiourea	6 to 1	2 h					100%					
4	OLAM	220	Diphenyl Thiourea	6 to 1	2 h					100%					
5	ODE and Tetraglyme	170	Thiourea	6 to 1	1 h				93.6%						Fe (43100 30) 6.4%
6	ODE and Tetraglyme	170	Methyl Thiourea	6 to 1	1 h				85%						Fe ((4310 030) 15%
7	ODE and Tetraglyme	170	3,5-(CF_3)Ph,Ph	6 to 1	1 h						100%				
8	ODE and Tetraglyme	170	Diphenyl	6 to 1	1 h						100%				
9	ODE	170	Thiourea	6 to 1	1 h			16.6%	22.7%		14.3%	23.5%	5.0%	17.9%	
10	ODE	170	Methyl Thiourea	6 to 1	1 h			25.8%	17.6%		17.8%	20.4%	3.5%	14.9%	
11	ODE	170	Acetyl Thiourea	6 to 1	1 h				70.75%		29.25%				
12	ODE	170	Phenyl Thiourea	6 to 1	1 h				100%						
13	ODE	170	3,5-(CF_3)Ph,Ph Thiourea	6 to 1	1 h				100%						
14	ODE	170	Diphenyl Thiourea	6 to 1	1 h				34.4%		65.6%				
15	ODE	195	Thiourea	6 to 1	1 h			7.2%	46.0%		15.7%	11.1%	6.0%	14.0%	
16	ODE	195	Methyl Thiourea	6 to 1	1 h			11.7%	54.5%		9.0%	5.3%	11.2%	8.3%	
17	ODE	195	Acetyl Thiourea	6 to 1	1 h				100%						
18	ODE	195	Phenyl Thiourea	6 to 1	1 h				100%						
19	ODE	195	3,5-(CF_3)Ph,Ph Thiourea	6 to 1	1 h				100%						
20	ODE	195	Diphenyl Thiourea	6 to 1	1 h				100%						
21	ODE	220	Thiourea	6 to 1	1 h	29.6%	18.8%	6.0%	16.8%		16.6%			12.2%	
22	ODE	220	Methyl Thiourea	6 to 1	1 h	10.4%			89.6%						
23	ODE	220	Acetyl Thiourea	6 to 1	1 h	25%			75%						
24	ODE	220	Phenyl Thiourea	6 to 1	1 h				100%						
25	ODE	220	3,5-(CF_3)Ph,Ph Thiourea	6 to 1	1 h				100%						
26	ODE	220	Diphenyl Thiourea	6 to 1	1 h				47.3%	52.7%					
27	ODE	245	Thiourea	6 to 1	1 h	34.1%	24.9%	10.3%	17.6%		8.0%			5.1%	
28	ODE	245	Methyl Thiourea	6 to 1	1 h	12.8%	43.4%	10.6%	25.0%		4.1%			4.1%	
29	ODE	245	Acetyl Thiourea	6 to 1	1 h	67.5%			32.5%						
30	ODE	245	Phenyl Thiourea	6 to 1	1 h				100%						
31	ODE	245	3,5-(CF_3)Ph,Ph Thiourea	6 to 1	1 h					100%					

32	ODE	245	Diphenyl Thiourea	6 to 1	1 h					100%					
33	ODE	220	Thiourea	6 to 1	1 min				70.5%			29.5%			
34	ODE	220	Thiourea	6 to 1	10 min	34.3%		7.2%	22.5%		18.6%				17.4%
35	ODE	220	Thiourea	6 to 1	4 h	40.4	46.1%		13.5%						
36	ODE	220	Thiourea	3 to 1	1 h				61.1%		38.9%				
37	ODE	220	Methyl Thiourea	3 to 1	1 h				100%						
38	ODE	220	Acetyl Thiourea	3 to 1	1 h				100%						
39	ODE	220	Phenyl Thiourea	3 to 1	1 h				100%						
40	ODE	220	3,5-(CF_3)Ph,Ph	3 to 1	1 h				89.5%	10.5%					
41	ODE	220	Diphenyl	3 to 1	1 h					100%					
42	ODE	170	1-Hexyl-3-Phenyl-2-Thiourea	6 to 1	1 h						100%				
43	ODE	225	Acetyl Thiourea	12 to 1	2 h	98.5%									S8 (4124791) 1.5%
44	ODE	245	Diphenyl Thiourea then injection of Acetyl Thiourea	6 to 1 then 4 to 1	1 h then 1 h	9%	81%			10%					
45	ODE	245 then 160	Diphenyl Thiourea then injection of Acetyl Thiourea	6 to 1 then 3 to 1	1 h then 4 h			70%		30%					
46	ODE/OLAM then pure ODE	245	Diphenyl Thiourea then addition of Acetyl Thiourea	6 to 1 then 3 to 1	2 h then 1 h	14%	86%								

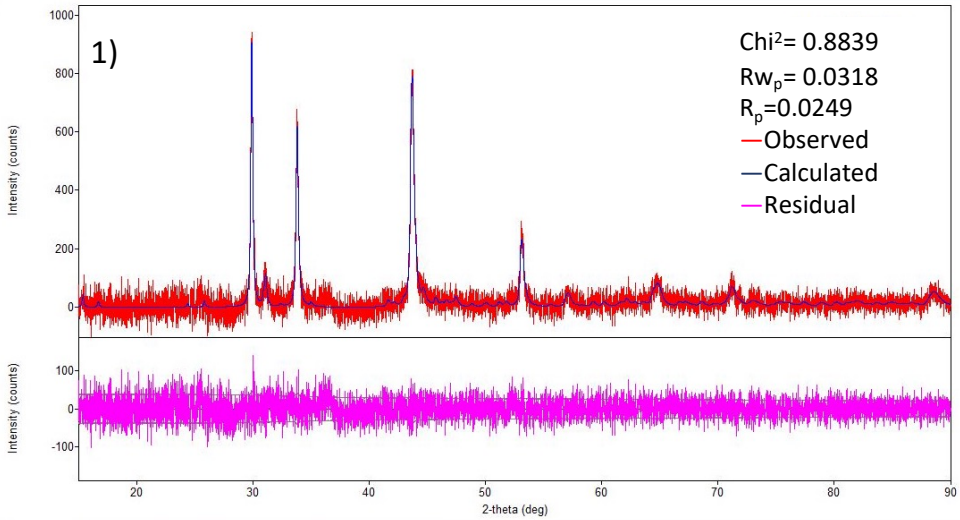
1)
Chi²= 0.8839
Rwp= 0.0318
Rp=0.0249
Observed
Calculated
Residual
Intensity (counts)
2-theta (deg)

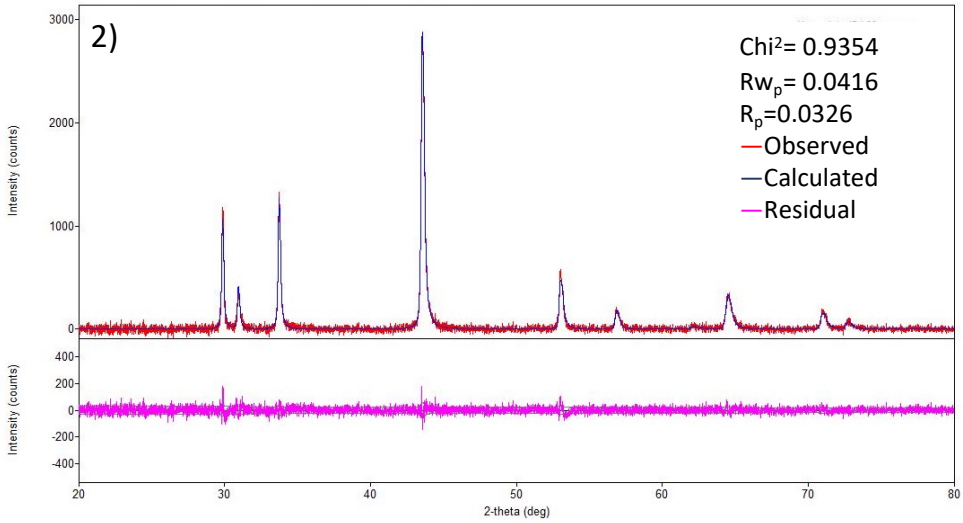
2)
Chi²= 0.9354
Rwp= 0.0416
Rp=0.0326
Observed
Calculated
Residual
Intensity (counts)
2-theta (deg)

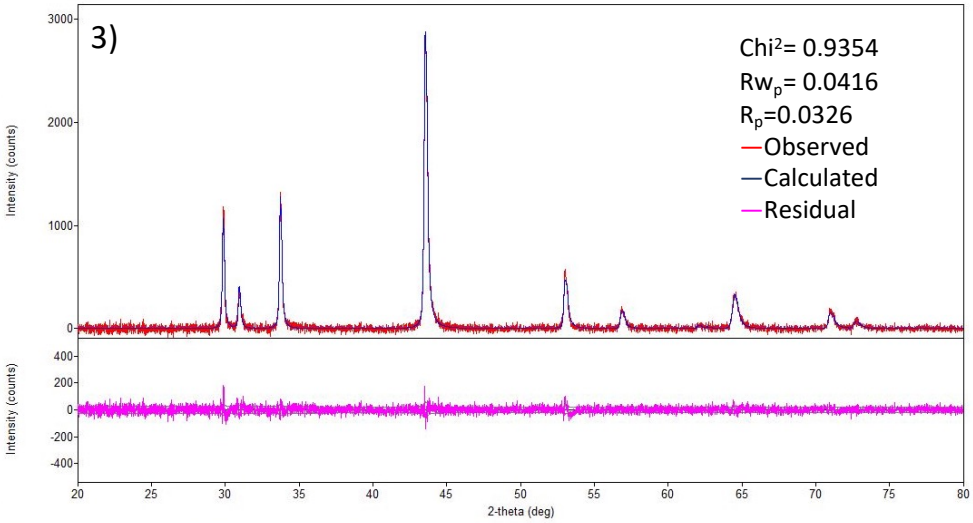
3)
Chi²= 0.9354
Rwp= 0.0416
Rp=0.0326
Observed
Calculated
Residual
Intensity (counts)
2-theta (deg)

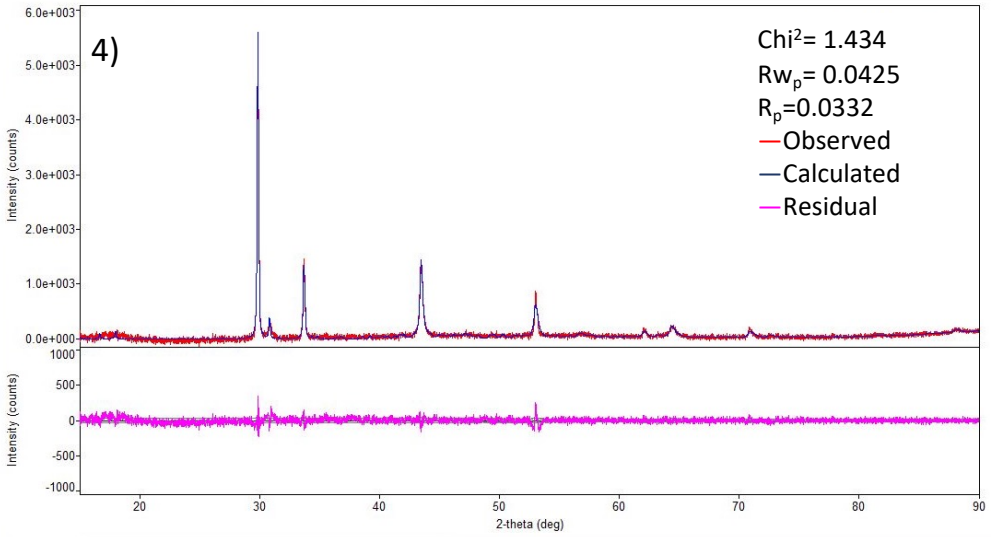
4)
Chi²= 1.434
Rwp= 0.0425
Rp=0.0332
Observed
Calculated
Residual
Intensity (counts)
2-theta (deg)

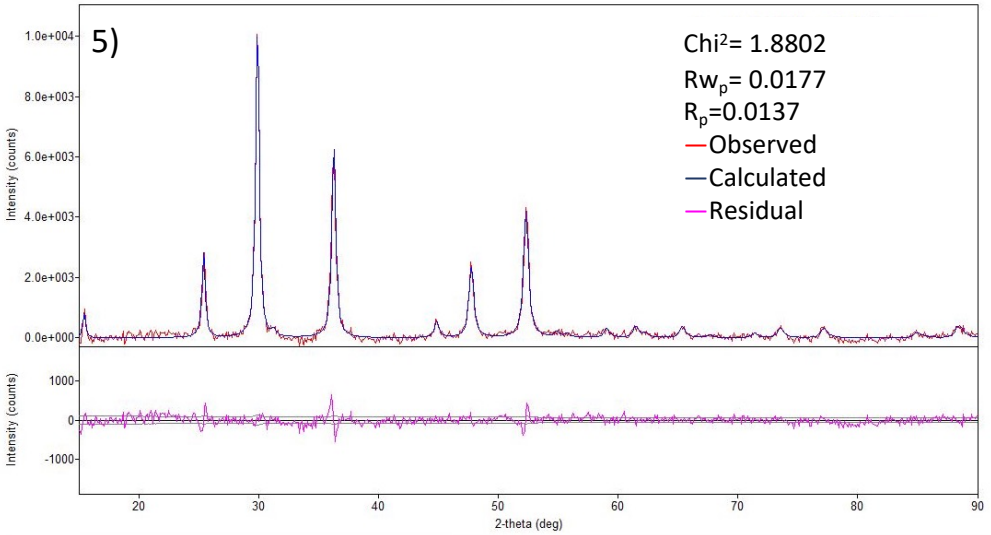
5)
Chi²= 1.8802
Rwp= 0.0177
Rp=0.0137
Observed
Calculated
Residual
Intensity (counts)
2-theta (deg)

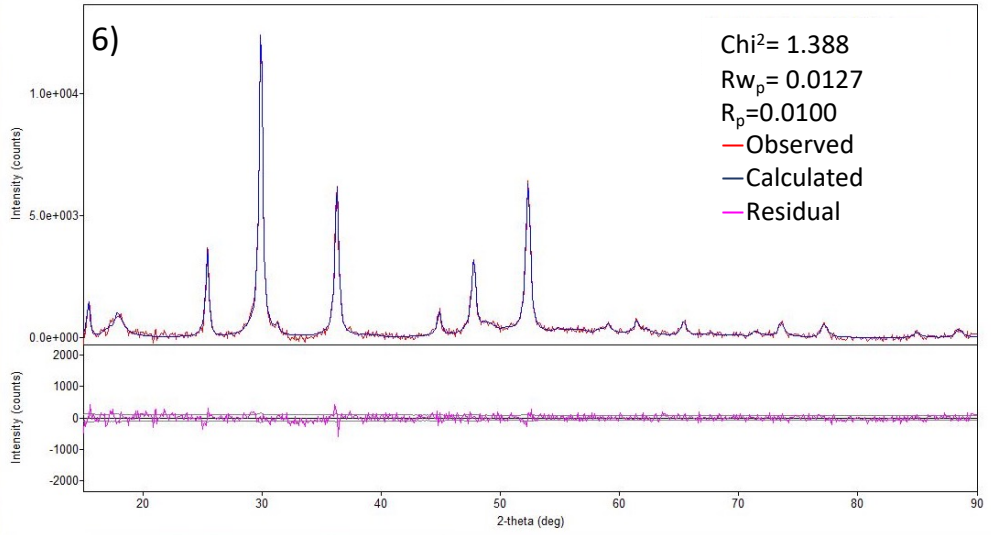
6)
Chi²= 1.388
Rwp= 0.0127
Rp=0.0100
Observed
Calculated
Residual
Intensity (counts)
2-theta (deg)

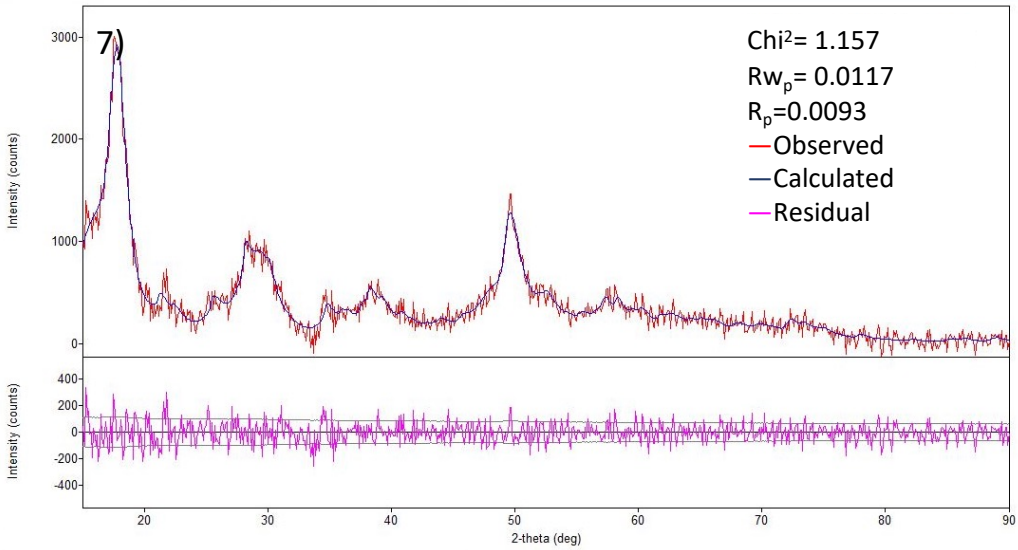
7)
Chi²= 1.157
Rwp= 0.0117
Rp=0.0093
Observed
Calculated
Residual
Intensity (counts)
2-theta (deg)

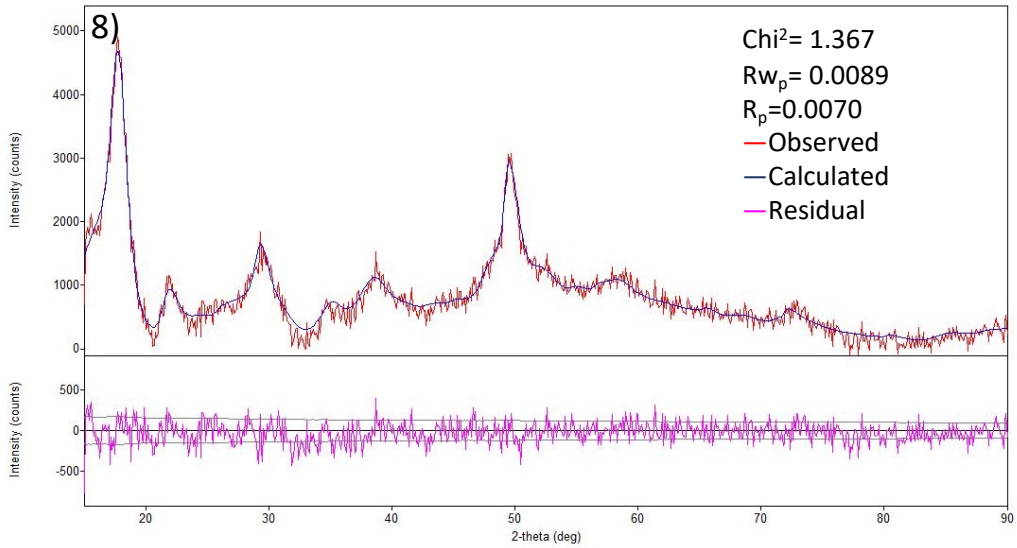
8)
Chi²= 1.367
Rwp= 0.0089
Rp=0.0070
Observed
Calculated
Residual
Intensity (counts)
2-theta (deg)

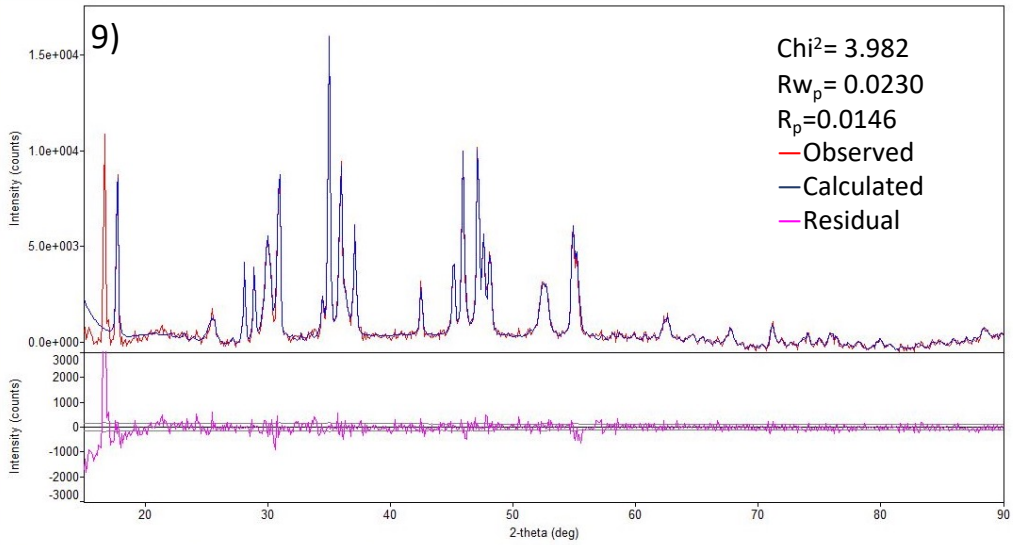
9)
Chi²= 3.982
Rwp= 0.0230
Rp=0.0146
Observed
Calculated
Residual
Intensity (counts)
2-theta (deg)

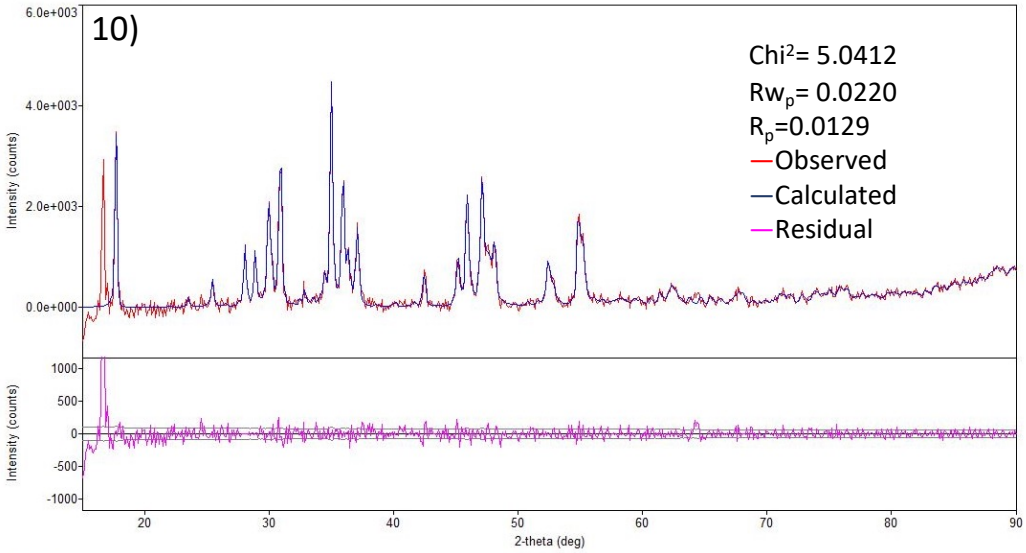
10)
Chi²= 5.0412
Rwp= 0.0220
Rp=0.0129
Observed
Calculated
Residual
Intensity (counts)
2-theta (deg)

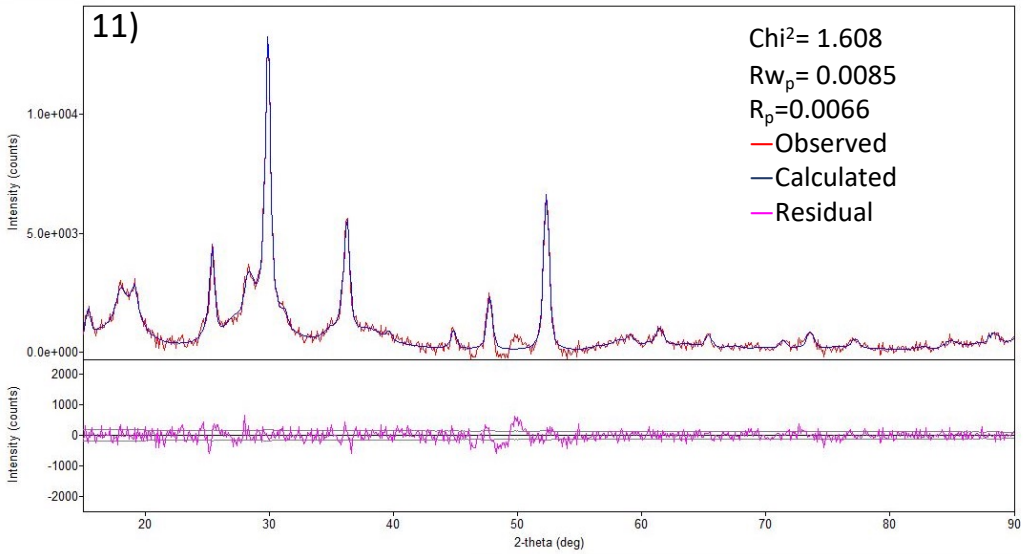
11)
Chi²= 1.608
Rwp= 0.0085
Rp=0.0066
Observed
Calculated
Residual
Intensity (counts)
2-theta (deg)

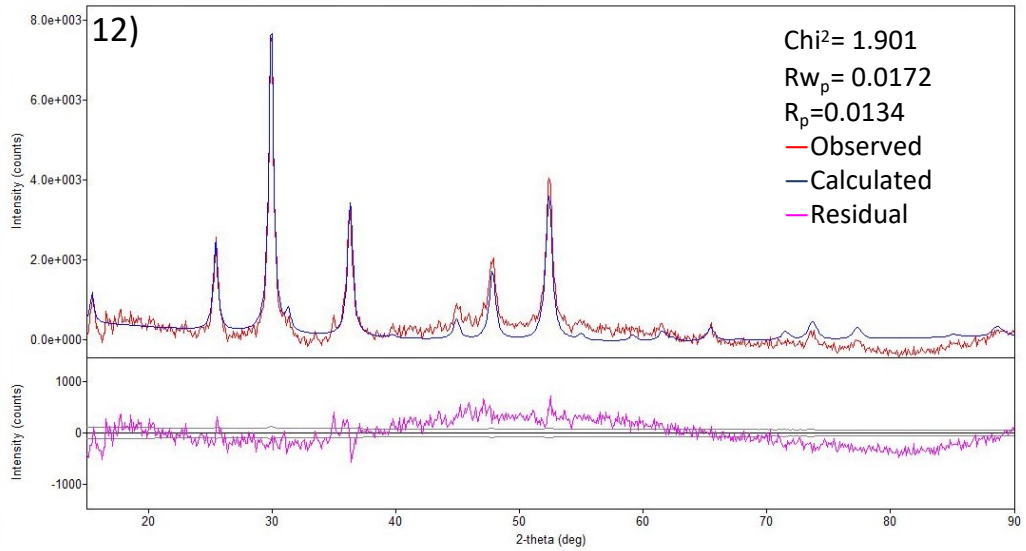
12)
Chi²= 1.901
Rwp= 0.0172
Rp=0.0134
Observed
Calculated
Residual
Intensity (counts)
2-theta (deg)

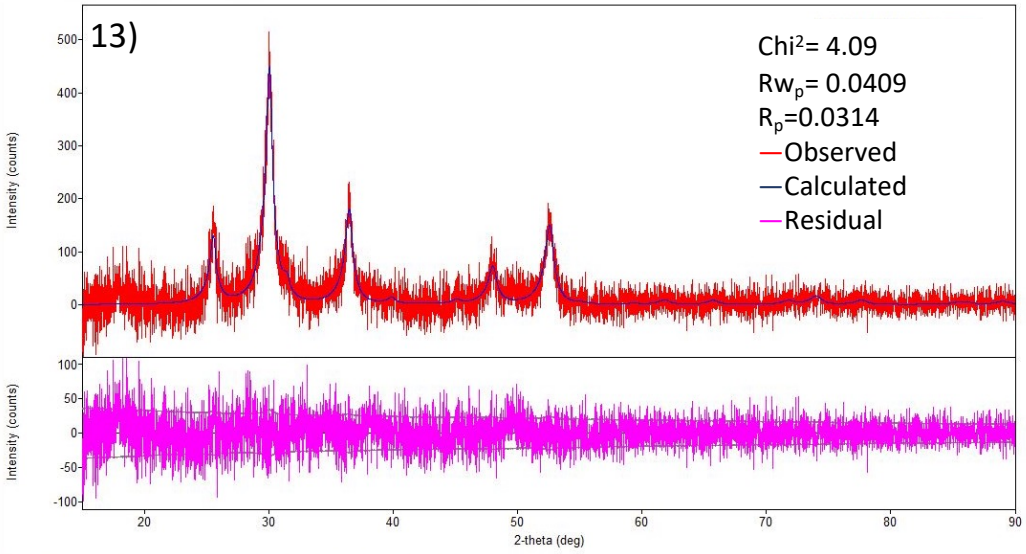
13)
Chi²= 4.09
Rwp= 0.0409
Rp=0.0314
Observed
Calculated
Residual
Intensity (counts)
2-theta (deg)

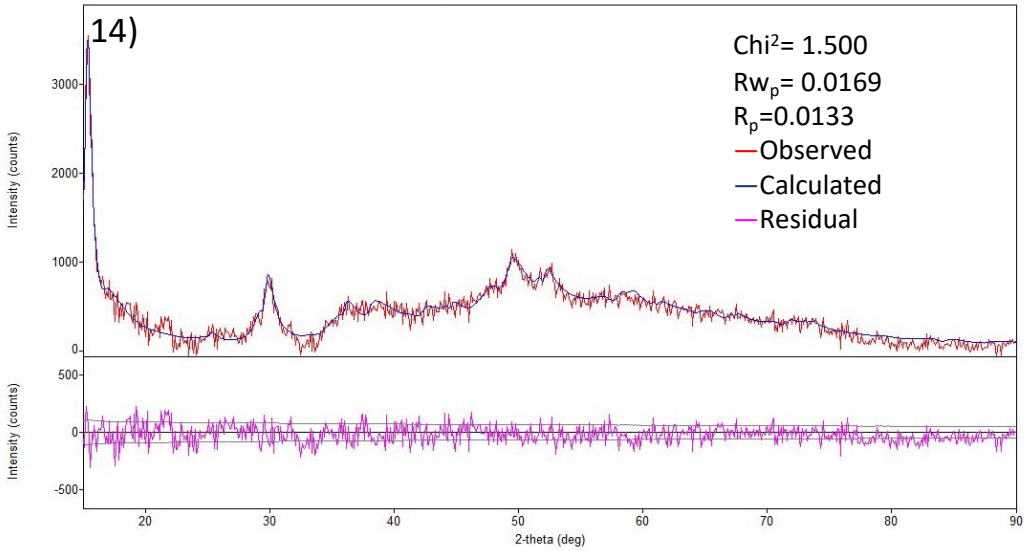
14)
Chi²= 1.500
Rwp= 0.0169
Rp=0.0133
Observed
Calculated
Residual
Intensity (counts)
2-theta (deg)

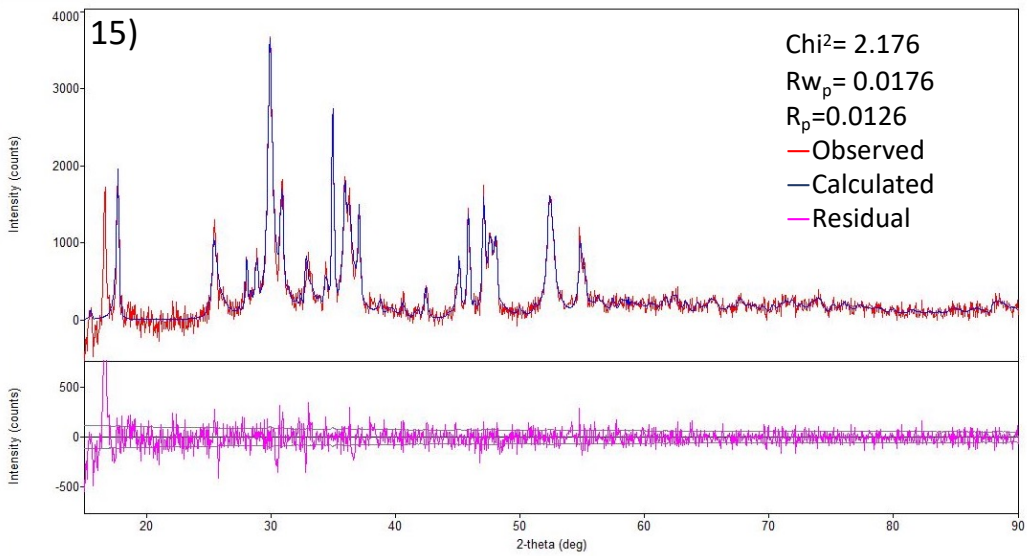
15)
Chi²= 2.176
Rwp= 0.0176
Rp=0.0126
Observed
Calculated
Residual
Intensity (counts)
2-theta (deg)

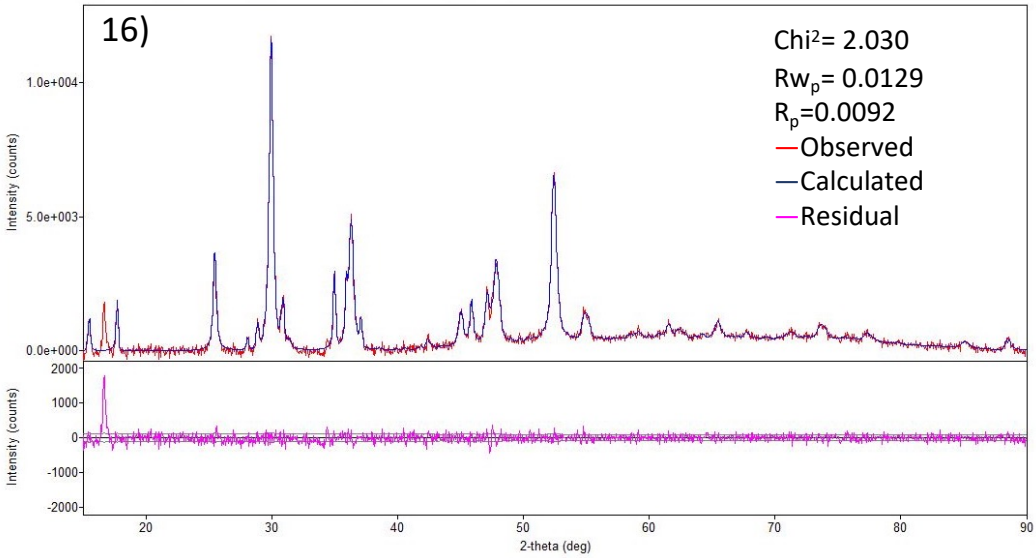
16)
Chi²= 2.030
Rwp= 0.0129
Rp=0.0092
Observed
Calculated
Residual
Intensity (counts)
2-theta (deg)

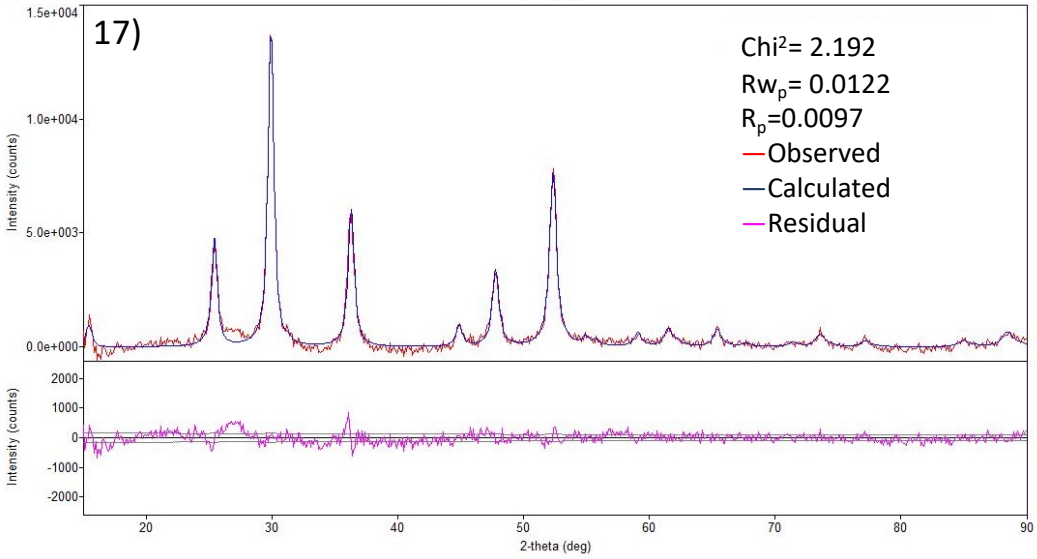
17)
Chi²= 2.192
Rwp= 0.0122
Rp=0.0097
Observed
Calculated
Residual
Intensity (counts)
2-theta (deg)

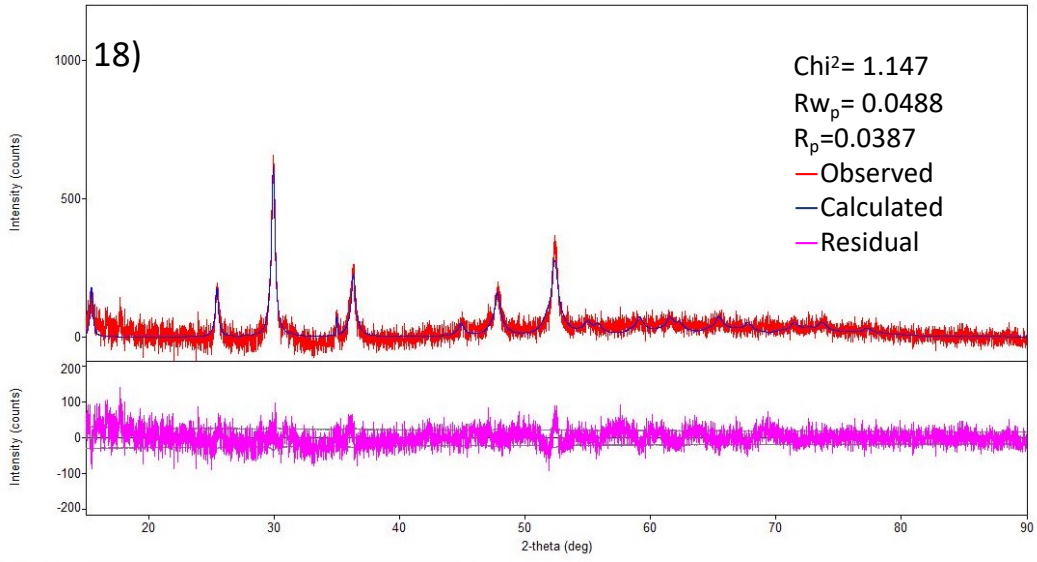
18)
Chi²= 1.147
Rwp= 0.0488
Rp=0.0387
Observed
Calculated
Residual
Intensity (counts)
2-theta (deg)

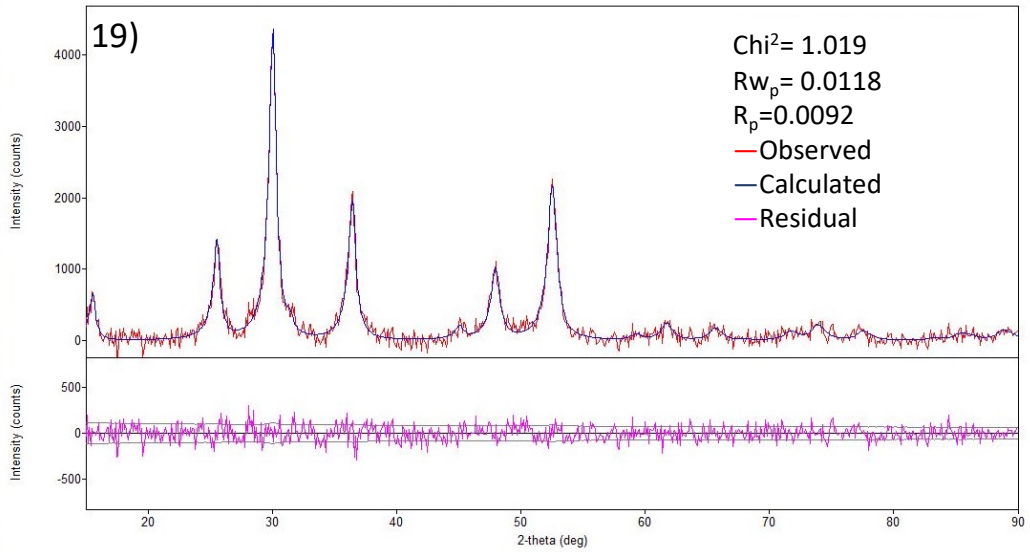
19)
Chi²= 1.019
Rwp= 0.0118
Rp=0.0092
Observed
Calculated
Residual
Intensity (counts)
2-theta (deg)

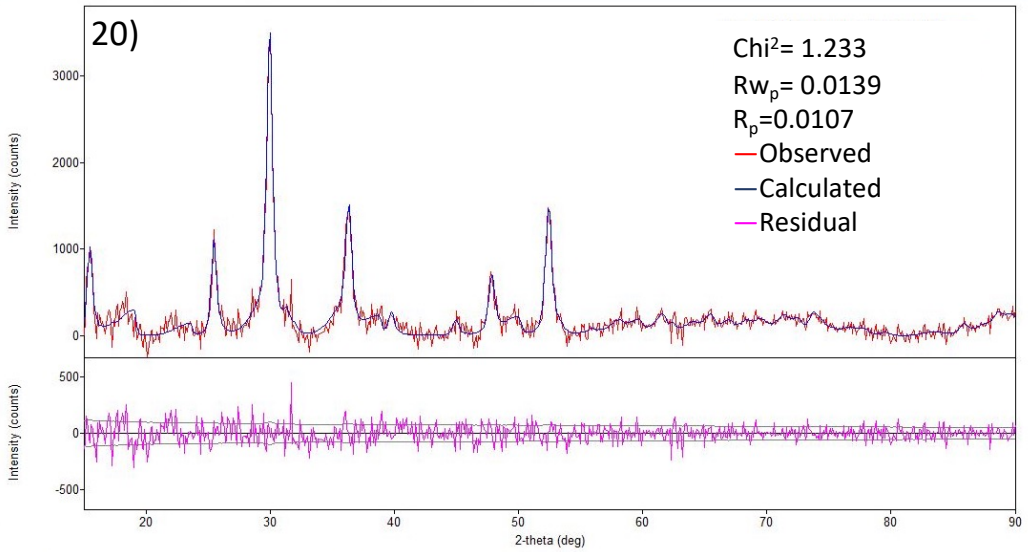
20)
Chi²= 1.233
Rwp= 0.0139
Rp=0.0107
Observed
Calculated
Residual
Intensity (counts)
2-theta (deg)

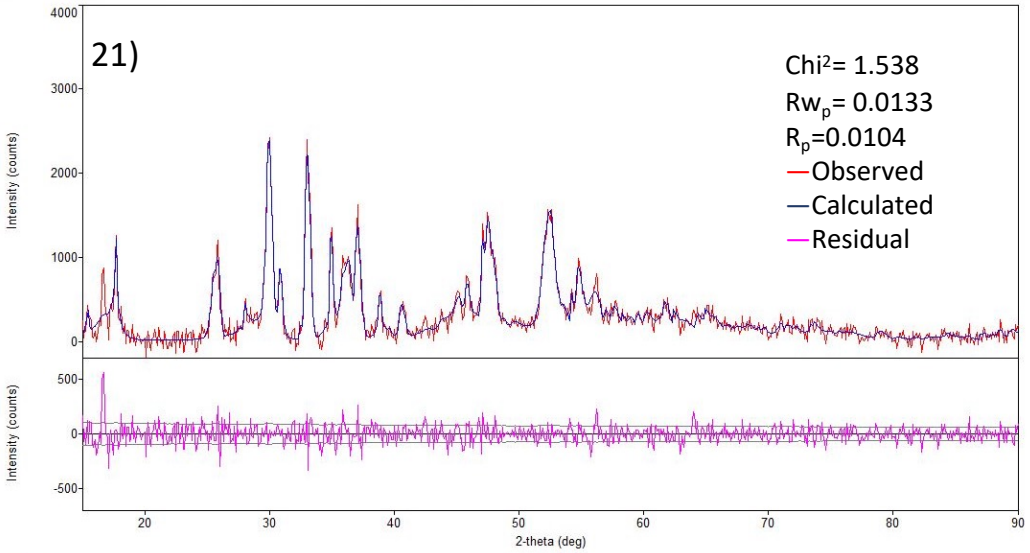
21)
Chi²= 1.538
Rwp= 0.0133
Rp=0.0104
Observed
Calculated
Residual
Intensity (counts)
2-theta (deg)

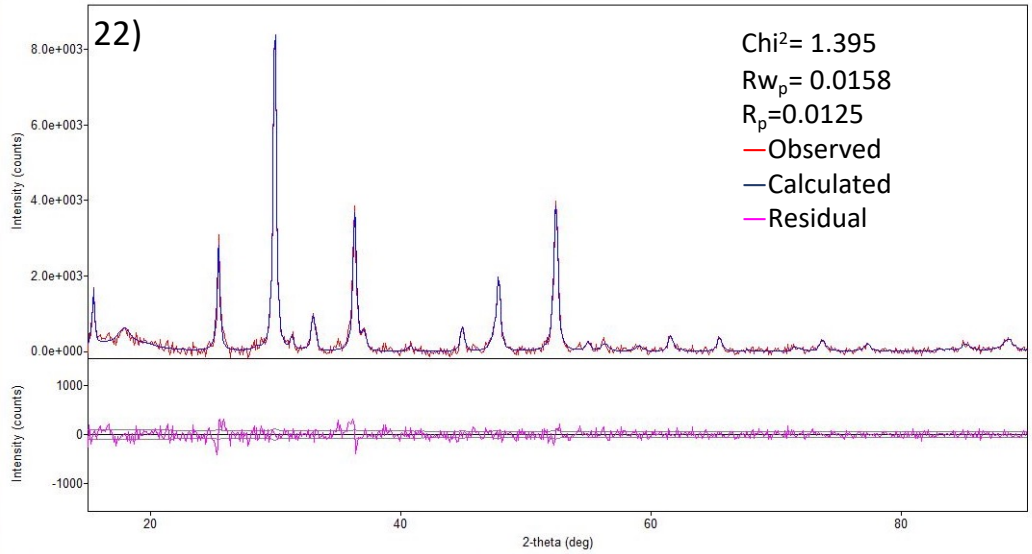
22)
Chi²= 1.395
Rwp= 0.0158
Rp=0.0125
Observed
Calculated
Residual
Intensity (counts)
2-theta (deg)

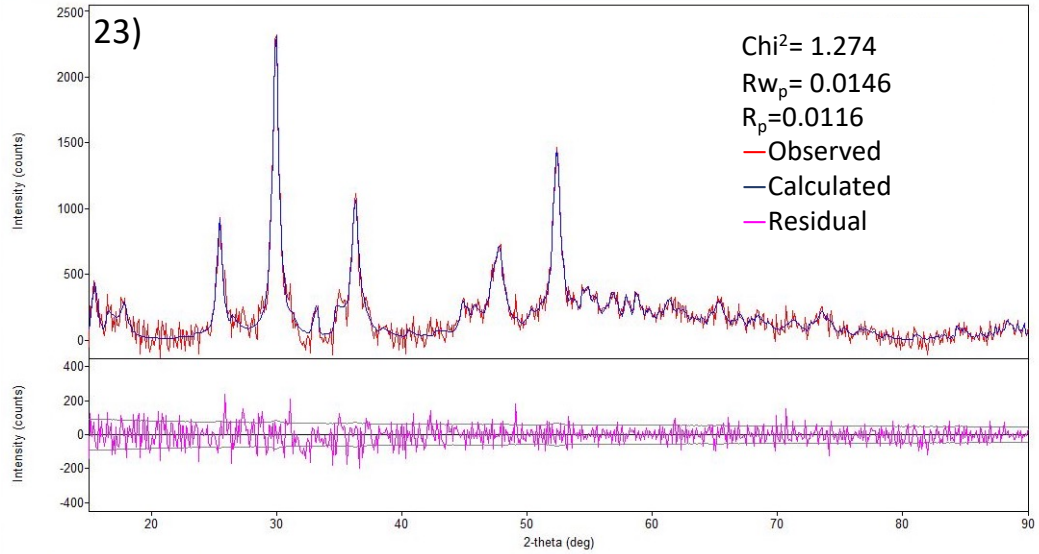
23)
Chi²= 1.274
Rwp= 0.0146
Rp=0.0116
Observed
Calculated
Residual
Intensity (counts)
2-theta (deg)

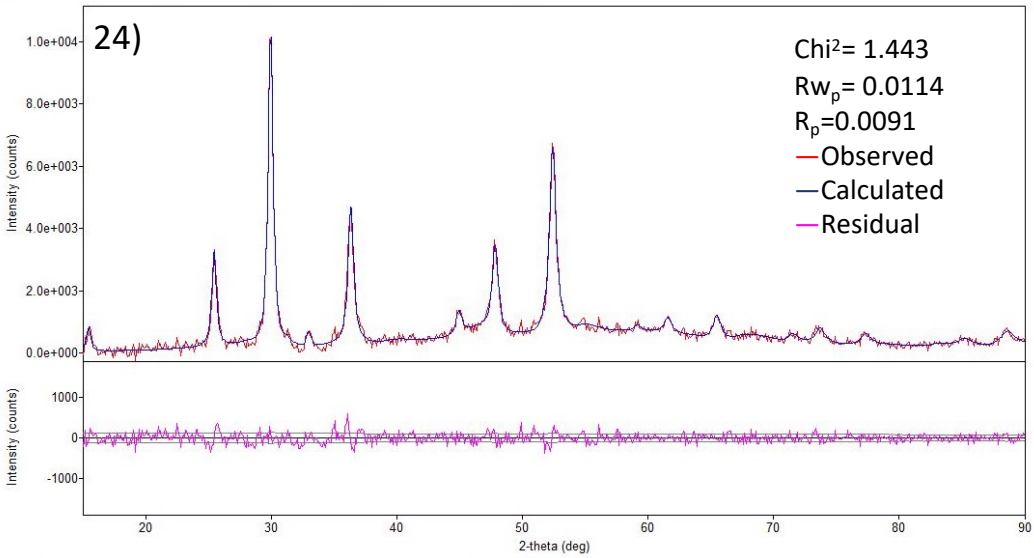
24)
Chi²= 1.443
Rwp= 0.0114
Rp=0.0091
Observed
Calculated
Residual
Intensity (counts)
2-theta (deg)

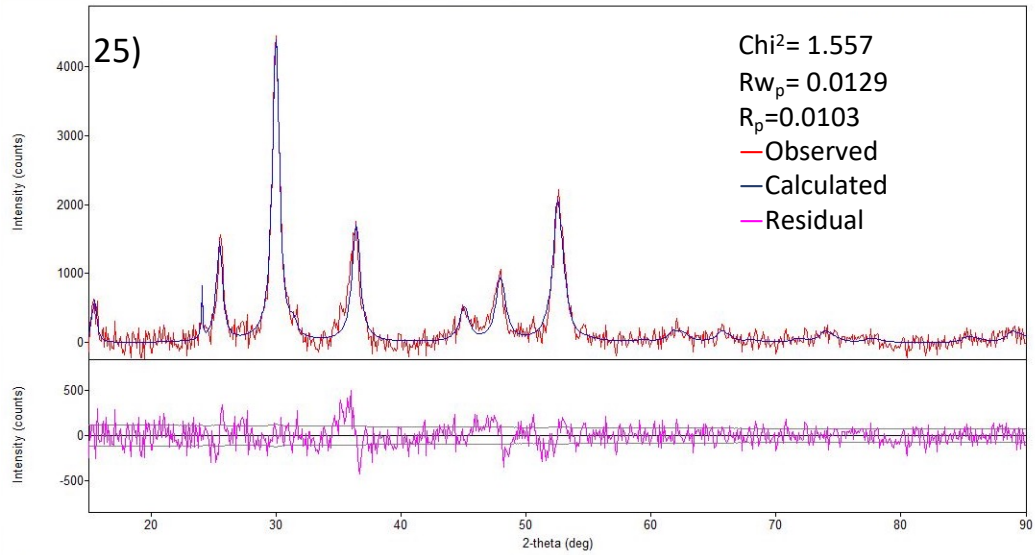
25)
Chi²= 1.557
Rwp= 0.0129
Rp=0.0103
Observed
Calculated
Residual
Intensity (counts)
2-theta (deg)

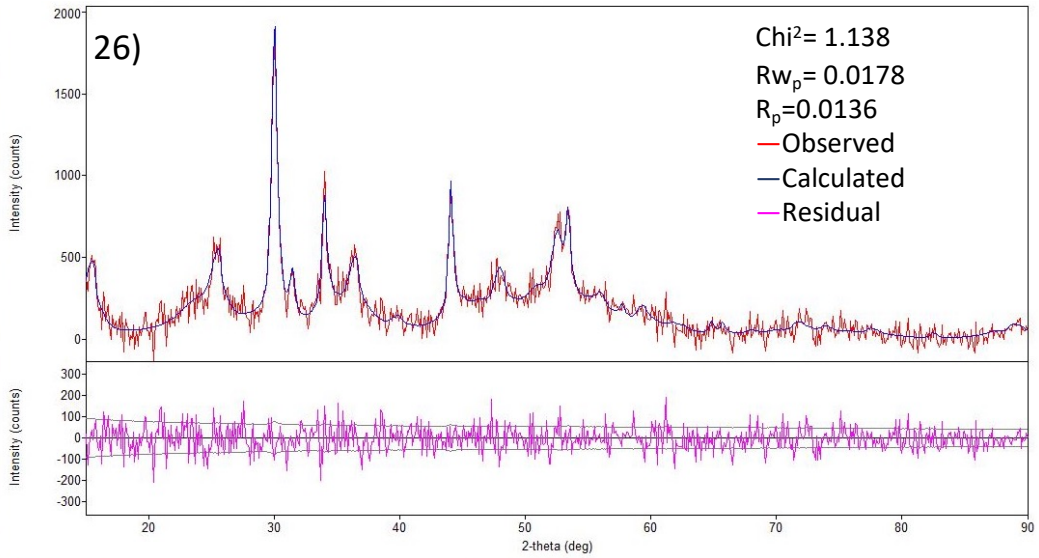
26)
Chi²= 1.138
Rwp= 0.0178
Rp=0.0136
Observed
Calculated
Residual
Intensity (counts)
2-theta (deg)

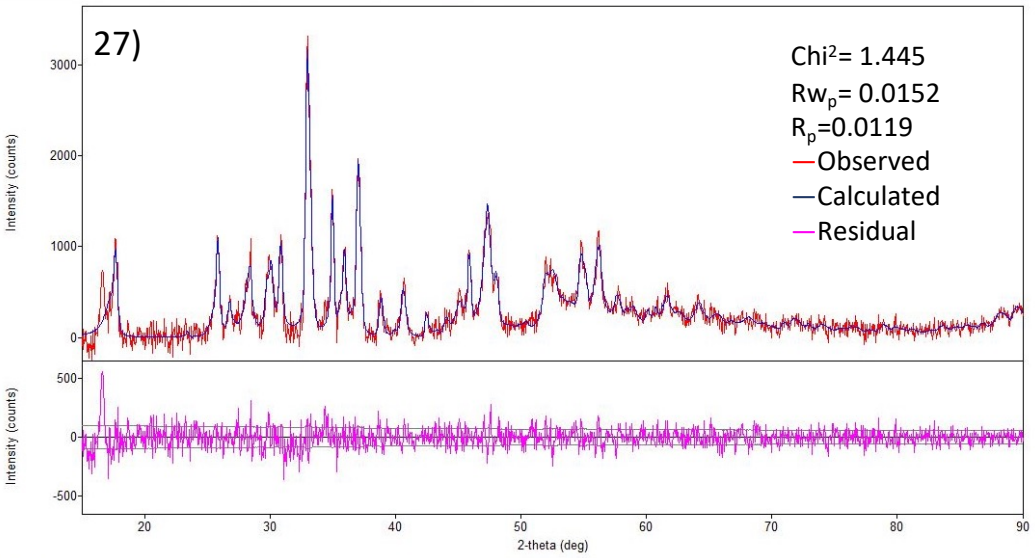
27)
Chi²= 1.445
Rwp= 0.0152
Rp=0.0119
Observed
Calculated
Residual
Intensity (counts)
2-theta (deg)

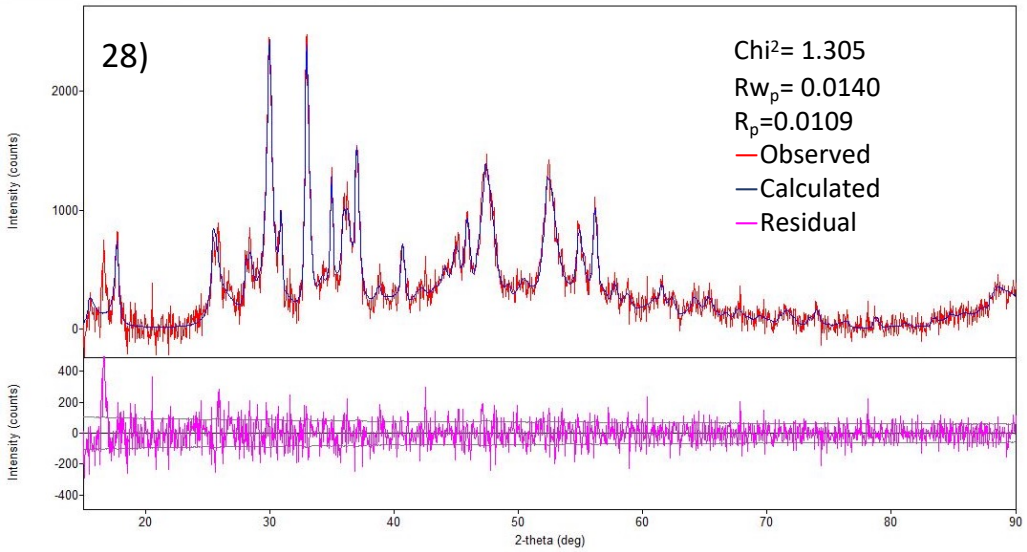
28)
Chi²= 1.305
Rwp= 0.0140
Rp=0.0109
Observed
Calculated
Residual
Intensity (counts)
2-theta (deg)

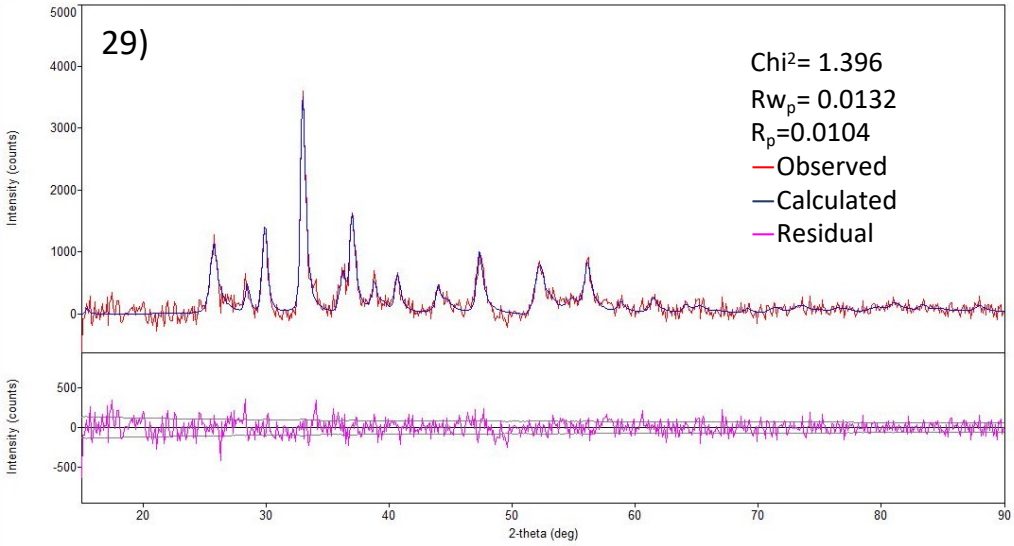
29)
Chi²= 1.396
Rwp= 0.0132
Rp=0.0104
Observed
Calculated
Residual
Intensity (counts)
2-theta (deg)

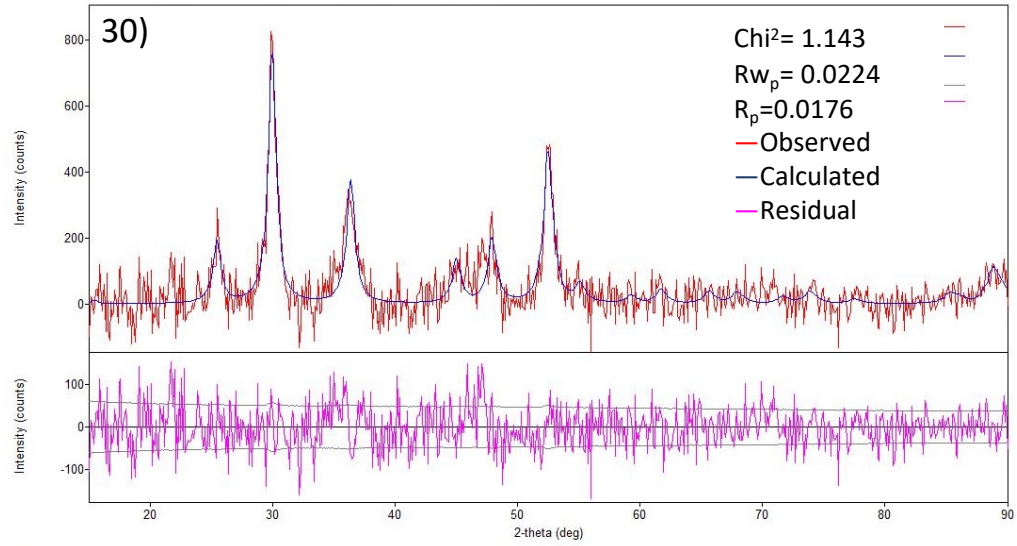
30)
Chi²= 1.143
Rwp= 0.0224
Rp=0.0176
Observed
Calculated
Residual
Intensity (counts)
2-theta (deg)

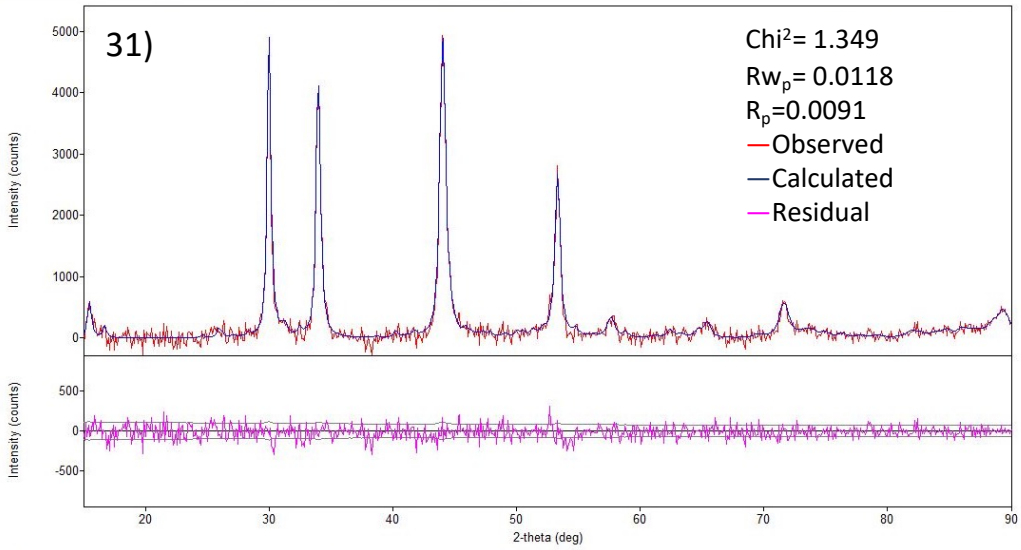
31)
Chi²= 1.349
Rwp= 0.0118
Rp=0.0091
Observed
Calculated
Residual
Intensity (counts)
2-theta (deg)

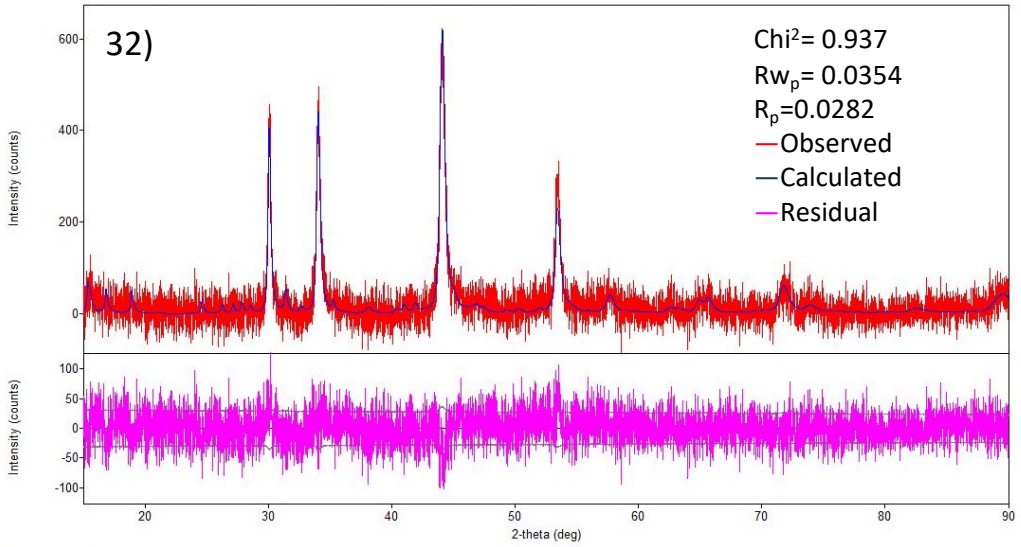
32)
Chi²= 0.937
Rwp= 0.0354
Rp=0.0282
Observed
Calculated
Residual
Intensity (counts)
2-theta (deg)

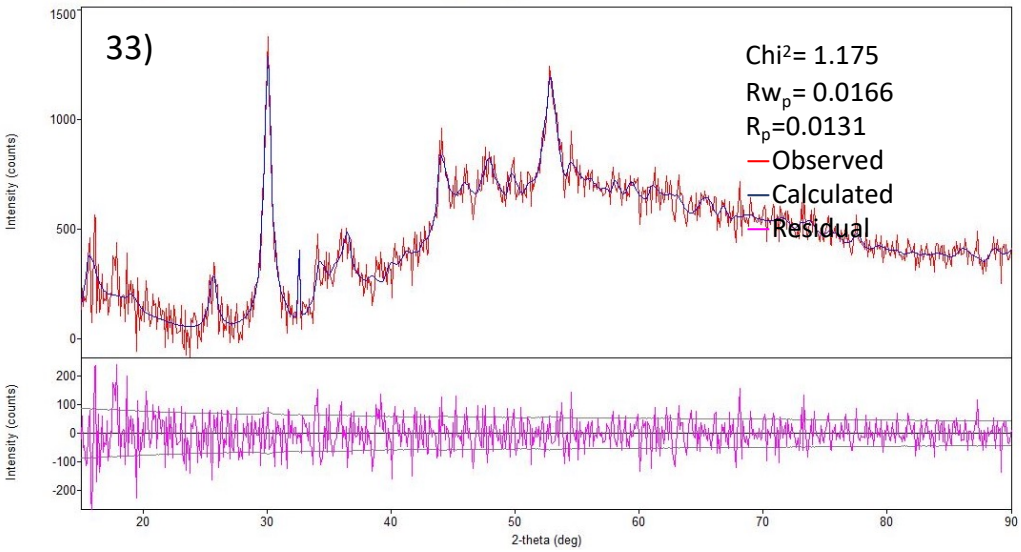
33)
Chi²= 1.175
Rwp= 0.0166
Rp=0.0131
Observed
Calculated
Residual
Intensity (counts)
2-theta (deg)

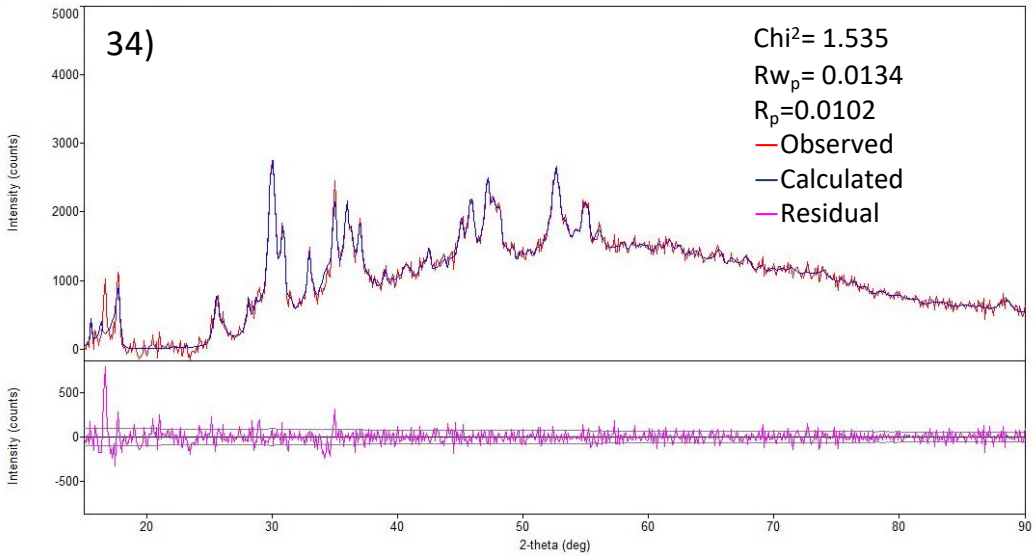
34)
Chi²= 1.535
Rwp= 0.0134
Rp=0.0102
Observed
Calculated
Residual
Intensity (counts)
2-theta (deg)

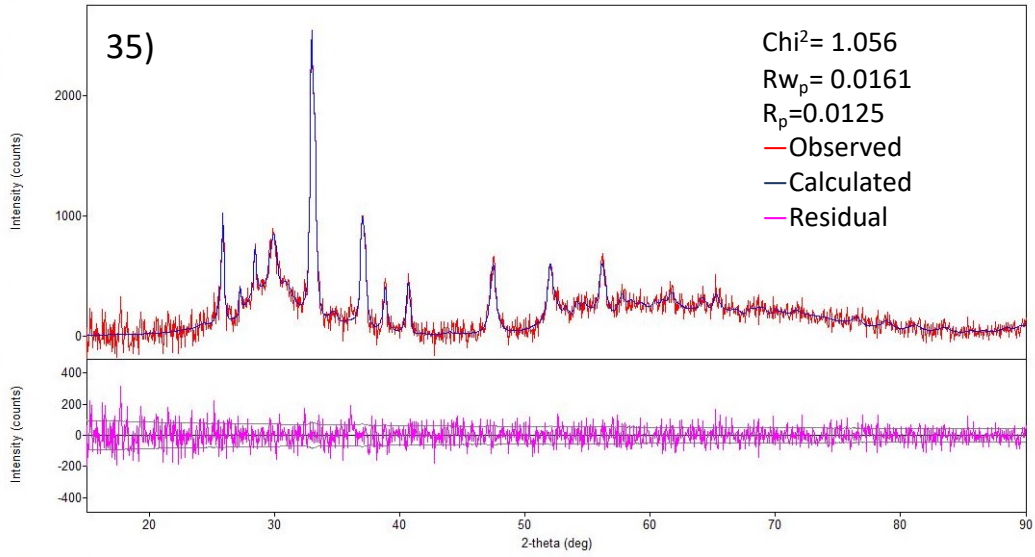
35)
Chi²= 1.056
Rwp= 0.0161
Rp=0.0125
Observed
Calculated
Residual
Intensity (counts)
2-theta (deg)

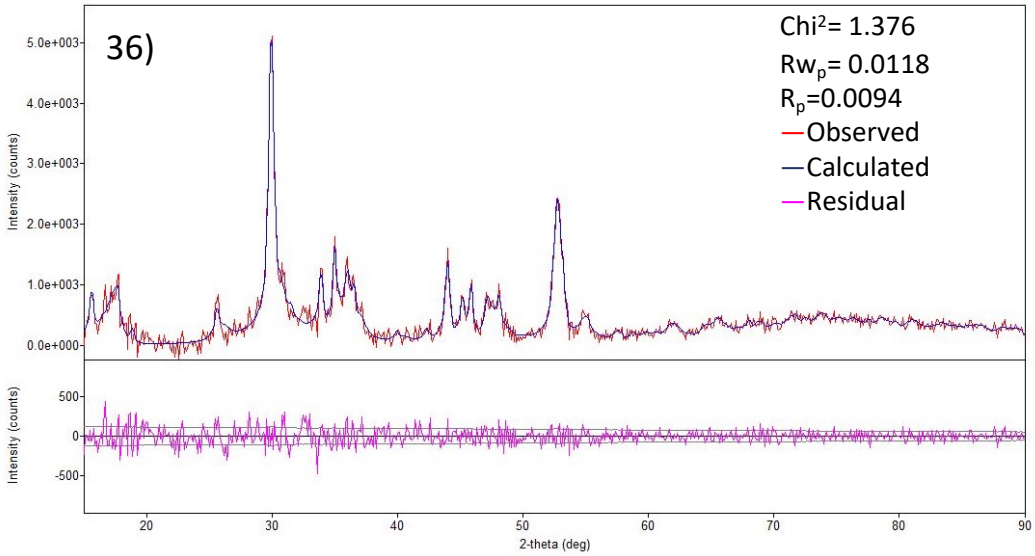
36)
Chi²= 1.376
Rwp= 0.0118
Rp=0.0094
Observed
Calculated
Residual
Intensity (counts)
2-theta (deg)

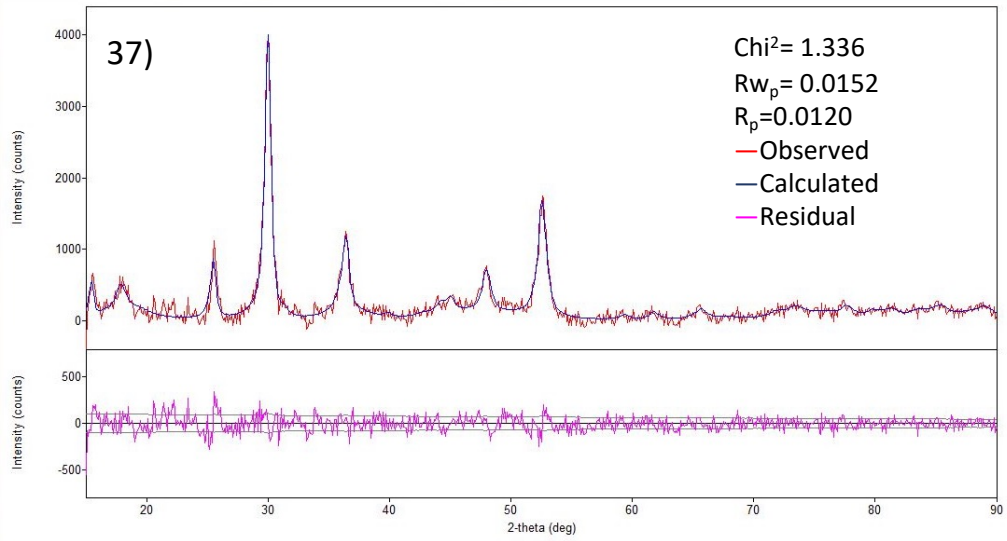
37)
Chi²= 1.336
Rwp= 0.0152
Rp=0.0120
Observed
Calculated
Residual
Intensity (counts)
2-theta (deg)

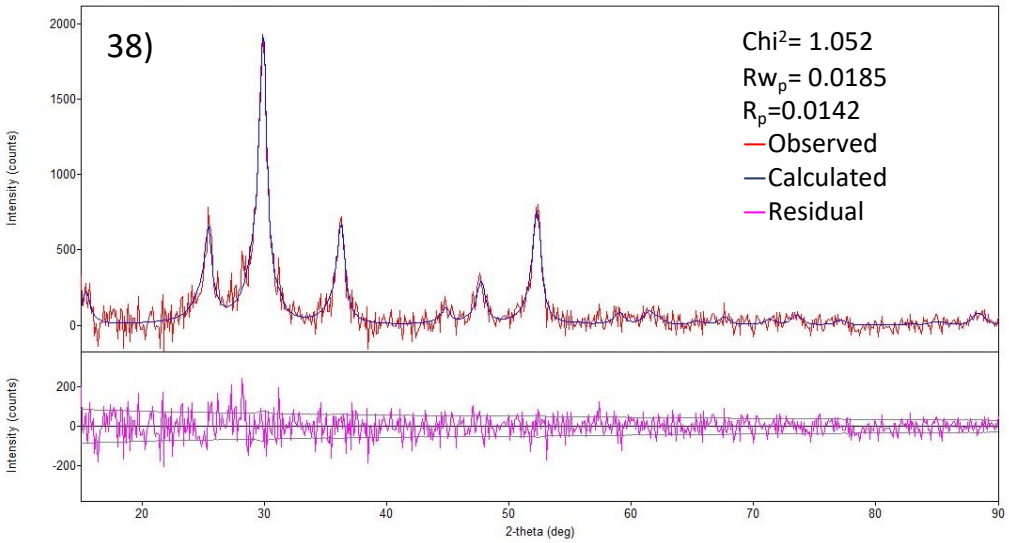
38)
Chi²= 1.052
Rwp= 0.0185
Rp=0.0142
Observed
Calculated
Residual
Intensity (counts)
2-theta (deg)

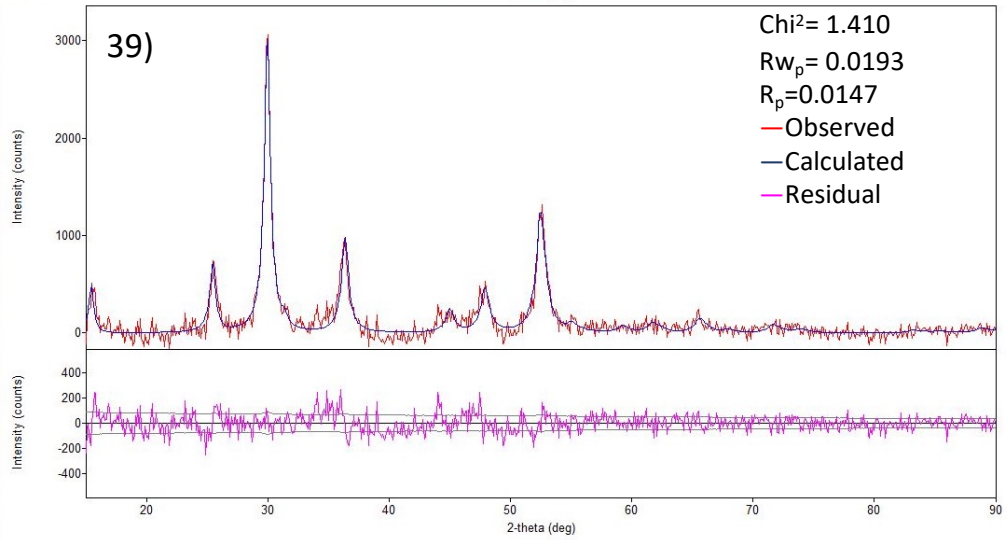
39)
Chi²= 1.410
Rwp= 0.0193
Rp=0.0147
Observed
Calculated
Residual
Intensity (counts)
2-theta (deg)

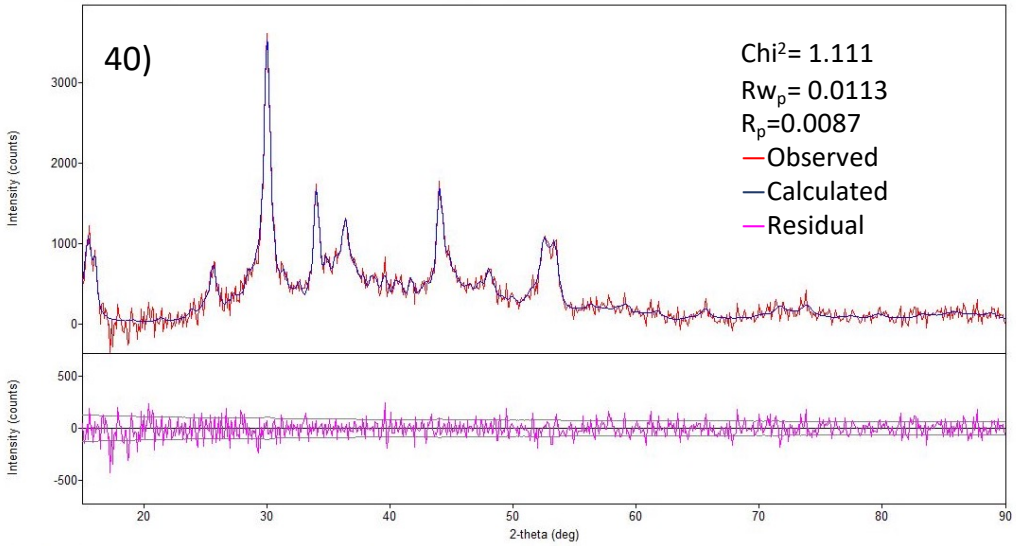
40)
Chi²= 1.111
Rwp= 0.0113
Rp=0.0087
Observed
Calculated
Residual
Intensity (counts)
2-theta (deg)

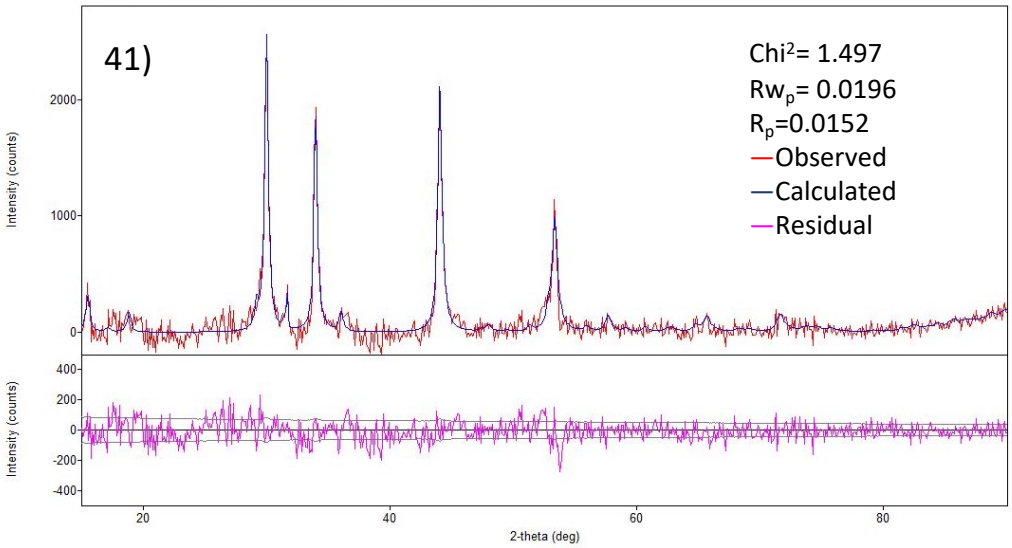
41)
Chi²= 1.497
Rwp= 0.0196
Rp=0.0152
Observed
Calculated
Residual
Intensity (counts)
2-theta (deg)

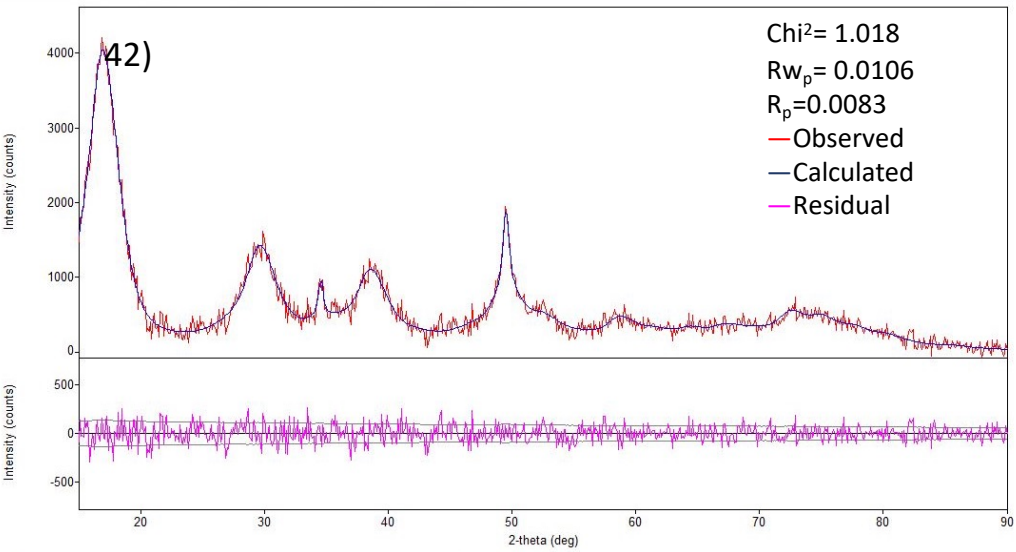
42)
Chi²= 1.018
Rwp= 0.0106
Rp=0.0083
Observed
Calculated
Residual
Intensity (counts)
2-theta (deg)

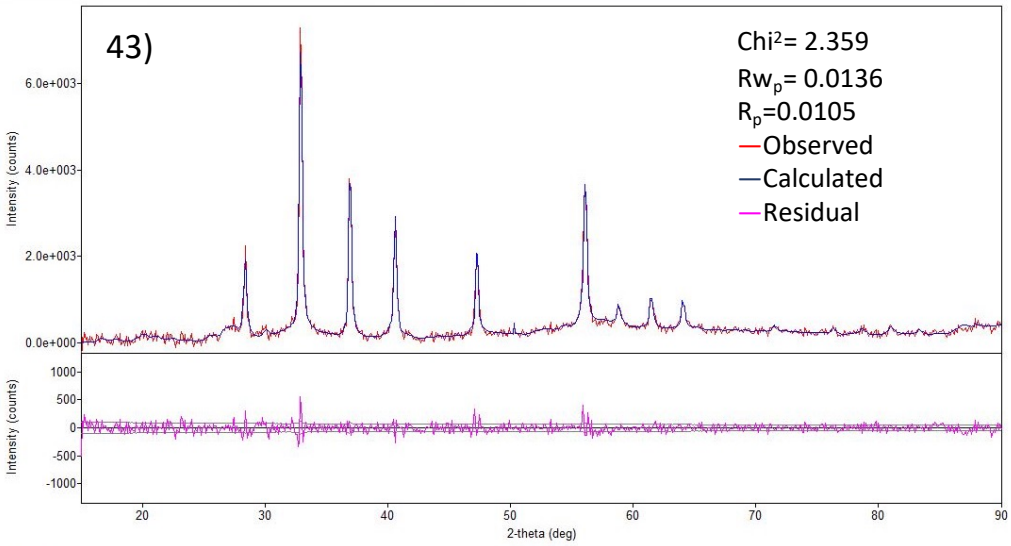
43)
Chi²= 2.359
Rwp= 0.0136
Rp=0.0105
Observed
Calculated
Residual
Intensity (counts)
2-theta (deg)

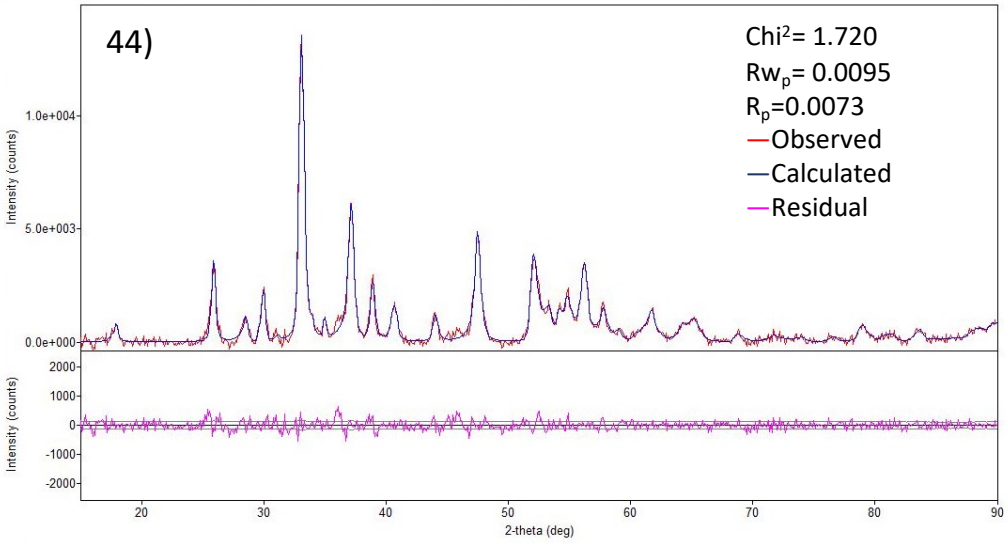
44)
Chi²= 1.720
Rwp= 0.0095
Rp=0.0073
Observed
Calculated
Residual
Intensity (counts)
2-theta (deg)

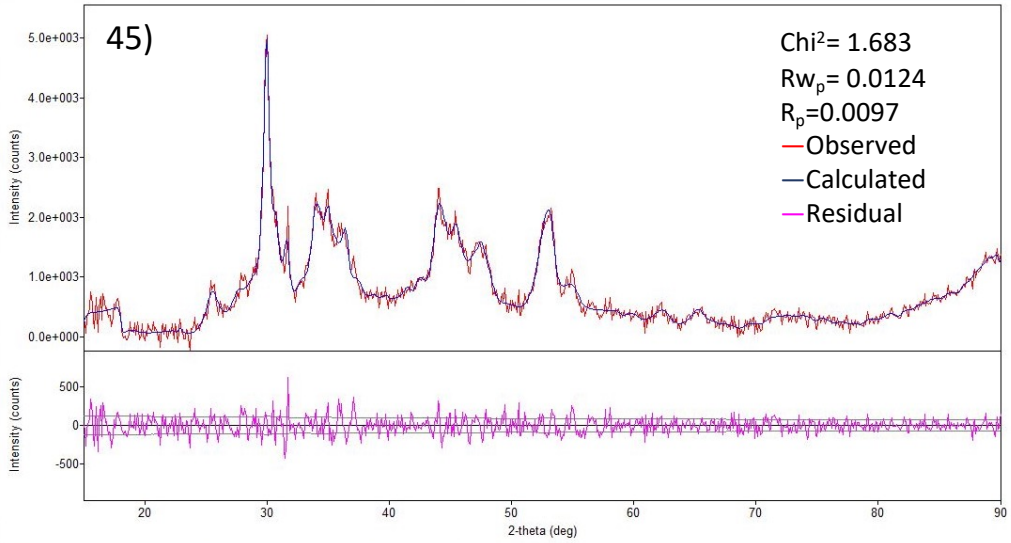
45)
Chi²= 1.683
Rwp= 0.0124
Rp=0.0097
Observed
Calculated
Residual
Intensity (counts)
2-theta (deg)

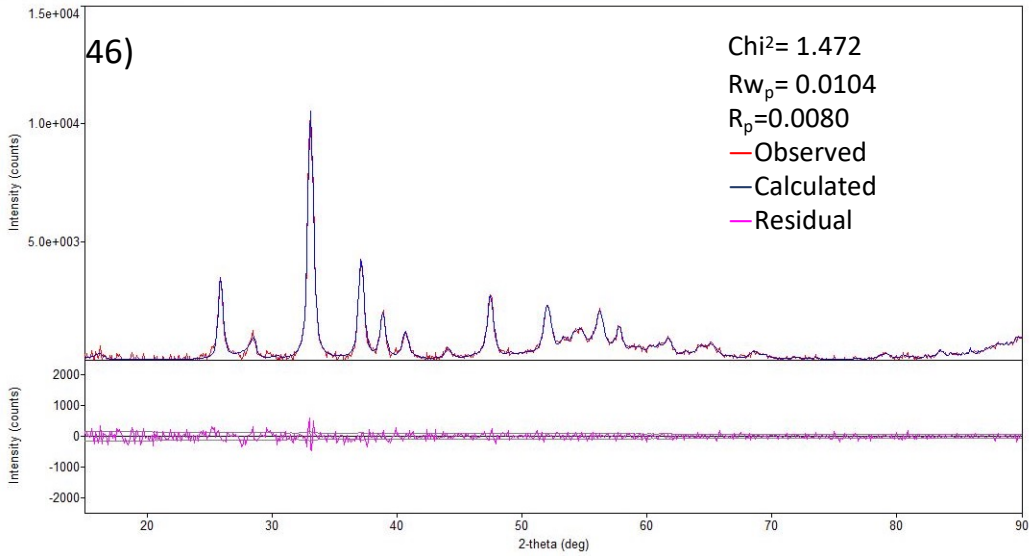

Figure A.9 Reitveld Refinements corresponding to **Table S1**, included in each is the experimental (red) and calculated curves (blue) as well as the difference curves (pink)

References

(1) Hendricks, M. P.; Campos, M. P.; Cleveland, G. T.; Plante, I. J.-L.; Owen, J. S. A Tunable library of substituted thiourea precursors to metal sulfide nanocrystals. *Science* **2015**, *348* (6240), 1226-1230. DOI: 10.1126/science.aaa2951.

(2) Rotondo, A.; Barresi, S.; Cusumano, M.; Rotondo, E.; Donato, P.; Mondello, L. NMR characterisation and dynamic behaviour of [Pt(bipy)(R-Thiourea)2]Cl2 and [Pt(phen)(R-Thiourea)2]Cl2 complexes. *Inorganica Chimica Acta* **2014**, *410*, 1-10. DOI: 10.1016/j.ica.2013.10.014.

(3) Csákberényi-Malasics, D.; Rodriguez-Blanco, J. D.; Kis, V. K.; Rečnik, A.; Benning, L. G.; Pósfai, M. Structural properties and transformations of precipitated FeS. *Chemical Geology* **2012**, *294-295*, 249-258. DOI: 10.1016/j.chemgeo.2011.12.009.

Appendix A Supplemental Figures for Chapter 3

Table S3.1

	Solvent	T(°C)	Thiourea	S:Ni	Time	Catteirite (CoS_2)	Linnaeite (Co_3S_4)	Cobaltpentlandite (Co_9S_8)	Jaipurite (CoS)
1	ODE	170	Thiourea	6 to 1	1 h	98%			2%
2	ODE	170	Methyl Thiourea	6 to 1	1 h	61%			39%
3	ODE	170	Phenyl Thiourea	6 to 1	1 h	27%	53%		19%
4	ODE	170	Diethyl Thiourea	6 to 1	1 h		45%		55%
5	ODE	170	Diphenyl Thiourea	6 to 1	1 h		58%	10%	32%
6	ODE	220	Thiourea	6 to 1	1 h	98%			2%
7	ODE	220	Methyl Thiourea	6 to 1	1 h	34%	37%		29%
8	ODE	220	Phenyl Thiourea	6 to 1	1 h		39%		61%
9	ODE	220	Diethyl Thiourea	6 to 1	1 h		30%		70%
s	ODE	220	Diphenyl Thiourea	6 to 1	1 h		47%		53%
11	ODE	270	Thiourea	6 to 1	1 h	66%			34%
12	ODE	270	Methyl Thiourea	6 to 1	1 h	30%	31%		39%
13	ODE	270	Phenyl Thiourea	6 to 1	1 h		55%		45%
14	ODE	270	Diethyl Thiourea	6 to 1	1 h		40%		60%
15	ODE	270	Diphenyl Thiourea	6 to 1	1 h		70%		30%
16	ODE	220	Thiourea	12 to 1	1 h	100%			
17	ODE	220	Diphenyl Thiourea followed by	6 to 1*	1 h		100%		
18	ODE	220	1-Hexyl-3-Phenyl Thiourea followed by Diphenyl Thiourea	0.5 to 1 Followed by 1 to 6	1 h			100%	
19	ODE	155	Diethyl Thiourea	18 to 1	1 h				100%

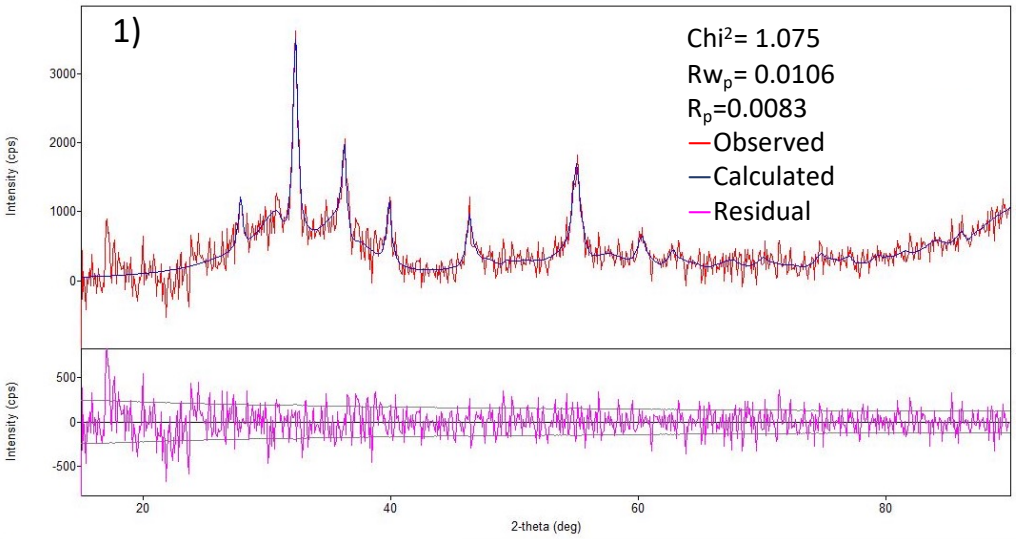
1)
Chi²= 1.075
Rwp= 0.0106
Rp=0.0083
Observed
Calculated
Residual
Intensity (cps)
2-theta (deg)

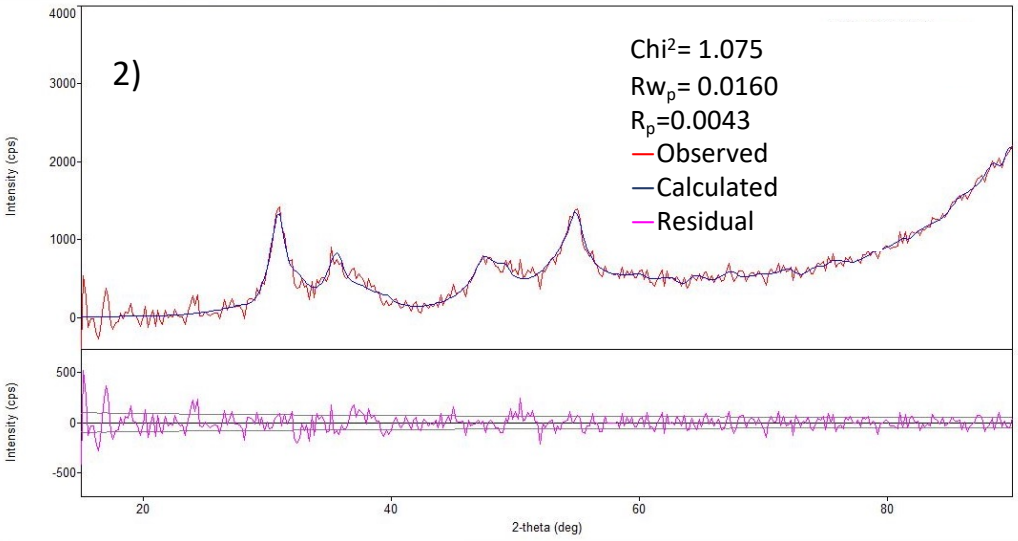
2)
Chi²= 1.075
Rwp= 0.0160
Rp=0.0043
Observed
Calculated
Residual
Intensity (cps)
2-theta (deg)

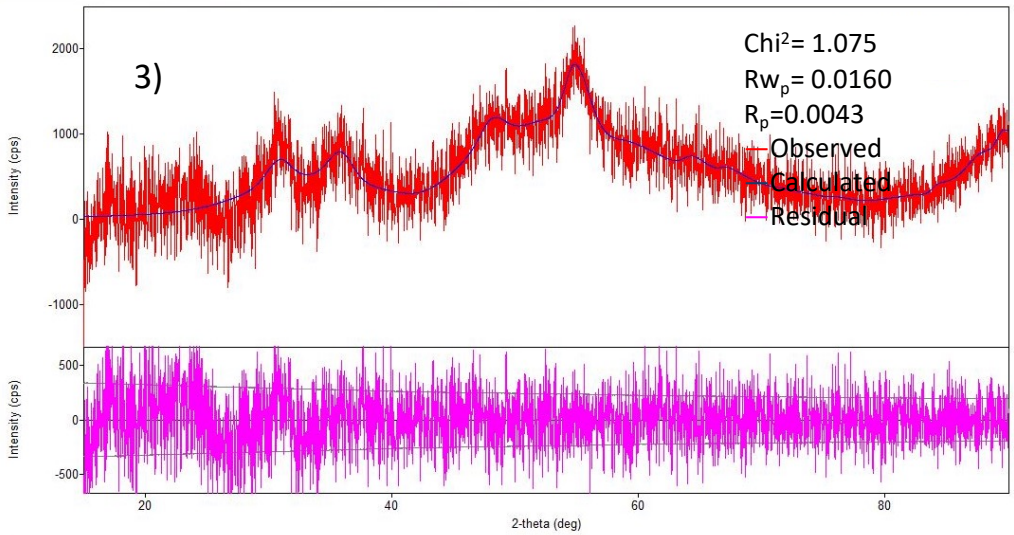
3)
Chi²= 1.075
Rwp= 0.0160
Rp=0.0043
Observed
Calculated
Residual
Intensity (cps)
2-theta (deg)

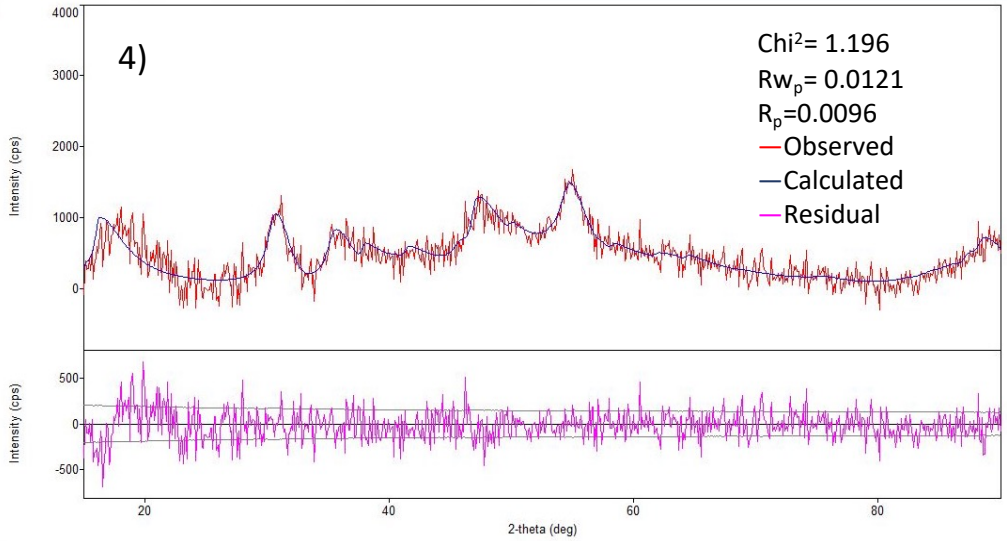
4)
Chi²= 1.196
Rwp= 0.0121
Rp=0.0096
Observed
Calculated
Residual
Intensity (cps)
2-theta (deg)

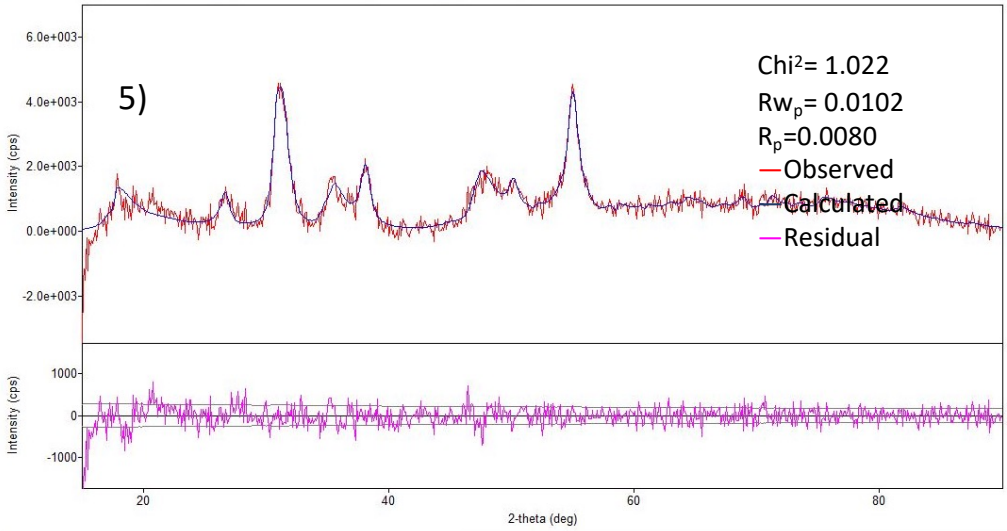
5)
Chi²= 1.022
Rwp= 0.0102
Rp=0.0080
Observed
Calculated
Residual
Intensity (cps)
2-theta (deg)

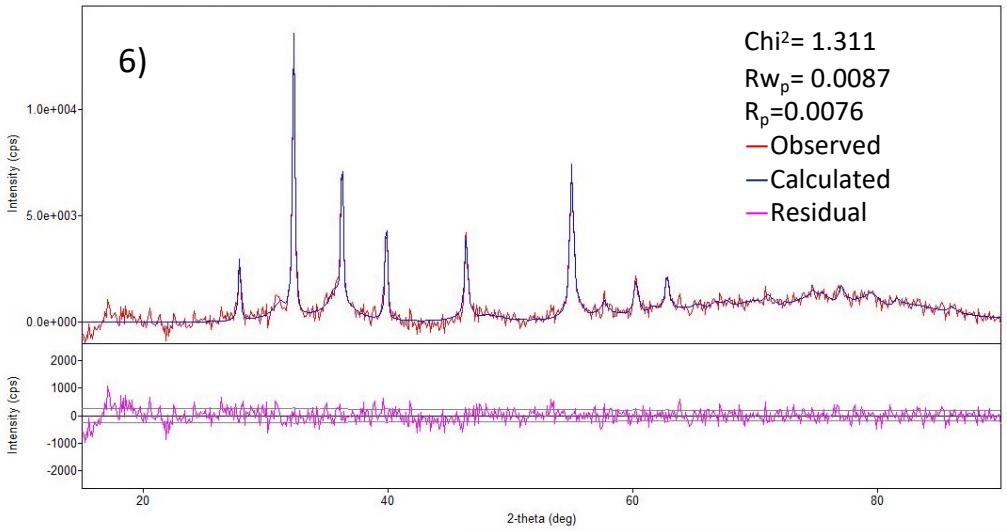
6)
Chi²= 1.311
Rwp= 0.0087
Rp=0.0076
Observed
Calculated
Residual
Intensity (cps)
2-theta (deg)

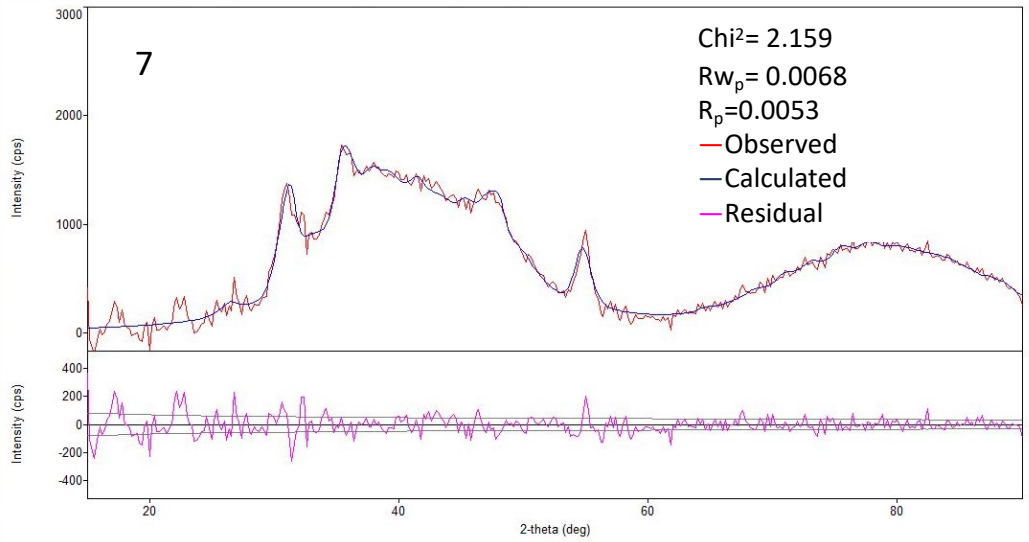
7
Chi²= 2.159
Rwp= 0.0068
Rp=0.0053
Observed
Calculated
Residual
Intensity (cps)
2-theta (deg)

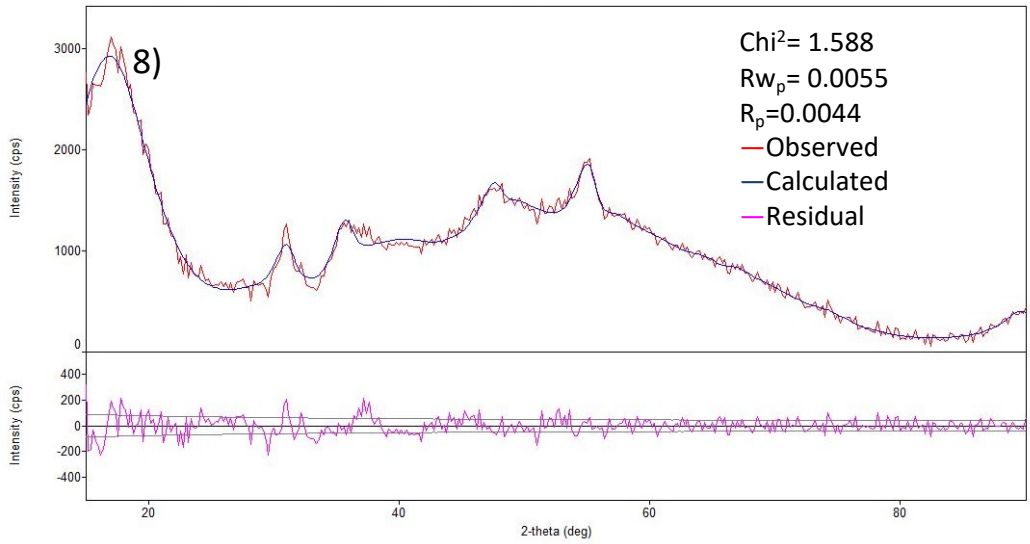
8)
Chi²= 1.588
Rwp= 0.0055
Rp=0.0044
Observed
Calculated
Residual
Intensity (cps)
2-theta (deg)

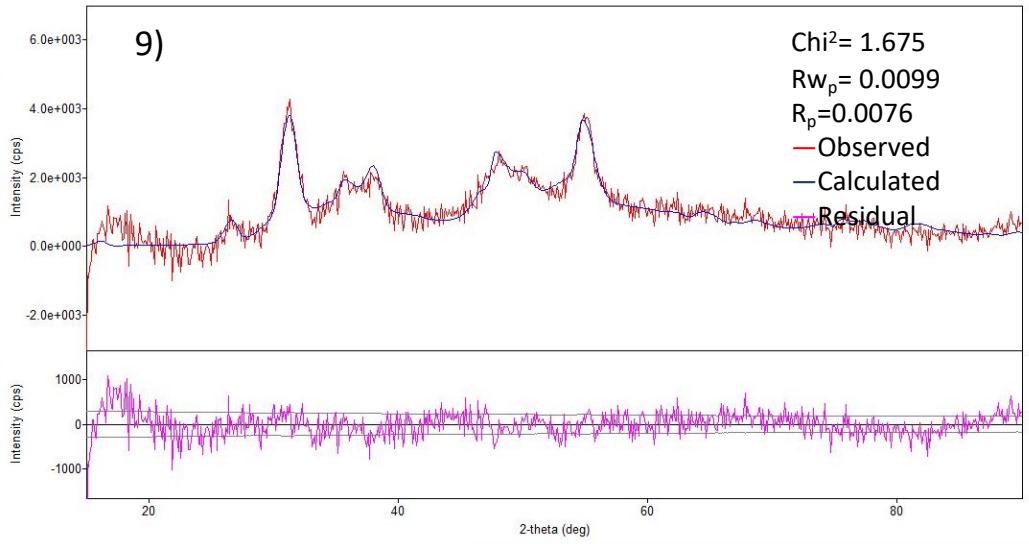
9)
Chi²= 1.675
Rwp= 0.0099
Rp=0.0076
Observed
Calculated
Residual
Intensity (cps)
2-theta (deg)

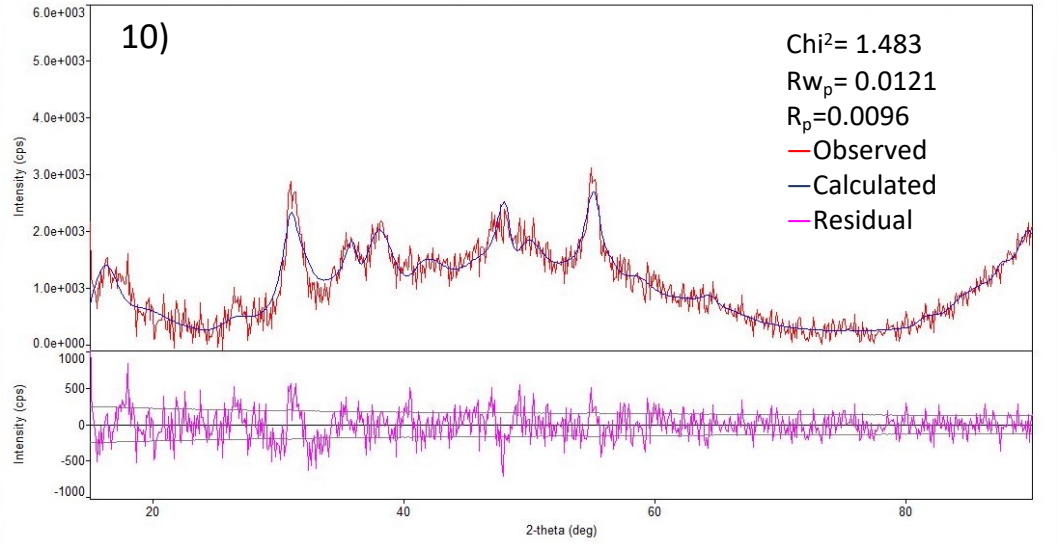
10)
Chi²= 1.483
Rwp= 0.0121
Rp=0.0096
Observed
Calculated
Residual
Intensity (cps)
2-theta (deg)

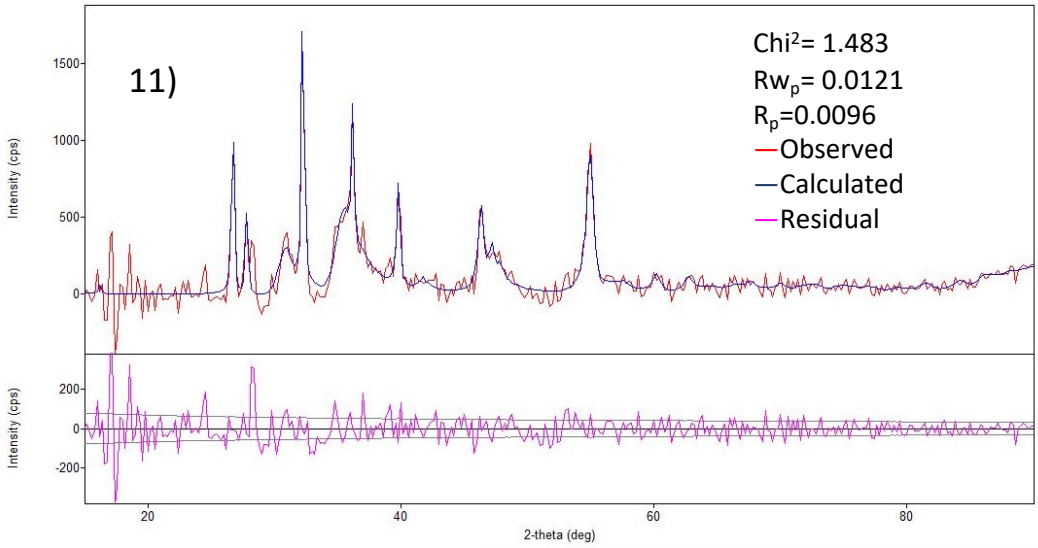
11)
Chi²= 1.483
Rwp= 0.0121
Rp=0.0096
Observed
Calculated
Residual
Intensity (cps)
2-theta (deg)

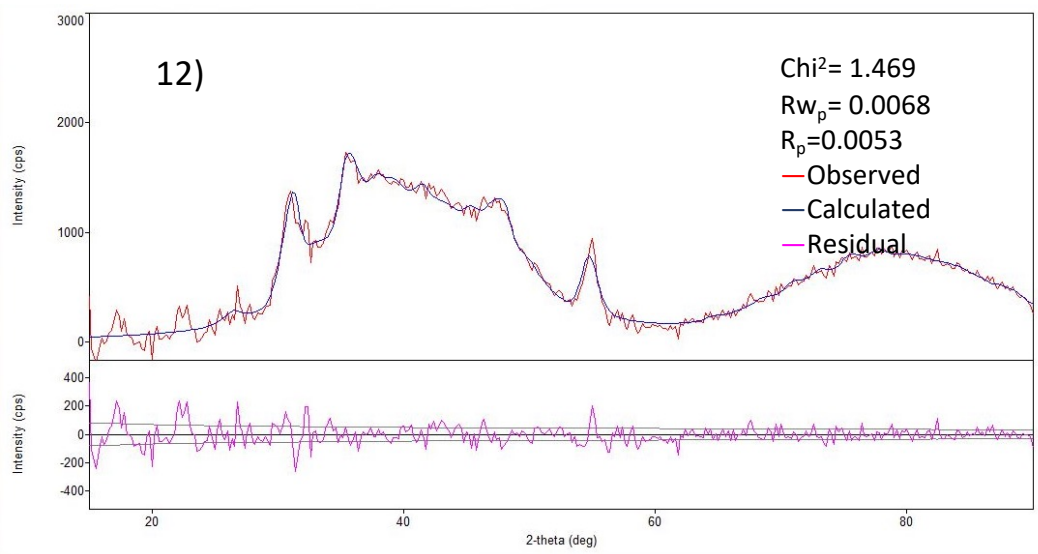
12)
Chi²= 1.469
Rwp= 0.0068
Rp=0.0053
Observed
Calculated
Residual
Intensity (cps)
2-theta (deg)

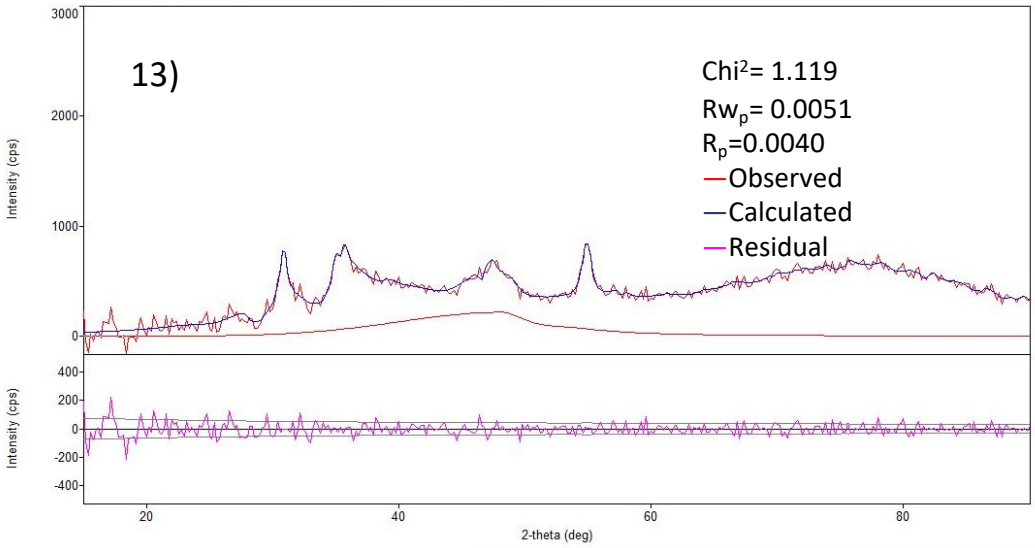
13)
Chi²= 1.119
Rwp= 0.0051
Rp=0.0040
Observed
Calculated
Residual
Intensity (cps)
2-theta (deg)

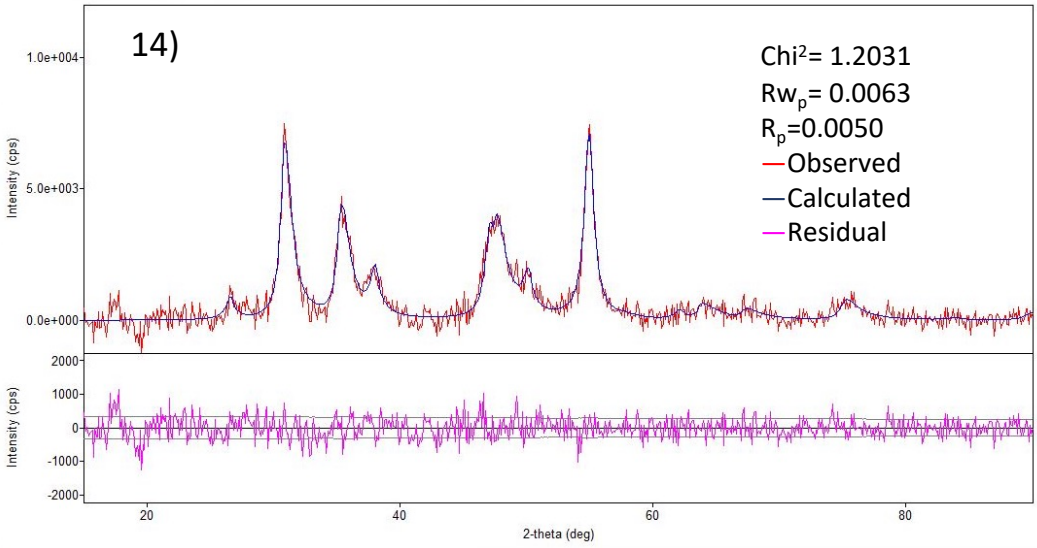
14)
Chi²= 1.2031
Rwp= 0.0063
Rp=0.0050
Observed
Calculated
Residual
Intensity (cps)
2-theta (deg)

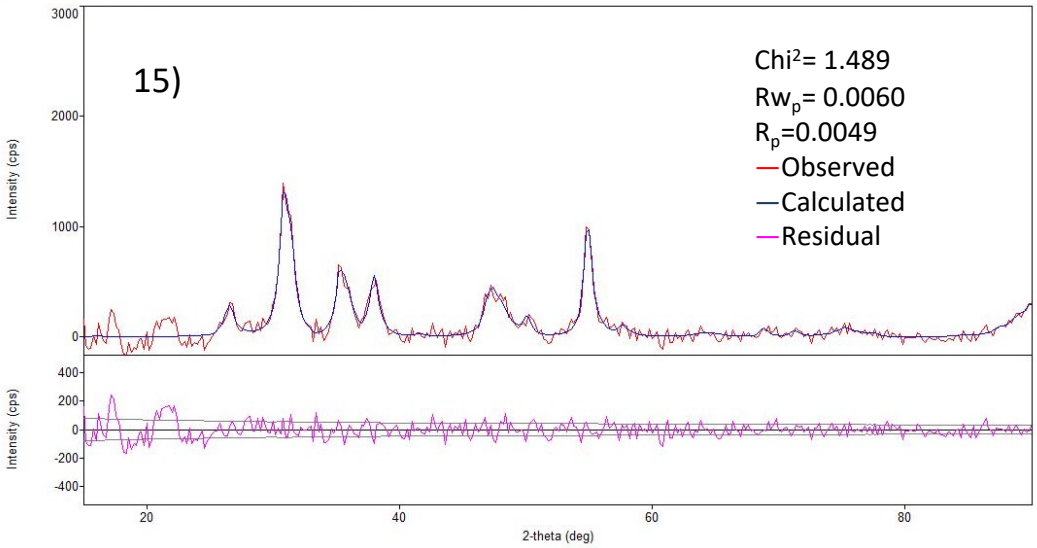
15)
Chi²= 1.489
Rwp= 0.0060
Rp=0.0049
Observed
Calculated
Residual
Intensity (cps)
2-theta (deg)

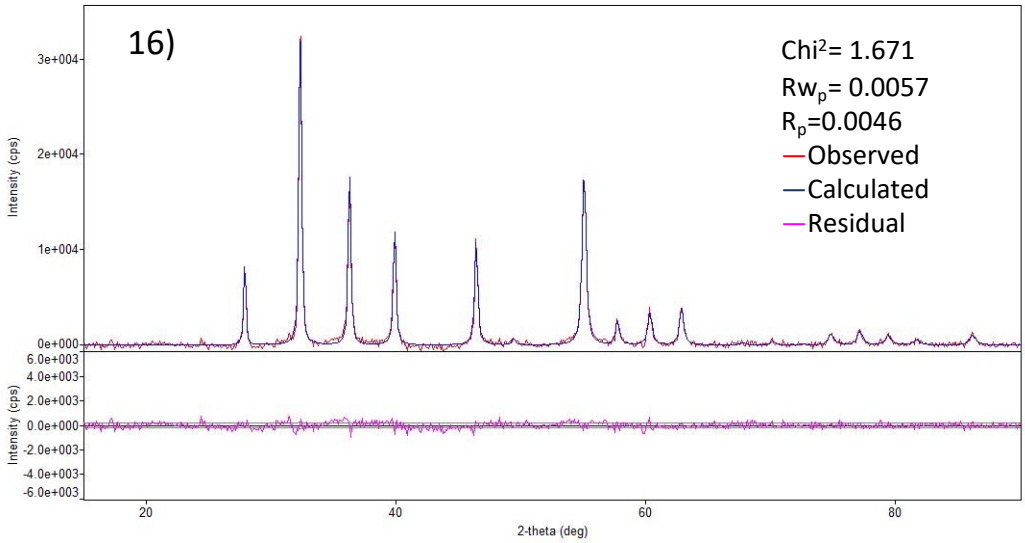
16)
Chi²= 1.671
Rwp= 0.0057
Rp=0.0046
Observed
Calculated
Residual
Intensity (cps)
2-theta (deg)

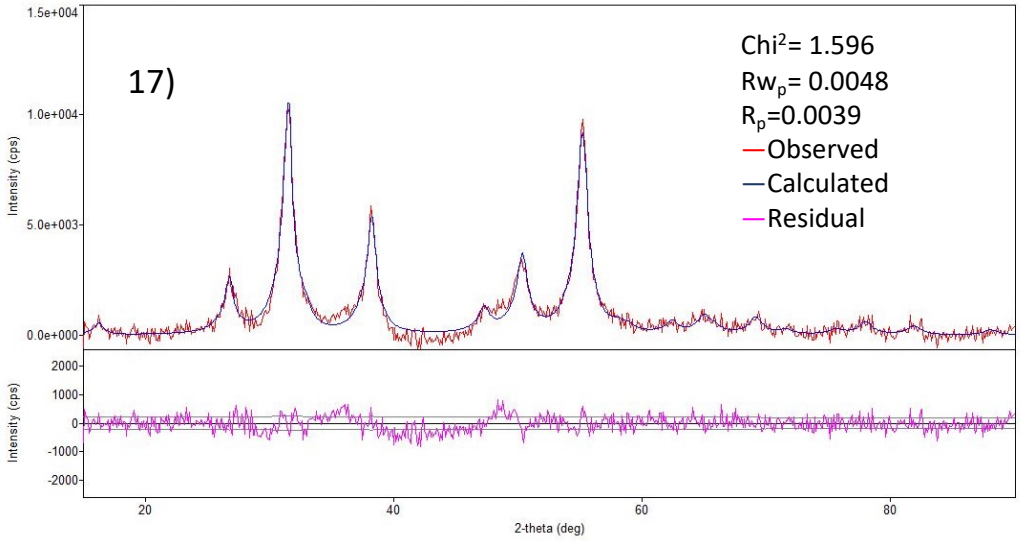
17)
Chi²= 1.596
Rwp= 0.0048
Rp=0.0039
Observed
Calculated
Residual
Intensity (cps)
2-theta (deg)

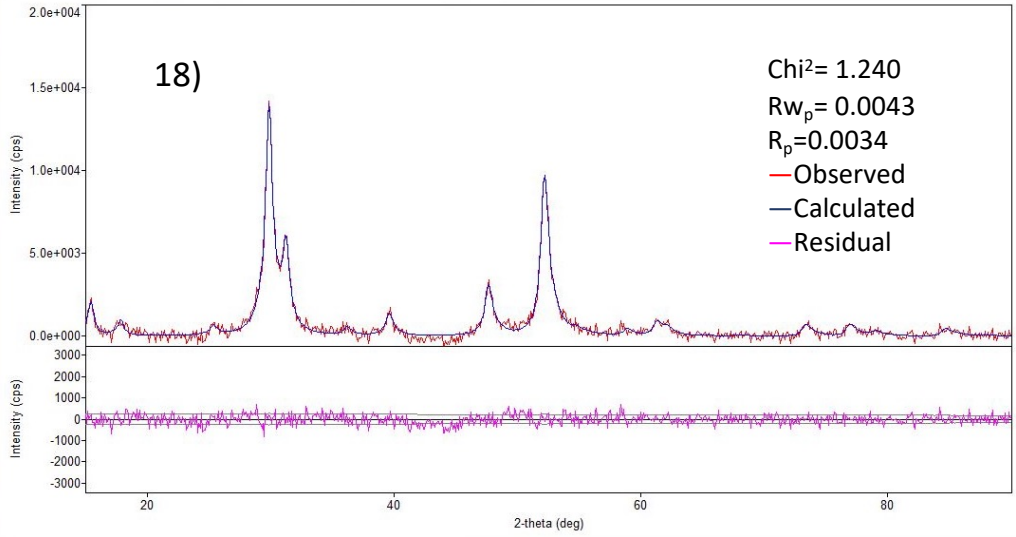
18)
Chi²= 1.240
Rwp= 0.0043
Rp=0.0034
Observed
Calculated
Residual
Intensity (cps)
2-theta (deg)

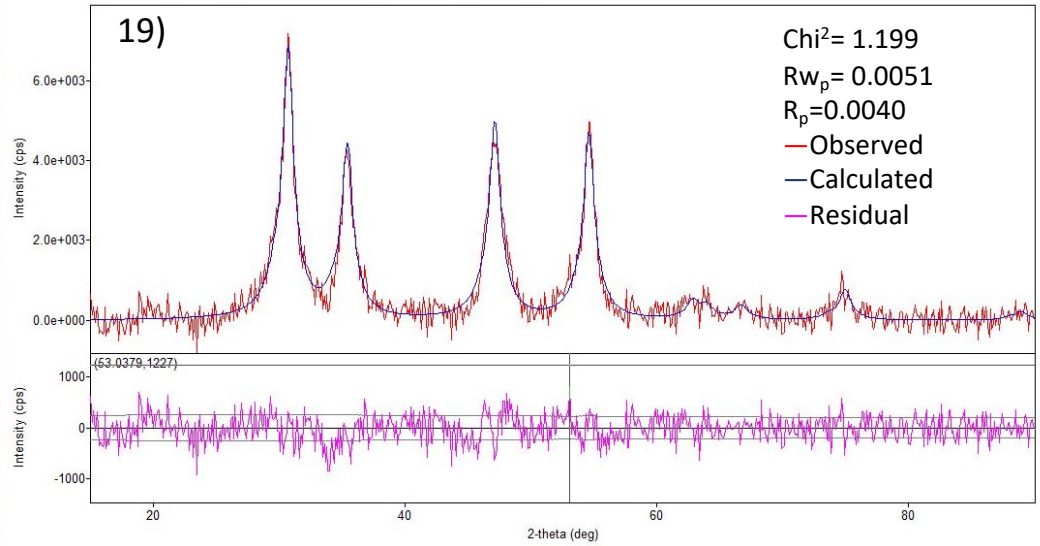

Figure B.1 Rietveld refinements of the cobalt sulfides from table **Table B.1**, included in each is the experimental (red) and calculated curves (blue) as well as the difference curves (pink)

Table C.1

	Solvent	T(°C)	Thiourea	S:Ni	Time	NiS	Vaesite	Millerite	Heazlewoodite	Godlevskite	Polydimite
1	ODE	170	Thiourea	6 to 1	1 h	100%					
2	ODE	170	Methyl Thiourea	6 to 1	1 h	100%					
3	ODE	170	Phenyl Thiourea	6 to 1	1 h	100%					
4	ODE	170	Diethyl Thiourea	6 to 1	1 h	100%					
5	ODE	170	Diphenyl Thiourea	6 to 1	1 h	100%					
6	ODE	220	Thiourea	6 to 1	1 h	48.4%	51.6%				
7	ODE	220	Methyl Thiourea	6 to 1	1 h	69.2%	30.8%				
8	ODE	220	Phenyl Thiourea	6 to 1	1 h	65.7%	34.3%				
9	ODE	220	Diethyl Thiourea	6 to 1	1 h	100%					
s	ODE	220	Diphenyl Thiourea	6 to 1	1 h	100%					
11	ODE	270	Thiourea	6 to 1	1 h	64.6%	35.4%				
12	ODE	270	Methyl Thiourea	6 to 1	1 h	57.1%	42.9%				
13	ODE	270	Phenyl Thiourea	6 to 1	1 h	59.3%	40.7%				
14	ODE	270	Diethyl Thiourea	6 to 1	1 h	100%					
15	ODE	270	Diphenyl Thiourea	6 to 1	1 h	100%					
16	ODE	270	1-Hexyl-3-Phenyl-2-Thiourea	6 to 1	1 h	86.3%		13.7%			
17	ODE	270	1-Hexyl-3-Phenyl-2-Thiourea	2 to 1	1 h	23.6%		76.4%			
18	ODE	270	1-Hexyl-3-Phenyl-2-Thiourea	1 to 1	1 h	7.4%		53.7%	22.4%	16.5%	
19	ODE	250	Diphenyl Thiourea	1 to 1	2 h			51.9%		48.1%	
20	ODE	260	Diphenyl Thiourea	1 to 1	2 h			25.8%		74.2%	
21	ODE	270	Diphenyl Thiourea	1 to 1	2 h				28.7%	71.3%	
22	ODE	295	Diphenyl Thiourea	1 to 1	2 h				100%		
23	ODE	270	1-Hexyl-3-Phenyl-2-Thiourea	1 to 1	1 min	100%					
24	ODE	250	Diphenyl Thiourea	1 to 1	4 h					100%	
25	ODE	220	Phenyl Thiourea	18 to 1	1 h		100%				
26	OLAM	220	1-Hexyl-3-Phenyl-2-Thiourea	1.7 to 1	1 h			100%			
27	OLAM	310	Diphenyl Thiourea	0.75 to 1	2 h				100%		
28	ODE	290 followed by 200	1-Hexyl-3-Phenyl-2-Thiourea followed by Phenyl Thiourea	1 to 1 followed by	2 h then 10 min						100%

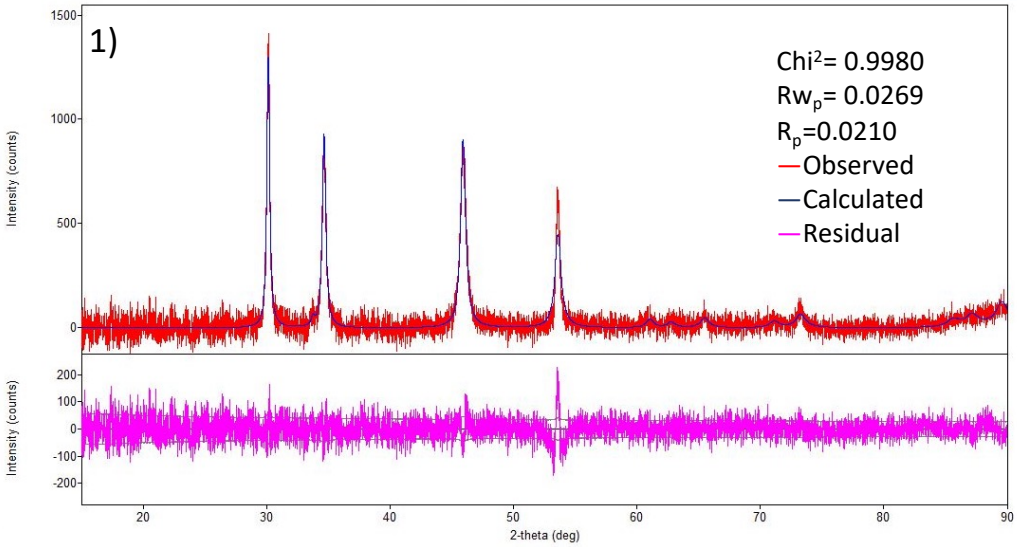
1)
Chi²= 0.9980
Rwp= 0.0269
Rp=0.0210
Observed
Calculated
Residual
Intensity (counts)
2-theta (deg)

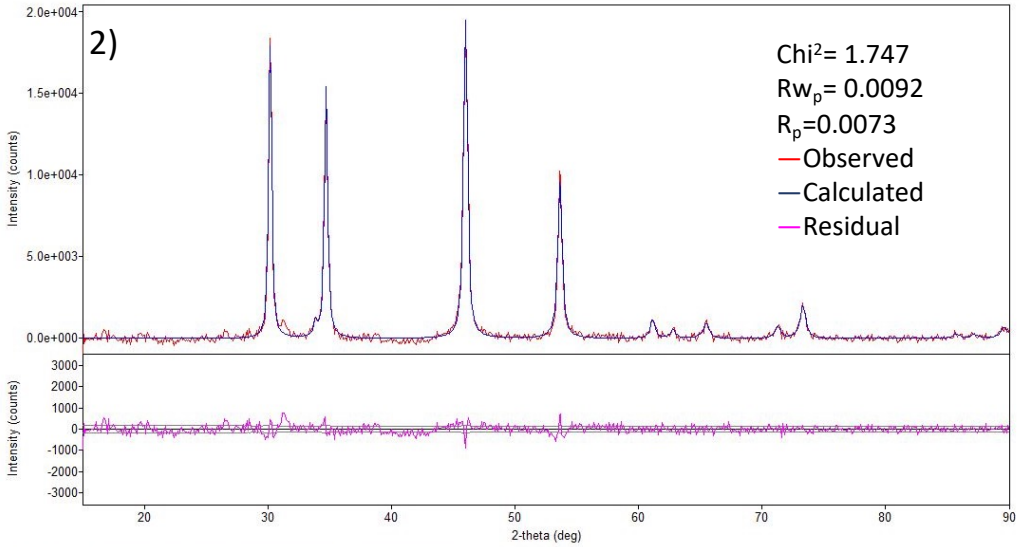
2)
Chi²= 1.747
Rwp= 0.0092
Rp=0.0073
Observed
Calculated
Residual
Intensity (counts)
2-theta (deg)

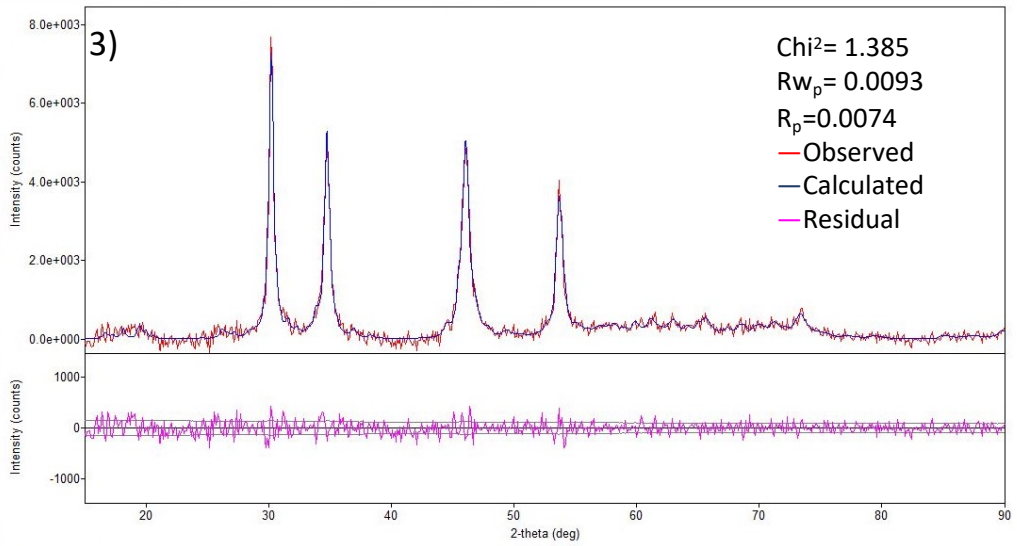
3)
Chi²= 1.385
Rwp= 0.0093
Rp=0.0074
Observed
Calculated
Residual
Intensity (counts)
2-theta (deg)

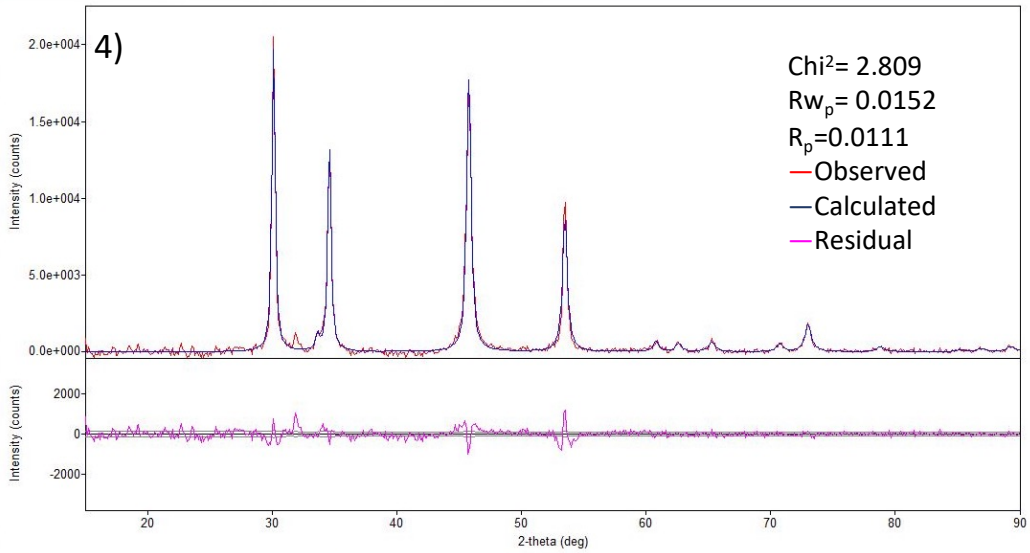
4)
Chi²= 2.809
Rw$_p$= 0.0152
R$_p$=0.0111
Observed
Calculated
Residual
Intensity (counts)
2-theta (deg)

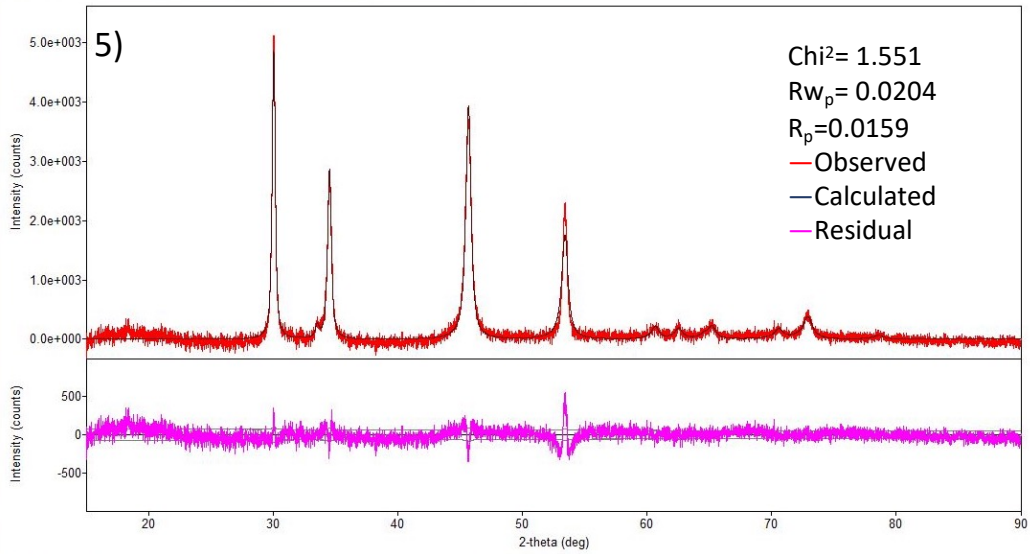
5)
Chi²= 1.551
Rw$_p$= 0.0204
R$_p$=0.0159
Observed
Calculated
Residual
Intensity (counts)
2-theta (deg)

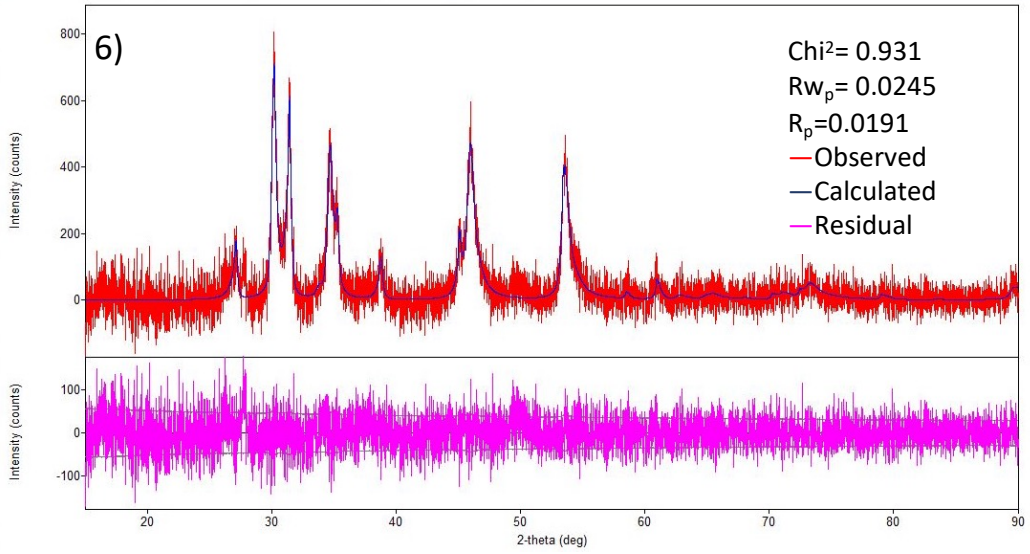
6)
Chi²= 0.931
Rw$_p$= 0.0245
R$_p$=0.0191
Observed
Calculated
Residual
Intensity (counts)
2-theta (deg)

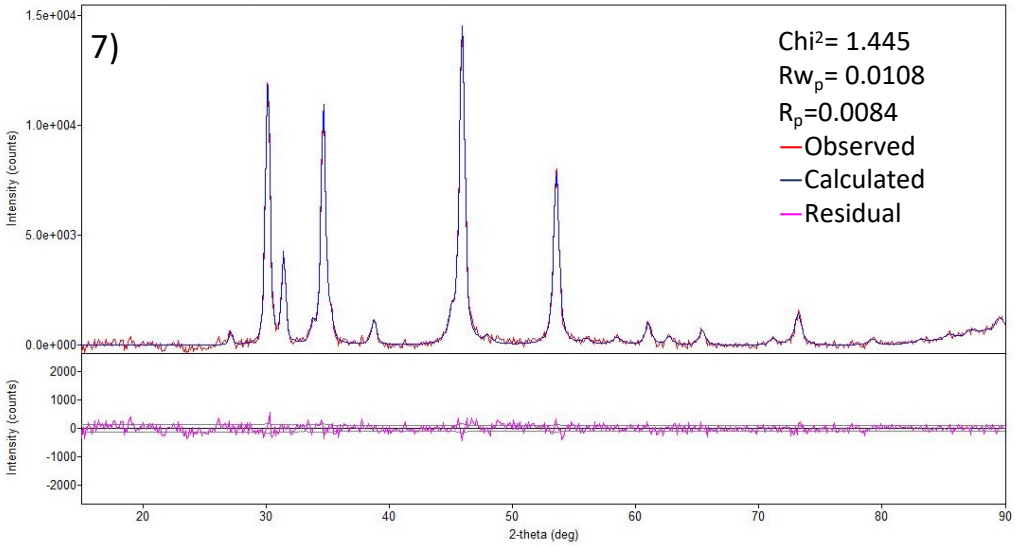
7)
Chi²= 1.445
Rw$_p$= 0.0108
R$_p$=0.0084
Observed
Calculated
Residual
Intensity (counts)
2-theta (deg)

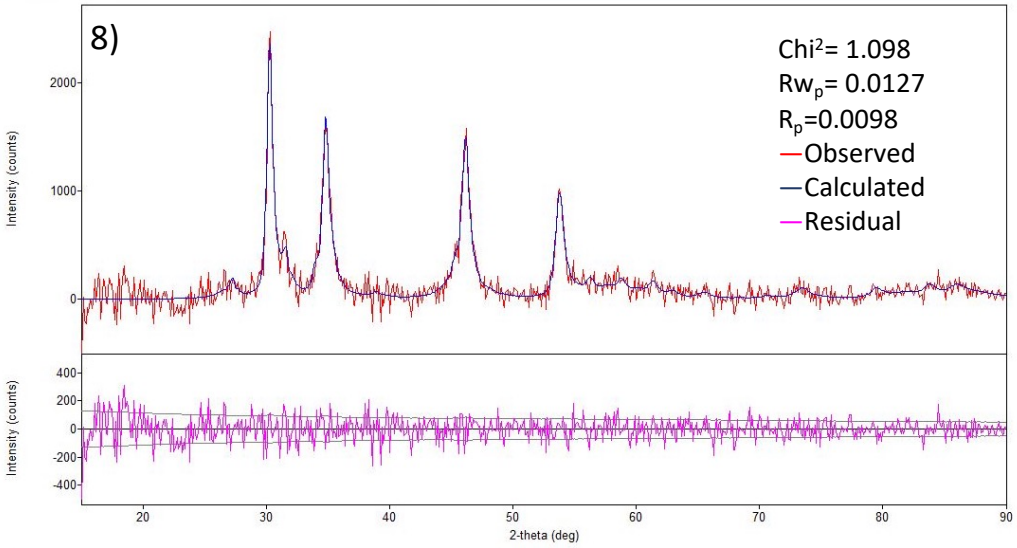
8)
Chi²= 1.098
Rw$_p$= 0.0127
R$_p$=0.0098
Observed
Calculated
Residual
Intensity (counts)
2-theta (deg)

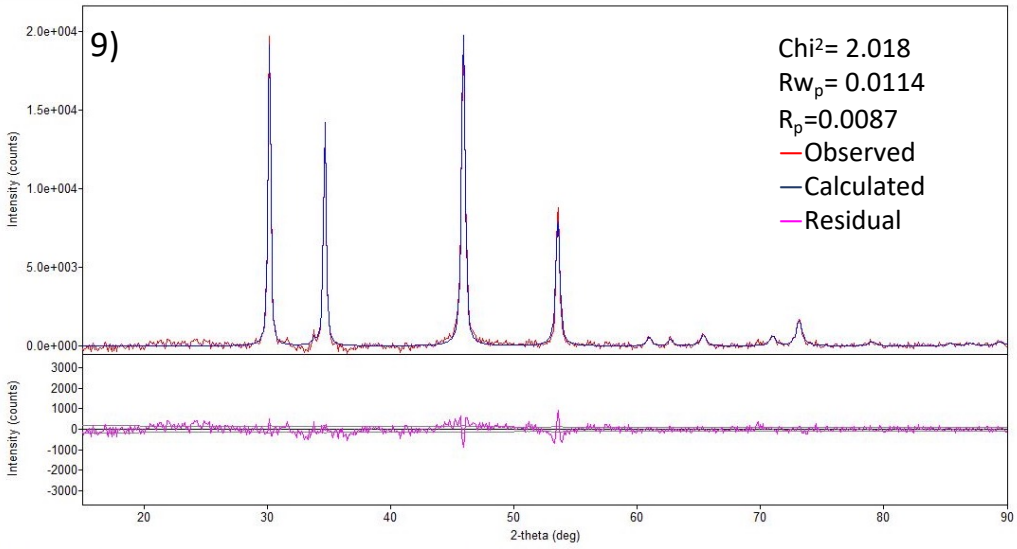
9)
Chi²= 2.018
Rw$_p$= 0.0114
R$_p$=0.0087
Observed
Calculated
Residual
Intensity (counts)
2-theta (deg)

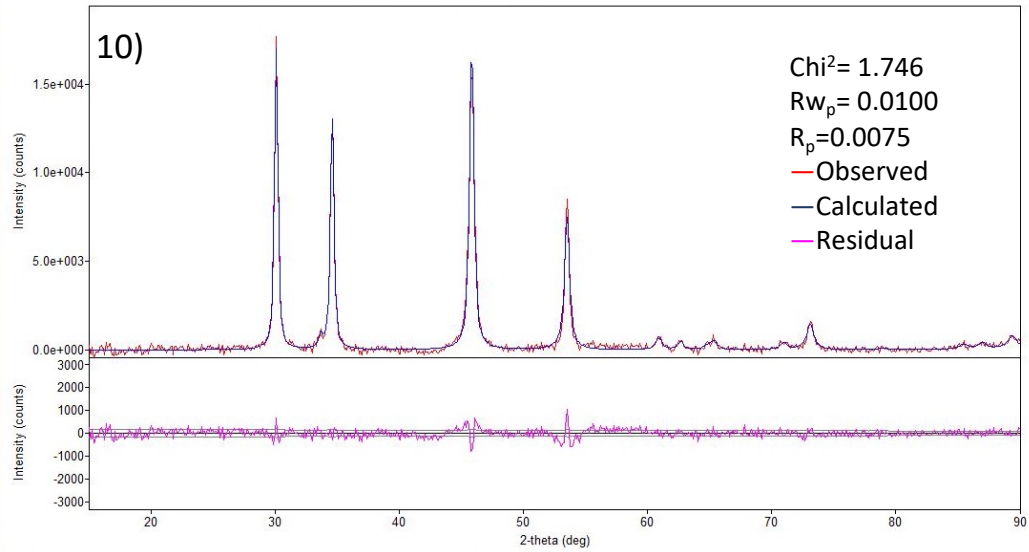
10)
Chi²= 1.746
Rwp= 0.0100
Rp=0.0075
Observed
Calculated
Residual
Intensity (counts)
2-theta (deg)

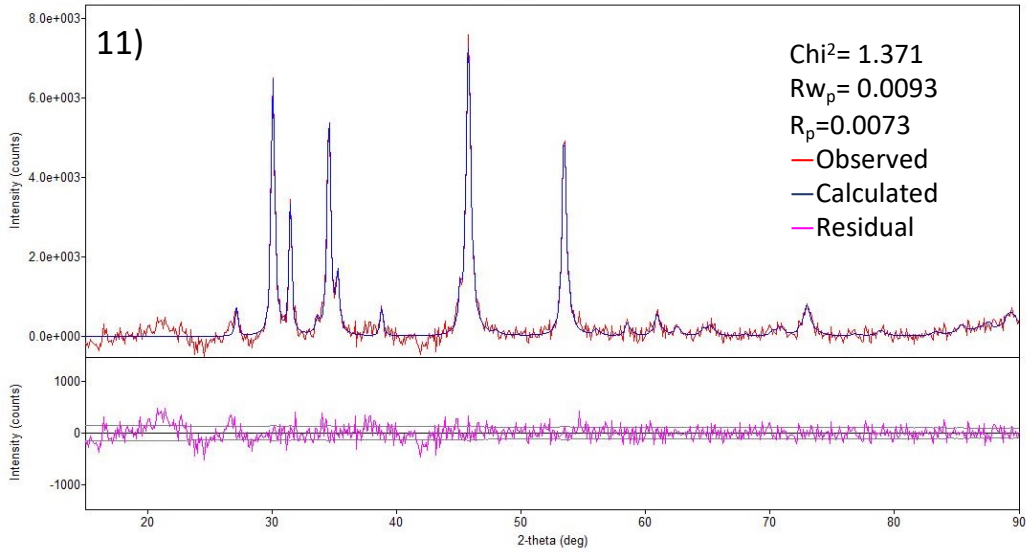
11)
Chi²= 1.371
Rwp= 0.0093
Rp=0.0073
Observed
Calculated
Residual
Intensity (counts)
2-theta (deg)

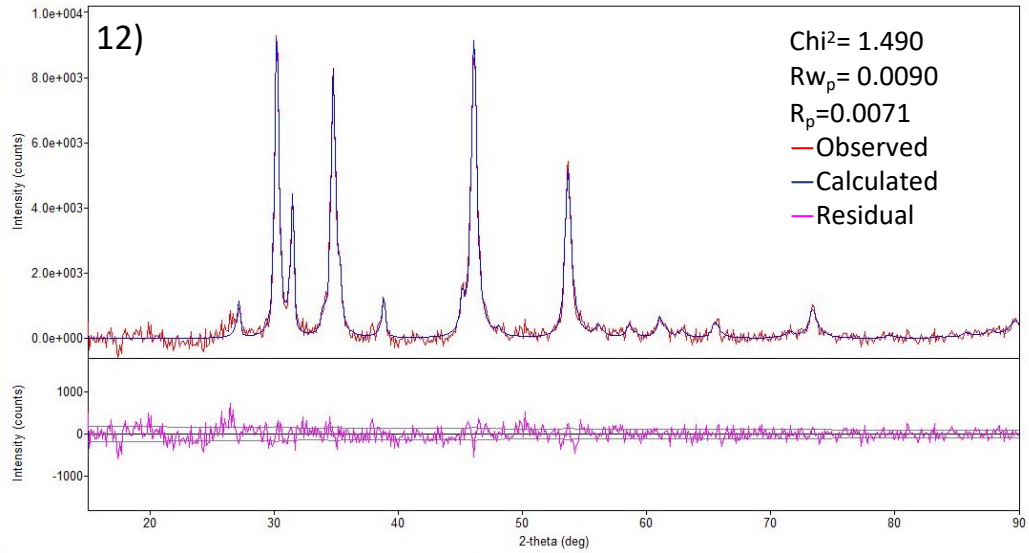
12)
Chi²= 1.490
Rwp= 0.0090
Rp=0.0071
Observed
Calculated
Residual
Intensity (counts)
2-theta (deg)

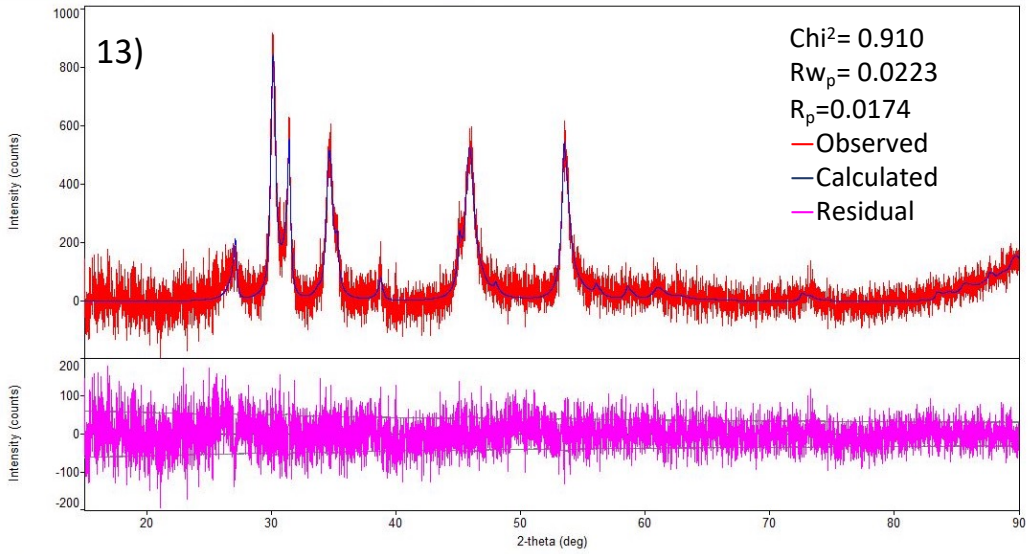
13)
Chi²= 0.910
Rwp= 0.0223
Rp=0.0174
Observed
Calculated
Residual
Intensity (counts)
2-theta (deg)

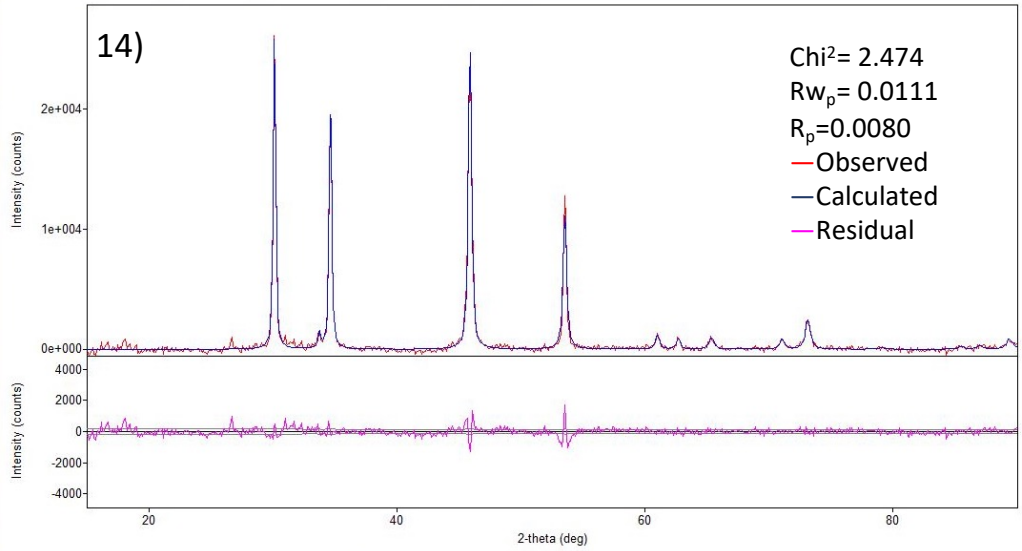
14)
Chi²= 2.474
Rwp= 0.0111
Rp=0.0080
Observed
Calculated
Residual
Intensity (counts)
2-theta (deg)

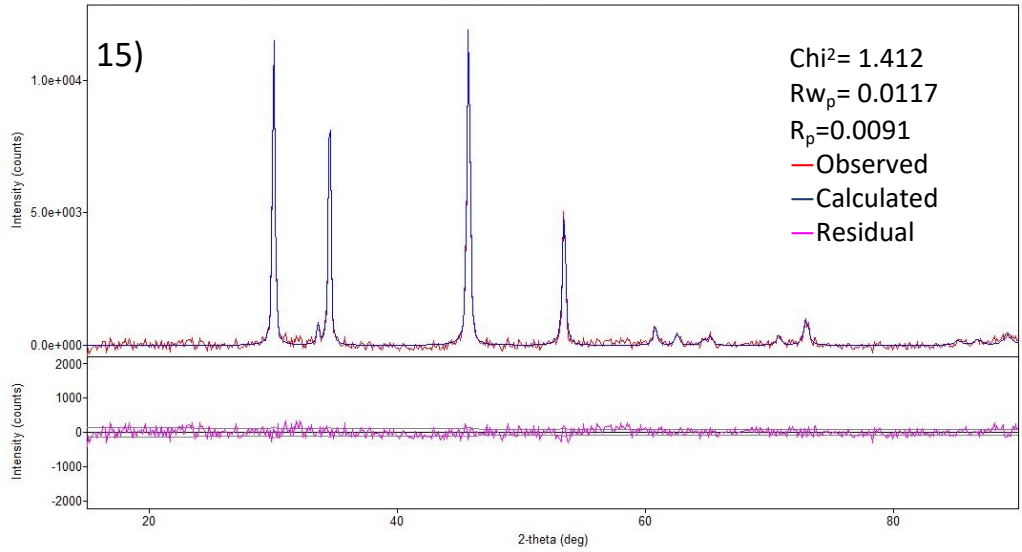
15)
Chi²= 1.412
Rwp= 0.0117
Rp=0.0091
Observed
Calculated
Residual
Intensity (counts)
2-theta (deg)

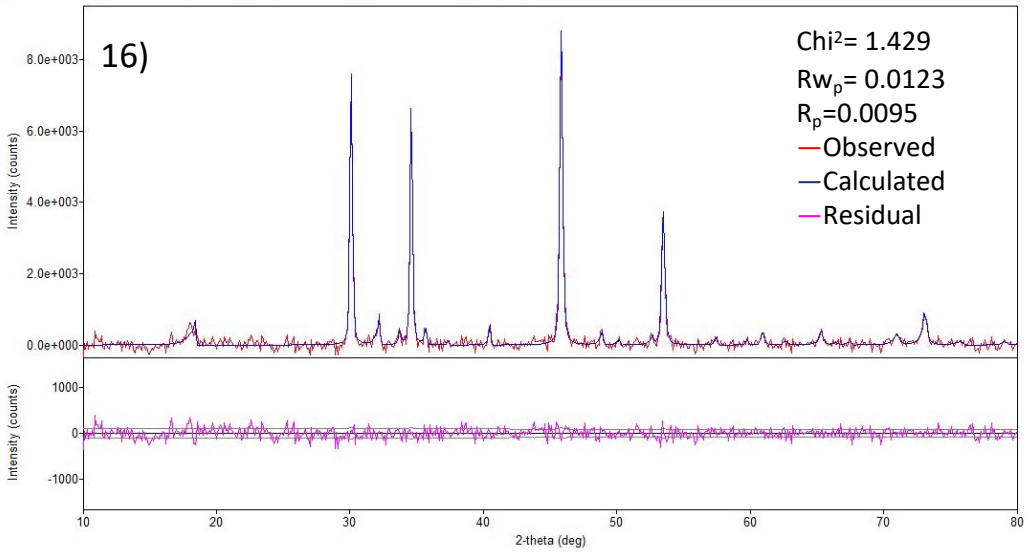
16)
Chi²= 1.429
Rwp= 0.0123
Rp=0.0095
Observed
Calculated
Residual
Intensity (counts)
2-theta (deg)

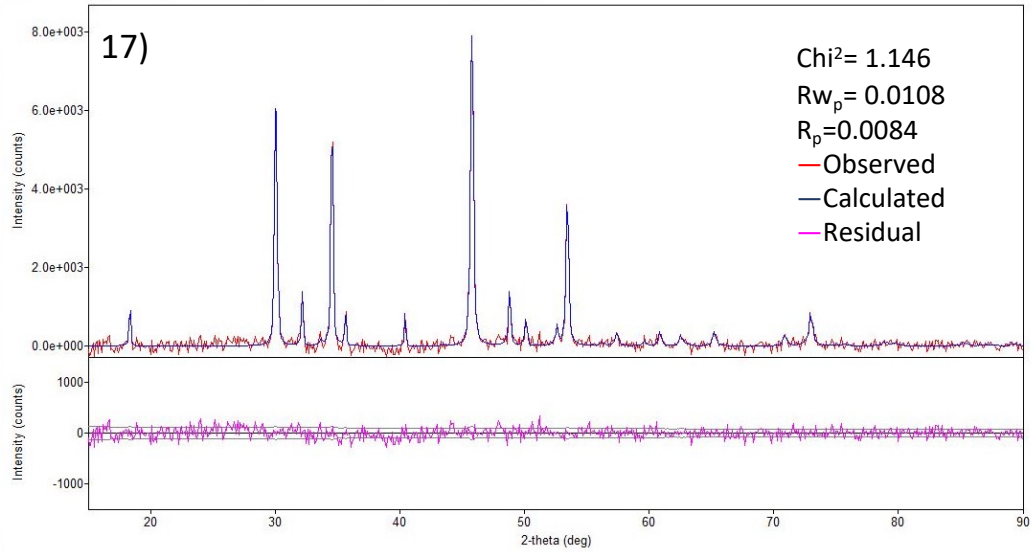
17)
Chi²= 1.146
Rwp= 0.0108
Rp=0.0084
Observed
Calculated
Residual
Intensity (counts)
2-theta (deg)

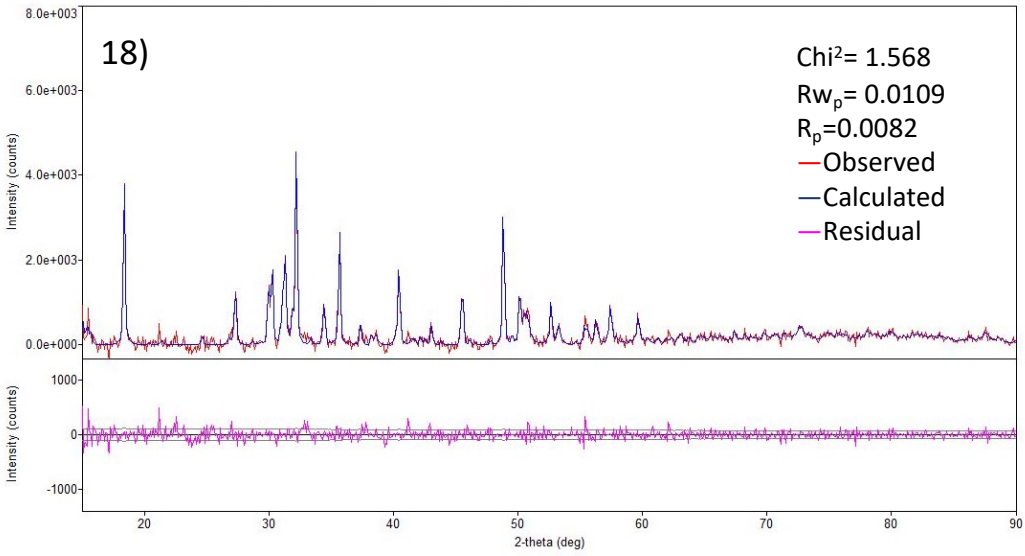
18)
Chi²= 1.568
Rwp= 0.0109
Rp=0.0082
Observed
Calculated
Residual
Intensity (counts)
2-theta (deg)

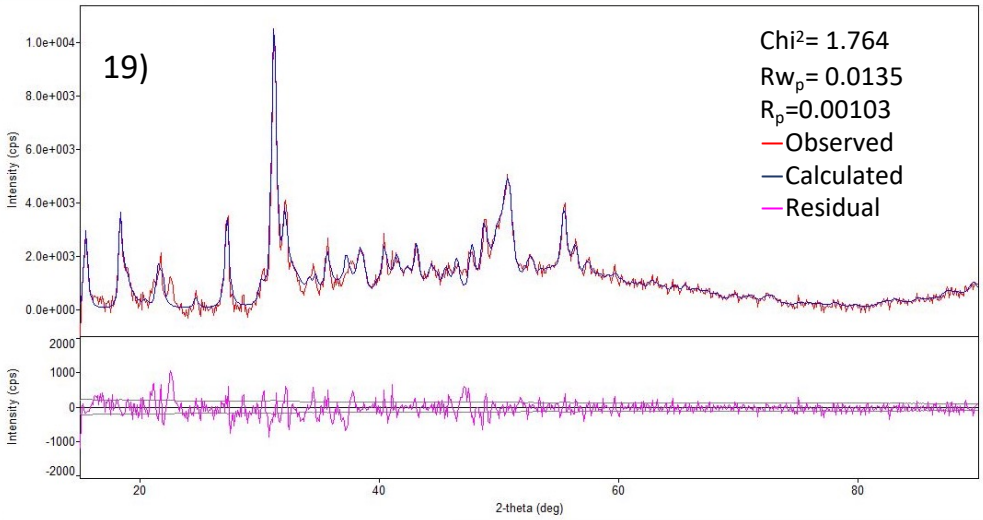
19)
Chi²= 1.764
Rwp= 0.0135
Rp=0.00103
Observed
Calculated
Residual
Intensity (cps)
2-theta (deg)

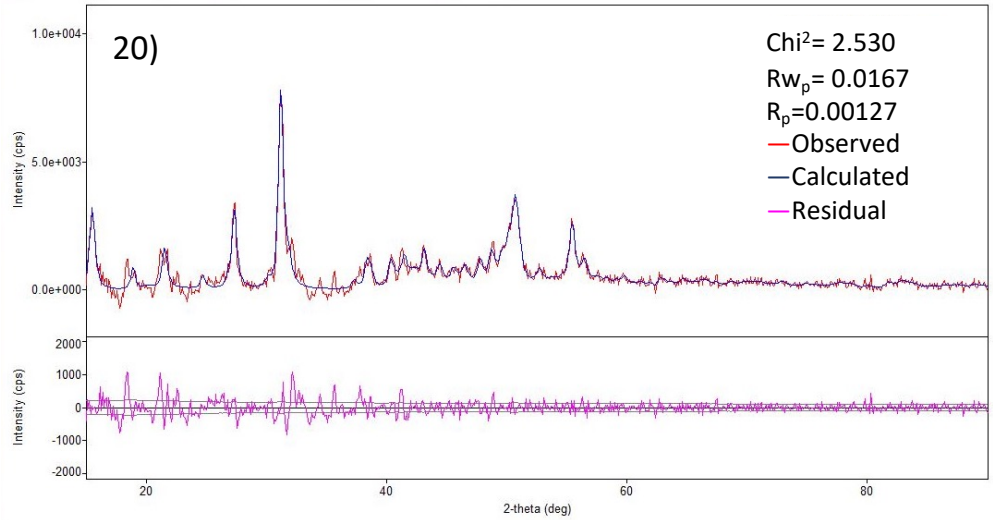
20)
Chi²= 2.530
Rwp= 0.0167
Rp=0.00127
Observed
Calculated
Residual
Intensity (cps)
2-theta (deg)

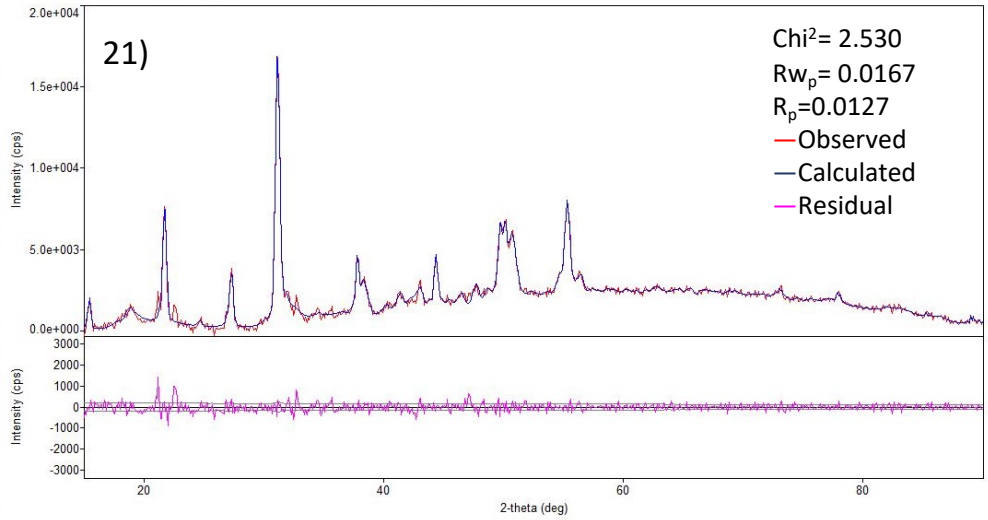
21)
Chi²= 2.530
Rwp= 0.0167
Rp=0.0127
Observed
Calculated
Residual
Intensity (cps)
2-theta (deg)

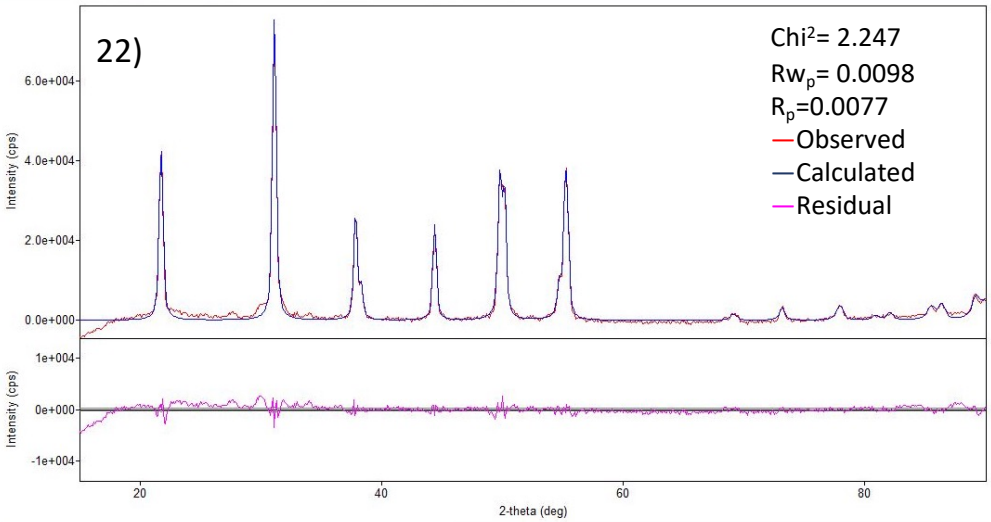
22)
Chi²= 2.247
Rwp= 0.0098
Rp=0.0077
Observed
Calculated
Residual
Intensity (cps)
2-theta (deg)

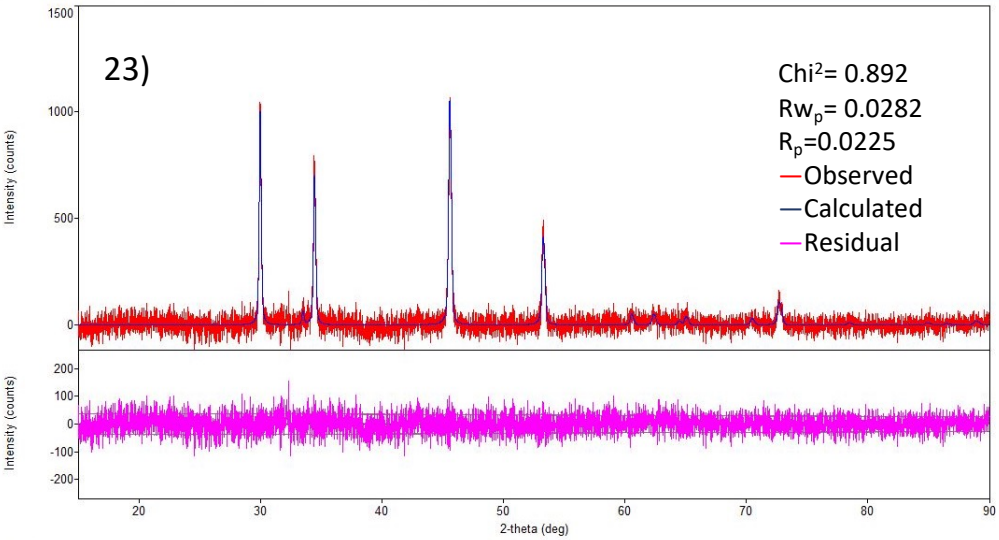
23)
Chi²= 0.892
Rwp= 0.0282
Rp=0.0225
Observed
Calculated
Residual
Intensity (counts)
2-theta (deg)

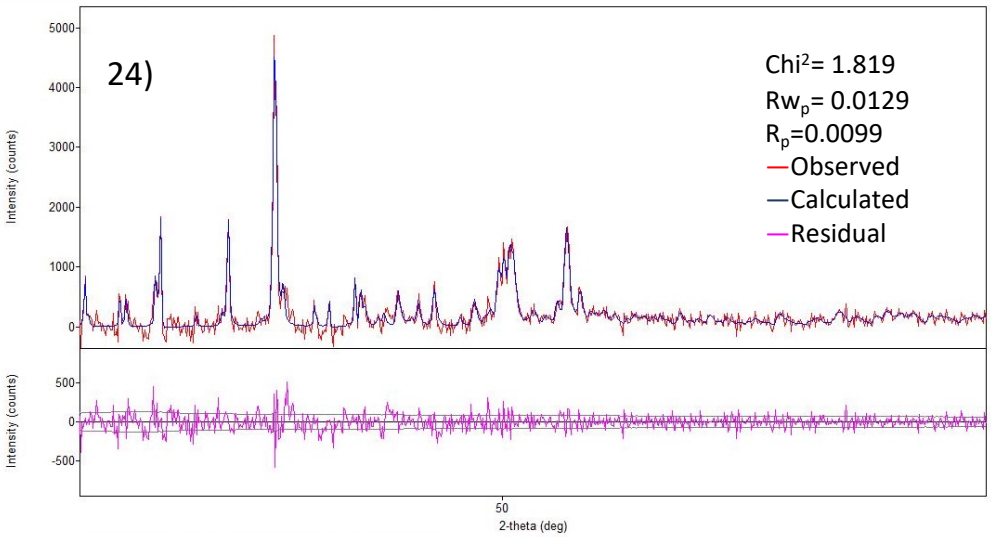
24)
Chi²= 1.819
Rwp= 0.0129
Rp=0.0099
Observed
Calculated
Residual
Intensity (counts)
2-theta (deg)

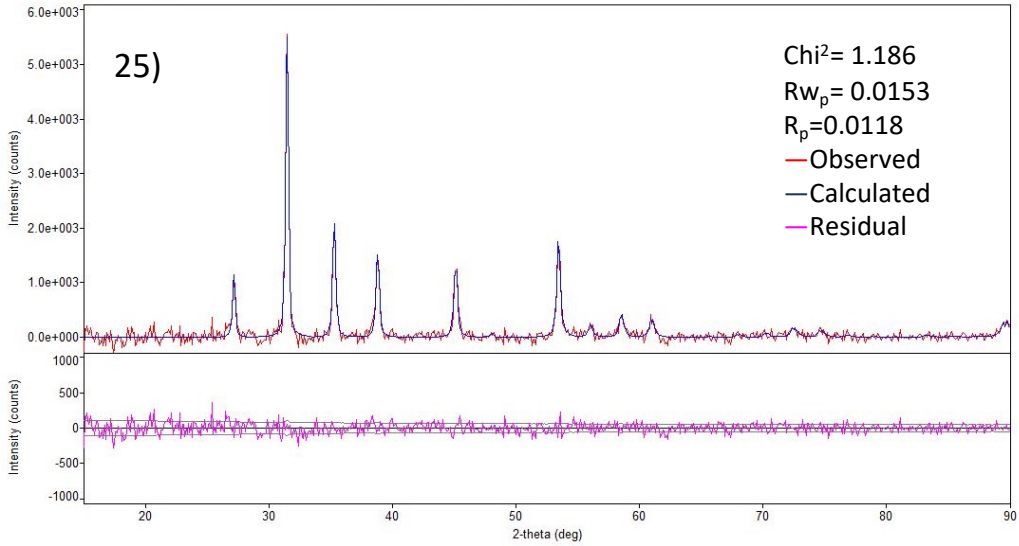
25)
Chi²= 1.186
Rwp= 0.0153
Rp=0.0118
Observed
Calculated
Residual
Intensity (counts)
2-theta (deg)

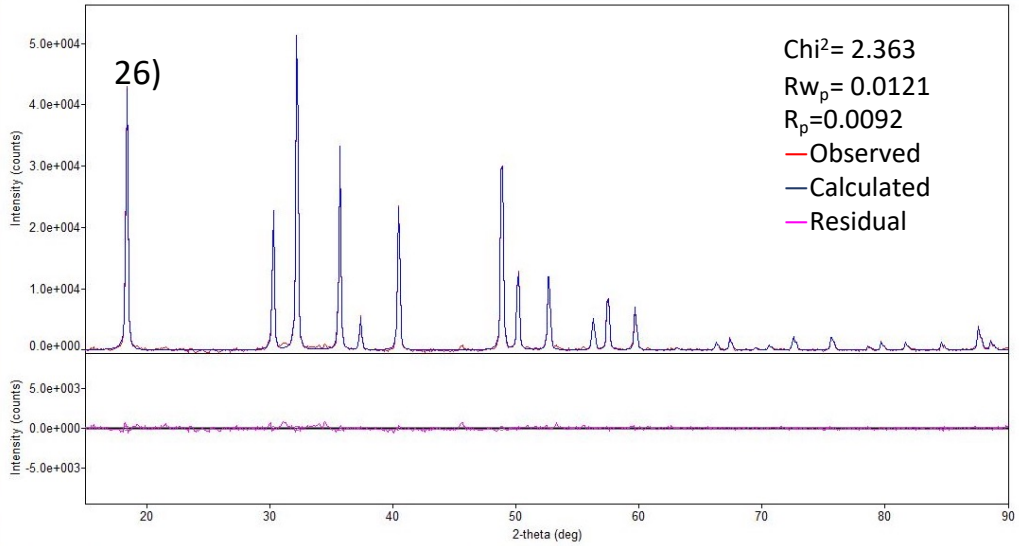
26)
Chi²= 2.363
Rwp= 0.0121
Rp=0.0092
Observed
Calculated
Residual
Intensity (counts)
2-theta (deg)

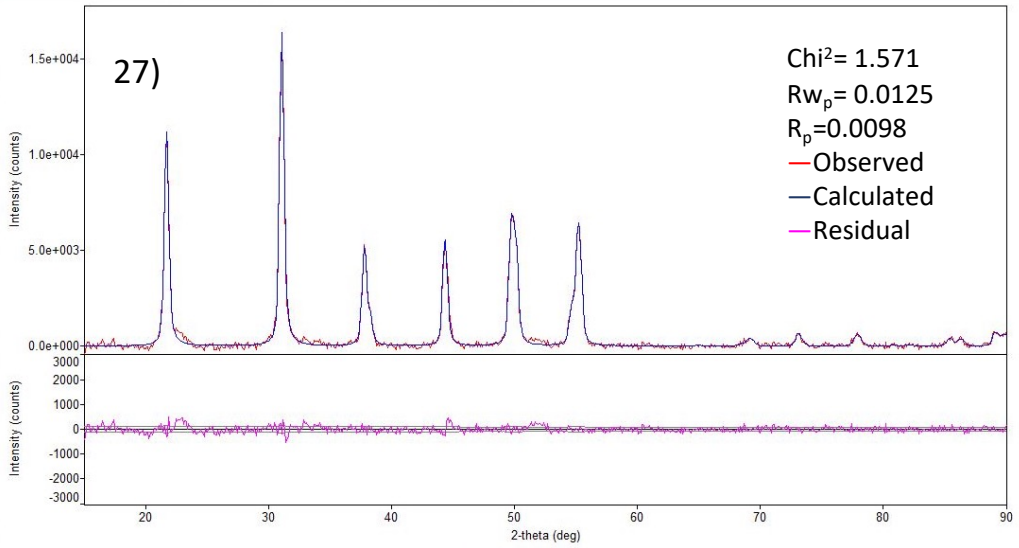
27)
Chi²= 1.571
Rwp= 0.0125
Rp=0.0098
Observed
Calculated
Residual
Intensity (counts)
2-theta (deg)

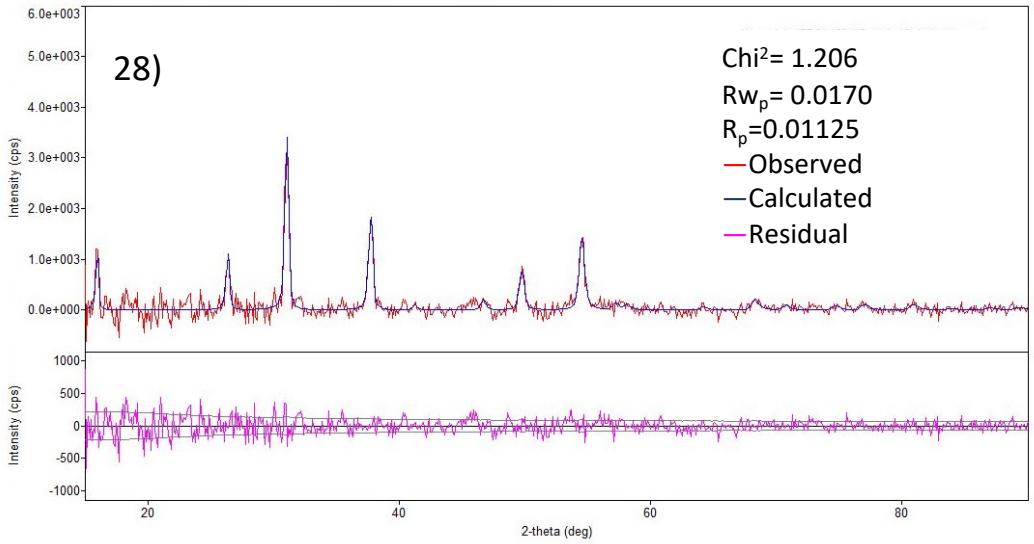
28)
Chi²= 1.206
Rw_p= 0.0170
R_p=0.01125
Observed
Calculated
Residual
Intensity (cps)
6.0e+003
5.0e+003
4.0e+003
3.0e+003
2.0e+003
1.0e+003
0.0e+000
1000
500
0
-500
-1000
20
40
60
80
2-theta (deg)